

DYNAMIC COUPLING IN A MODEL ROCKET COMBUSTOR

A Dissertation

Submitted to the Faculty

of

Purdue University

by

Tristan L. Fuller

In Partial Fulfillment of the

Requirements for the Degree

of

Doctor of Philosophy

August 2019

Purdue University

West Lafayette, Indiana

**THE PURDUE UNIVERSITY GRADUATE SCHOOL
STATEMENT OF DISSERTATION APPROVAL**

Prof. William E. Anderson, Chair

School of Aeronautics and Astronautics

Prof. Robert P. Lucht

School of Mechanical Engineering

Prof. Stephen D. Heister

School of Aeronautics and Astronautics

Prof. Carson D. Slabaugh

School of Aeronautics and Astronautics

Dr. Swanand V. Sardeshmukh

School of Aeronautics and Astronautics

Approved by:

Prof. Weinong W. Chen

Head of the School Graduate Program

ACKNOWLEDGMENTS

I would not have been able to progress without the patience and support from my love Ivana, thank you. I have been fortunate to have the advisement from Prof. W. E. Anderson with the assistance of Dr. S. V. Sardeshmukh. I would like to thank BJ Austin for his help and taking the time to assist me with this project. I would also like to thank Scott Meyer, Rohan Gejji, Mike Bedard, Brandon Kan, Zach Hallum and Matthew Casiano for their insight and helpful advice. I would like to give special thanks to Felix Kuehne, Wolfgang Armbruster and Hideo Sunakawa without whom the experiment would not have progressed nearly as efficiently. I would like to thank my committee for taking the time to be a part of the review process.

TABLE OF CONTENTS

	Page
LIST OF TABLES	vii
LIST OF FIGURES	viii
SYMBOLS	xix
ABSTRACT	xxi
1 INTRODUCTION	1
1.1 Problem Identification	1
1.2 Motivation of Study	2
1.3 Objectives and Approach	3
1.3.1 Approach	3
1.3.2 Objectives	4
1.4 Document Structure	6
2 BACKGROUND AND THEORY	9
2.1 Instabilities in Rocket Engines	9
2.1.1 Chug and Buzz	10
2.1.2 Thermoacoustic	10
2.1.3 Recent Work on Combustion Driven Thermoacoustic Instabilities	11
2.2 Fundamentals	17
2.2.1 Acoustics	20
2.2.2 Hydrodynamic Structures and Mixing	25
2.2.3 Flame Characterization	33
2.2.4 Flame and Fluid State Indicators	36
2.3 Measurement Techniques	41
2.3.1 Acoustic and Pressure Measurements	42
2.3.2 Temperature Measurements	47
2.3.3 Optical Measurements	47
2.4 Verification and Validation	50
3 EXPERIMENTAL APPROACH	53
3.1 Experimental Setup	57
3.1.1 Experiment Parameters	57
3.1.2 Design Details	59
3.1.3 Design, Analysis and Verification of Target Measurements	86
3.2 Observation and Overview of Experimental Results	96
3.2.1 Basic Operation	96

	Page
3.2.2	Configuration Listing 99
3.2.3	Performance and Mean Properties 101
3.2.4	Dynamic Trends 106
4	METHODS OF DATA ANALYSIS 114
4.1	Statistics and Stationarity 114
4.2	Correlation, Transformation and Filtering Methods 115
5	ANALYSIS OF EXPERIMENTAL RESULTS 117
5.1	Base Level Analysis 117
5.1.1	Measurement Verification 118
5.1.2	Assumption Testing 122
5.2	Analysis of Main Features 127
5.2.1	Identification of Acoustic Modes 128
5.2.2	Intermittency and Modulation 135
5.2.3	Thermoacoustic and Hydrodynamic Investigation 140
5.3	Auxiliary Analysis and Interesting Features 155
5.3.1	Chug and Buzz 155
5.3.2	Growth Rate 160
5.3.3	Exceptional Test Case 161
5.4	Summary of Experimental Results 162
6	CFD MODEL COMPARISON 164
6.1	Global Characteristic Features 167
6.2	Dynamics 174
6.2.1	Acoustics 174
6.2.2	Combustion and Heat Release 184
6.2.3	Hydrodynamic Features 196
6.2.4	Coupling Characteristics 203
6.3	Summary 219
7	CONCLUSIONS 221
7.1	Summary of Observations 221
7.2	Comments on Objectives 225
7.3	Future Work 228
	REFERENCES 230
A	SELECTED IMPORTANT MECHANICS 238
A.1	Diffusion 238
A.2	Acoustic Theory Pertaining to Circular Ducts 239
A.2.1	1D Transfer Matrices for Selected Geometries of a Duct 239
A.2.2	Three Dimensional Waves in Inviscid Moving Medium within a Circular Duct 241
B	DATA TABLES 242

	Page
C AUXILIARY EXPERIMENTAL DATA	248
C.1 General Trends	248
D TECHNICAL DATA	255
D.1 PMT Calibration Curves [86]	255
E PLUMBING AND INSTRUMENTATION DIAGRAMS	259

LIST OF TABLES

Table	Page
2.1 Powers of x describing the downstream variation of U_s , l and Re_l . Also listed are the values of Re_T and are independent of position. [38]	27
3.1 HAMSTER design parameters as per AFOSR project.	58
3.2 HAMSTER nominal flow conditions and typical ranges.	58
3.3 HAMSTER nominal design geometric configuration.	62
3.4 Comparison of designed and actual dimensions of the HAMSTER injector.	62
3.5 Critical thermophysical properties of propellants injected into HAMSTER.	77
3.6 Changes to macroscale flow parameters due to change in input flow parameters. Some controlled outcomes are determined by specific geometric changes to the injector.	84
3.7 Summary of instrumentation and their locations.	87
3.8 Geometric configurations, testing parameters and hypotheses tested in HAMSTER.	99
3.9 Geometric configurations, testing parameters and hypotheses tested in HAMSTER (Continued).	100
6.1 Comparison summary between the global characteristics of the experimental and simulation data.	169
A.1 Arguments of the functions associated with transverse (m) and radial (n) modes.	241
B.1 Lennard-Jones parameters for selected species [101].	242
B.2 Collision integrals for diffusivity, viscosity and thermal conductivity based on Lennard-Jones potential.	243
B.3 HAMSTER density ratio for different propellant temperatures [K].	245
B.4 HAMSTER velocity ratio for different propellant temperatures [K].	246
B.5 HAMSTER momentum flux ratio for different propellant temperatures [K].	247

LIST OF FIGURES

Figure	Page
2.1 Simulated Rayleigh index and phase maps for thermoacoustic cycling in CVRC. [11]	12
2.2 Description of acoustic pulse timing in the CVRC. [13]	14
2.3 Acoustic response in the CVRC with respect to oxidizer temperature. [14]	15
2.4 Relative acoustic timing in the CVRC. The acoustic timing is defined as the amount of time it would take an acoustic pulse to travel the full distance of the duct and back to its source. [14]	15
2.5 Hypothesized coupling mechanisms for self-excited thermoacoustic instabilities in a single element combustor.	16
2.6 Effect of oscillating boundary layer on the velocity profile in the injector recess in the CVRC. [14]	19
2.7 Mixing layer models of unequal injected velocities for two geometric configurations. [40]	28
2.8 Large-structure array and induction velocities in vortex convection frame. [50]	30
2.9 Visualization of an unstable RayleighTaylor instability configuration where baroclinic torque at the interface creates vorticity and induces a velocity field that increases the baroclinic torque. [53]	32
2.10 Baroclinic torque action along the shear layer, where the dense fuel is against the wall and the less dense oxidizer in the core. [13]	33
2.11 Characteristic parametric relationships of premixed turbulent combustion. The Reynolds numbers are based on Kolmogorov microscales, Taylor microscales and integral scales respectively. [54]	34
2.12 Possible reaction pathway diagram for the oxidation of methane. [55] . . .	40
2.13 Absorption affected spectral emission line shape of OH.	42
2.14 Non-dimensionalized error in static pressure measurement for different geometries and Reynolds numbers. [68]	44
2.15 Temperature and geometry dependence of Helmholtz resonance of Kulite pressure transducer cavity. [71]	46

Figure	Page
2.16 Three aspects of model validation.	51
3.1 Time averages of CVRC simulation data.	53
3.2 DMD spectrum of vorticity from CVRC simulation data.	54
3.3 DMD spectrum of pressure from HAMSTER simulation data.	55
3.4 DMD spectrum of heat release from HAMSTER simulation data.	56
3.5 Cross-section view of HAMSTER.	59
3.6 Hierarchy of design criteria.	60
3.7 Acoustic reflection coefficient due to the specific impedance change between oxidizer and combustion gases at the dump plane.	64
3.8 Evolution of fundamental system acoustic mode during resonance with mean flow. The acoustic length is modeled from the oxidizer manifold distribution plate to the exit nozzle, both of which are choked providing a hard acoustic boundary condition.	65
3.9 Map of resonant acoustic frequencies expected in HAMSTER during nominal operation. The dark line denotes the 1D assumption limit based on the oxidizer manifold diameter.	66
3.10 Possible fundamental acoustic mode shape, showing the velocity fluctuation near the head-end.	67
3.11 A priori acoustic response of HAMSTER based on mean flow and an arbitrary input impedance for an oxidizer post of 6".	68
3.12 Schematic representation of the fuel injector assembly. With choke ring (Left) and without (Right), allowing coupling participation of fuel manifold during injection.	70
3.13 Effect of losses on flow in oxidizer post as a function of oxidizer temperature and hypothetical stagnation temperature of the flow in the recess.	72
3.14 Stagnation temperature of propellant mixture assuming immediate heat transfer from combustion.	72
3.15 Schematic of flow and vortex generation over the fuel collar.	73
3.16 Entrainment ratio trend for change in oxidizer temperature. Values above the threshold represent entrainment of oxidizer, whereas below represents entrainment of fuel.	75
3.17 Ignition delay of CH_4/O_2 for different local equivalence ratios and temperatures.	80

Figure	Page
3.18 Reaction metrics of CH_4/O_2 for different local temperatures.	81
3.19 Instrumentation type and measurement locations on HAMSTER.	86
3.20 Port designs affected by Helmholtz resonance effect.	90
3.21 Acoustic attenuation in combustion chamber due to Helmholtz resonance of HF pressure ports. The red lines signify a band where the vortex shedding frequency of the collar is expected to be.	91
3.22 Schematic of the fiber optically coupled optical module, housing the optomechanics and PMTs to measure chemiluminescence [85].	92
3.23 Line losses expected to occur during transmission from chamber to PMT modules. [86].	93
3.24 PMT port location and design to measure chemiluminescence in the combustion chamber with high spatial and temporal resolution.	94
3.25 PMT probe volume domains. (Left) Ideal port geometry, (Right) extreme fitting case due to tolerance bounds.	95
3.26 Fraction of light bias within a typical emission probe volume within HAMSTER.	96
3.27 Pressure trace during a typical hotfire cycle.	97
3.28 Temperature trace during a typical hotfire cycle.	97
3.29 Combustion efficiency of tests conducted in HAMSTER. The trend line is fitted to the nominal geometry, oxidizer rich cases.	101
3.30 Injector pressure drop of tests conducted in HAMSTER.	102
3.31 Density ratio of propellants injected during tests conducted in HAMSTER.	104
3.32 Velocity ratio of propellants injected during tests conducted in HAMSTER.	104
3.33 Momentum flux ratio of propellants injected during tests conducted in HAMSTER.	105
3.34 Head end wall temperature during tests conducted in HAMSTER.	105
3.35 Entrainment of fuel during tests conducted in HAMSTER.	107
3.36 Thermoacoustic chug amplitude as a function of oxidizer temperature. . .	108
3.37 Thermoacoustic chug frequency as a function of oxidizer temperature. . .	108
3.38 Thermoacoustic fundamental mode amplitude as a function of oxidizer temperature.	109

Figure	Page
3.39 Thermoacoustic fundamental mode frequency as a function of oxidizer temperature.	110
3.40 Reflection coefficient at the chamber/ox post interface.	111
3.41 Thermoacoustic mode amplitude comparison, showing the approximate threshold at which a strong thermoacoustic coupling takes place.	112
5.1 Raw pressure data acquired at the head end of the chamber, 0.300" downstream of the dump plane.	119
5.2 Raw pressure data acquired at the aft end of the chamber, 13.150" downstream of the dump plane.	120
5.3 PSDs of the port Helmholtz response of the pressure transducers in the oxidizer post and the chamber for various oxidizer temperatures.	121
5.4 Cross correlation between data collected by transducers at head end of chamber 0.300" downstream for the dump plane.	123
5.5 PSD of pressure response in the oxidizer manifolds as a function of oxidizer temperature.	124
5.6 Expected acoustic modes in the oxidizer manifold as a function of oxidizer temperature.	125
5.7 PSDs of the pressure response in the oxidizer post and the chamber for various oxidizer temperatures.	126
5.8 Comparison of the expected acoustic response with the PSD of the experimental data collected for an oxidizer temperature of 440K.	128
5.9 Comparison of the expected acoustic response with the PSD of the experimental data collected for an oxidizer temperature of 600K.	129
5.10 Comparison of the expected acoustic response with the PSD of the experimental data collected for an oxidizer temperature of 700K.	130
5.11 Low frequency acoustic mode shape predicted by 1D model of HAMSTER.	131
5.12 High frequency, one possible fundamental acoustic mode shape predicted by 1D model of HAMSTER.	131
5.13 Zoomed in response of the fundamental acoustic mode shape, predicted by 1D model of HAMSTER, in the contracting portion of the nozzle.	132
5.14 Acoustic mode shape comparison between the experiment and theoretical prediction for an oxidizer temperature of 440K.	133

Figure	Page
5.15 Acoustic mode shape comparison between the experiment and theoretical prediction for an oxidizer temperature of 600K.	134
5.16 Acoustic mode shape comparison between the experiment and theoretical prediction for an oxidizer temperature of 700K.	134
5.17 Wavelet transform of data from head end of chamber. The white dotted lines represent the cone of influence; outside of which the edge effects of the wavelet become significant.	136
5.18 Raw pressure data acquired at the head end of the chamber, 0.300" downstream of the dump plane. Zoomed in plot of Figure 5.1 on an interval of 80 <i>ms</i>	137
5.19 Instantaneous changes in the dominant high frequency mode for the case with an oxidizer temperature of 700K.	138
5.20 Bispectrum analysis for the case with an oxidizer temperature of 700K.	139
5.21 Number density (m^{-3}) distributions of potential absorbing species within HAMSTER during combustion, as predicted by the prior simulations.	141
5.22 Transmissivity of CH and OH as a function of number density for varying optical path lengths [66].	142
5.23 PSD comparison between CH* PMT and pressure data for an oxidizer temperature of 440K.	143
5.24 PSD comparison between CH* PMT and pressure data for an oxidizer temperature of 600K.	144
5.25 PSD comparison between CH* PMT and pressure data for an oxidizer temperature of 700K.	145
5.26 Phase relationship between the CH* chemiluminescence and pressure signals for the thermoacoustic chug mode, as a function of oxidizer temperature.	146
5.27 Phase relationship between the CH* chemiluminescence and pressure signals for the thermoacoustic 1L mode, as a function of oxidizer temperature.	147
5.28 Magnitude squared coherence between the CH* and pressure measurements in the recess, for an oxidizer temperature of 440K.	150
5.29 Magnitude squared coherence between the CH* and pressure measurements at the head end of the chamber, for an oxidizer temperature of 440K.	150
5.30 Magnitude squared coherence between the CH* and pressure measurements in the recess, for an oxidizer temperature of 600K.	151

Figure	Page
5.31 Magnitude squared coherence between the CH* and pressure measurements at the head end of the chamber, for an oxidizer temperature of 600K.	152
5.32 Magnitude squared coherence between the CH* and pressure measurements in the recess, for an oxidizer temperature of 700K.	152
5.33 Magnitude squared coherence between the CH* and pressure measurements at the head end of the chamber, for an oxidizer temperature of 700K.	153
5.34 Summary of higher frequency modes calculated by the magnitude squared coherence between the CH* and pressure measurements.	153
5.35 Comparison of estimated vortex shedding frequency off of the fuel collar based on the oxidizer flow, and the high frequency magnitude squared coherence data summarized in Figure 5.34.	154
5.36 Chug predictions using models stipulated in Casiano's thesis [4]; for the case with an oxidizer temperature of 440K.	156
5.37 Chug predictions using models stipulated in Casiano's thesis [4]; for the case with an oxidizer temperature of 600K.	157
5.38 Chug predictions using models stipulated in Casiano's thesis [4]; for the case with an oxidizer temperature of 700K.	158
5.39 Chug response in the oxidizer manifold for all oxidizer temperature cases. The interval of the time series is over 0.4s	159
5.40 Chug response in the chamber for all oxidizer temperature cases. The interval of the time series is over 0.4s	159
5.41 Growth of the longitudinal acoustic mode proceeding a transition from limit cycle to chug, for the case with an oxidizer temperature of 700K. The correlation factor of the exponential fit was 0.915.	160
5.42 PSDs of two consecutive tests at the same operating conditions.	161
6.1 Computational domain for the simulations of HAMSTER [96].	165
6.2 Detailed view of the mesh in the vicinity of the injector recess and dump plane [96].	165
6.3 Simulated average near-wall gas temperatures at the head end of the combustor with comparable data from the experiments.	170

Figure	Page
6.4 Qualitative comparison of the linearly detrended pressure traces between the simulation and experiment at oxidizer temperatures of 400K and 440K respectively.	172
6.5 Qualitative comparison of the linearly detrended pressure traces between the simulation and experiment at an oxidizer temperature of 700K.	173
6.6 Comparison of the PSDs between the simulation and experiment at an oxidizer temperature of 400K/440K.	175
6.7 DMD generated acoustic mode shapes for the 400K oxidizer temperature case. The scale ranges from red to blue, where red is the maximum amplitude and blue is the minimum amplitude.	176
6.8 Comparison of the PSDs between the simulation and experiment at an oxidizer temperature of 700K.	178
6.9 DMD generated acoustic mode shapes for the 700K oxidizer temperature case. The scale ranges from red to blue, where red is the maximum amplitude and blue is the minimum amplitude.	179
6.10 Simulated pressure in HAMSTER for an oxidizer temperature of 700K. This represents approximately one cycle of the fundamental acoustic mode.	180
6.11 Bispectral (bicoherence) analysis of the simulated pressure response.	182
6.12 Local temperature fluctuation with pressure during chug cycle.	183
6.13 Comparison of the pressure, CH* and OH* signals in the simulation, complementing the exact locations expected in the experiment, for an oxidizer temperature of 400K.	185
6.14 Comparison of the pressure, CH* and OH* signals in the simulation, complementing the exact locations expected in the experiment, for an oxidizer temperature of 700K.	186
6.15 Simulated heat release in HAMSTER for an oxidizer temperature of 700K.	187
6.16 Comparison of phase averaged signals of CH*, OH* and pressure at -0.350" (Injector Recess), for an oxidizer temperature of 400K/440K.	189
6.17 Comparison of phase averaged signals of CH*, OH* and pressure at 0.300" (Chamber Head End), for an oxidizer temperature of 400K/440K.	190
6.18 Comparison of phase averaged signals of CH*, OH* and pressure at -0.350" (Injector Recess), for an oxidizer temperature of 700K.	191
6.19 Comparison of phase averaged signals of CH*, OH* and pressure at 0.300" (Chamber Head End), for an oxidizer temperature of 700K.	192

Figure	Page
6.20 DMD generated heat release spatial maps for the 400K oxidizer temperature case.	193
6.21 DMD of the heat release in HAMSTER for an oxidizer temperature of 700K.	194
6.22 DMD generated heat release spatial maps for the 700K oxidizer temperature case.	195
6.23 DMD of vorticity in HAMSTER for an oxidizer temperature of 700K. . .	196
6.24 Oscillating oxidizer post centerline velocity near fuel collar tip for the case with an oxidizer temperature of 400K.	198
6.25 Oscillating oxidizer post centerline velocity near fuel collar tip for the case with an oxidizer temperature of 700K.	199
6.26 Simulated velocity profile of the oxidizer at the tip of the fuel collar. The evolution of the velocity profile and boundary layer of the oxidizer flow through 27.5ms, with increments of 0.75ms.	200
6.27 Simulated vortex shedding frequency off the fuel collar due to the oxidizer flow calculated using Equation 2.13. The vortex shedding is calculated using a boundary layer thickness approximated by using 95% of the mean velocity profile at each time step.	201
6.28 Schematic cross-section of where the PMT probe volumes intersect the domain.	203
6.29 Raw PMT data from experiment at 500K. Only diameter cutting measurements are shown in 6.29(b).	204
6.30 Raw PMT data from experiment at 700K. Only diameter cutting measurements are shown in 6.30(b).	204
6.31 Raw PMT data from the simulation at 400K. Only diameter cutting measurements are shown in 6.31(b).	205
6.32 Raw PMT data from simulation at 700K. Only diameter cutting measurements are shown in 6.32(b).	205
6.33 PSDs of PMT data from experiment at 500K, set 1 of 2.	206
6.34 PSDs of PMT data from experiment at 500K, set 2 of 2.	207
6.35 PSDs of PMT data from experiment at 700K, set 1 of 2.	207
6.36 PSDs of PMT data from experiment at 700K, set 2 of 2.	208
6.37 PSDs of PMT data from simulation at 400K, set 1 of 2.	209
6.38 PSDs of PMT data from simulation at 400K, set 2 of 2.	209

Figure	Page
6.39 PSDs of PMT data from simulation at 700K, set 1 of 2.	210
6.40 PSDs of PMT data from simulation at 700K, set 2 of 2.	210
6.41 CPSD of the chordal positions relative to the PMT measurement taken at 0.300" downstream of the dump plane, in the experiment for an oxidizer temperature of 500K.	211
6.42 CPSD of the chordal positions relative to the PMT measurement taken at 1.300" downstream of the dump plane, in the experiment for an oxidizer temperature of 500K.	212
6.43 CPSD of the axial chamber positions relative to the PMT measurement taken at 0.300" upstream of the dump plane (injector recess), in the experiment for an oxidizer temperature of 500K.	212
6.44 CPSD of the chordal positions relative to the PMT measurement taken at 0.300" downstream of the dump plane, in the experiment for an oxidizer temperature of 700K.	213
6.45 CPSD of the chordal positions relative to the PMT measurement taken at 1.300" downstream of the dump plane, in the experiment for an oxidizer temperature of 700K.	214
6.46 CPSD of the axial chamber positions relative to the PMT measurement taken at 0.300" upstream of the dump plane (injector recess), in the experiment for an oxidizer temperature of 700K.	214
6.47 CPSD of the chordal positions relative to the PMT data extracted at 0.300" downstream of the dump plane, in the simulation for an oxidizer temperature of 400K.	215
6.48 CPSD of the chordal positions relative to the PMT data extracted at 1.300" downstream of the dump plane, in the simulation for an oxidizer temperature of 400K.	216
6.49 CPSD of the axial chamber positions relative to the PMT data extracted at 0.300" upstream of the dump plane (injector recess), in the simulation for an oxidizer temperature of 400K.	216
6.50 CPSD of the chordal positions relative to the PMT data extracted at 0.300" downstream of the dump plane, in the simulation for an oxidizer temperature of 700K.	217
6.51 CPSD of the chordal positions relative to the PMT data extracted at 1.300" downstream of the dump plane, in the simulation for an oxidizer temperature of 700K.	218

Figure	Page
6.52 CPSD of the axial chamber positions relative to the PMT data extracted at 0.300" upstream of the dump plane (injector recess), in the simulation for an oxidizer temperature of 700K.	218
C.1 Thermoacoustic chug amplitude as a function of oxidizer temperature. . .	248
C.2 Thermoacoustic chug frequency as a function of oxidizer temperature. . .	249
C.3 Thermoacoustic chug amplitude as a function of frequency.	249
C.4 Thermoacoustic fundamental mode amplitude as a function of oxidizer temperature.	250
C.5 Thermoacoustic fundamental mode frequency as a function of oxidizer temperature.	250
C.6 Thermoacoustic fundamental mode amplitude as a function of frequency. . .	251
C.7 Thermoacoustic mode amplitude comparison for all test cases, showing the approximate threshold at which a strong thermoacoustic coupling takes place.	251
C.8 Raw pressure data acquired at the aft end of the chamber, showing the entropic fluctuations at the nozzle end, but minimally affecting the upstream mechanics.	252
C.9 PSDs of the fuel manifold response with and without the fuel manifold choke ring at an oxidizer temperature of 500K.	253
C.10 PSDs of the fuel manifold response with and without the fuel manifold choke ring at an oxidizer temperature of 700K.	253
C.11 PSDs of the injector recess response with and without the fuel manifold choke ring at an oxidizer temperature of 500K.	254
C.12 PSDs of the injector recess response with and without the fuel manifold choke ring at an oxidizer temperature of 700K.	254
D.1 Spectral responsivity of the H11903-210 PMTs from Hamamatsu.	255
D.2 Power to voltage calibration check for the PMTs over a series of gains set. . .	256
D.3 Voltage output calibration check versus gain for the PMTs for different levels of inputted light power.	256
D.4 Normalized spectral flux transmission into the PMTs over the selected bandwidths corresponding to OH^* , CH^* and truncated band of CO_2^* . . .	257
D.5 Normalized spectral transmission calibration for PMT collecting CH^* chemiluminescence signals.	257

Figure	Page
D.6 Normalized spectral transmission calibration for PMT collecting OH^* chemiluminescence signals.	258
D.7 Normalized spectral transmission calibration for PMT collecting truncated band of CO_2^* chemiluminescence signals.	258

SYMBOLS

Constants

c_0	speed of light in a vacuum
h	Planck's constant
k_B	Boltzmann's constant
N_A	Avogadro's number
R_u	universal gas constant
σ	molecular collision diameter
Ω	gas collision integral

Variables

a, ℓ, x, D, L	distance metrics
c	gas sonic speed
f, ω	frequency
k	wavenumber
k_{th}	thermal conductivity
n	molar coefficient
t, τ	time
u, v	velocity
z	specific acoustic impedance
A	area
C_D	discharge coefficient
Fr	Fanning friction factor
I	irradiant flux
J	momentum flux ratio
MW	molecular mass

N	particle number density
NA	numerical aperture
P	pressure
R	specific gas constant
$S_{L,T}$	flame speed
T	temperature
V	volume
ℓ	integral length scale
\mathcal{D}	molecular gas diffusivity
α	attenuation coefficient
γ	ratio of specific heats
δ	boundary layer thickness
$\delta_{L,T}$	flame thickness
λ	mean free path, wavelength
μ, ν_T, ν	viscosity, frequency
ρ	density
τ_{ign}	ignition delay
χ	mole fraction
Non-dimensionalized Parameters	
Da	Damökhler number
Le	Lewis number
M	Mach number
Pr	Prandtl number
Re	Reynolds number
Ri	Richardson number
Sc	Schmidt number
Sr	Strouhal number

ABSTRACT

Fuller, Tristan L. Ph.D., Purdue University, August 2019. Dynamic Coupling in a Model Rocket Combustor. Major Professor: William E. Anderson.

Thermoacoustic instabilities in rocket engines have been studied for decades and models have been attempted, however, the heat release fluctuations and overall response is still poorly understood. To understand the heat release mechanism in a rocket combustion chamber the effect of hydrodynamics and chemical kinetics on the mode/s of combustion need to be studied. Using prior simulations of the CVRC, an initial design for a new model rocket combustor was proposed. The new design improved on past experiments by having better control of all important boundary conditions; facilitate higher-fidelity pressure and optical measurements with emphasis on quantifying the results and using them to validate simulation models of the design; and allow good control over the characteristic parameters of the injection mechanics. A prior simulation was done on the proposed design to allow fine tuning of the design elements. Three distinct modes of self-excited instability were observed in the experiment, two of which transitioned between one another with a sweep in oxidizer temperature. A number of configurations and operating conditions were tested, but the primary focus was on three oxidizer rich cases, at different oxidizer temperatures. The two extreme cases were compared to the simulations conducted. At low oxidizer temperatures there was good agreement, where at high oxidizer temperatures there was a fairly good agreement in the type of mechanics observed, but there were a few discrepancies. The vortex shedding off of the fuel collar was captured using chemiluminescence measurements and compared quite well with the simulations. It was found that the fuel collar vortex shedding did not directly contribute to the generation of instabilities.

1. INTRODUCTION

1.1 Problem Identification

Thermoacoustic instabilities in rocket engines have been a problem that has been studied for several decades and still plagues rocket development today. It is well known that this problem is complex and coupled making it difficult to solve. By simplifying the geometry and the physics, but still utilizing a system representative of high pressure, self-excited resonance, high frequency thermoacoustic instabilities can be studied in more detail. This study aims to utilize a model rocket combustor experiment to provide high-fidelity data with complementary simulations to further our understanding of thermoacoustic combustion instabilities.

It has been proven that thermoacoustic resonance occurs when the heat release and acoustic modes of a spatially bounded flame are synchronized. This is known as Rayleigh's criterion. Rayleigh's criterion works well with simple flames, but does not account for the complex mechanics involved with diffusive and distributed flames at high pressure found in rocket engines. A large amount of effort has been done to model the flame mechanics, but because of the inherent sophistication required to capture the heat release behavior it is still not clear what set of mechanisms are dominant in their contribution towards thermoacoustic instabilities. We can confidently say that in rocket combustors the three primary physics are acoustics, hydrodynamics and combustion kinetics. All three physics sets are coupled in some way that is still being studied.

1.2 Motivation of Study

This study is focused on the injection mechanics and head-end hydrodynamics and how they respond to acoustic perturbation. A model rocket combustor is used, comprising a single shear coaxial injector element flowing gaseous oxygen and methane into a dump combustor. The key areas of focus with respect to the injection characteristics are the vortex shedding off of the fuel collar (the collar that separates the propellant), combustion in the injector recess behind the collar, and further vortex formation off of the backward facing step at the injector face. The fuel collar, assumed to act like a splitter plate between two moving fluids, provides an initial location where the propellants can be mixed at the tip. The velocity shear between the propellant jets and the stagnant point at the tip of the fuel collar drives a Kelvin-Helmholtz instability which turns into a von Kármán vortex street of mixing propellants (shear layer). The mean velocity and boundary layer thicknesses of the injected propellants are critical parameters which determine the circulation strength and the rate at which the vortices are shed from the collar tip. It is unclear whether the vortices produced from the fuel side, oxidizer side, or both, play a crucial role in the oscillatory behavior of the flame.

It is suspected that the oxidizer vortex shedding may have a more significant impact on the heat release modes in this study. The vortices shed off of the collar from the oxidizer flow are expected to have longer timescales and larger spatial scales than the vortices shed off of the collar from the fuel flow; this makes them have a larger impact on the combustion modes when perturbed or modulated. It then obviously follows that if the mean velocity of the fluid upstream of the vortex shedding point changes then the frequency and strength of the vortices shed will change as well. Acoustic waves traveling within the oxidizer post will modulate the velocity of the propellants prior to injection, thus the acoustics and hydrodynamics are coupled. The relative influence of the acoustics on fuel injection versus the oxidizer is another aspect of the injection coupling to be considered.

The recirculation zone behind the backward facing step can greatly affect the shear layer exiting the injector. The recirculation zone has its own dynamics controlled by large scale features such as the backward facing step height, resonant acoustics and jet velocity. It is a low velocity region that promotes vortex roll-up by effectively providing a larger velocity difference between itself the shear layer. The vortex shedding off the backward facing step has much larger scales than that of the vortex shedding off the fuel collar. The present study seeks to provide information regarding the dynamic coupling between the recirculation zone and the reacting flow exiting the injector.

1.3 Objectives and Approach

1.3.1 Approach

The complexity of the problem demands that it is studied using high-fidelity simulations. The experiment is intended to provide validation data for the simulations so they can be used with confidence, hence the combustor must be modelable and key flow parameters must be measurable. The new model rocket combustor HAMSTER is an improvement of previous designs, which is a culmination of over 10 years of self-excited model rocket thermoacoustic instability research. This design can provide high-fidelity high frequency measurements at 1MHz of pressure and chemiluminescence. This combustor is designed with the main focus of providing data about the injection behavior and how it responds to acoustic perturbation. The general premise of the design was based on previous experimental and simulation data from the CVRC. The lessons learned and limitations experienced from the CVRC experiment helped to provide a platform upon which the new design could be improved and upgraded. One significant change of the design was to move away from decomposed 90wt% peroxide to warm oxygen provided by a H_2/O_2 preburner.

HAMSTER was designed in detail using prior simulations. The simulations served to help fine tune the boundary conditions and determine the geometric features of the experiment. Specifically, the chamber length, dump plane step height, fuel manifold,

injector recess length and contraction portion of the nozzle were all sized based on the data provided by the prior simulations of the preliminary design of HAMSTER. Once a design was finalized for HAMSTER, another simulation was done prior to the experiments to help determine the optimal measurement locations in the experiment. The purpose of these measurements were to provide validation data toward the prior simulation. A corollary to the fine adjustment of the HAMSTER design and measurement locations was the accommodation of the optical measurements.

Together with lowering the main chamber pressure three changes are purposed towards giving confident chemiluminescence and laser based measurements of the flow, as opposed to optical density of the flow reducing the confidence of the measurement techniques. The conditioning of the injected propellants was paramount; the system has an introduced modularity which allows or denies the acoustic participation of either of the propellant manifolds during operation. The injector geometry was made to be fully modular and provide variable acoustics, without sacrificing robustness. The injection characteristics can be controlled and estimated with high confidence. The optical measurements have been improved by using PMTs at locations that gather information only about the recirculation zone, and injection recess.

1.3.2 Objectives

This objectives of this study are listed below:

- Experimentally investigate the effect of injector dynamics on thermoacoustic instabilities.
 - Design, build, and test a model rocket combustor with self-excited thermoacoustic instabilities.
 - Investigate the effect of the oxidizer temperature on acoustic and hydrodynamic time scales.

- Investigate how much of an effect (if any) the recess length has on system thermoacoustic response.
- Investigate the physics of the recirculation zone behind the backward facing step and the reacting shear layer from the injector.
 - Determine if the temperature in the recirculation zone correlates with the observed changes in system behavior.
 - Discern oscillations of combustion in the chamber resulting from the vortex generation off of the dump plane backward facing step.
 - Attempt to identify vortex shedding frequency off fuel collar using chemiluminescence measurements in the injector recess.
 - Identify oscillations that may result of free shear layer Kelvin-Helmholtz instabilities.
 - Investigate the coupling between the mixing shear layer and recirculation zone.
- Produce verifiable high-fidelity measurements to validate computational models.
 - Design and construct an experiment with well-defined boundary conditions and well-controlled input parameters.
 - Use strategically placed high frequency response pressure measurements to spatially resolve fundamental acoustic mode and determine manifold responses.
 - Verify one dimensional acoustics assumption using high frequency response pressure measurements.
 - Utilize high temporal resolution, spatially refined probes to measure chemiluminescence oscillations related to the combustion.

1.4 Document Structure

This document presents transitional thermoacoustic instability behavior as the oxidizer temperature is varied, and a high level validation between the experimental and simulated data from HAMSTER. A background on the acoustics, hydrodynamic and combustion mechanisms is provided. An experiment designed based on a fully detailed approach is shown, with emphasis on the boundary conditions and measurements taken. The observations from the experiment are made and the data analyzed. A comparison between the experimental and computational models is made in an attempt to perform a high level validation of the computational model. Lastly, a summary of the findings is made, where the completed objectives are discussed and proposals for improvements are suggested when necessary.

Physics related to combustion stability and verifying measurement techniques are detailed in Chapter 2. The main focus of the background is toward acoustic-hydrodynamic mechanics. The acoustics section is in depth so that the acoustics can be well identified and separated from other effects that may be measured. Hydrodynamic instabilities and mixing mechanisms for gases are documented. In particular, vortex shedding mechanisms related to injection characteristics of the model rocket combustor are reviewed. Information regarding analysis and verification of the measurement techniques planned on being used is reviewed. An overview of the effect of chemical kinetics on oxy-methane combustion is presented. Chemiluminescence is reviewed for the purpose of understanding its measurement. The measurement techniques and their limitations are detailed, followed by the paradigm of the verification and validation process.

The experiment design and preliminary characterization is documented in Chapter 3. This chapter serves as a background for the tangible application of the motivated study. The details and quantification of the simpler mechanism and measurement verification are shown to serve as a springboard for the proposed studies. The experiment is detailed thoroughly in this chapter. The design approach involves a priori

analysis of the expected acoustics, hydrodynamics and some aspects of the combustion. The expected system performance is characterized to provide a basis to facilitate the dynamics analysis in the chapters that follow. The properties and mechanics underlying the methods of measurements are discussed and quantified. The general trends of all the tests conducted are presented to allow the reader to get a grasp on the nature of the observations made. The trends also highlights some of the important mechanics of the study.

Chapter 4 focuses on the techniques used to analyze the experimental and simulation data pertinent to the HAMSTER study. The purpose of this chapter is to introduce the reader to the techniques used in this study and to discuss their uses and drawbacks. A concise literature review of the selected techniques provides the reader with an information source to provide the necessary understanding, if needed.

Over 150 tests were conducted. Chapter 5 presents selected datasets from the tests conducted with the HAMSTER experiment. The experimental analysis focuses on the transitional behavior observed due to the change in oxidizer temperature. Three oxidizer temperatures were selected at 440K, 600K and 700K, with all having an equivalence ratio of 0.8. The 440K and 700K cases provide a direct set of data to compare to the CFD simulation conditions conducted. The acoustic modes in the system are identified; comparisons to a one dimensional model are made. Key resonant mechanisms in the combustor are discussed and quantified. Chemiluminescence measurements are used to identify vortex shedding mechanics in the injector recess.

In Chapter 6, results from two simulations of the combustor are presented and compared to the experimental results. The two cases have nearly congruent equivalence ratios to the experiment datasets chosen, while the oxidizer temperatures used are at 400K and 700K.

Finally, a summary of the observations from the experiment and simulations are documented in Chapter 7. A transition between two dominant thermoacoustic modes in HAMSTER during a sweep in oxidizer temperature. These modes are identified and their characteristics are summarized. The comparisons between the experiment

and simulations are discussed and the discrepancies are highlighted. An assessment of whether the objectives were achieved is done and discussion of the failures are made. Future improvements and studies are suggested.

2. BACKGROUND AND THEORY

Combustion instability is a complex problem whereby the many physical phenomena are coupled. It is useful first to identify and detail the potential mechanisms at work. Once the more dominant physical mechanisms are identified for this particular study, the experimental measurement techniques together with supporting simulation data can be used to validate the hypothesis. This chapter provides an overview of past research and highlights the theorized potential physics responsible for combustion instabilities, the dampening of said processes and the mechanisms upon which the experimental measurement were chosen.

2.1 Instabilities in Rocket Engines

In reacting fluid systems instabilities can manifest in a number of ways. Per NASA SP-194 [1] pressure response based instabilities in rocket engines can be classified into chug, pogo, buzz and screech, increasing in frequency response respectively. Each type of mode in the combustion chamber could, theoretically, be excited via some sort of external forcing such as a structural vibration, feedback response of the cooling jacket, pulsations in flow from other system components [2], but for the purpose of this study, external influences are neglected. Pogo instabilities in particular arise in the feed system, such as from the valves, pumps, bends, etc., and will not be considered. The frequency response of a typical combustion coupled instability can range from the tens to tens of kilohertz range [3].

2.1.1 Chug and Buzz

Chugging instabilities are usually classified as a purely hydrodynamic or bulk mode instabilities arising from propellant feed fluctuations that can be caused by resistances, sudden fluid property changes within the system and a delayed combustion response [1]. The combustion chamber acoustic response is usually coupled with the dynamics in the injector/s, manifold and feed systems. Because of the low bulk motion behavior of chugging the response of the system is generally at low frequencies.

Casiano [4] presented a thorough review on analytical models representing chugging behavior, which were extended and improved upon. A criterion that is potentially the most important measure of chugging is the approximation of the upper frequency threshold response by Summerfield [5]. This value, calculated using Equation 2.1, represents the upper bound for the possibility of a chugging response.

$$\tau_T < \frac{L_f \dot{m}}{p_c A_f} + \frac{2c^* L^* \Delta p_{inj}}{p_c R T_c} \quad (2.1)$$

2.1.2 Thermoacoustic

The Rayleigh criterion [6] has been the standard when describing thermoacoustically driven oscillations. In the general sense, the Rayleigh criterion suggests that if energy can be applied to or taken away from a condensation or rarefaction at the appropriate phase of an acoustic oscillation then the vibration will be amplified or attenuated. This theory has been proven for simple systems at long time scales such as Rijke tubes. The theory is reliant on the assumption of simple coherent processes which can easily modeled analytically. The Rayleigh criterion is suited for describing thermoacoustic coupling gains for simple, compact flames. In our recent research efforts it has been found that for diffusive heat sources that it is difficult to apply the Rayleigh criterion simply to quantify the coupling efficiency. The main reason for this is because the periodicity of the response of the system is quite complex; and per the Rayleigh criterion, the spatio-temporal distribution of the combustion may not

align with the pressure oscillations to result in a coupling gain despite an identified instability.

High frequency combustion instabilities, sometimes referred to as *screeching*, have been determined to be thermoacoustically driven. Thermoacoustic instabilities are defined as a combustion coupled response with the fundamental or higher acoustic modes of the chamber and/or the ducted acoustic system [2] (injector, manifold, etc.).

How the oscillation couples with the acoustics is generally not known, but some mechanisms which are known to drive thermoacoustic instabilities are vortex shedding, modulation of the flame area, periodic fluctuations in equivalence ratio and sharp changes in fluid properties such as atomization effects. Crocco [7] derived an analytical expression known as the "n-tau" model, which uses a heuristic time lag approach to represent the coupling between the acoustics, combustion and any other process which can initiate a time delay in the combustion process. The simplicity of the "n-tau" model is unable to capture the modes resulting from the complex interactions between mechanisms driving combustion instabilities in even the simplest of combustors. Culick's report to NATO [3] and NASA SP-194 [1] summarize works leading up to 2005 involved with studying thermoacoustic combustion instabilities.

According to Byrne, thermoacoustic instabilities in dump combustors can arise from vortex driven combustion oscillations [8]. The identification of the fact that hydrodynamic instabilities can drive thermoacoustic instabilities logically leads to the notion that less severe hydrodynamic disruptions most likely influence the modes of combustion in non-premixed combustion systems. It is therefore required that the general model for combustion instability includes a coupled response between the acoustics, combustion and the hydrodynamic features due to injection.

2.1.3 Recent Work on Combustion Driven Thermoacoustic Instabilities

A well-known model rocket combustor used for studying self-excited combustion instabilities in rocket engines is the Continuously Varying Resonant Combustor

(CVRC) [9]. The CVRC, which uses the propellant combination of 90%wt decomposed hydrogen peroxide and methane gas in an oxidizer rich mixture ratio, had the unique ability to alter its oxidizer post during operation. By changing the oxidizer post length the system could be tuned in and out of resonance during hot fire. This revealed the direct effect of injector geometry on self-exciting thermoacoustic combustion instabilities [10].

Work done by Harvizinski et al. [11] showed that while using a spatially resolved approach to applying Rayleigh index to a distributed region of heat release, the index and phase heavily depended on how it was modeled.

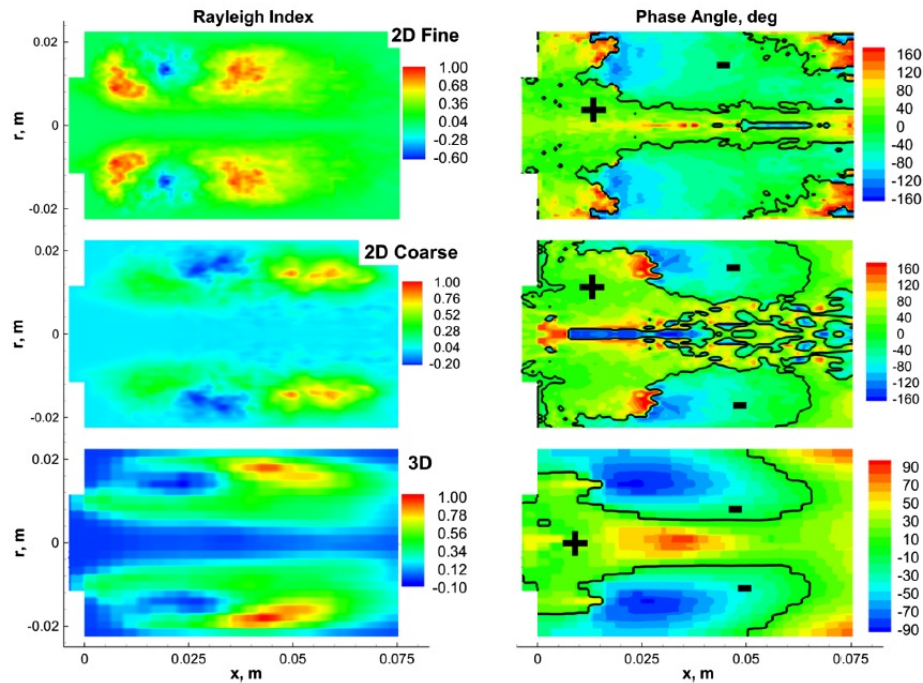


Figure 2.1.: Simulated Rayleigh index and phase maps for thermoacoustic cycling in CVRC. [11]

To address the problem of self-excited thermoacoustic instabilities it is necessary to quantify all the dominant processes involved and determine their relationship and whether a simple phase analysis between processes be sufficient in describing and quantifying the coupling phenomenon. Self-excited instabilities were computation-

ally studied on the CVRC with a varying oxidizer post length [12]. The effect of the relative acoustic pulse timing has been shown to be a potential driver of thermoacoustic instabilities within rocket combustors. Figure 2.2 shows a proposed theory of the relative acoustic timing of plane waves traveling in the CVRC.

Further study with regard to the timing in the CVRC was conducted by Sardeshmukh et al. [14], where instead of changing the oxidizer post length the oxidizer temperature was varied with a constant post length to achieve different resonant behaviors. Figure 2.3 shows the effect of oxidizer on the acoustic response of the system, and Figure 2.4 shows the relative acoustic timings of the oxidizer post and chamber associated with specific oxidizer temperatures. The acoustic timing is defined as the amount of time it would take an acoustic pulse to travel the full distance of the duct and back to its source. Although Figure 2.4 shows a monotonic decrease in the relative difference in timing, Figure 2.3 shows that it was found that there existed an optimal oxidizer temperature to produce maximum synchronization.

Since it was not apparent if the acoustic timing was solely responsible for the different behaviors, the time scales of the hydrodynamic oscillations produced by different parts of the injector geometry were also considered. With the time scales not synchronized with the dominant frequency it was then suggested that the ignition delay resulting from the chemical kinetics or a combination of the ignition delay with the hydrodynamics could be responsible for driving the thermoacoustic oscillations.

The CVRC has set the foundation for further study into self-excited thermoacoustic instabilities. The dominant mechanisms which drive the heat release fluctuations and the physics behind the coupling between the acoustics, hydrodynamics and heat release are still not entirely known. Simulated models (LES/RANS hybrid, Flamelet, etc.) have been useful in developing a basic hypothesis scaffold to further investigate the heat release mechanisms [15–20]. Figure 2.5 shows a basic representation of the hypothesis. The timescales of the physics responsible for the dominant behavior in the thermoacoustic coupling process determine the timing needed (or phase) between processes to ensure maximum coupling efficiency and resonance. For non-premixed

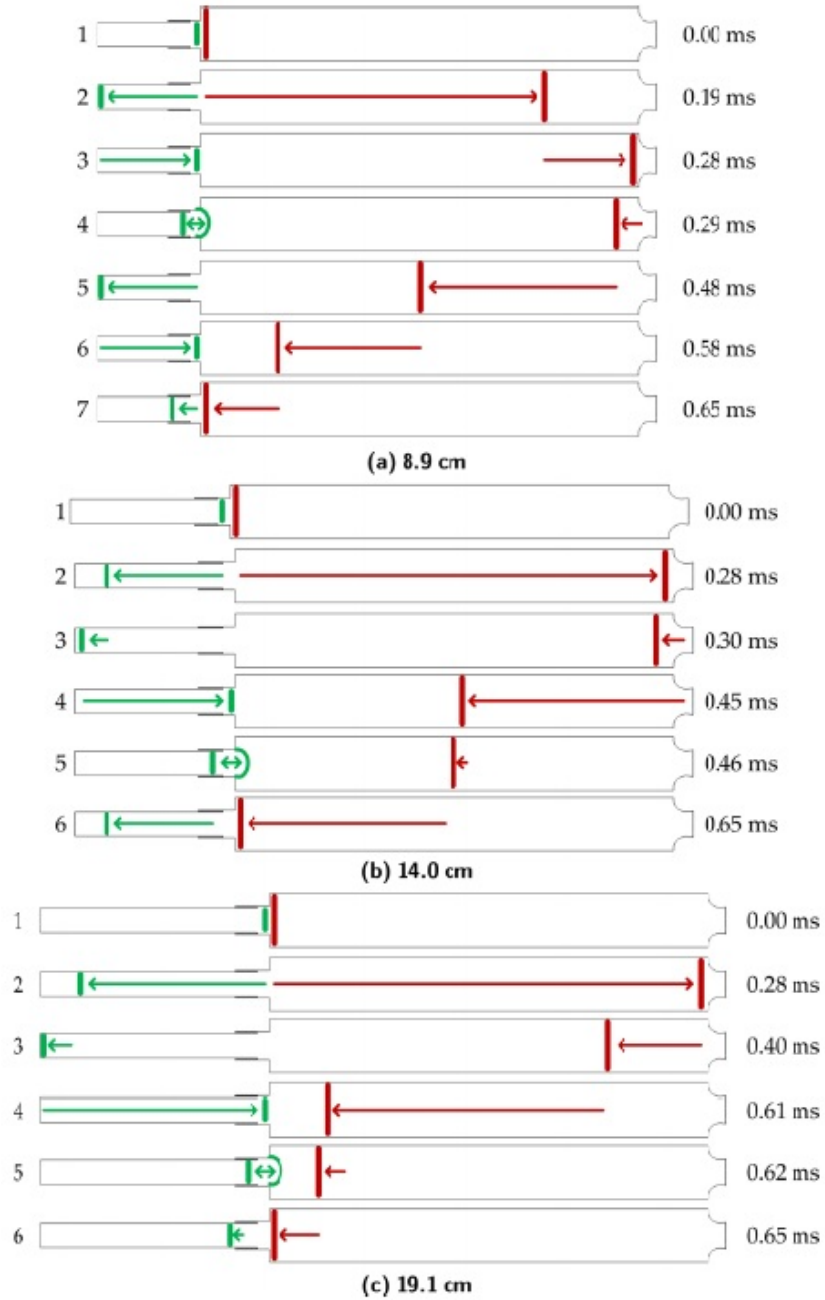


Figure 2.2.: Description of acoustic pulse timing in the CVRC. [13]

flames the limitation of the rate of heat release appears to be diffusion limited, but pockets of preheated well mixed regions of propellant that suddenly ignite can also occur. Depending on how well a localized region is mixed, and the temperature of

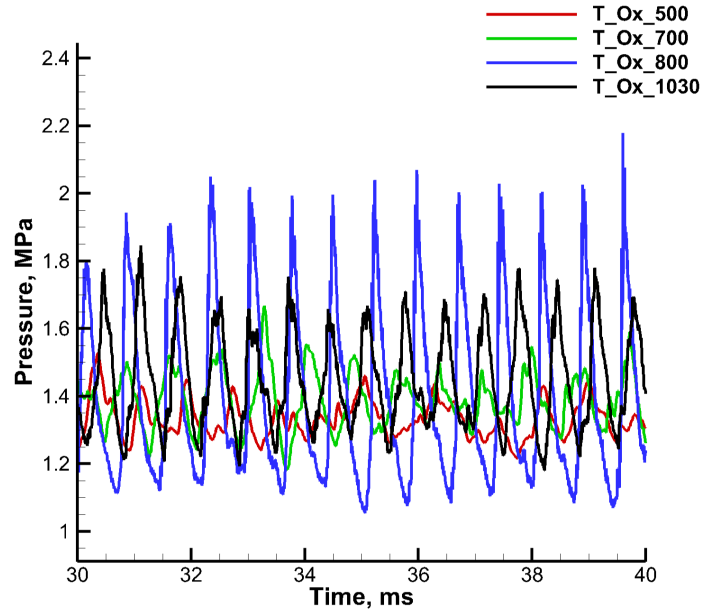


Figure 2.3.: Acoustic response in the CVRC with respect to oxidizer temperature. [14]

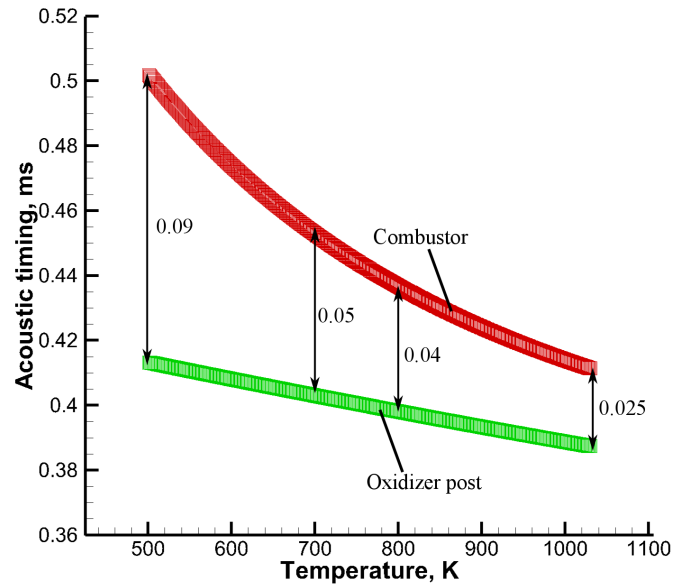


Figure 2.4.: Relative acoustic timing in the CVRC. The acoustic timing is defined as the amount of time it would take an acoustic pulse to travel the full distance of the duct and back to its source. [14]

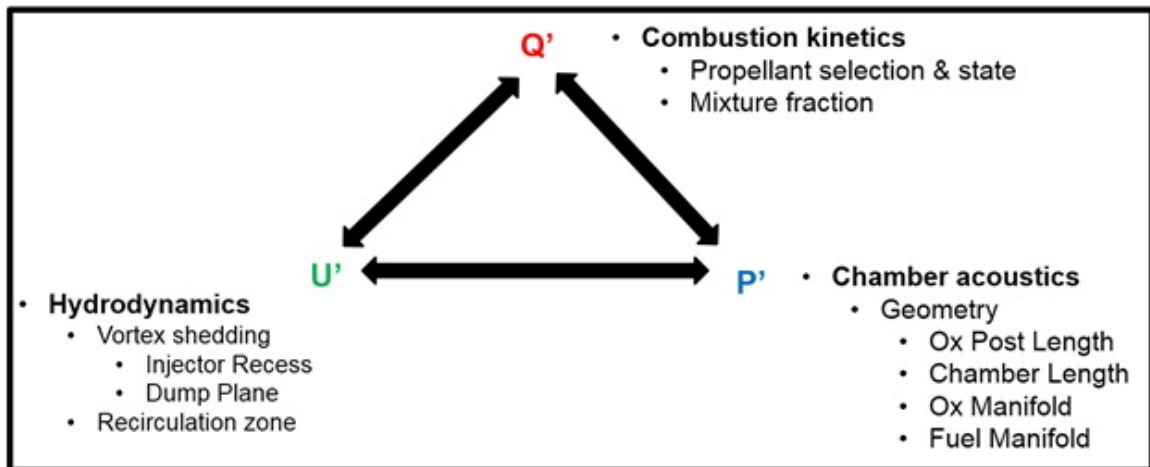


Figure 2.5.: Hypothesized coupling mechanisms for self-excited thermoacoustic instabilities in a single element combustor.

that region, the rate of chemical reaction may be limited. These concepts further reinforce the idea that the physical subprocesses need to be quantified relative to each other in terms of length and time scales.

The injector and the flow characteristics of the propellants define the nature of mixing in the combustor. Injectors with a low pressure drop across the orifice/s tend to be more responsive to external perturbation from the combustion flow-field. The hydrodynamics over edges and orifices are quite predictable for quiescent and stable flows, but can be very sensitive when the flow-field upstream is perturbed. Additionally, unsteady combustion downstream of the injector can also alter the injection pressure drop and hence the injection velocity, and can therefore have a large impact on the hydrodynamic features produced by the injector.

In some cases the hydrodynamics can drive the combustion instabilities in combustors [21–23]. Some of the hydrodynamic features that have been identified to cause self-excited combustion instabilities in dump combustors are vortex shedding from the oxidizer post inlet/s, called "whistling", from the backward facing step at the injector face and from the fuel collar or splitter plate in a coaxial injector.

Any acoustics present in the combustion chamber may perturb the flow-field upstream of the combustion zone, but once the acoustics reach a high enough amplitude the acoustic pressure waves have the ability to fully modulate propellant feed. Once the propellant feed is modulated by the acoustics in the chamber and a strong resonance is formed it is unlikely for the system to fall back into a more stable and quiet mode of operation.

2.2 Fundamentals

The transition from a stable mode of operation to a mode of incipient instability is still not well understood. This study will focus on the effect of hydrodynamics on the mixing and combustion processes and how it affects the coupling efficiency of thermoacoustic oscillations.

Acoustic waves are the initial response of the flow within the combustor as a result of heat release. The sound speed and shape of the combustor allow standing waves to form with a particular frequency. If the acoustic response is driven with an appropriate phase the standing waves within the combustor will increase in amplitude. Moderately large pressure oscillations will begin to modulate the injection feed.

The acoustic energy transmitted from one part of the combustor depends on the geometry and the attenuation generated by thermoviscous and boundary layer effects. The flow response in the fuel manifold, oxidizer post and combustion chamber may become synchronized in the sense that the perturbation on the propellant feed allows for an excess amount of combustible mixture to be injected into the chamber prior to the return of the reflected acoustic wave in the chamber. When the timing between the heat release and the pressure condensation near the head end of the chamber coincide the acoustics may be amplified.

In this axisymmetric combustor dominated by axial wave motion, it is assumed that the pressure waves traveling within the combustor are planar and therefore generate longitudinal acoustic standing wave modes. The acoustic modes that form within

the combustor ducts depend on the sound speed of the fluid and the geometry of the different sections of the duct, and is possible that non-longitudinal acoustic modes at the head end of the chamber are driven locally by the heat release process which would then have the ability to strongly couple with the combustion process. Generally, out-of-plane acoustics can also be driven by longitudinal acoustic modes if the longitudinal frequency is large enough for the out-of-plane mode to cut-on.

Mixing of gaseous propellants is achieved through diffusion and advection. Typically on a macro-scale the primary mixing process tends to be advection driven, but locally, diffusion effects might be important in how the flame is anchored or the rate of combustion achieved. Diffusion of ideal gases is mainly driven by concentration gradients, however for densities close enough to the critical density point (real gas effects) of a mixture the diffusion process can be affected by pressure and temperature as well.

In a shear coaxial injector the primary method of large-scale mixing is vorticity generation of the trailing edges of the injector geometry. The local residence time of the propellants rolled up into vortices allows for them to diffuse and mix well. The vortices are transported downstream into the chamber. Depending on how well the vortices are mixed and how high the ambient temperature is, these well mixed vortices may help to stabilize the flame at the injector face. The turbulent shear layer also promotes mixing with finer length and time scales. The growth of the shear layer and vortex size can be used to estimate the size of the mixed region.

The acoustic oscillations in the oxidizer post or the fuel annulus of the injector can lead to large oscillations of the boundary layer thickness on the fuel collar. The oscillating velocity, together with the oscillating boundary layer thickness results in a modulated vortex production which, in turn, produces an oscillation in the mixing and therefore the combustion modes. The effects of upstream oscillations of the injector velocity on the velocity profile in the recess is shown in Figure 2.6 [14].

Hydrodynamic instabilities such as the Kelvin-Helmholtz (velocity driven) and Richardson-Taylor (density driven) can cause shear layer mixing. Baroclinic torque

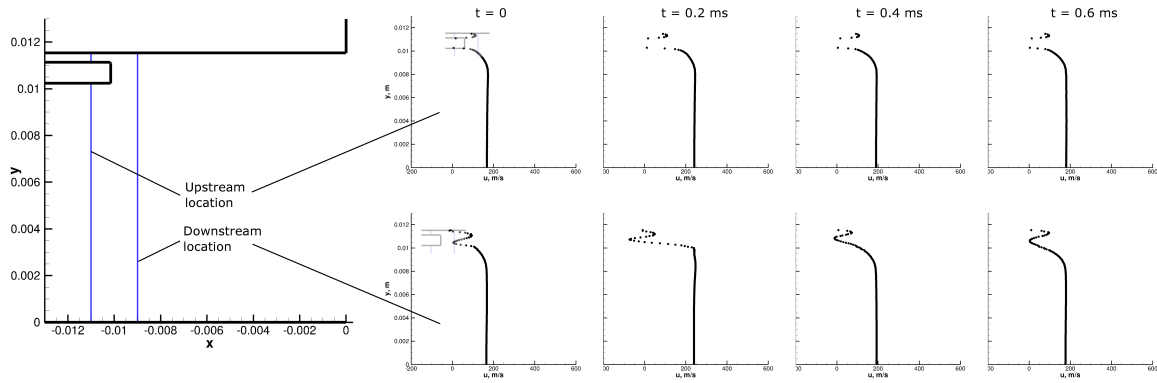


Figure 2.6.: Effect of oscillating boundary layer on the velocity profile in the injector recess in the CVRC. [14]

of the shear layer can also produce vorticity to generate good mixing regions. These mixing mechanisms can be negated or forced by the introduction of a pressure or velocity fluctuation such as an acoustic wave.

The propellant feed effectively is sourced from the manifolds. The manifolds can also respond acoustically. If the manifold response is large enough it will modulate the velocity and density at which the propellant is fed into the chamber, thus changing the injection and mixing characteristics. All of the aforementioned mixing processes are dependent on the advection, so if the advection is modulated by pressure oscillations so will each of the mixing processes.

Turbulent flames are irregularly shaped zones of exothermic, highly reactive chemistry. The flow of reactants prior to combustion are in the turbulent regime. A non-premixed flame is a combustion process whereby the reactants are not fully mixed prior to combustion.

Non-premixed gaseous turbulent jet flames in a rocket chamber can be stabilized through recirculation zones, swirled flow or in and around a geometric feature. These types of flames can have different timescales associated with burning at various localized regions. It may become apparent that portions of these flames show diffusion limited burning, while others show kinetically limited burning. The characteristics of

the flame of a gas-gas shear coaxial injector in a rocket is highly dependent by the injection characteristics and propellant states. Furthermore, in the event of perturbation the flame characteristics can evolve and change.

Some important characteristics of the flame, which play a role in how well the combustion process couples with the rest of the system, are the flame shape and size. The susceptibility of the flame to oscillate in the presence of external influence can be largely dependent on how well and where the flame is anchored relative to the injector geometry, deposition of propellants and product recirculation zones.

2.2.1 Acoustics

High frequency combustion instabilities are thermoacoustic in nature. It is therefore paramount that acoustic physics, which has been well studied, be well understood for this particular phenomenon. This section will go through the basic descriptions of linear acoustics with emphasis on sound speed and response, but will deviate slightly into the nonlinear processes.

The linearized Euler's equations and the linearized wave equation are descriptions of linear acoustic propagation for small amplitudes. These expressions are derived under the assumption that the flow is inviscid, and therefore sometimes called the lossless acoustic equations [24]. The propagating vector $\vec{k} = k_x \hat{x}$ which has the magnitude $k = \frac{\omega}{c}$ can be used to determine if a wave will propagate with dissipation in a certain direction. By definition the specific acoustic impedance of plane waves is given by:

$$\vec{z} = \frac{\vec{P}}{u} = \pm \rho_0 c \quad (2.2)$$

In the most simplest sense the specific impedance will determine how much acoustic power is transmitted or reflected through acoustic boundaries, whether it is a rigid wall, geometry change or fluid interface. The fraction of acoustic power reflected is determined by:

$$R_{\Pi} = |\mathbf{R}|^2 = 1 - T_{\Pi} \quad (2.3)$$

Where:

$$\mathbf{R} = \frac{z_2 - z_1}{z_2 + z_1} \quad (2.4)$$

The specific impedance of the fluid domain from where the acoustic wave originates is given by Z_1 and the exiting for the exiting domain it is given by Z_2 . This concept is important in duct acoustics especially, but in some instances represents an important realization that acoustic energy can be reflected at a fluidic interface. This idea is extremely important in combustors where the gradients of density and sound speed at the flame front may be incredibly large. The effect of Mach number, or mean flow, on the acoustic response of a system, specifically the input impedance has been investigated [25]. It has been found that high Mach number convective flows generally lowers the resonant frequency of the system.

One dimensional approximations are useful for longitudinal modes in ducted systems. However, for gradual changes in area, such as a nozzle or horn, the acoustic response becomes more complicated; higher order and transverse then need to be considered [26].

Transfer Matrix Approach

The longitudinal acoustic response and phase of a plane wave propagating in a duct can be modeled using the 1D transfer matrix approach where the variables of acoustic particle velocity and pressure at interfaces of acoustic domains are calculated. Such an approach is well documented [27–30].

For a slow moving inviscid fluid the effect of Mach number and attenuation coefficient become negligible. There are a number transfer matrices for different systems and methods for higher dimensions, especially lumped ones; these will be discussed further when needed and are presented in Appendix A for further reference.

Lumped Acoustic Systems

In some special instances some acoustic systems can be modeled as lumped systems. The assumption of a lumped system requires that $k_0L \ll 1$, where L is the largest geometric length scale of the system. The long wavelength limit is based on the idea that if an acoustically lumped system is small compared to the wavelength of the driving acoustic perturbation then the relative particle velocity difference between two points on opposite sides of the acoustic domain will be negligible. Impedances for lumped systems are presented in Appendix A.2 for further reference.

One example of a lumped acoustic system is the Helmholtz resonator. A cavity tapped off a main duct can have a bulk fluidic response provided that the neck and cavity are small. The resonant frequency of the Helmholtz resonator assuming a linear response is given by [31]:

$$f_{res} = \frac{c}{2\pi} \sqrt{\frac{A_N}{L'V}} \quad (2.5)$$

Where the cavity volume is V , the neck cross-sectional area is A_N , the effective inertial neck length is $L' = L + \frac{1.7a}{1+0.625(2a/D_c)}$ for flanged neck; L is the length of the neck, D_c is the cavity diameter and a is the neck radius. The discharge coefficient of the neck can be calculate using the relation [31]:

$$C_D = \frac{1}{8} \left(\frac{d}{L'} \right)^2 \quad (2.6)$$

If thermoviscous losses are neglected then the Helmholtz resonator will act as a band-stop filter to duct, where the transmission fraction is formulated as [24]:

$$T_{II} = \frac{1}{1 + \left(\frac{c/(2A_c)}{\omega L' / (\pi a^2) - c^2 / (\omega V)} \right)^2} \quad (2.7)$$

The nonlinear response of a Helmholtz resonator has been empirically studied and analytically modeled [31]. For a weakly nonlinear response the effective length can be corrected using $L' \approx L'|_0 \left[1 - \frac{4\epsilon}{9\pi} \right]$. The measure of the nonlinearity for the linear and weakly nonlinear cases is defined by Equation equation (2.8):

$$\epsilon = 64 \left[\frac{L}{2a} + \frac{0.85}{1 + 0.625(2a/D_c)} \right]^2 \left[\frac{P_i}{\rho(2\omega a)^2} \right] \quad (2.8)$$

,where P_i is the duct pressure. For the nonlinear regime the measure of nonlinearity is defined by Equation equation (2.9):

$$E = 0.26 \left[1 + \frac{1}{9} \frac{L}{2a} \right] \sqrt{\frac{\rho(2\omega a)^2}{P_i}} \quad (2.9)$$

The discharge coefficient then becomes:

$$C_D = 0.545 \left[1 + \frac{2}{9} \frac{L}{2a} \right] \quad (2.10)$$

The nonlinear regime only becomes important when dealing with an $SPL \geq 130B$, of which the Helmholtz resonator behaves like a broadband sound absorber rather than a narrow band-stop filter [31].

Transverse Acoustic Modes in Circular Ducts

Out-of-plane acoustic modes are common in multi-injector combustion chamber, and occasionally occur in single element rocket combustors and motors. It is therefore prudent to identify any out-of-plane acoustics to determine if they play role in a system with exclusively expected longitudinal modes, and whether they significantly contribute to the coupled resonance of the system.

Transverse modes in a duct that resonate due to a disturbance are dependent on the frequency of the disturbance; in the case of a longitudinal acoustic mode the frequency will determine if transverse modes are able to propagate down the duct. For a circular duct with a moving inviscid medium of a certain Mach number the response of the resonant modes can be calculated analytically [30].

The main determining factor of whether the mode can propagate down a duct is the directional wave number (propagating constant); if the propagating constant is determined to be complex in value then the mode is described as evanescent and will decay exponentially down the length of the duct. It should be emphasized though, that despite the fact that a transverse acoustic mode could be evanescent it can still be driven locally by a source, such as a combustion event.

Since combustion can be an acoustic driver it is possible that coupled transverse and longitudinal acoustic modes can be excited. For a linear analysis, without mean flow, the normalized frequency can be calculated using Equation 2.11 [1].

$$\frac{\omega}{c_0} = \sqrt{\left(\frac{s_{\nu\eta}}{D_c/2}\right)^2 + \left(\frac{j c \pi (1 - M^2)}{L_c}\right)^2} \quad (2.11)$$

Where D_c and L_c are dimensions associated with the combustor geometry, s is the root of the Bessel function of the first kind with ν , η and j being parameters associated with the acoustic eigenmodes. Tables showing the set of normalized acoustic eigenmodes is shown in Appendix A.2.

Absorption and Attenuation

Acoustic attenuation originates in two areas: thermoviscous losses and molecular thermal relaxation. The effect of absorption and attenuation manifests itself in the complex portion of the speed of sound or wave number shortly mentioned previously. Acoustic attenuation coefficients in general can be summed to determine the overall acoustic attenuation for a given system [24].

Thermoviscous losses are particularly important at a rigid wall. When an orifice or gap is quite small the relative size of the boundary layer could be quite large. With a larger boundary layer is it possible that thermoviscous losses can occur when transmitting acoustic energy.

When acoustic energy is transferred from one particle to another it is possible that some of the energy can be distributed amongst the modes of energy storage within the molecule itself. For monatomic gases (ideal gases) which only have three degrees of freedom associated with translational motion there is usually* no relaxation time so all energy transmitted to the particle will be deposited directly into the mode of kinetic energy of motion for that particle. For polyatomic molecules other modes of energy storage include rotation and vibration of the molecule. The ability for an atom/molecule to store energy internally is described using the gas heat capacity of constant volume.

Acoustic absorption occurs predominantly when the sound frequency is close to the relaxation time of the particular energy state of the molecules. The absorption effect of each molecular mode on sound speed needs to be characterized individually and can be quite laborious and intense algebraically. Further work needs to be done to characterize the acoustic absorption of a mixture of molecules at high temperature.

2.2.2 Hydrodynamic Structures and Mixing

The hydrodynamic and other mixing processes pertinent to turbulent non-premixed combustion are discussed below. Processes that may not be insignificant are also listed to investigate their effects locally and whether they play a role in ignition delay and flame anchoring. In later sections some simple unit problem cases relevant to the experiment will be simply modeled and sensitivity analyses based on the external stimuli are conducted.

With a number of physical mechanisms driving the mixing process during injection, it is necessary to characterize the fluid states before injection so that different scenarios can be comparable. A common measure of injection through gas-gas coaxial injectors is momentum flux ratio, defined by:

$$J = \frac{\rho_1 U_1^2}{\rho_2 U_2^2} \quad (2.12)$$

Other parameters, such as pressure, temperature, compressibility, should also be defined to insure a correct analyses and deductions. The relative differences between the fluids injected will invariably lead to some sort of interaction or mixing and these processes are described and measured hereafter.

Diffusion

Thermal and mass diffusion generally have important roles in non-premixed flames. In a local region where the transport of the fluid is somewhat quiescent each of the diffusion processes may limit the speed at which the flame front propagates through

a reactive mixture. A sometimes useful metric for characterizing the relative speeds of the diffusion process is the Lewis number [32].

The thermal diffusivity is fairly simple to estimate for either a homogeneous or heterogeneous mixture of ideal gases. For mixtures of real gases the state equations need to account for the effects of intermolecular forces, of which, depending on the gases and their states can become quite complicated very quickly.

Mass diffusion for ideal gases, whether homogeneous or heterogeneous is well represented by the Chapman-Enskog equation [32]. The method for calculating diffusion rates of homogeneous and binary gases are shown in Appendix A.1. It should be cautioned that the Chapman-Enskog equation does not work well for situations where the concentration gradients are too steep, such as across a shock wave. For the dilute limit or ideal gas scenario the diffusion rates can be computed quite easily with kinetic gas theory, however it has been shown that this approach has limitations when the gas densities exceed a threshold value [33].

The transport properties of the gases are within 1% of the dilute limit if the gas densities do not exceed the reduced density value [33]. The viscosity of a dilute gas can be well approximated with gas kinetic theory if needed [34]. If the density of the gases appears to too high to be assumed dilute within a reasonable margin then the correction factor of Equation equation (A.1) can be used. There are a number of modifications to the binary diffusion coefficient equation, and in some cases it is recommended that a binary diffusion coefficient be determined for a unique pair at a given set of conditions to ensure greatest accuracy [35].

The thermophysical properties of a mixture may also needed. The heat capacity of the mixture can be well approximated using the Peng-Robinson equation of state. The thermal conductivity of a mixture may be a little more involved; depending on the temperature and pressure of the mixture. The thermal conductivity for gases can be determined from theory with the methods by Chung et al. [36] or directly from the NIST web database. The thermal conductivity of a gas mixture can be determined

by the Wassiljewa equation [37]. Errors are typically $< 8\%$, but greater deviations can occur if the gases are in vastly different in size and polarity.

Turbulent Jets and Mixing Shear Layer

RANS approximations for simple boundary free turbulent flows, such as mixing layers, planar and axisymmetric turbulent jets are well approximated. Using a self-similarity approach the variation of mean velocity, cross-stream characteristic length and Reynolds number based on the cross-stream characteristic length have been related to powers of downstream distance. Table 2.1 shows these aforementioned values and the typical turbulent Reynolds numbers. Unfortunately work in this area is lim-

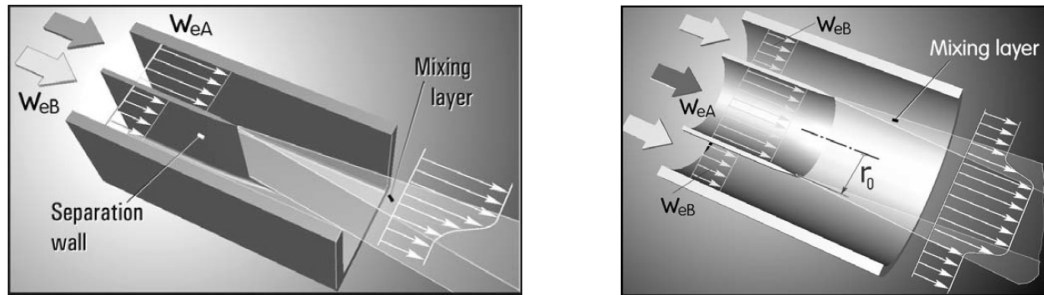
Table 2.1.: Powers of x describing the downstream variation of U_s , l and Re_l . Also listed are the values of Re_T and are independent of position. [38]

Powers of x for				
	U_s	l	Re_l	Re_T
Mixing Layer	0	1	1	17.3
Plane Jet	-1/2	1	1/2	25.7
Axisymmetric Jet	-1	1	0	32

ited and it has been found that the turbulence models do not predict the difference in jet spreading for axisymmetric and planar jets well, however a two equation similarity solution has been developed that does predict turbulent jet behavior well. In the work done by Tesař [39] the spreading anomaly surrounding axisymmetric jets has been addressed, but the scaling factors of velocity and jet spreading remain somewhat the same.

It has been demonstrated that, for all practical purposes, turbulent transport in a shear layer coming from coaxial jets and that of planar jets are effectively the same.

The effect of curvature, although curvature radius is of the same order of magnitude as the boundary layers on either side of the partition, is negligible for a mixing layer produced by coaxial jets, and can be approximated using a similarity solution for a mixing layer of planar jets [40]. Figure 2.7 below illustrates how the mixing layer forms during injection.



(a) Mixing layer between parallel flows is quite thin because momentum diffusion from the flow of higher velocity W_{eA} towards the lower velocity W_{eB} is slower than the streamwise motion. The character of the flow is here represented by time-mean velocity profile.

(b) A transversally curved mixing layer forms when flow of higher velocity W_{eA} leaves the central nozzle and mixes with the outer flow of lower velocity W_{eB} . Transversal curvature radius varies with axial distance differently than the layer thickness. This renders an exact similarity of the profiles impossible.

Figure 2.7.: Mixing layer models of unequal injected velocities for two geometric configurations. [40]

The disadvantage of the self-similar solutions is that the factor relating mixing layer spreading and thickness must be obtained by comparing to existing data. The solutions are elegant and accurate, but the basis of the argument is that the partition from where the mixing begins assume that the partition thickness is infinitely thin. In practice this is not the case; in coaxial injectors the collar or partition has finite thickness and eddy structures are produced as a result. These structures tend to dominate the mixing process.

Jets tend to exhibit instability. The instabilities develop as a result of the shear layer being perturbed. The result is the development of coherent structures such as vortices. Michalke [41] gives an excellent summary of jet instability theory. Linear instability theory is employed in the survey, with investigations on the effects of Mach number, Reynolds number and temperature on how the jet stability behavior changes. Weakly nonlinear effects are also included.

Vortex Production

Vortex production in an injector can enhance mixing. In a coaxial injector vortices are usually produced over the fuel collar and backward facing step leading into the combustion chamber. There have been numerous studies on how vortices are produced over a 2D backward facing step [42–47], however most investigate this mechanism at lower Reynolds numbers. A particularly interesting numerical study of flow over an axisymmetric backward facing at very high Reynolds numbers ($\approx 10^6$) showed evidence of the formation of a helical instability besides the typical instabilities associated with a 2D backward facing step [48]. Regardless, the Strouhal numbers associated with this mechanism usually lie between 0.06 and 0.35.

In some cases the fuel collar can be thought of as two dimensional plate and depending on the boundary layer of the fluid approaching the edge can be treated as a thick or thin plate. The prediction of Strouhal number based on boundary layer thickness, plate thickness and pressure coefficient allow to estimate the vortex shedding frequency off the fuel collar. The velocity profile in a coaxial injector recess as result of the boundary layer thickness on the plate is well illustrated in Figure 2.6. The Strouhal number over the plate can be estimated with Equation equation (2.13) [49].

$$Sr = \frac{\left(0.225 + 0.056\sqrt{1 - \epsilon/\sqrt{2}}\right)\epsilon}{1.54(\delta/D) - C_{p*}} \quad (2.13)$$

where the coefficient of pressure C_{p*} is assumed to have an approximate value of -0.3 , ϵ is the fraction of boundary layer vorticity that goes into the Kármán Vortex Street, which takes on values around 0.5, δ/D is the ratio of the thickness of the boundary layer to the thickness of the plate.

The transport of the vortices in the shear layer is also an important feature during injection. As the vortices are convected there may be an influence by the shear layer itself, or the adjacent jets which may have unequal velocities. The jet streams may become entrained in the shear layer and traveling vortices and further enhance mixing. The structure, transport and growth of the Kármán Vortex Street has been investigated and a simple model of how the shear layer grows with length and how much entrainment occurs [50].

A simple model describing the growth of the mixing layer in two dimensions has been based on a geometric sequence, as illustrated below in Figure 2.8. The vortex formation model relies on the fluid interface instabilities and shear layer evolution, it is unclear how vortex production off of the splitter plate geometry is affected by these changes. From the vortex rest frame, U_c is the receding velocity of the trailing

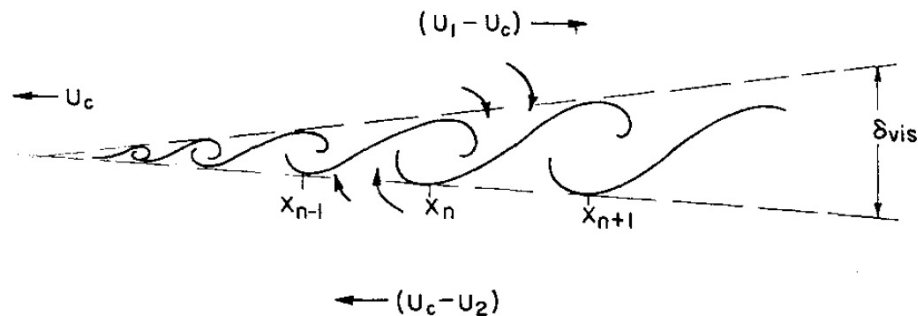


Figure 2.8.: Large-structure array and induction velocities in vortex convection frame. [50]

edge of the splitter plate. U_1 and U_2 correspond to the absolute velocities of the jets. Each vortex x_n has a subscript relating it to the order of the geometric sequence. The

normalized convection velocity $r_c = U_c/U_1$ is related to the velocity and density ratios of the jets in Equation (2.14) [50].

$$r_c = \frac{1 + r\sqrt{s}}{1 + \sqrt{s}} \quad (2.14)$$

where $r = U_2/U_1$ and $s = \rho_2/\rho_1$. The ratio of thickness of the shear layer (or vortex growth) to the distance downstream can be determined by Equation (2.16) [50].

$$\frac{\delta}{x} = \epsilon \left(\frac{1 - r}{1 + r\sqrt{s}} \right) \left[1 + \sqrt{s} - \frac{1 - \sqrt{s}}{1 + 2.99(1 + r)/(1 - r)} \right] \quad (2.15)$$

where $\epsilon = 0.18/2$ is suggested. The average vorticity spacing ℓ appears to increase with increasing distance from the splitter plate. This is estimated using the relation [50]:

$$\frac{\ell}{x} = C \frac{1 - r}{1 + r} \quad (2.16)$$

where C is determined experimentally, $C = 0.68$ has been suggested. It has been determined that the spacing is not a function of density ratio. Thus, the mass flux entrainment ratio $E_m = E_v/s$, where the volume flux entrainment ratio is given by [50]:

$$E_v = \sqrt{s} \left(1 + \frac{\ell}{x} \right) \quad (2.17)$$

Additionally, Dahm et al. [51], which worked on a nested coaxial injector followed the aforementioned work to produce an equation which describes the frequency at which a vortex would pass a fixed point. Equation (2.18) is developed from the assumption that $f_v = U_c/\ell$.

$$\frac{f_v}{U_1} = \frac{r_c}{\ell} = \frac{1}{Cx} \left(\frac{1 + r}{1 - r} \right) \left(\frac{\sqrt{s} + r}{\sqrt{s} + 1} \right) \quad (2.18)$$

It was suggested by Dahm et al. [51] that the circulation strength of the vortices scales by $\Gamma \propto (U_1 - U_2)\ell$.

Mixing Metrics

There are many methods to quantify how well fluids mix and how well mixed they become. A simple measure of the dominant mechanisms which drive mixing at small

scales is the Schmidt number. The concentration of one fluid mixing into another via a vortex structure has been characterized quite well by Meunier and Villermaux [52].

Fluid Interface Instabilities

The interface between the fuel and oxidizer jets in a coaxial injector can result in instabilities if there are differences in density and/or velocity. Two typical instabilities at an interface between gas phase fluids are the Rayleigh-Taylor and Kelvin-Helmholtz instabilities. The Rayleigh-Taylor instability is based on a density gradient across the interface boundary, while the Kelvin-Helmholtz instability is based on velocity shear across the interface boundary. Both instabilities can be somewhat characterized by the Richardson number for small density gradients (Boussinesq approximation). For $Ri < 0.25$ buoyancy effects become negligible and it is thought that the Kelvin-Helmholtz instability occurs and dominates. The mechanism which drives the Rayleigh-Taylor instability is baroclinic torque as shown in Figure 2.9. Baroclinic torque is defined by the relation $(\nabla\rho \times \nabla P)/\rho^2$, and although the density

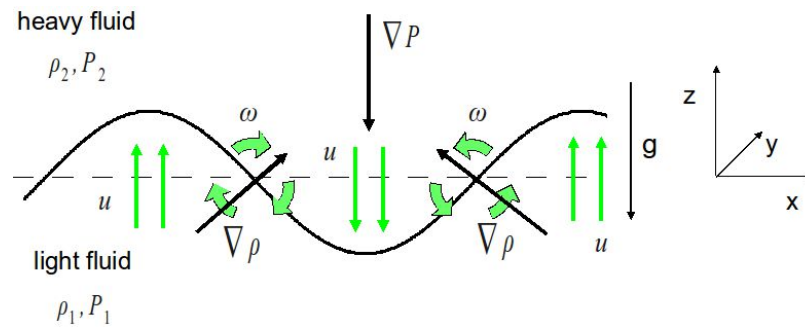


Figure 2.9.: Visualization of an unstable RayleighTaylor instability configuration where baroclinic torque at the interface creates vorticity and induces a velocity field that increases the baroclinic torque. [53]

gradient across the interface must exist normal to the interface layer the pressure gradient does not. This effect can exist in the presence of a pressure wave parallel to the interface layer, which then can drive a torque at the interface and destabilize the

interface layer introducing more vorticity. A diagram of this effect is shown in Figure 2.10 below.

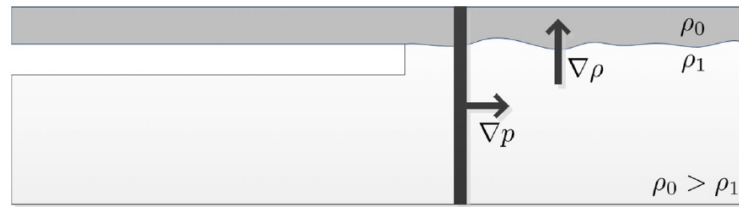


Figure 2.10.: Baroclinic torque action along the shear layer, where the dense fuel is against the wall and the less dense oxidizer in the core. [13]

2.2.3 Flame Characterization

In thermoacoustic instabilities unsteady heat addition is the main driving force. The combustion of non-premixed turbulent flames is not fully understood and is quite difficult to model. Unfortunately, this process needs to be well understood to understand the combustion instability mechanisms in a rocket.

The best way to characterize the flames for this particular experiment may be to break the problem down into its different components and try to understand the bounds of the problem. The hydrodynamics and mixing which heavily affect the heat release have already been overviewed, but now the nature and profile of the heat release needs to be detailed.

Metrics

The Lewis number is a measure of the thermal versus the molecular diffusion rates; this is good measure of when a mixture is partially premixed and is subjected to local heating via thermal conduction. The Lewis number, however, falls short in describing the flame characteristics of reacting flow. A more important metric of flame behavior is the Damköhler number.

The Damköhler number is a metric of the ratio between the characteristic flow time to the characteristic chemical time. These parameters may have different meaning depending on the problem being studied, but for the purpose of this study it is the ratio between the characteristic mixing time to the characteristic time of ignition delay due to chemical kinetics.

Turbulent non-premixed flames may exhibit behaviors locally that resemble turbulent premixed flames or even laminar flames (flamelets). It is therefore important to characterize these limiting regimes to be measured against. The Damköhler number has been used to describe different regimes of turbulent premixed combustion; this is shown in Figure 2.11. When the flame thickness is much smaller than the smallest

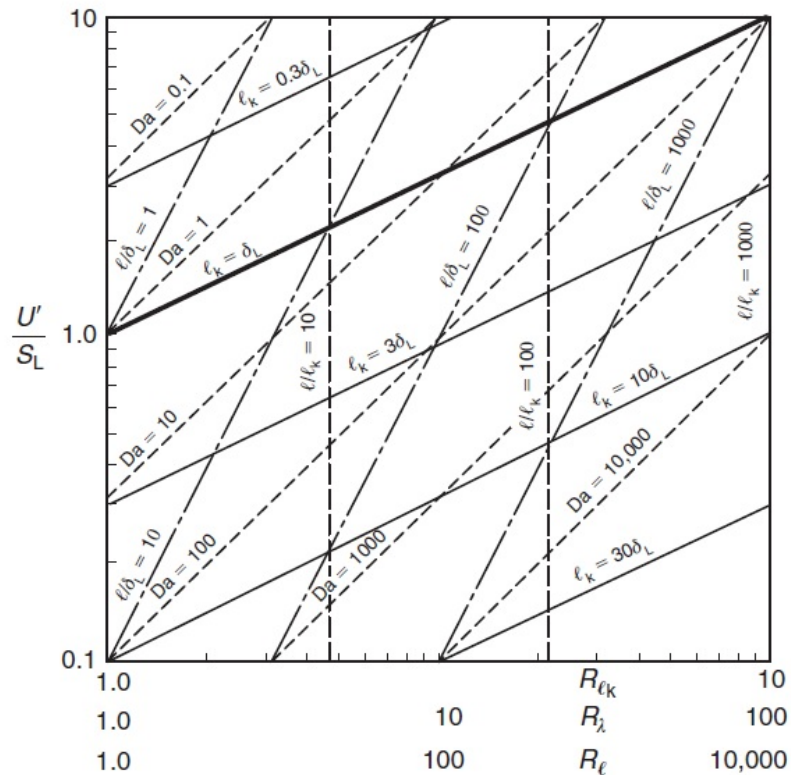


Figure 2.11.: Characteristic parametric relationships of premixed turbulent combustion. The Reynolds numbers are based on Kolmogorov microscales, Taylor microscales and integral scales respectively. [54]

scale of turbulence (ℓ_K) then the turbulence can only distort or wrinkle the flame, this is known as the Williams-Klimov criterion. At the other end of the spectrum, if the flame thickness is large than all turbulent scales then transport within the reaction zone is not solely governed by molecular processes. This criterion is known as the Damköhler criterion. The region between these criteria is sometimes referred to as flamelets-in-eddies [32]. Some efforts to characterize flames have used strain rate as a metric, which is described by Taylor microscales. It has been found that the 3 Reynolds number descriptions have the following relationship: $Re_{\ell_0} \approx Re_{\lambda}^2 \approx Re_{\ell_K}^4$ [54]. It should be cautioned that Figure 2.11 is a theoretical description and further research is being done on the topic of turbulent flames. Turbulent non-premixed flames do not necessarily have a propagation velocity, thus identifying a characteristic time scale is not simple. For an associated Damköhler number (one based on Kolmogorov scales) of approximately unity describes a scenario where the residence time within the reaction zone is not long enough to sustain combustion, and thus is prone to extinction [55]. For slower chemical reaction times, eddies at all scales can induce flame quenching, so no reaction sheet is formed and a distributed reaction zone exists [55]. As with Figure 2.11, it should be mentioned that this diagram is representative of the concepts, but should not be used to characterize a flame in detail.

Chemical Kinetics

To characterize the heat release with respect to combustion instability it is necessary to characterize the chemical time scales of the reaction. It is therefore crucial to identify which parameters and chemical species provide important information of the dominant physics in play during combustion.

The chemical reaction between methane and oxygen is well studied. The elementary reactions, their rates and intermediate species are modeled with GRI Mech 3.0 [56]. Although GRI Mech 3.0 is the most complete model of methane/oxygen combustion it is very computationally expensive to use in CFD simulations. In some

cases it is adequate to use less accurate predecessors to GRI Mech 3.0 such as GRI Mech 2.1. These models, with added fluid state state input, can be used to help identify the most dominant chemical reactions during the combustion process. Further, these dominant chemical reactions can then be used to identify intermediate species which are produced in higher concentrations during the reaction processes.

The characteristic time of the chemical reactions can then be mapped based on parametric studies such that $\tau_{chem} = f(P, T, \phi)$. It has been determined that ignition delay caused by the relatively slow speed of the characteristic time of the chemical reactions during combustion of the CVRC [57].

2.2.4 Flame and Fluid State Indicators

Accurate measurements require a very high level of certainty. Although the concept of measuring a particular parameter may seem trivial in nature, it can plague the validity of the conclusions made in a scientific investigation, especially in the case of a complexly convoluted system.

Unique markers or indicators of the flame and fluidic states need to be identified to ensure that the measurements made accurately reflect the parameters investigated. Furthermore, depending on the study, the parameter temporal and spatial resolution requirements may need to be considered. The distribution of the parameter/s investigated could have a significant role in how the physical system under scrutiny behaves, therefore the method and limitations of the measurement techniques employed are incredibly important to realize.

Fluid State

In general, some of the most important and fundamental parameters that describe a fluid are pressure, temperature and density. In typical rocket engines the fluids are in the supercritical range. At these conditions the fundamental parameters are not truly independent. Operating a combustor at subcritical fluid states allows for the

fluid to be described by two independent parameters, making the analysis easier. Depending on the physical feature examined the local versus distributed effects of each parameter are important.

For the purpose of measuring acoustics in a rocket chamber pressure measurements need to be well resolved and non-intrusive. For all practical purposes traveling and standing acoustic waves in the model rocket chamber can be assumed to be planar in nature. To resolve the amplitude, phase and speed of the acoustic waves, high frequency pressure transducers have to be placed in strategic locations. The resonant acoustic mode shapes can be resolved using high frequency pressure transducers placed at the circumference of the inner chamber diameter to measure pressure fluctuations at key nodal and anti-nodal wave locations.

Other pressure fluctuations due to local hydrodynamic structures are also possible to measure. Usually, the pressure fluctuations that arise due convecting vortical structures are relatively fast and low in amplitude, therefore this type of fluctuation is difficult to detect; the sensitivity and temporal resolution of the measuring equipment needs to be high and the experiment is setup to allow it.

The density of fluid is rarely measured in moving flows, especially high pressure reacting flows. Density can only be indirectly measured in a control volume type process. The most common methods used to infer density involve techniques which use the refractive index of the fluid, namely Shadowgraphy and Schlieren. Sharp gradient changes in refractive index give high contrast pictures of the flow, and with a calibrated measurement of a known density in the fluid the changes in density can be determined. Unfortunately Shadowgraphy and Schlieren heavily rely on an optical equipment setup that provides undistorted images. For diffusive light sources any unwanted lensing effects can distort the image such that the domain of measurement becomes indeterminate.

The temperature of a fluid can be measured in a number of ways where some methods are non-intrusive, but all methods require that, at least locally, the flow is in thermal equilibrium. The best type of non-intrusive methods require spectrum

measurements of emission. Whether the measurements are temporally and spatially resolved is dependent on the technique used. Currently there is a limitation on producing measurements which are spatially resolved beyond a single point.

Reaction and Flame States

In reactive flow the local dominant chemical reactions are determined by the local fluidic state (pressure, temperature, entropy, etc.), local equivalence ratio, strain rate and by the kinetic rates of the chemical elementary reactions. The rate of energy release in an exothermic reaction, especially in the case of combustion, depends wholly on the aforementioned parameters, where all parameters are coupled in some way or another and where some parameters can limit the speed of the reaction process.

Some intermediate chemical species can be correlated towards the main heat release path and because of their unique relationship with the main reaction they may be used to identify the flame zone within a reacting fluid flow [58]. The spatial, temporal and concentration distribution of these chemical markers can shed light on the nature of the flame. To identify these chemical species the emission and absorption spectra can be exploited through the use of laser probing and high speed high resolution imaging.

During combustion some exothermic chemical reactions produce excessive amounts of energy leading to the formation of products that may be vibrationally or electronically excited. The molecules that are produced excited electronically usually have the chance to energetically decay to the ground state energy level and in the process a photon is emitted. This emission process is called chemiluminescence. Depending on the molecule formed the emission may be in the ultraviolet or short wavelength visible spectrum. Because of the molecules' energetic birth it has been assumed that chemiluminescence may correlate directly with the main reaction and heat release process of the flame during combustion.

At this point in time there is still some debate on the use of certain chemiluminescent species as heat release and flame markers. The debate centers around the uniqueness of the production of these chemiluminescent species:

- Recombination reactions do not necessarily exist in the main flame zone, but do have enough energy output to produce electronically excited molecules.
- There have been proposals that electronically excited species can be produced through transfer of kinetic energy only (particle collisions), which would mean that the emission process would not be chemiluminescence anymore, but incandescence.
- Although the energy produced during chemiluminescent reactions is high, the reactions themselves may not form as part of the main heat release process.

Other intermediate species that have been identified as part of the main reaction branch of the heat release process can be forced to emit light in targeted spectra. Laser Induced Fluorescence (LIF) and other technique variants use the concept of taking advantage of the photoelectric effect. An absorption spectrum of the intermediate species is determined and laser light at that wavelength is beamed at the combustion gases. The targeted species will then emit light at slightly lower energy level (longer wavelength) and is imaged with narrow band filtered high speed cameras. If the wavelength of light chosen is unique to the combustion gases' radiation output then the measured light will show where and when the flame zone occurs.

As with chemiluminescence, there is always a constant debate as to whether the species fluorescing actually represent the flame zone. In this study only species that have been identified as most probable markers of the main reaction branch will be used.

The excited species CH^* , OH^* , C_2^* and CO_2^* have all been considered as possible candidate markers of heat release [59] in the process of methane combustion. Studies by [insert refs] have shown that C_2^* and CO_2^* are not good markers because they vary monotonically with equivalence ratio and do not vary uniquely with a single

heat release in high pressure, non-premixed systems, the measurement suffers from the effect of line-of-sight integration and its resulting bias.

To test the hypothesis that OH^* might be produced thermally an investigation into the spectrum shape of the emission band of OH^* . The first electro-rovibrational spectral band namely the (0,0) $A^2\Sigma^* - X^2\Pi$ band is usually centered around 308nm [58]. Chemiluminescent processes are not in thermal equilibrium and the spectral shapes of the emission bands do not correlate with the local gas temperature. Thermally produced electronically excited species will have a rotational band Boltzmann distribution of which the statistics will be based on the local gas temperature. For chemiluminescence emissions experiencing significant self absorption, especially in the case of OH^* , the spectral line shape is expected to deviate from a chemiluminescent source with no absorption. The reason for a different line shape is because the absorption spectrum reveals that at each wavelength the level of absorption is not the same; if a emission spectral line is stronger then the absorption strength at that same line is expected to be stronger and vice versa. This effect is shown below in Figure 2.13.

Measurements using the absorption spectrum can tell, within some assumption of spatial resolution, the average number density of the absorbing species in the probed medium. The number density can give insight into the reacting flow that may be used as a simulation validation tool.

2.3 Measurement Techniques

Robust and valid methods of measurement are just as important as the effort to understand the problem studied. There is no just cause to take a measurement that does not represent the feature under study. In the effort to validate models of combustion instability the methods of measurement need to be verified and their limitations understood. Descriptions of the measurement techniques are given here within.

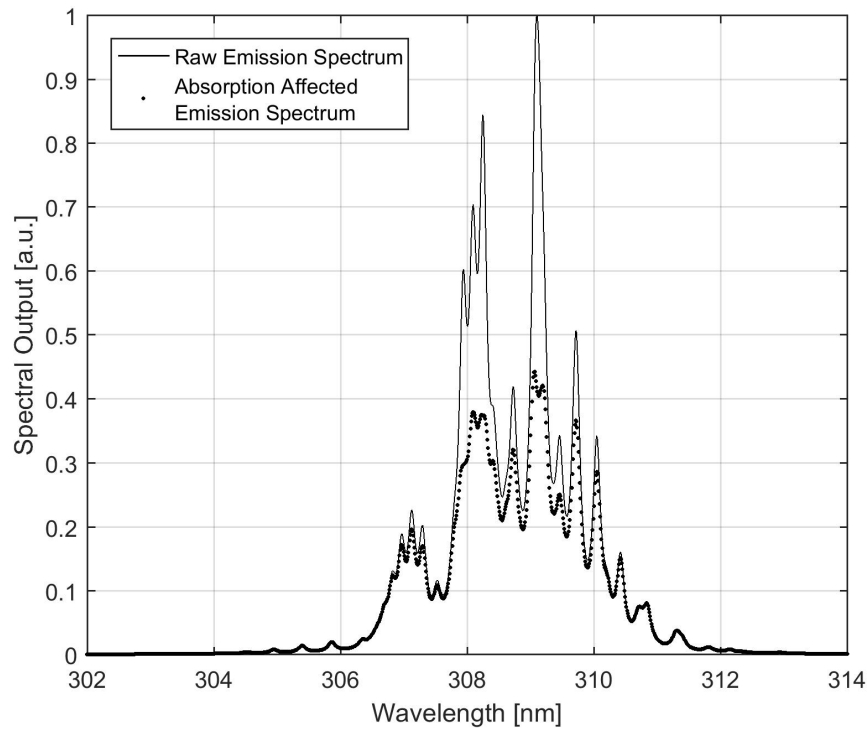


Figure 2.13.: Absorption affected spectral emission line shape of OH.

2.3.1 Acoustic and Pressure Measurements

Generally, in the case of studying combustion stability the focus of pressure measurements is predominantly on static pressure and acoustic features. Static pressure measurements can reveal the flow state changes from one system sub-compartment to the next. Manifold and chamber pressure can yield information on injection characteristics and combustion performance. Absolute dynamic pressure measurements can be used to determine acoustic and their frequencies, as well as the standing wave mode shapes. There is a possibility that the high frequency pressure instruments can measure hydrodynamic fluctuations locally, this type of measurement may be useful in determining periodic formations of the injected flow.

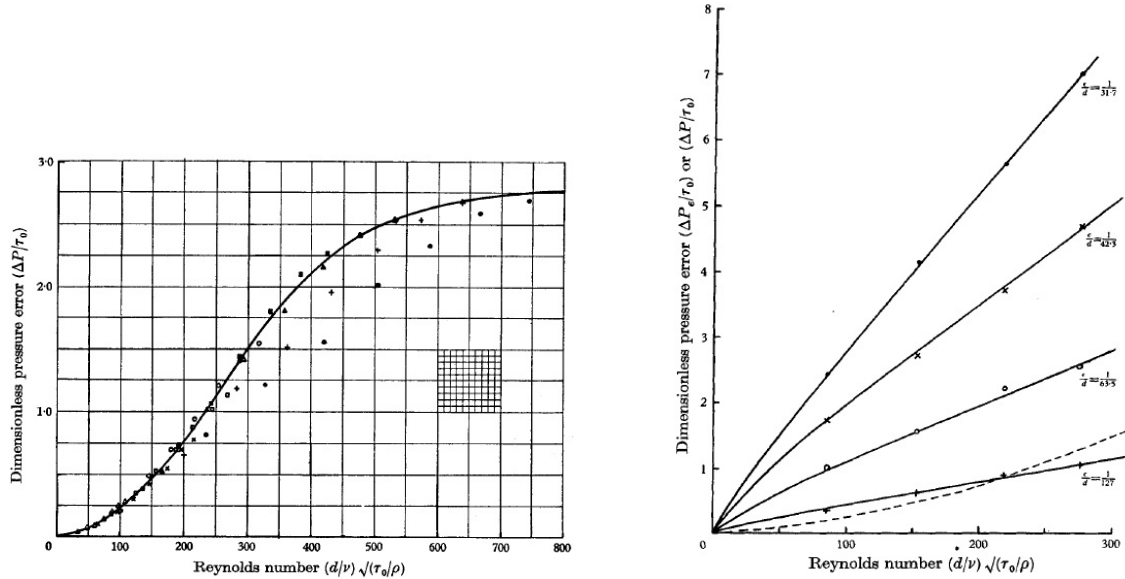
Determination of Static Pressure Measurement Error

Low frequency or static pressure measurements are used to measure the hydrostatic or mean and low frequency oscillations of pressure of the flow within the combustor. Tapped off measurements are usually used in high temperature systems to preserve instrumentation. This means that the measurement is not infallible to geometric effects of the port on the response of the measurement. Work has been done to provide a correction to the pressure measure at the wall [67].

The work done by Shaw [68] showed that for an incompressible turbulent flow at a Reynolds number of approximately 2×10^5 the static pressure error due to hole $\frac{1}{10}$ the diameter of the pipe reached a maximum of 1% of the mean dynamic pressure. Shaw used the idea that the error in static pressure measurements were based on geometry (length and diameter of immediate tap hole, size of burr on hole edge) and shear stress over the hole. The effect of shear stress over the hole was characterized using a Reynolds number based on the hole size, kinematic viscosity of the fluid and the friction velocity. The effect of burrs on the hole edge on static pressure measurement error were also studied and characterized. Figure 2.14 below shows the charts that will be used, from which the data extrapolated will be used to determine the effect of hole geometry and fluid state on error of static pressure measurement.

Pressure Port Response

Typically, measurements of static pressure rely on a negligible acoustic response. This is achieved by a very long thin tube connected to the tapped off port. It is assumed that the acoustics within the tube will attenuate over the length. Although this type of measurement is useful for determining operating bulk pressures and performance of a rocket, a measurement of the dynamic response is more important with respect to combustion stability because any fluctuation or modulation of the pressure field from the manifolds to the nozzle needs to be determined to insure the correct physical characteristics are achieved within the experiment. Therefore for any absolute



(a) l/d ratios 1.5 to 6. Hole diameter (in): \bullet 0.175; $+$ 0.150; \blacktriangle 0.125; \blacksquare 0.100; \circ 0.075; \square 0.0636; \times 0.050; \triangle 0.025.

(b) For 0.0635 inch diameter holes with varying heights of radial burr: l/d ratio of 4. - $\frac{\Delta P_{err}}{\tau_0}$; — $\frac{\Delta P}{\tau_0}$.

Figure 2.14.: Non-dimensionalized error in static pressure measurement for different geometries and Reynolds numbers. [68]

measurement of pressure that is expected to have dynamics needs to be evaluated and any irregularities corrected for. Zhang et al. [69] did a decent study on the response and losses of pressure ports.

Using the criterion for a lumped system the measurement port's type of response needs to be evaluated. Often it has been found that relatively short length measurement ports respond as Helmholtz or quarter wave resonators. If it is found that the port does not have a Helmholtz resonance then the port needs to be treated as a branched off duct with an associated impedance with a corresponding amplitude and phase response.

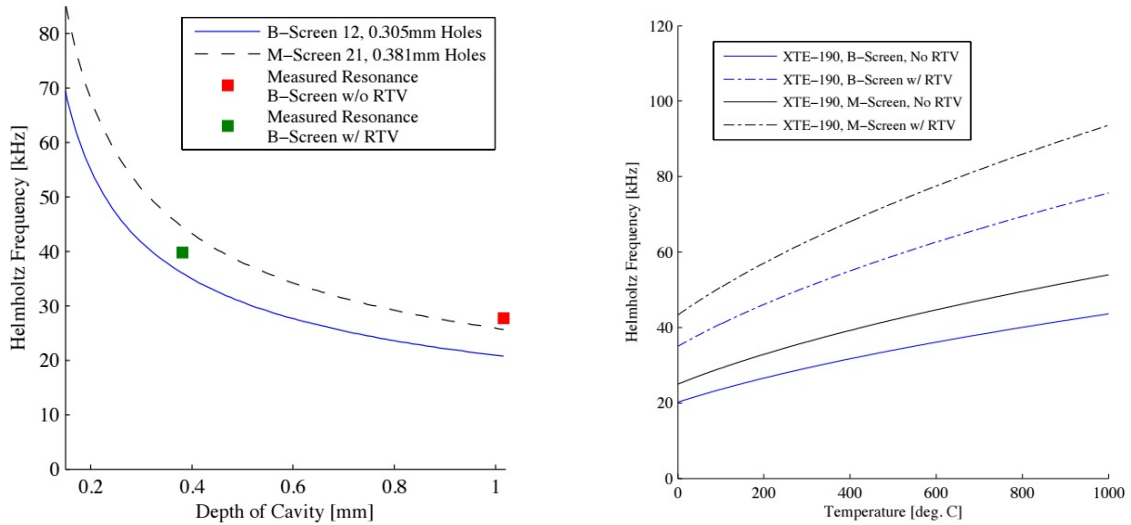
Englund and Richards [70] gave the typical form of the pressure response for a port which does not respond as a lumped system and does not have an acoustic impedance change. For a more accurate representation of a port with an impedance

change, such as an area change, the transfer matrix approach should be used. Unless the tapped port and tube are long, the acoustic attenuation is usually very low for gases; except for the case of high acoustic frequencies.

Pressure Measurement Hardware

In high temperature flowing environments, such as rockets and gas turbines, most measuring devices cannot be submerged in the flow. The cross sectional area of such devices is usually large enough to perturb the flow in an unwanted fashion, and if they are made small enough then the material cannot conduct heat fast enough away to cool the device and melt or burn as a result. The method favored by experimentalists conducting combustion research of rockets and gas turbines involves either flush mounted or tapped off ports from the combustion chamber, both of which are usually cooled.

Measuring high frequency acoustics require devices which can respond as such. For high frequency response pressure transducers either use a hardware architecture involving piezoelectric or piezoresistive based response. Two common examples of high frequency pressure transducers are PCB (piezoelectric) and Kulite (piezoresistive) transducers. PCB devices are AC power coupled and therefore can only measure the dynamic pressure response. Kulite devices are DC power coupled and can measure absolute pressure. Each device has a limitation in the bandwidth of frequencies that it can measure, but the it almost always excessively exceeds the measurement requirements. For some Kulite transducer designs the transducer employs a perforated plate to guard the sensing diaphragm from harmful particulates. The cavity produced between the plate and the sensing diaphragm can cause a Helmholtz resonance response as explored by Hurst et al. [71]. Figure 2.15 below illustrates the possible resonant frequency ranges for changes in cavity volume and temperature of the gas inside the cavity.



(a) Modified Helmholtz screen-cavity packaging resonance of XTE-190 with B-screen and M-screen.

(b) Temperature dependence of modified Helmholtz screen-cavity packaging resonance of XTE-190 transducer (atmospheric pressure).

Figure 2.15.: Temperature and geometry dependence of Helmholtz resonance of Kulite pressure transducer cavity. [71]

The signal produced from high frequency pressure transducers are analog. The signal must be converted to digital, amplified and conditioned to insure a good signal to noise ratio. To condition the signal a filter must be applied at no more than half the sampling rate to eliminate the effects of aliasing. The response of the filter should not only roll-off at the high frequencies, but the phase characteristics of the amplifier as well. Sampling at double the rate of the pressure oscillation frequency will adhere to the Nyquist criterion and produce the correct frequency response, however it will not resolve the amplitude and phase response of the oscillations. The pressure response signal outputted by the transducer should be sampled at not only twice, but at least 10 times the highest frequency of interest to resolve amplitude and phase correctly.

2.3.2 Temperature Measurements

Measurements of gas temperature can be achieved through direct and indirect means. Direct measurement usually involves the measurement device making contact with the gas, the device will achieve thermal equilibrium with its surroundings and produce a signal corresponding to the temperature change. The direct measurement devices rely on property changes of the material the device is made of when exposed to a change of temperature. A common example of such a device is a thermometer (mercury or alcohol) where the fluid inside a closed cavity expands and contracts, the rate of volume change is calibrated for temperature change. In high gas temperatures it is common to use thermocouples where the probing component is made of two different materials, usually metals, where a temperature change results in a potential difference produced between the two dissimilar materials.

Thermocouples have limitations with respect to material compatibility with the environment and can be quite expensive when more exotic materials are sought out. Another limitation of thermocouples is the response time. The fastest thermocouples respond at a rate no faster than 0.1s, which cannot resolve the temperature fluctuations in a reacting flow. Thermocouples can also be susceptible to noise and drift in their signals.

2.3.3 Optical Measurements

Optical measurements have the advantage of not influencing the fluid field, it is a non-intrusive method of measurement. Another major advantage that optical measurements have is the achievable spatio-temporal resolution. For certain optical measurement methods care must be taken to make provision and correction for spatial integrated measurements. The different techniques that will be used in this study of high temperature reacting flow are discussed hereafter and the pros and cons of each method will be highlights and investigated in detail.

Emission Measurement

Emission measurements are measurements of the radiative output directly from a source. In the case of combustion the radiation source (flame and chemical reactions) is not a single point and usually not homogeneous. Corrections and estimation techniques need to be used to determine the spatial distribution of the radiative output because the measurement is inherently line-of-sight integrated. In some more extreme scenarios corrections to the received signal need to be made for refractive index and absorption.

Since the radiative source is expected radiate in all directions the optical measurement taken will only be a portion of the total radiative output. The portion of light measured from the source is determined by the optics used in the setup of the measurement. The magnification and focal lengths are approximately inversely proportional, so the the amount of light received decreases with increasing magnification.

The range of angles of light that can be collected or emitted by an optical system is characterized by the metric *numerical aperture*. The numerical aperture is constant throughout the optical system. The numerical aperture is especially important when characterizing optic system assemblies and long light path systems such as a fiber optic cable. The image brightness is proportional to the square of the numerical aperture.

For highly refractive/reflective optics and thick lenses light rays originating from the same source, but with slightly different trajectories may experience refraction that will distort the image. These distortions are called aberrations. Spherical aberrations occur when the rays originating from a source fail to converge at a single image point. Spherical aberrations occur especially at the fringes of lenses and mirrors. Chromatic aberrations occur when the refracting object refracts light waves of different wavelengths by different amounts. This effect results in chromatic dispersion. Prudent planning of the optical setup can avoid these aberration effects [72].

The solid angle is another metric which helps characterize the amount of light received by an optical measurement system. The solid angle is 2D angle representing the size of the arc subtended by that angle in 3D space. Effectively, it is a measurement of apparent size of an object, or the fraction of area of light collected from/emitted to a sphere.

For a diffusive source the emissions can be thought of as originating from infinitely many point sources distributed within the area of radiative emission. Each point source would then have a corresponding solid angle associated with its position relative to the optic collection hardware. It is not practical to evaluate a diffusive light source in an experiment in this manner, but using some basic assumptions, data from a simulation can be used to calculate the solid angle for various positions within the area of interrogation.

There are a number of methods of measuring light at a high frequency. Currently there are high speed cameras and intensifiers that record in excess of 250kHz. Photomultiplier tubes (PMTs) are analog and measure photons over a wide wavelength band. The technology of temporally resolving of emissions from short timescale reacting flows has been vastly improved in recent years, where some important high frequency features can be studied and used for model validation purposes.

Absorption Measurement

Spectroscopy of flames is a technique that has been used since the 1940s. The spectral output from electromagnetic (EM) radiation produced from excited particles in a flame can be used to determine the temperature and some of the more energetic constituents of that flame. In high pressure flames there may be an effect of absorption by some of the ground state species. The amount of absorption is proportional to the number density of the particles and therefore the pressure.

Absorption spectroscopy is a technique that can yield quantitative information about the average number density of an absorbing species within a fluid. A constant

light source with a known spectral output is needed to determine the absorption fraction of the species in a fluid. There are mainly two ways of providing a reference light source for absorption spectroscopy: continuous band and tuned wavelength. In each scenario a reference measurement of the light source is needed to determine how much absorption occurs. It should be noted that for higher frequency measurements there is a danger of measurement obscurity because in practice even the most well behaved light sources fluctuate in time. It is therefore left to the user to make prudent use of simultaneously measuring the reference beam and the absorbed light to obtain an accurate measurement. The absorption fraction is determined by the Beer-Lambert law:

$$\frac{I(\nu_0)}{I_0(\nu_0)} = \exp \left[- \sum_{\nu_i}^{\nu_N} [K(N, \nu_0)g(\nu_0, \nu_i, T, P)]L \right] \quad (2.19)$$

where:

- I is the radiant flux, which is a function of central wavelength ν_0 , the subscript denotes the reference measurement,
- the line strength K is a function of number density N and ν_0 ,
- the line shape g takes the form of the Voigt profile which is a function of ν_0 , detuned wavelength ν_i , temperature and the effect of pressure on line broadening,
- and L is the optical path distance.

The absorption fraction for a specific wavelength has contributions from neighboring spectral lines, hence the summation in the exponent. The level of contribution to absorption at a spectral line from neighboring lines depends on the nature of the fluid and needs to be determined on a case-by-case basis.

2.4 Verification and Validation

A problem such as combustion instability is inherently complex; there are number of different types of mechanisms all coupled and interlinked, where each mechanism

has a series of modes of behavior and most are nonlinear. This makes it difficult to accurately model the behavior. Currently there have been numerous efforts to accurately predict thermoacoustic instabilities in high pressure combustion devices. Therefore there is a dire need for experimental validation to prove these models. Oberkampf and Trucano [73] provide a scaffold method (Figure 2.16) to verify and validate complex scientific models.

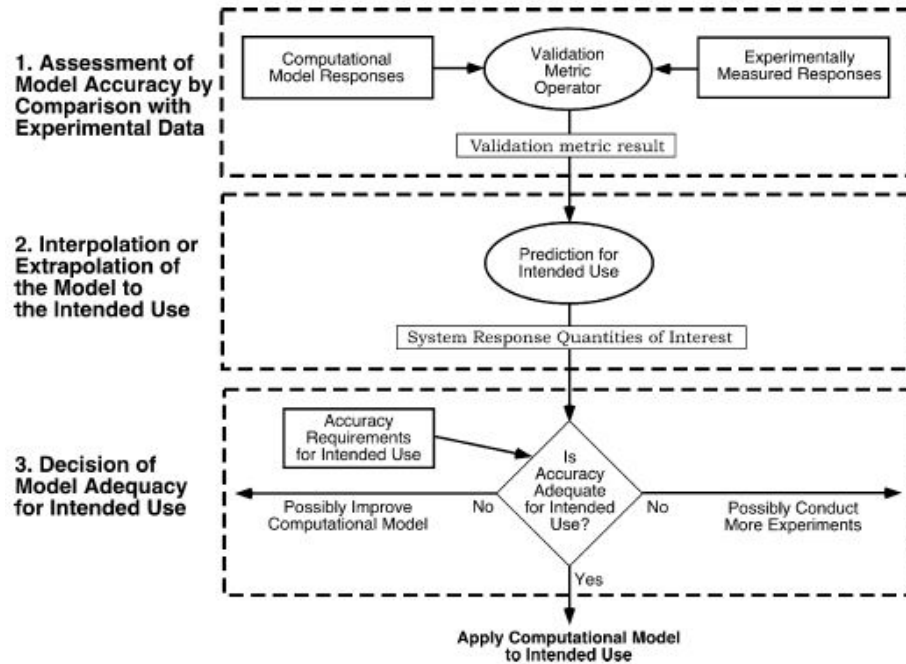


Figure 2.16.: Three aspects of model validation.

Verbatim from Oberkampf and Trucano, the following guidelines are useful when trying to validate a computational model:

- Guideline 1: A validation experiment should be jointly designed by experimentalists, model developers, code developers, and code users working closely together throughout the program, from inception to documentation, with complete candor about the strengths and weaknesses of each approach.

- Guideline 2: A validation experiment should be designed to capture the essential physics of interest, including all relevant physical modeling data and initial and boundary conditions required by the code.
- Guideline 3: A validation experiment should strive to emphasize the inherent synergism between computational and experimental approaches.
- Guideline 4: Although the experimental design should be developed cooperatively, independence must be maintained in obtaining both the computational and experimental results.
- Guideline 5: A hierarchy of experimental measurements of increasing computational difficulty and specificity should be made, for example, from globally integrated quantities to local measurements.
- Guideline 6: The experimental design should be constructed to analyze and estimate the components of random (precision) and bias (systematic) experimental errors.

3. EXPERIMENTAL APPROACH

The experiment HAMSTER (Hydrodynamic And Mixing Study of a Thermoacoustically Excited Rocket) was designed to study thermoacoustic instabilities. The study focuses on measuring acoustic fluctuations, flame emissions and velocity fields within the combustion chamber. The injector design was purposed to have as much control of the flow as possible in order to study the hydrodynamics associated with the heat release mechanisms during rocket combustion. Injector predictions and design parameters were based on previous CVRC simulations. These simulations provided a foundation of what the fluid mechanics of the injector might be like. Figure 3.1 shows time averages of a number of variables for a simulation of the CVRC. The vorticity is

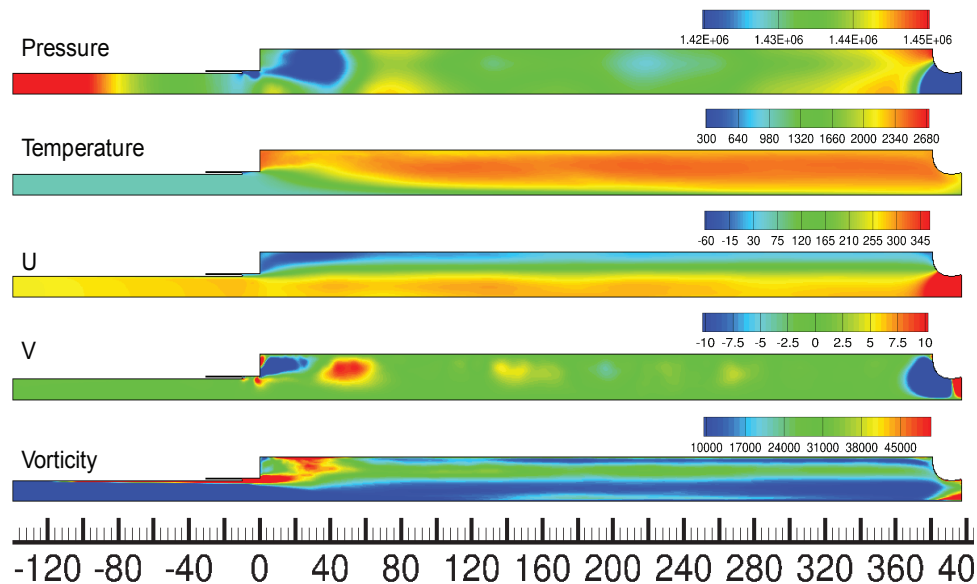


Figure 3.1.: Time averages of CVRC simulation data.

of particular interest as it show evidence of vortex formation and transport from the injector to the combustor wall, as well as the approximate size of the recirculation

zone off of the dump plane step. This information together with a reconstructed Dynamic Mode Decomposition (DMD) spectrum (Figure 3.2) of the vorticity not only show that the injection dynamics can be dominated by the fundamental acoustic mode and its harmonics, but that features such as the dump plane backward facing step and collar together with the recess, all elements of the injector design, contribute to the modes of heat release. In particular it was found that the vortex shedding from the collar from both the oxidizer and fuel may be major contributors towards mixing the reactants prior to entry into chamber. The vortex shedding from the dump plane step further enhanced mixing while providing a geometric feature to set up the recirculation zone behind the backwards facing step.

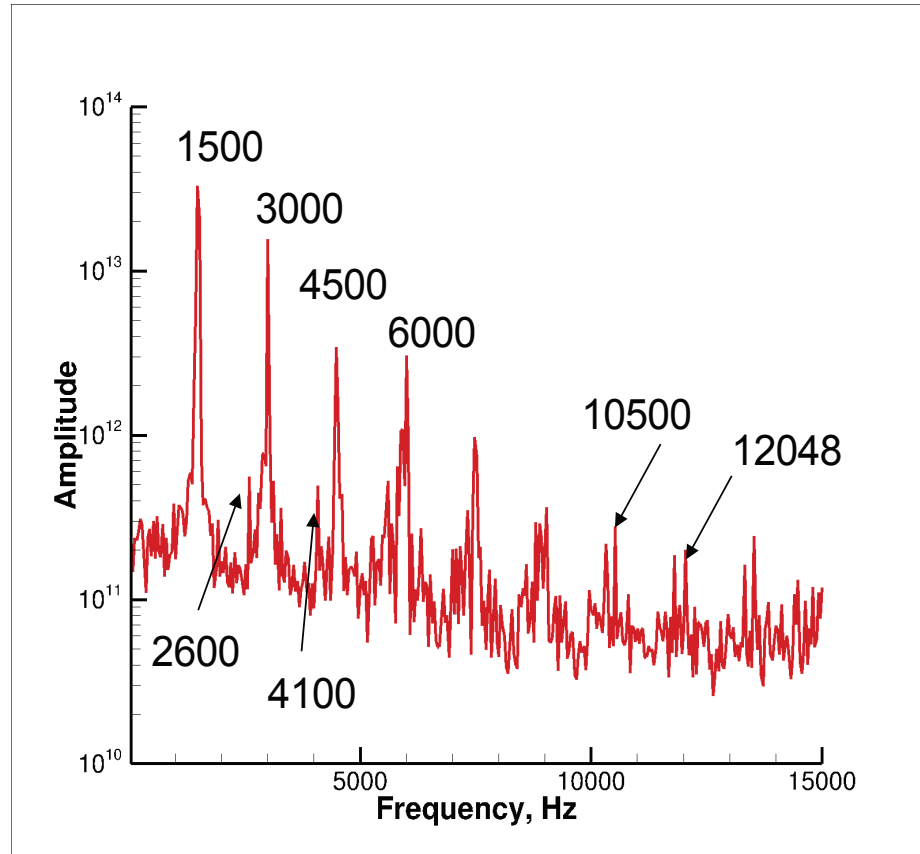


Figure 3.2.: DMD spectrum of vorticity from CVRC simulation data.

The experiment has been designed in cooperation with the modelers so that it can be modeled with a high level of confidence, as per Guideline 1 when developing a validation experiment. An emphasis on boundary conditions was made during the design process. Flow conditioning, acoustic boundaries and heat transfer effects were all considered, per Guideline 2. A prior CFD simulation was done to check the feasibility of the design, per Guidelines 3 and 4; the CFD results showed that the experimental design resulted in a thermoacoustically unstable state with a number of auxiliary features with respect to the acoustics and heat release. The DMD spectra of the pressure (Figure 3.3) and heat release (Figure 3.4) have been extracted from the initial HAMSTER simulation based on the proposed design conditions.

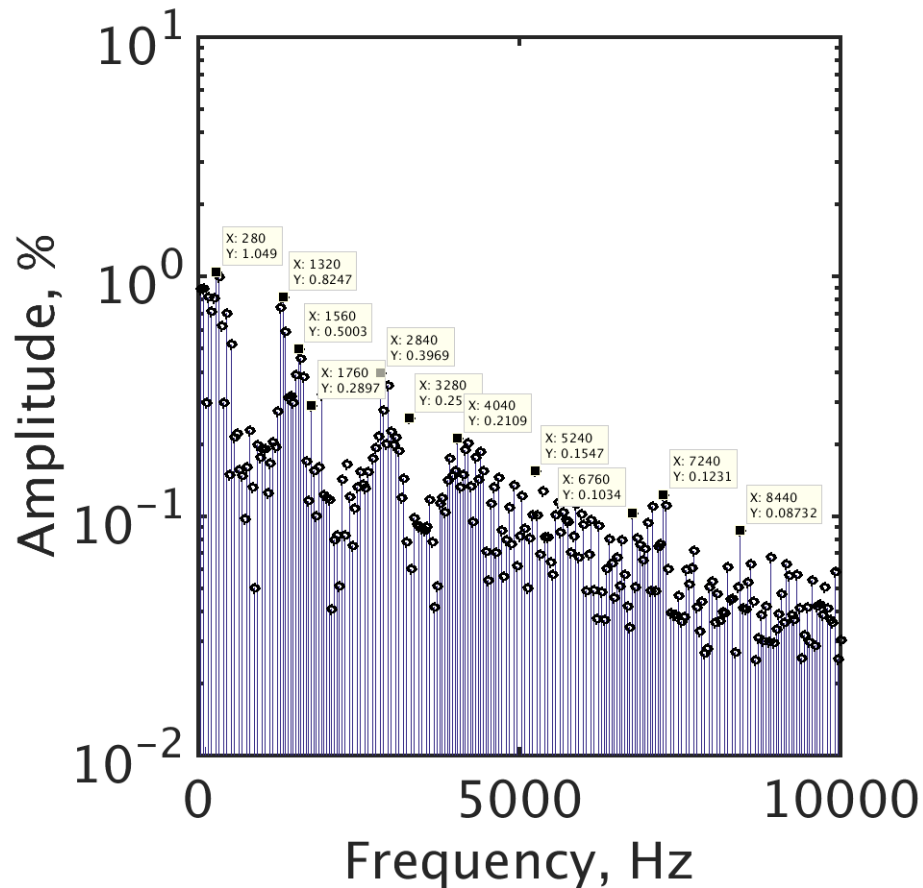


Figure 3.3.: DMD spectrum of pressure from HAMSTER simulation data.

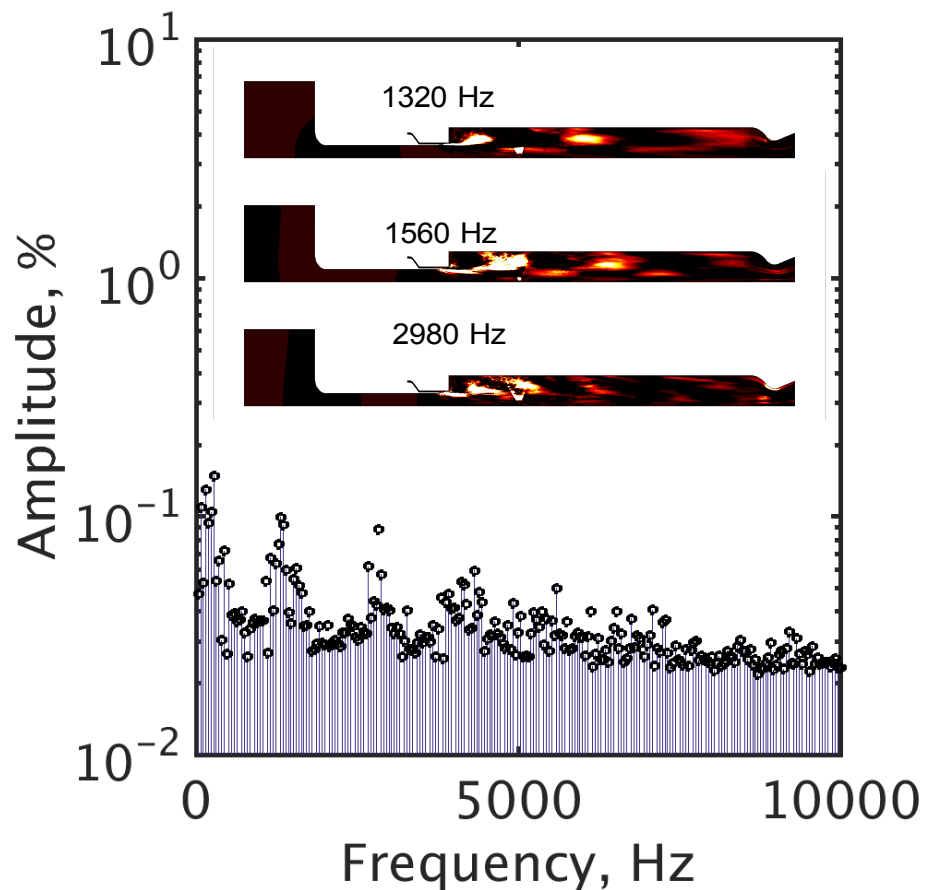


Figure 3.4.: DMD spectrum of heat release from HAMSTER simulation data.

The system was designed to be modular in order to tune the chamber acoustically and modify the injection characteristics. The experiment also focused on producing high fidelity measurements that would be used to validate any corresponding model.

Improvements over previous designs include:

- control of and confidence in the propellant conditions
- laser ignition in chamber to provide soft start in order to not excite the system unnecessarily, eliminate unnecessary geometric features that could influence the chamber flow, and allow a full field for view
- ability to acoustically isolate both the oxidizer and fuel manifolds

- optical access for high rate chemiluminescence measurements
- higher-fidelity measurements
- full modularity of injector
- ability to control one independent injection variable at a time

All of these improved features together form up to one goal: improved control over the injection characteristics and providing a good platform to study said characteristics.

3.1 Experimental Setup

3.1.1 Experiment Parameters

The experimental parameters are tabulated below. The CVRC was used as a template since it has been well studied and modeled, however because of the different propellants and injection properties it is expected that the current experiment will behave differently. Subcritical injection of gaseous propellants was chosen because the injection characteristics are easier to study; the physics conform to theory and simulation better and in general there are fewer variables to consider. Methane and oxygen were specifically chosen because the chemical kinetics are accurately modeled as mentioned in Section 2.2.4. A prototypical injector from the oxidizer rich combustion cycle was chosen.

The effect of propellant temperature has been hypothesized to have a significant effect on ignition delay and injection characteristics; nominally the oxidizer temperature will be high, similar to that of staged combustion, and the fuel will be at ambient temperature. The change in oxidizer temperature also effectively changes the acoustic length of the oxidizer manifold and post. The propellant temperatures will be varied to study the effect on combustion stability. The Mach number in the oxidizer post is restricted to allow for the acoustics to initially set-up a standing wave without too much of an effect due to mean flow. The chamber diameter and pressure have

Table 3.1.: HAMSTER design parameters as per AFOSR project.

Parameter	Value	Notes
Propellant Combination	CH_4/O_2	Both gaseous
Equivalence Ratio	$\phi = 0.8$	More predictable behavior
Propellant Temperature	$O_2 Temp: 620 - 980 F$	800 F nominal
Oxidizer Post Mach No.	$\bar{M} \approx 0.38$	
Large Chamber Diameter	$D = 2''$	For possible PIV, PLIF measurements
Chamber Pressure	170 psi	To accommodate optical measurements

been chosen to accommodate laser based measurement techniques such as PIV. A low chamber pressure also ensures that the propellants do not undergo a phase change or experience real gas effects prior combustion and post injection.

The design of HAMSTER is depicted below in Figure 3.5. The design is highly modular and using a hydraulic jack to clamp the assembled system together allows for a quick turnaround when substituting alternative parts. The resulting nominal flow conditions are listed in Table 3.2. By only changing the propellant temper-

Table 3.2.: HAMSTER nominal flow conditions and typical ranges.

Parameter	Value
Oxidizer Mass Flow Rate	0.87 lbm/s
Fuel Mass Flow Rate	0.17 lbm/s
Momentum Flux Ratio	$J = 2.22$
Adiabatic Flame Temperature	$T = 5480 F$

ature a change in ignition delay due to chemical kinetics is not the only variation produced. Keeping the mass flow constant at a given pressure, a change in propel-

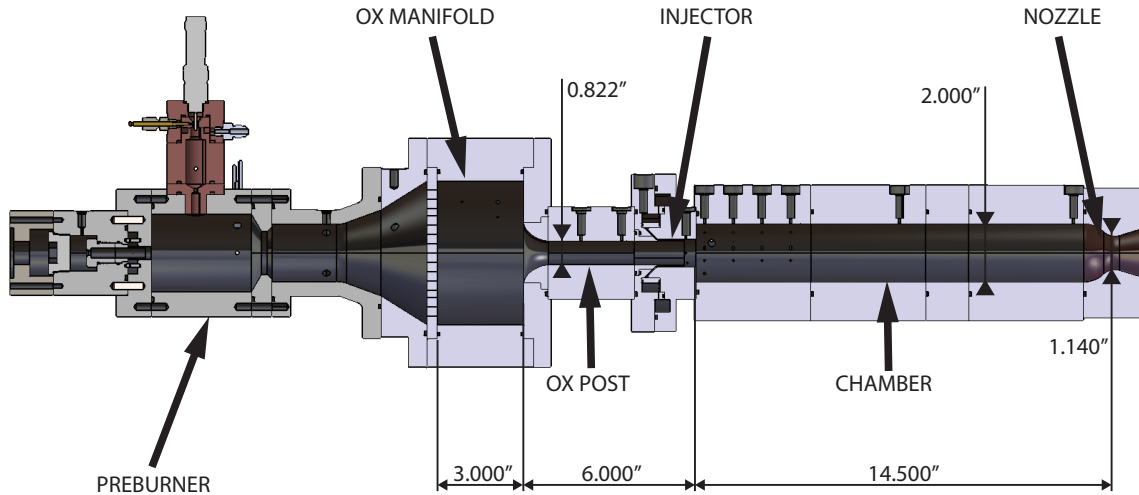


Figure 3.5.: Cross-section view of HAMSTER.

lant temperature will lead to a change in the gas density of the propellant. This, in turn, will inversely affect the propellant velocity during injection. From Equation equation (2.12), the relationship of momentum flux ratio to propellant temperature is shown below:

$$J = \frac{\rho_{ox} U_{ox}^2}{\rho_f U_f^2} = \frac{MW_f}{MW_{ox}} \left(\frac{\dot{m}_{ox} A_f}{\dot{m}_f A_{ox}} \right)^2 \frac{T_{ox}}{T_f} \propto \frac{T_{ox}}{T_f} \quad (3.1)$$

A summary of the velocity, density and momentum flux ratios of HAMSTER for different propellant temperatures are given in Appendix B. It is interesting to note that for certain propellant temperature combinations, that are easily achievable, the density and velocity ratios become unity.

3.1.2 Design Details

Per Guideline 2 of the approach to designing a validation experiment, the hardware was designed, first and foremost, to capture the physics of interest. The flow chart in Figure 3.6 shows the hierarchal importance of each design criterion that needed to be met. The over-arching physical behavior that was to be emulated was the presence and

control of self-excited thermoacoustic instabilities. In cooperation with the personnel responsible for modeling the physics (Guideline 3), the boundary conditions were designed to be easily modelable and have the highest degree of certainty. Lastly, a strategy was developed to produce measurements of high fidelity that could be directly compared with the simulations of the experiment, from global to localized detail per Guideline 5.

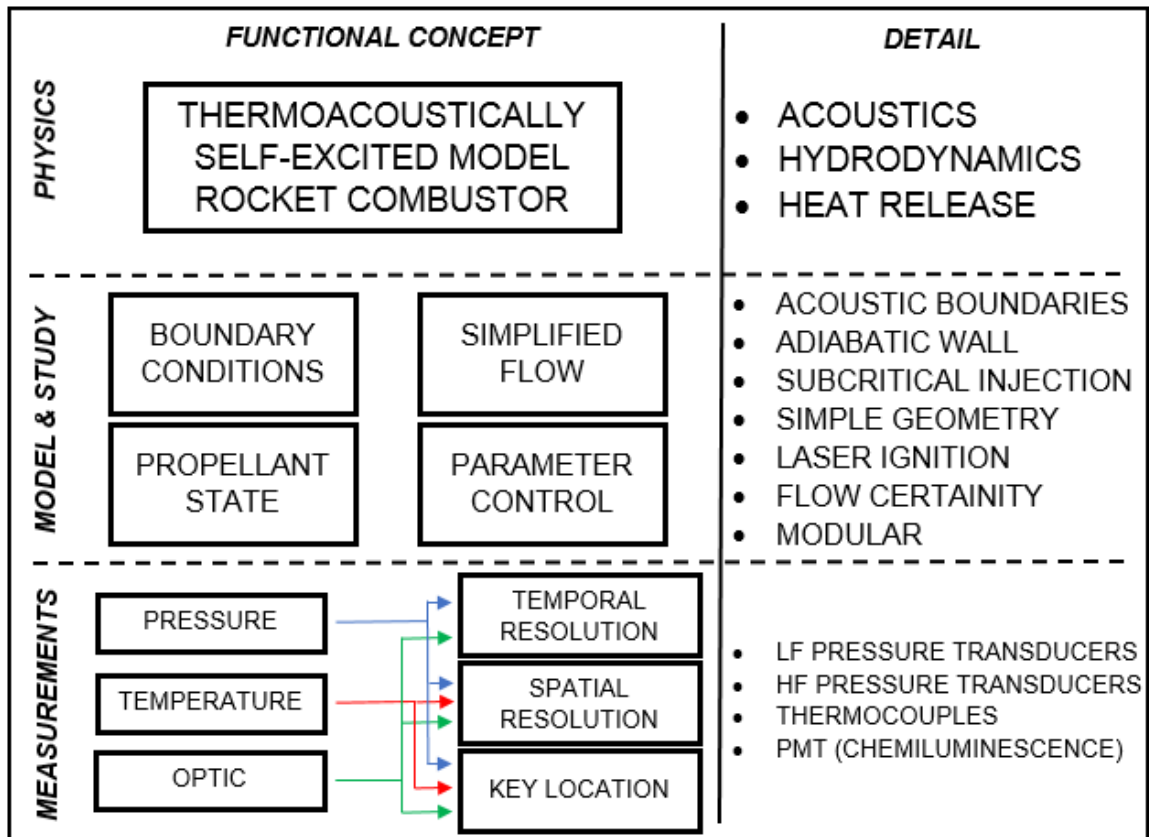


Figure 3.6.: Hierarchy of design criteria.

Experiment Dimensions, Scaling and Propellant Flow

The HAMSTER is designed to emulate a specific set of hydrodynamic features, such as vortex shedding off of the collar and the injection dump backward facing step.

Experimental and CFD results from the CVRC were a template for the production of self-excited instabilities. Since the oxidizer properties are different, most features were not directly scalable. The vortex shedding off of the backward facing step was scaled with an estimated velocity-length from the CVRC. The vortex shedding off of the collar was estimated using Equation equation (2.13), and for verification a reference estimated value of the CVRC collar vortex shedding frequency was used.

Based on experience with the CVRC, fuel-lean operation was chosen to ensure repeatable results. The combustion chamber diameter and pressure were set to provide optical access to the regions of interest in the recess and injector exit. The injector orifices were then calculated to produce a similar oxidizer post Mach number and momentum flux ratio to that of the CVRC and what is generally found in practice. The orifice sizes were also designed in tandem with the dump plane step height and fuel collar thickness to produce anticipated vortex shedding frequencies. To mimic the adiabatic boundary wall condition usually imposed in simulations the oxidizer manifold, combustion chamber and exit nozzle were all coated with an yttria-stabilized zirconia thermal barrier coating (TBC). The nominal system dimensions are shown in Table 3.3.

The experiment was designed with very high precision tolerance to achieve the most confidence when comparing the real system with simulated models of the experiment. High tolerance features were especially important in the injector where the hydrodynamic characteristics are very sensitive to geometry change. The test article was machined and assembled, with the actual injector dimensions shown in Table 3.4. Once the actual acoustic response in the system is well characterized the loss of heat through the walls can then be characterized; all data with regards to flow performance will be reconciled before attempting to analyze the flow field in more detail.

Table 3.3.: HAMSTER nominal design geometric configuration.

Geometric Feature	Value
Overall effective system length	23.00 <i>in</i>
Oxidizer manifold diameter	5.00 <i>in</i>
Oxidizer post length	6.00 <i>in</i>
Oxidizer post diameter	0.822 <i>in</i>
Injector recess length	0.400 <i>in</i>
Injector recess diameter	0.986 <i>in</i>
Fuel collar thickness	0.032 <i>in</i>
Effective chamber length	14.26 <i>in</i>
Chamber diameter	2.00 <i>in</i>

Table 3.4.: Comparison of designed and actual dimensions of the HAMSTER injector.

Geometric Feature	Dimension Achieved	Designed Geometric Tolerance	Achieved Geometric Tolerance
Oxidizer post diameter	0.8220 ± 0.0002 <i>in</i>	0.001 <i>in</i>	0.0001 <i>in</i>
Injector recess diameter	0.9847 ± 0.0002 <i>in</i>	0.001 <i>in</i>	0.0001 <i>in</i>
Fuel collar outer diameter	0.88635 ± 0.0001 <i>in</i>	0.001 <i>in</i>	0.0002 <i>in</i>
Fuel gap width	0.0492 ± 0.0002 <i>in</i>	0.002 <i>in</i>	0.001 <i>in</i>

Acoustic Response

Since the physical phenomenon studies is thermoacoustic instabilities, the acoustic response of the combustor needs to be well designed. How the chamber acoustics communicate and transmit energy to the injection system is an interesting and im-

portant problem. In some cases the injector and chamber acoustic systems can be thought of as separate systems, where one (usually the chamber) provides a noise source to drive acoustic oscillations in the injector, however, this premise only holds if the transmission of energy from the chamber is effectively low - the injector may be directly coupled to the combustion, but the acoustics in the injector and chamber are somewhat decoupled. On the other hand, if the transmission of acoustic energy is efficient from the chamber to the injector, and vice versa, then the acoustic resonance of the system can get more complicated; the acoustic resonance of the system needs to be analyzed in its entirety. A simple way to evaluate which type of behavior might occur is to check the impedance (or admittance) change of the injector/chamber interface. Figure 3.7 shows the reflection coefficient (Equation 2.4) at the dump plane as a function of oxidizer temperature, and shows a generally low reflection, which suggests that the system will respond as a single duct with area and gas property changes.

A preliminary design of the acoustic response of the system was done using GIM (Generalized Instability Model [74]); the acoustic response of HAMSTER was mapped and used to tune the length of the oxidizer post and chamber. Using the expected mean Mach number flows in the oxidizer post and chamber, the evolution of the fundamental mode shape was plotted in Figure 3.8.

It was later found that the impedance of the oxidizer post interface due to the area change may not have been adequately modeled by GIM, and the effects due to higher Mach number needed to be improved. Using the transfer matrix approach, where each discrete geometric element and the impedance interfaces between them were modeled, the acoustic resonance and anti-resonance map was modeled. The full system and each geometric section (duct) contributes to the overall acoustic response (input impedance) of the system, and the harmonics thereof; a full preliminary map of the acoustic response at nominal conditions is shown below in Figure 3.9.

The acoustic map accounts for acoustic attenuation, mean flow effects, lumped system response and improved impedances at the geometric interface area changes.

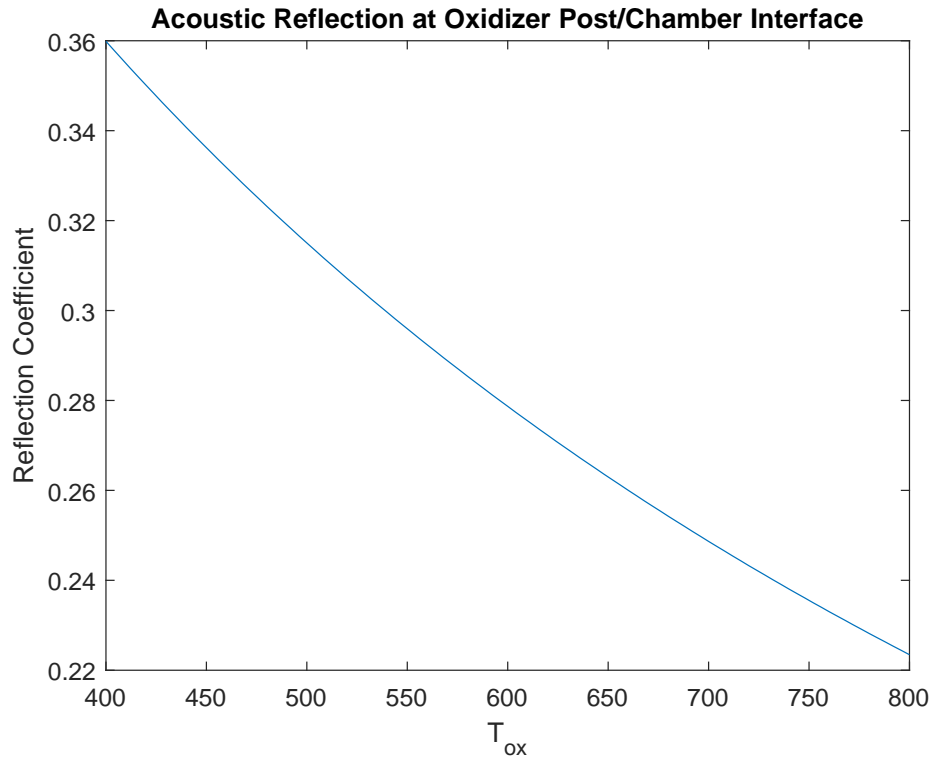
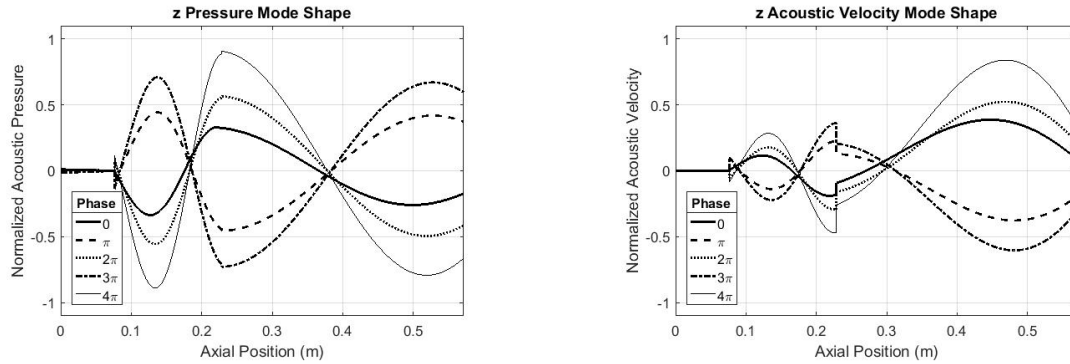


Figure 3.7.: Acoustic reflection coefficient due to the specific impedance change between oxidizer and combustion gases at the dump plane.

The fundamental acoustic frequency was required to be low enough so that any optical measurements made with high speed cameras were able to resolve the system temporally; this drove the choice for the length of the combustion chamber. The oxidizer post length was chosen based on two criteria: (1) based on the acoustic map, where the approximate fundamental mode in the chamber is close to the resonant frequency in the oxidizer post, (2) the acoustic mode shape follows a natural progression of a standing wave between the chamber and oxidizer post, whilst allowing for some velocity fluctuation near the head-end of the injector. A representation of this concept is shown in Figure 3.10.

For the proposed nominal design it is necessary to characterize all possible acoustic modes that may occur so that when the experimental data are analyzed the modes



(a) Acoustic mode shape evolution.

(b) Particle velocity mode shape evolution.

Figure 3.8.: Evolution of fundamental system acoustic mode during resonance with mean flow. The acoustic length is modeled from the oxidizer manifold distribution plate to the exit nozzle, both of which are choked providing a hard acoustic boundary condition.

for other physical mechanisms can be deduced by elimination. Figure 3.11 shows an a priori 1D acoustic model of the system, without heat release, but approximately accounts for property changes such as sound speed.

The nozzle was designed to adhere to the short nozzle approximation where the length of the nozzle is much shorter than the length of the chamber ($L_N/L_c \ll 1$) [75]. The reduction in pressure amplitude due to attenuation produced by a short nozzle can be described by Equation equation (3.2).

$$\frac{P}{P_0} = \exp(-\alpha_N t) \quad (3.2)$$

where P_0 is the pressure amplitude and α_N is the attenuation coefficient of the nozzle. From experiments with an acoustic standing wave in air, a correlation was found for the nozzle acoustic attenuation based on mean sound speed, length of chamber and inverse contraction ratio [75]:

$$\alpha_N = 0.3 \frac{\bar{c}}{L_c} \frac{A^*}{A_c} \quad (3.3)$$

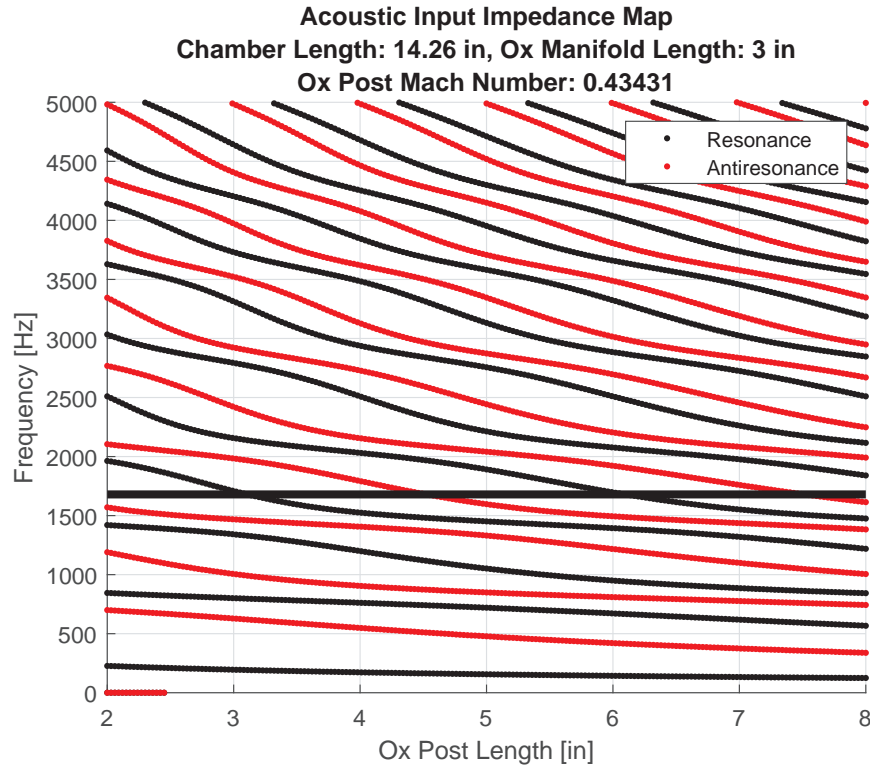


Figure 3.9.: Map of resonant acoustic frequencies expected in HAMSTER during nominal operation. The dark line denotes the 1D assumption limit based on the oxidizer manifold diameter.

From Zinn [75] using averaged compressible flow theory an expression for the nozzle acoustic attenuation for low flow Mach numbers is expressed as:

$$\alpha_N = \left(\frac{\gamma + 1}{2} \right)^{\left(\frac{\gamma - 3}{2(\gamma - 1)} \right)} \frac{\bar{c}}{L_c} \frac{A^*}{A_c} \quad (3.4)$$

From CEA with the experimental parameters shown in Table 3.1, the acoustic attenuation of a nozzle with an inverse contraction ratio of 0.3249 is calculated to be $686.11s^{-1}$ for theory (Equation equation (3.4)) and approximately $298s^{-1}$ adjusted from the experimental data (Equation equation (3.3)). Using Equation equation (3.2) the percentage drops in amplitude are approximated to be 35% and 17% respectively; these values provide a range in which one should expect a quantifiable effect on acous-

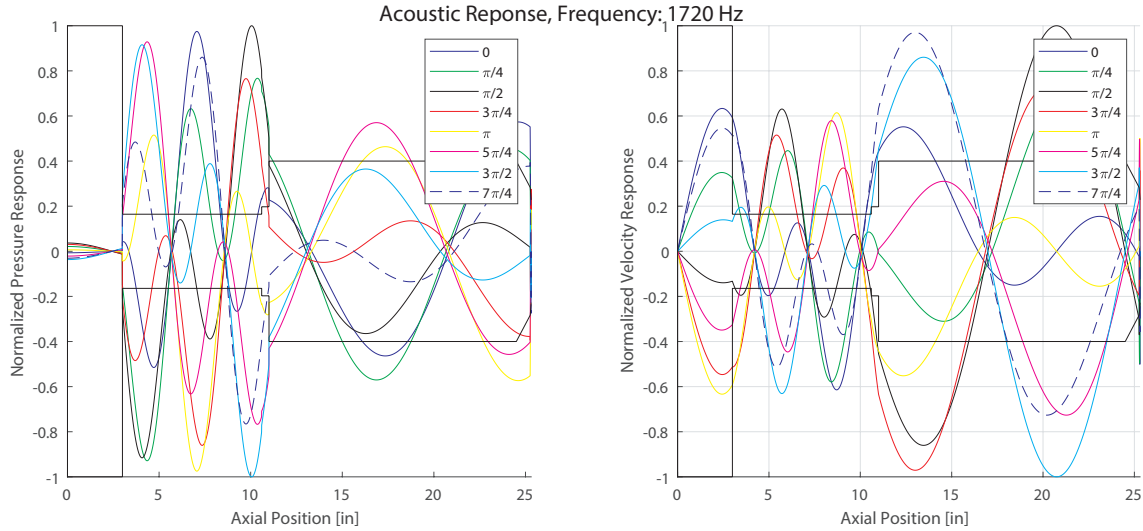


Figure 3.10.: Possible fundamental acoustic mode shape, showing the velocity fluctuation near the head-end.

tic attenuation due to the short nozzle. If the effect of attenuation seems to fall outside this range it is necessary to characterize the nozzle's effect experimentally.

Acoustic attenuation throughout the system can be characterized for each subsection of the combustor, namely: combustion chamber, oxidizer post/manifold and fuel annulus/manifold. Bulk fluid thermoviscous losses are expected to occur in the oxidizer post/manifold and the combustion chamber while narrow passage thermoviscous losses could occur in the fuel annulus of the injector. For nominal experimental conditions (see Table 3.1) and data provided by NIST [76], the acoustic attenuation expected in the combustor was calculated to be negligible.

Since the acoustic attenuation is negligibly small the Goldberg number $\Gamma \gg 1$, thus if acoustic perturbations persist and resonate the wavefronts will skew and become nonlinear in nature. All radial and transverse modes are expected to be evanescent within the chamber, however in the oxidizer manifold it is expected that a transverse mode will cut-on at $\approx 1754 \text{ Hz}$, while the first tangential mode expected in the main chamber is 13 kHz for the lower bound of cases.

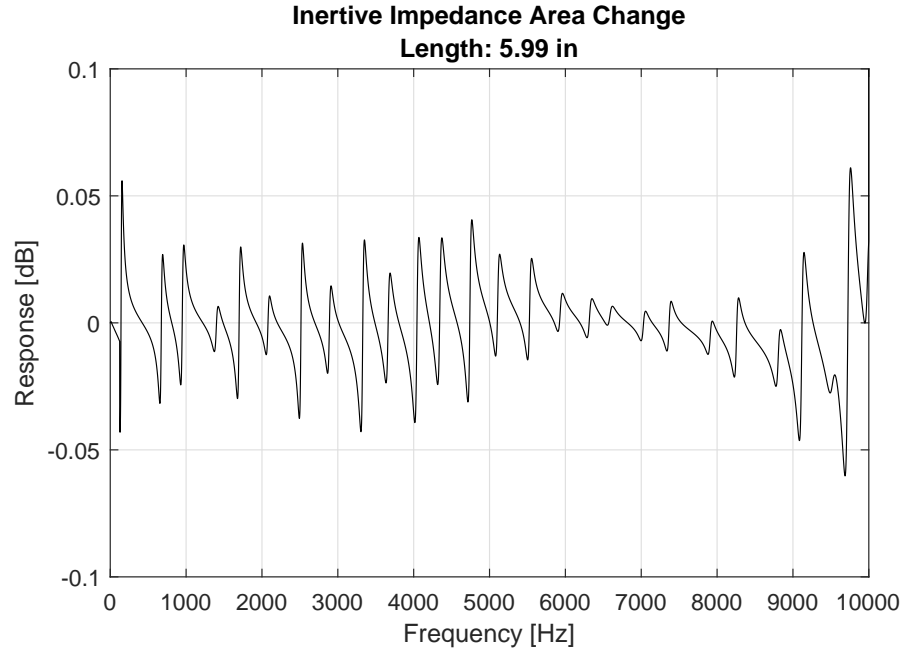


Figure 3.11.: A priori acoustic response of HAMSTER based on mean flow and an arbitrary input impedance for an oxidizer post of 6".

Hydrodynamics

Flow Conditioning

Ideally, the flow through the injector is steady and without perturbations from upstream. Firstly, any geometric features that could possibly cause unnecessary hydrodynamic instabilities needed to be addressed. The probable source of hydrodynamic instability that has been identified as one of the possible causes of driving thermoacoustic instabilities is the oxidizer post inlet. Many rocket combustors use sharp edged inlets, but this can induce discharge coefficient sensitivities such a hydraulic flip [1], or worse, "whistling". "Whistling" occurs when the flow separates from inlet geometry and induces vortex shedding, which in turn, convects down the oxidizer tube, effectively modulating the propellant injected into the chamber. Currently, without a simulation of the fluid mechanics of the orifice for the case of an axisymmetric area change, with a long tube, the vortex shedding frequency and how

it varies is difficult to predict a priori. For this reason the oxidizer post inlet was designed to produce smooth flow [77].

To achieve well conditioned injected flow the straight flow lengths need to be long enough to achieve fully-developed flow or as developed as possible. The hydrodynamic entrance length for turbulent flow can be calculated using [78]:

$$L_{h,turbulent} = 4.4D_h Re^{\frac{1}{6}} \quad (3.5)$$

For a pipe the hydraulic diameter is the diameter of the pipe, while for an annulus the hydraulic diameter is calculated to be $D_h = 2t$, where t is the annular gap distance. For the oxidizer post the required length for fully developed flow was calculated to be approximately 33.44 *in*; the entry length is far longer than the tuned oxidizer post length, this indicates that the boundary layer will not fully form across the radius of the tube.

The outlet from the fuel manifold can be either be choked or subsonic depending on configuration. In either case the flow passing through the fuel annulus may be initially at least slightly disrupted. The converging portion of the fuel annulus will help settle the flow because the area will decrease, thus making the fuel accelerate. When the flow enters the constant area portion of the annulus the flow must then be allowed to develop before entering the injector recess. The required entry length to ensure fully developed flow through the fuel annulus was calculated to be approximately 3.2 *in*, however from the same source [77] it has been suggested that entrance length effects on the flow can be neglected beyond approximately ten times the hydraulic diameter of the flow passage. Based on a length of ten times the hydraulic diameter of the fuel annulus the length of the constant area section was computed to be 0.984 *in*.

Distribution of the propellant flow in each of the manifolds is also important. Even a non-negligible maldistribution in the flow can introduce further irregularity in the combustion, especially in the azimuthal direction (if there is any). To produce an evenly distributed flow from and into the manifolds, where the flow remains evenly distributed under strong acoustic perturbation, it is necessary to choke the flow strongly. Furthermore, a large number of small orifices were used to minimize

the length scale of the effects produced by the choked sections. A cross-section of the injector is shown in Figure 3.12. The fuel injector has the modularity to exclude or include fuel manifold participation; this will allow a study to be performed to assess the importance of the modulation of the fuel flow on combustion stability.

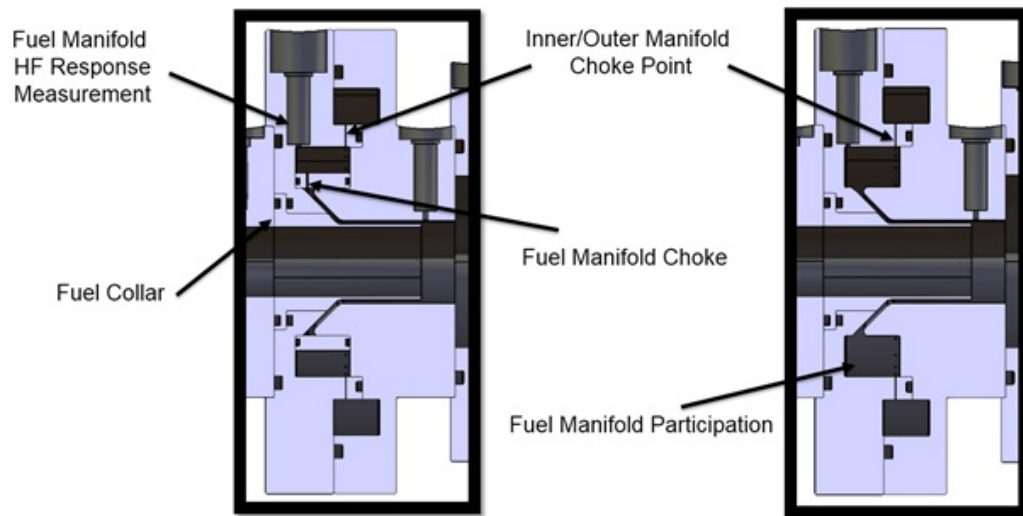


Figure 3.12.: Schematic representation of the fuel injector assembly. With choke ring (Left) and without (Right), allowing coupling participation of fuel manifold during injection.

Flow Losses

Losses due to Fanno, Rayleigh flow and discharge losses in the fuel annulus, oxidizer post and injector recess were also considered. The importance of losses on the injector is the determination on how the injector might respond. Specifically, the "stiffness" of the injector is determined based on pressure drop, although this effect only applies to bulk fluid flow response or chug.

Since the fuel annulus was designed to have a small hydraulic diameter while having a long run-up distance to insure a well developed boundary layer there was a possibility of pressure losses in the fuel flow. For this experiment pressure losses would only result in an alteration of the feed pressure; an adjustment so that the

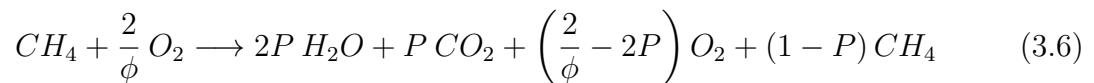
fuel feed remains adequately choked at all times. For the oxidizer feed the flow is compressible and therefore the 1D compressible flow equations are needed.

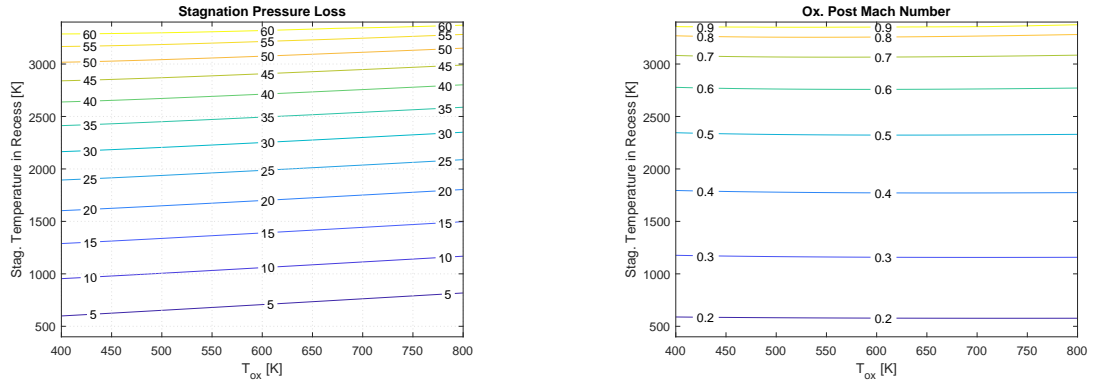
The pressure loss due to Fanno flow can be described with the incompressible flow pressure loss equation [79], where the Fanning friction factor which be determined from Nikuradse's work [80]. Loss coefficients for incompressible pipe flow with a sudden area change are also included. Kangovi et al. [81] showed that losses due to a sudden expansion can be approximated well with using an incompressible flow loss relation for Mach numbers up to 0.5, and that the location of recovered pressure (stagnation pressure) downstream of the area expansion is approximately eight step heights downstream. For compressible flow losses due to friction, the 1D expression for a constant area duct can be found in the book Gas Dynamics [82].

Burning in the recess can result in pressure loss. Compressible flow losses in 1D due to heat transfer or Rayleigh flow for a constant area duct can also be found in the book Gas Dynamics [82]. Unfortunately it is not easy to predict how much combustion occurs in the recess and how the heat is transferred to the propellant before it is injected into the chamber. For that reason the losses in the injector need to be characterized over an expected range of expected stagnation temperature change in the recess.

The injector losses in the oxidizer flow are modeled using three discrete sections respectively: Fanno flow in the oxidizer post, Rayleigh flow in the recess and a sudden expansion into the chamber. The pressure losses in the injector are shown in Figure 3.13 for the full range of oxidizer temperature.

Modeling the combustion in the recess using a single step reaction (Equation 3.6), the adiabatic flame temperature is calculated based on equivalence ratio (ϕ) of propellants injected and percent of fuel burned (P). The stagnation temperature of the propellant mixture in the recess a a function of oxidizer temperature and percent of fuel burned by mole is shown in Figure 3.14.





(a) Total stagnation pressure loss percentage based on chamber stagnation pressure.

(b) Mach number in oxidizer post resulting from losses.

Figure 3.13.: Effect of losses on flow in oxidizer post as a function of oxidizer temperature and hypothetical stagnation temperature of the flow in the recess.

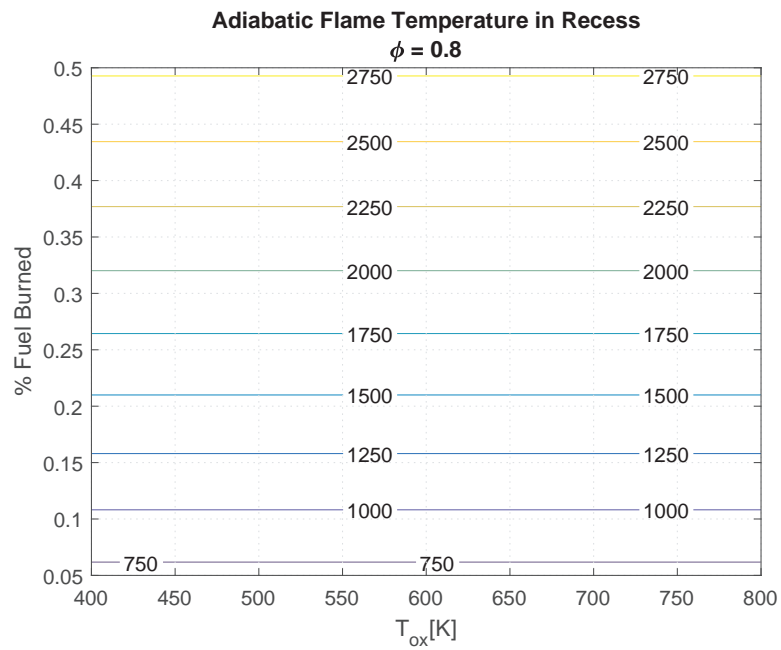


Figure 3.14.: Stagnation temperature of propellant mixture assuming immediate heat transfer from combustion.

Jet Stability, Vortex Production and Mixing

The hydrodynamics and mixing characteristics of the HAMSTER injector are quite complex, involving a number of different physical mechanisms over a large range of scales, both temporally and spatially. To find out which processes may occur together, dominate or be negligible, it is necessary to bound the mechanisms by the expected property ranges that they may occur. The HAMSTER experienced a number of different operating conditions, but the process of molecular diffusion will always be present. One location of focus is the mixing process near the fuel collar of the injector. Since the tip has a finite thickness, a stagnation point in the flow could occur, as shown in Figure 3.15. This location and the vortices developed during operation will have local regions where the relative velocity of the neighborhood of particles is low enough for diffusion to become important. Under the assumption of

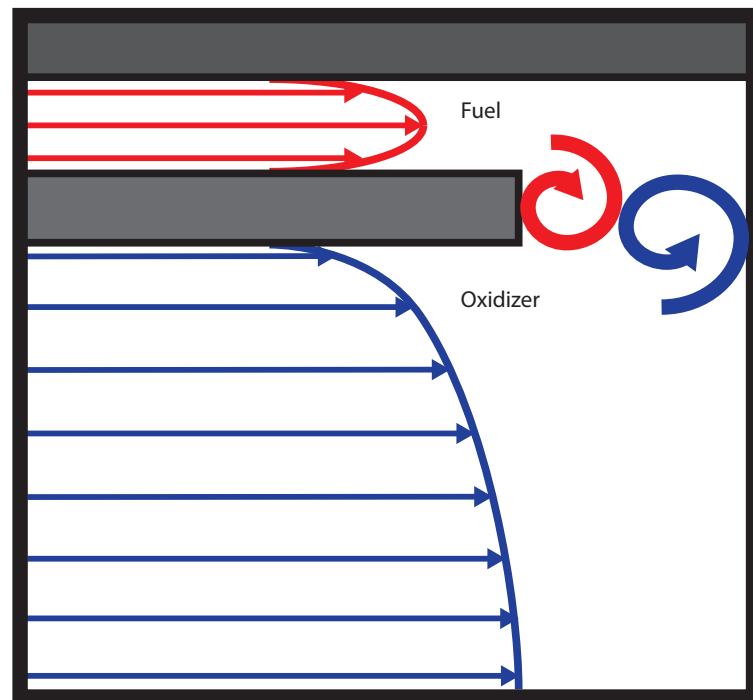


Figure 3.15.: Schematic of flow and vortex generation over the fuel collar.

negligible convective velocity in these regions the diffusive rates are calculated for an expected range of gas properties during operation.

Because the fuel collar has a finite thickness pressure drag causes hydrodynamic structures to be produced from its tip. The flow on each side of the fuel collar is different and therefore generally have different boundary layer thicknesses. Hence, the Strouhal number and therefore for each propellant the vortex shedding frequency off the fuel collar can be different. From Equation 2.13, with a ratio of the thickness of the boundary layer to the thickness of the fuel collar equal to 0.70 for the fuel injection and approximately 3.45 for the oxidizer injection (assuming a boundary layer thickness approximated by Equation 3.7 for turbulent boundary layer growth on a flat plate). It follows that the Strouhal numbers for the vortex shedding due to the fuel and oxidizer flow are 0.18 and 0.044 and respectively.

$$\frac{\delta}{x} = \frac{0.385}{Re_x^{0.2}} \quad (3.7)$$

The corresponding estimated vortex shedding frequencies for the fuel and oxidizer injection are $2.9 \times 10^4 Hz$ and $9.4 \times 10^3 Hz$. The vortex shedding over the step from the fuel collar to the injection recess inner diameter has a Strouhal number determined to be approximately 0.1 and a vortex shedding frequency of around $2100 Hz$ (boundary layer thickness is 1.29 times that of the fuel collar step height). From the DMD analysis done on the vorticity of the preliminary simulation, the vortex shedding frequencies for the fuel and oxidizer injection are $2.785 \times 10^4 Hz$ and $9.4 \times 10^3 Hz$.

As a result of vortex production the axial momentum directed along the direction of flow is transferred into momentum in the transverse direction and this allows a stagnation point to be established at the fuel collar, albeit for a brief amount of time. The vortex production allows the fuel/oxidizer flow to roll up into a ring with striations that have a much larger surface area than a smooth flat fluid interface. The effective mass flux at this new larger fluid interface is greatly increased as a result allowing for a much faster rate of mixing. Determination of the sizes of the striations is difficult to estimate, but it may be reasonable to assume the striations have a maximum size comparable to the turbulent boundary layer from whence the vortex forms. In the case of the vortices sourced from the oxidizer it is clear that the boundary layer is larger than the fuel collar thickness; this suggests that vortices are

far more likely to form over the fuel collar and the annular width, ie: the fuel collar step height. Even so, the length scale of the boundary layer is comparable to the step height and therefore it may be reasoned that the mixing process due to vortices formed from the oxidizer are not as efficient in mixing as the vortices formed from the fuel injection.

To illustrate how the mixing can be adjusted the entrainment of the propellants into the shear layer was calculated for different oxidizer temperatures [50]. Although the scaling factor may not be accurate, the trend will be similar, Figure 3.16 shows the entrainment ratio trend with oxidizer temperature. For entrainment ratios larger

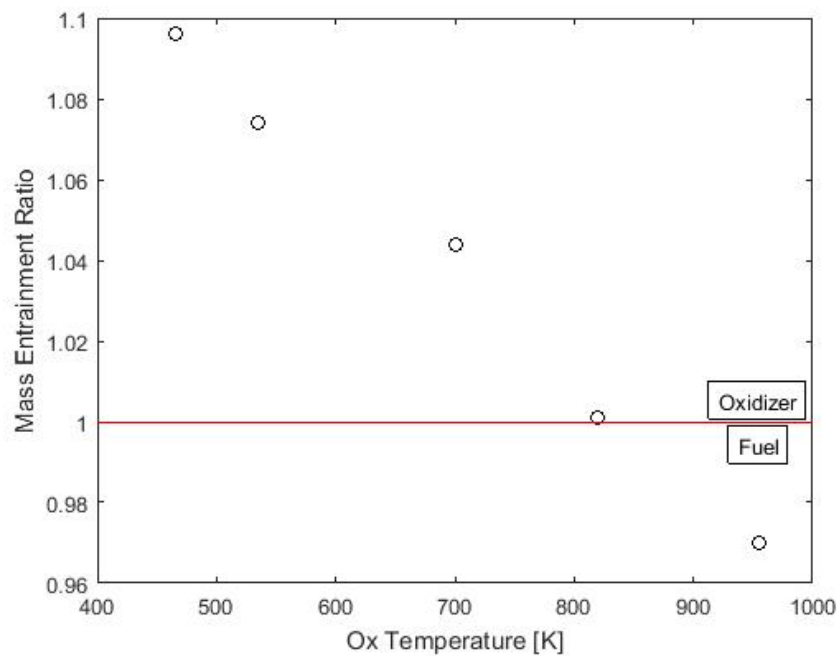


Figure 3.16.: Entrainment ratio trend for change in oxidizer temperature. Values above the threshold represent entrainment of oxidizer, whereas below represents entrainment of fuel.

than one more oxidizer is entrained than fuel, this suggests that the mixing layer equivalence ratio will effectively decrease. The ignition delay will decrease and local temperature gradients will increase, which in turn will quicken the burning rate of

the mixture. At an oxidizer temperature of around 500 K the velocity difference between the injected propellants is negligible; this in contrast to injection whereby the velocity difference causes a Kelvin-Helmholtz instability either at the fuel collar tip where vortices are shed, or further downstream in the shear layer where vorticity is generated as a byproduct of shear layer growth. In this scenario the mixing layer will not grow quickly, but there will be a non-negligible density gradient between the two fluids. Pressure waves could then induce a baroclinic torque on the fluid interface, which would then promote vortex generation and therefore shear layer growth.

Combustion and Heat Release Mechanics

The heat release during high pressure combustion is a topic that is still not well understood, especially for the case of turbulent non-premixed flames. In order to study the effects of this mechanism on combustion instability as a whole the uncertainty of the problem needs to be reduced. Certain aspects of the combustion process can be isolated, studied and quantified. This section attempts to reduce the uncertainty of the heat release mechanism in the HAMSTER combustor. For the purposes of modeling and simplicity, in line with Guidelines 3-6 the combustion and related mechanisms were chosen.

Subcritical Injection

Gaseous propellants were utilized to eliminate the need for modeling atomization. The combustor was designed so the propellants and combustion products are ideal gases. The critical pressure, temperature and density for methane and oxygen are shown in Table 3.5 [76].

By first inspection of these properties, bearing in mind that the manifold, injector and chamber pressures do not exceed $30 \times 10^5 Pa$ in any test, the propellants appear to exhibit sub-critical properties. However, the limiting propellant critical properties are the vapor pressure of water and the critical density of methane.

Table 3.5.: Critical thermophysical properties of propellants injected into HAMSTER.

Gas	T_c [K]	P_c [10^5 Pa]	ρ_c [kg/m^3]
Methane	190.6 ± 0.3	46.1 ± 0.3	162 ± 3
Oxygen	154.58 ± 0.0015	50.43 ± 0.005	435 ± 0.45
Water	647 ± 2	220.64 ± 0.05	322 ± 4

The oxidizer rich preburner injects warm oxygen with trace amounts water ($< 5\%wt$), but the lowest temperature it operates at is around 440 K. At a pressure well below the vapor pressure for water, there is a strong possibility to produce water droplets. It is expected that oxidizer manifold temperatures of below 500 K and the typical operating pressures ($\approx 1.2 \times 10^5$ Pa) that a phase change will occur. Since the water content was usually insignificant, especially at low preburner temperatures, the effect of the phase change of water on combustion was ignored.

The typical density of methane during injection does not exceed 10 kg/m^3 , the reduced density is on the order of 0.063 . This seems like an insignificant value, but for the purposes of modeling diffusion, which usually assumes the dilute limit (ideal gas properties), methane tends to have atypical diffusion behavior and the validity of the assumption needs to be checked. It is suggested that methane be utilized at conditions which are well characterized. From Childs and Hanley [33] the transport properties of methane are within the 1% of the dilute limit if the reduced density (kinetic gas theory) does not exceed $\rho^* = 0.007$ (Equation A.3). This reduced density is based on kinetic gas theory and therefore the critical reduced density for methane equals to $\rho^* = 1.35 \times 10^{-4}$, which suggests that the assumption is valid for the conditions for operation.

Based on the nominal parameters in Table 3.1, the expected binary diffusion rate of methane and oxygen near the collar tip was calculated using Equation A.1

to be $0.716 \times 10^{-5} \text{ m}^2/\text{s}$. This value was calculated using a mass weighted average temperature based on equivalence ratio, like Equation 3.8.

$$T = \frac{\frac{O}{F}|_{stoich} T_{ox} + \phi T_f}{\frac{O}{F}|_{stoich} + \phi} \quad (3.8)$$

The Lennard-Jones potential correcting factor was determined to be 0.842, determined from Appendix B.

Using a characteristic length of half the thickness of the fuel collar (0.016"), the approximate time scale for the propellants to fully mix was calculated to be 0.023 s. This calculation follow the approximation given in Equation 3.9.

$$\tau \sim \frac{R^2}{\mathcal{D}_{AB}} \quad (3.9)$$

The diffusion rate scales approximately by $\mathcal{D}_{AB} \propto T^{3/2}/P$ and thus the diffusion rate would only significantly increase when surrounded by high temperature products. For instance with combustion products at a high enough temperature to increase the mixture temperature to 1100 K, the time scale of the diffusion process is only reduced to $O(10^{-2})s$. This time scale is slow in comparison of the expected convective velocity from the collar into the chamber; the time taken to reach full mixing will be far longer (about 350 times) than the time for the mixture to convect through the injector recess an into the chamber. Thus, if the flame were to anchor itself at the collar it would have to be due an advection process of some kind; the flow would need to stagnate and convect far more slowly downstream, at least locally for the mixture to ignite at the injection dump plane, let alone the fuel collar.

Ignition Delay

Ignition delay has already been shown to have a significant influence on characteristics of combustion instability in the CVRC. Ignition delay can also be used to get an approximate idea of how the combustion is expected to behave in certain localize conditions. An attempt was made to quantify the fastest rate at which the combustion is expected to occur in partially mixed conditions.

Work done by Tsuboi and Wagner (1975) [83] of methane and oxygen in a shock tube showed that the chemistry ignition delay time is approximately based on Equa-

tion equation (3.10) for a temperature range of 1200 to 2100 K , a pressure range of 1 to 300 atm and equivalence ratio range of 0.6 to 1.4.

$$\tau_{ign} = 2.5 \times 10^{-15} \exp(26700/T) [CH_4]^{0.32} [O_2]^{-1.02} \quad (3.10)$$

An ignition delay parametric study was conducted for the temperature range of 600 to 1400 K at a pressure of 1.4 MPa was done. Using the Arrhenius fit used for the experimental data as a template and making pressure, temperature and equivalence ratio as the independent variables, the following relation was created.

$$\tau_{ign} = A \exp\left(\frac{B}{T}\right) \left(\frac{P}{R_u T}\right)^{C+D} \left(\frac{n_{ox}}{n_f}\right)_{stoich} \frac{\phi^C}{\left(\phi + \left(\frac{n_{ox}}{n_f}\right)_{stoich}\right)^{C+D}} \quad (3.11)$$

where $A = 2.1004E-10$, $B = 19732$, $C = 0.3539$, $D = -0.9125$ and $(n_{ox}/n_f)_{stoich} = 2$ for methane/oxygen. Comparing variables B , C and D to Equation equation (3.10) we can see that the resulting values are somewhat similar. It is interesting to note that the effective activation energy (parameter B) is comparable, but not close to the value presented for the experiments with Argon. The presence of Argon may have biased the speed of the reaction such that energy required for the reaction to begin was slightly higher in the experiment than in the well-stirred reactor model/study.

Figure 3.17 shows a map determined through the use of CHEMKIN, modeling the scenario as a well stirred reactor at different conditions. The resulting fit to the data is represented by Equation 3.11.

Assuming a local stoichiometric mixture, the Lewis number and second Damkohler number (reactive time versus mas diffusive time) were calculated to characterize the combustion, shown in Figure 3.18. These metrics were calculated using the ignition delay expression extracted from CHEMKIN, the mass diffusion rate using the half thickness of the fuel collar and the binary diffusion coefficient of methane and oxygen at the relevant conditions and a function of local temperature, and the thermal diffusivity of the mixture as a function of local temperature.

Although Figure 3.18 shows that the Lewis number is fairly insensitive to the local temperature, and remains approximately unity, the second Damkohler number

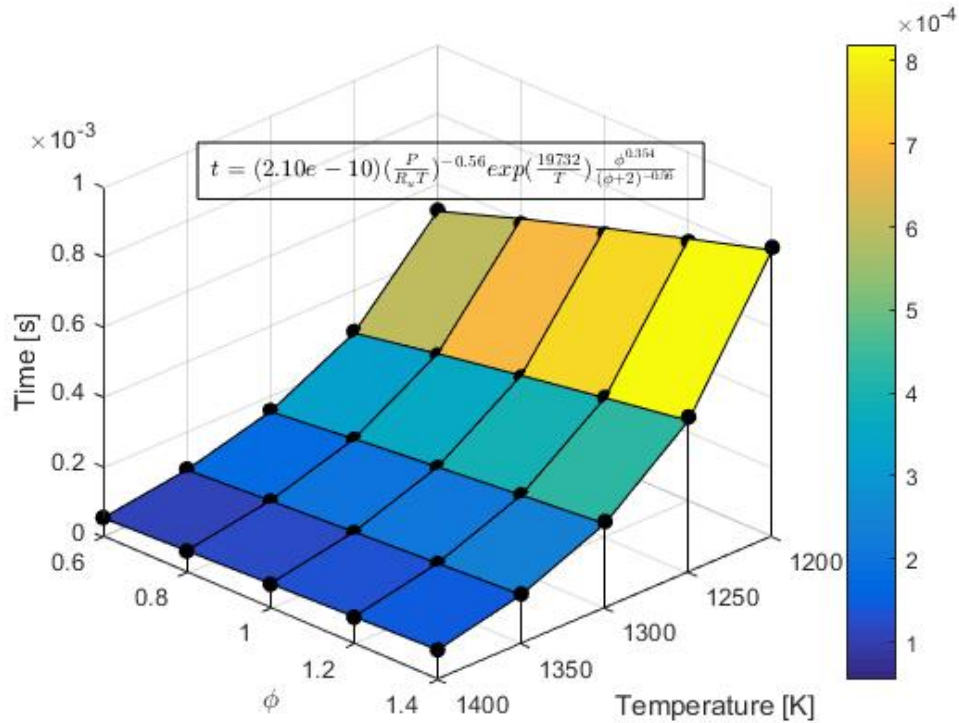


Figure 3.17.: Ignition delay of CH_4/O_2 for different local equivalence ratios and temperatures.

change significantly. There is an inherent amount of uncertainty while performing such analyses, but this process reveals that there is a strong possibility that there exists a threshold temperature whereby the local combustion goes from a kinetically limited behavior to a diffusion limited behavior. Since the oxidizer flow makes the bulk of the mass flow and its temperature is altered between tests, there could be a significant change in flame behavior with change in oxidizer temperature.

Boundary Conditions

The boundary conditions were designed to be easily emulated by the simulations, while reducing the computational cost. The relevant boundary conditions in this

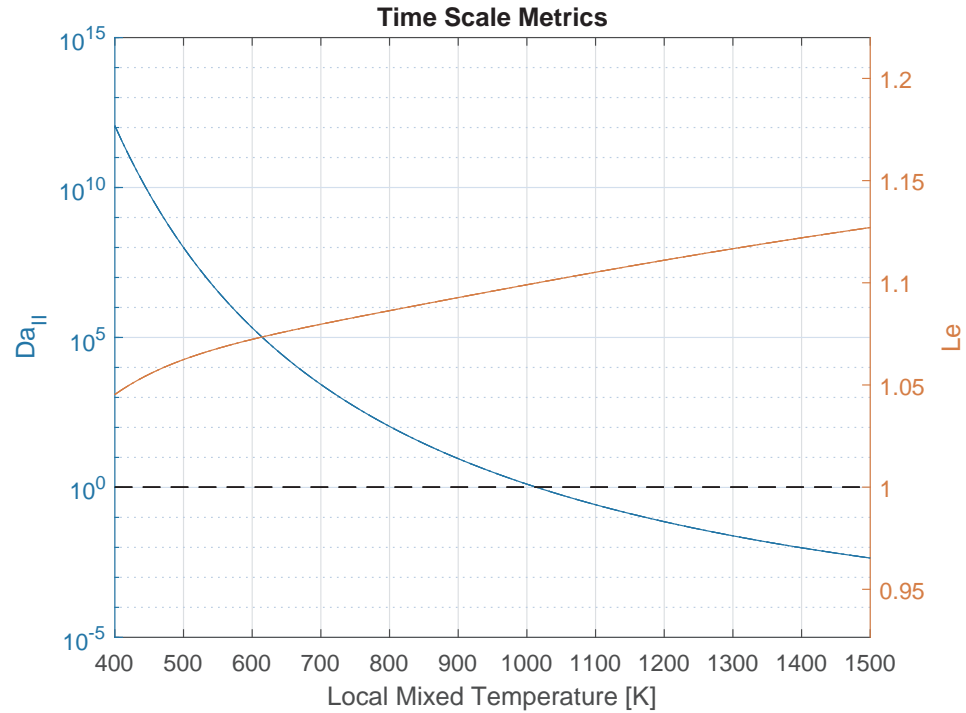


Figure 3.18.: Reaction metrics of CH_4/O_2 for different local temperatures.

experiment are the propellant states, flow rates, acoustic boundaries and heat transfer at the inner wall of the system.

Flow Metering and Propellant States Achieving very accurate and precise flow properties in a short duration experiment is unrealistic. The propellant states, specifically the temperature and pressure at each transition point in the hardware such as at choke points and in manifolds, need to be well characterized. An approximate radial thermal profile of the oxidizer temperature entering the manifold was measured with thermocouples at different depths, while upstream of choke points, such as in the fuel manifold and venturis, both the stagnation pressure and temperature were inferred from measurements.

Using the upstream measurements, the mass flow rates were controlled and metered using high discharge coefficient, high pressure recovery venturis, designed per the ASME code [77]. Typically, most flow rates for gases can be calculated with the

isentropic flow equations, with a correction for compressibility, to give an value with at least 1% error, but for methane, especially at pressures around and above the critical point that method results in errors of about 7%. For methane, an iterative scheme was employed to calculate the conditions at the throat in order to calculate an accurate mass flow rate.

Acoustic Boundaries Flow tends to have an impedance which scales with Mach number: $Z \propto (1 - M^2)^{-1}$. Therefore at choking conditions the impedance tends to infinity, resulting in a near perfect hard wall; in other words the acoustic information cannot be transmitted beyond the choke point and therefore reflects. The result is a pressure antinode for acoustic standing waves.

Choking the flow ensures that acoustic energy is not transmitted upstream to unwanted regions in the system, effectively decoupling the downstream flow device from the upstream one. It also serves to set the upstream boundary for the computational domain. The interfaces between the ox-rich preburner and the oxidizer manifold, fuel manifold and the fuel injector annulus, and the chamber with the ambient environment are all such acoustic boundary conditions. The pressure drop across the interfaces is designed to roughly double the needed pressure ratio to achieve critical flow to ensure choking when in the presence of high amplitude acoustic waves.

To limit the effect of flow on the downstream mechanics, the choke points were achieved by using interface plates with many small holes. The scales of the small holes allows the turbulent jets to dissipate quickly since the ratio of the mean velocity profile maximum to the initial jet velocity scales linearly with jet diameter and inversely with flow distance [38]. It is expected that the jet velocity profiles for the oxidizer flow coalesce near the inlet to the oxidizer post, while for the fuel flow it only about a quarter of an inch downstream because of how close the holes are to one another.

Thermal Boundary

Heat transfer due to convection is typically computational expensive. Therefore an adiabatic wall assumption is usually preferred for reacting flow simulations. To approximate this boundary condition in the experiment, a thermal barrier coating

was applied to the inner surfaces of the chamber and oxidizer manifold. The thermal barrier coating (TBC) was Yttria stabilized Zirconia, which falls under the family of MCrAlY alloy powder coatings. It has thermal conductivity of around $1.3 W/m - K$, while the thermal diffusivity is comparable to that of stainless steel. The rate at which heat is transferred to the walls beyond the TBC is extremely slow, while the TBC itself heats up extremely quickly; the TBC usually cannot last longer than a couple seconds during a hot fire test.

The oxidizer post and inlet were not coated to ensure that no unwanted flow effects and effects on the boundary layer development were negated. The approximate maximum temperature loss to heat transfer in the oxidizer post for steady flow was determined to be approximately no more than $5 K$ [84].

Modularity

Figures 3.5 and 3.12 shows modular design of the combustor, and more specifically the injector. A full detailed description of which features of the combustor are modular, with an explanation of how the changes will be implemented to achieve certain desired effects.

Starting with oxidizer manifold; the oxidizer post inlet can be interchanged with a different one that could have a different inlet profile, inlet diameter or to produce a choking effect. The oxidizer post can be changed with one with a different length or different inner diameter. The chamber and nozzle are fully modular in length, inner diameter and type of section. The fuel injector assembly is modular in the fuel collar and fuel manifold choke ring. Table 3.6 lists what's geometric changes need to be made and the reason to produce a desired effect (controlled effect). The effects of vortex shedding off of the fuel collar will be of most interest, but the control of velocity/density and momentum flux ratio will also provide some insight into the mixing mechanics of the injector.

Table 3.6.: Changes to macroscale flow parameters due to change in input flow parameters. Some controlled outcomes are determined by specific geometric changes to the injector.

Variable	Parameters Effected	To Keep Parameters Constant:	Required Geometric Changes	Secondary Parameters Affected
Oxidizer temperature	$M_{ox}, J, Re_{ox}, Sr_{ox-coll}, Sr_{ox-step}, f_{oxpost}, M_{chamber}$	$J, Sr_{ox-coll}, f_{oxpost}$	$D_{oxpostinlet}, D_{oxpost}, D_{recess}, \tau_{collar}, L_{oxpost}$	$Sr_{fuel-coll}, Sr_{ox-step}, Re_{ox}, M_{ox}, M_{chamber}$
Fuel temperature	$M_{fuel}, J, Re_{fuel}, Sr_{fuel-coll}, M_{chamber}$	$Sr_{fuel-coll}, Sr_{ox-coll}, f_{oxpost}$	$D_{oxpostinlet}, D_{oxpost}, D_{recess}, L_{oxpost}$	$J, Re_{fuel}, Sr_{ox-step}, M_{fuel}, M_{chamber}, Sr_{fuel-coll}, Re_{fuel}, Sr_{ox-step}, M_{fuel}, M_{chamber}$

continued on next page

Table 3.6.: *continued*

Variable	Parameters Effected	To Keep Parameters Constant:	Required Geometric Changes	Secondary Parameters Affected
Oxidizer mass flow	$M_{ox}, J, Re_{ox},$ $St_{ox-collor},$ $St_{ox-step}, f_{chamber},$ $M_{chamber}$	$M_{ox}, J, St_{ox-collor},$ $f_{chamber}$	$D_{oxpostinlet}, D_{oxpost},$ $D_{recess}, L_{chamber}$	$Re_{ox}, St_{ox-step},$ $M_{chamber}$
Fuel mass flow	$M_{fuel}, J, Re_{fuel},$ $St_{fuel-collor},$ $f_{chamber}, M_{chamber}$	$St_{ox-collor},$ $St_{ox-step}, f_{chamber}$	$D_{oxpostinlet}, D_{oxpost},$ $\tau_{annulus}, L_{chamber}$	$J, Re_{ox}, M_{chamber},$ $St_{fuel-collor}$ $Re_{fuel}, M_{chamber},$ $St_{ox-step}$

3.1.3 Design, Analysis and Verification of Target Measurements

The measurements and their verification process is described briefly in this section. The pursuit of model validation and high fidelity measurements requires that all measurements are not only verified, but their uncertainties quantified as well, per Guideline 6. Uncertainties in each method of measurement has to be done on a case by case basis.

Instrumentation on the combustion chamber is numerous and convoluted and a summary of the types of instrumentation used is detailed in Table 3.7 with reference to Figure 3.19. The standard used for instrumentation placement is the same between azimuthal locations per different axial locations. Instrumentation placement at the head-end of the chamber is complex and will be discussed together with the design of the chamber and targeted measurements so that it is well understood.

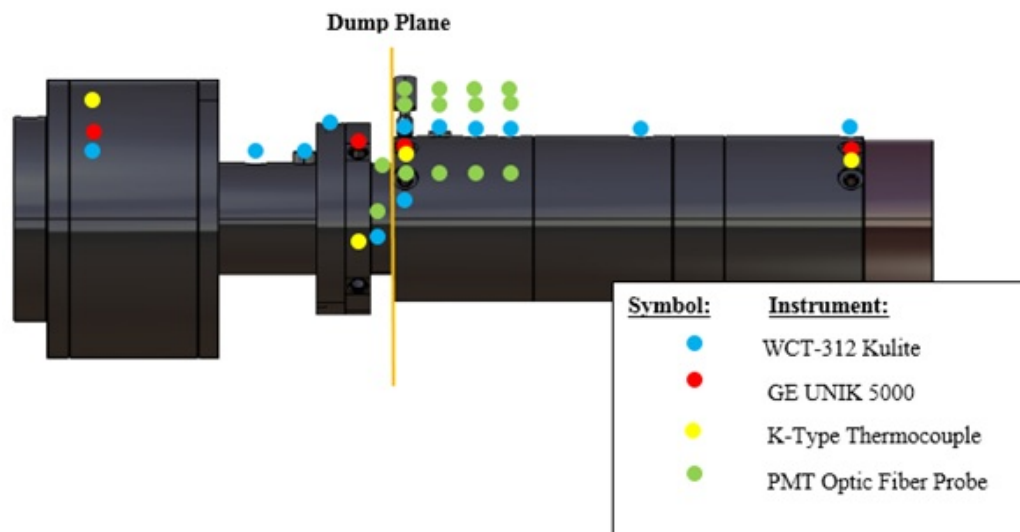


Figure 3.19.: Instrumentation type and measurement locations on HAMSTER.

Table 3.7.: Summary of instrumentation and their locations.

Instrument (Response Info)	Measurement (Accuracy)	Axial		Azimuthal Location Uncertainty
		Location/s (Ref: Dump Plane)	Axial Location Uncertainty	
K-Type	Fluid	Ox Manifold,		
Thermocouple (Analog, > 0.1s)	Temperature (max[2.2°C,0.75%])	Fuel Manifold, 0.3"	±0.005"	N/A
GE UNIK 5000 (0.5-3500 Hz)	LF Pressure (± 0.04% FSO BFSL)	Ox Manifold, Fuel Manifold, 0.3", 13.15"	±0.005"	N/A
WCT-312 Kulite (Analog, 1st Nat. Res. at 240kHz)	HF Pressure (±0.1% FSO BFSL)	Inner Fuel Manifold, Ox Manifold	N/A	N/A

continued on next page

Table 3.7.: *continued*

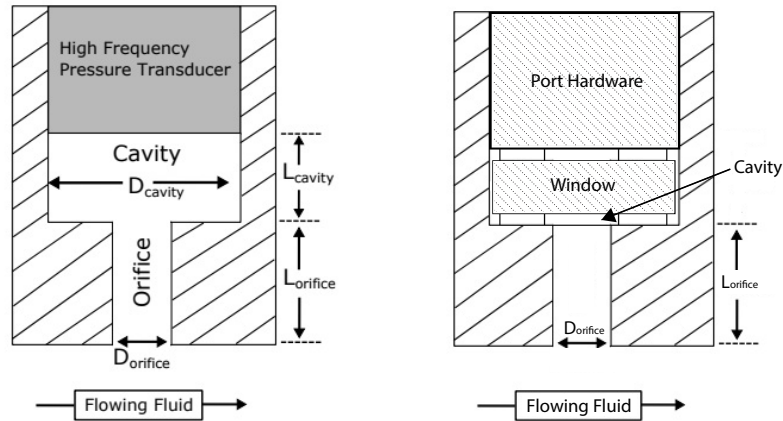
Instrument (Response Info)	Measurement (Accuracy)	Axial Location/s (Ref: Dump Plane)	Axial Location Uncertainty	Azimuthal Location/s	Azimuthal Location Uncertainty
WCT-312 Kulite	HF Pressure	-4" , -2.593" , -0.35" , 0.3" , 1.3" , 2.3" , 3.3" , 7.1" , 13.15"	$\pm 0.005"$	Standard & 135°	$\pm 0.5^\circ$
PMT Hamamatsu		-0.3" , -0.35" ,	Recess: $\pm 0.001"$,	Standard, 90° with	$\pm 0.5^\circ$ with
11903-210 (< 200 kHz)	Chemiluminescence	0.3" , 1.3" , 2.3" , 3.3"	Chamber: $\pm 0.005"$	0.080" and 0.600" offsets	$\pm 0.005"$ offset uncertainty

Pressure

High frequency (HF) pressure measurements were used to characterize the acoustic response in various parts of the combustor. With an assumption that the combustion and fluid mechanics have an axisymmetric profile most of the HF pressure transducers were located at the same azimuthal location at various axial locations throughout. At the head end of the chamber a HF pressure transducer placement was clocked 135° from the HF transducer in the combustion chamber closest to the dump plane; this will be used to verify the assumption of acoustic axisymmetry (no transverse or azimuthal modes) in the combustor. There were three HF pressure transducers located in the oxidizer post, with one located in the injection recess. A HF pressure transducer was located in each of the propellant manifolds to determine their response to acoustic perturbation. Each of the aforementioned locations were visualized in Figure 3.19, the positions correspond to locations that are meant to resolve acoustic mode shapes in the oxidizer post and combustion chamber (Figure 3.8), the pressure response profile near the head end of the chamber and be used for cross-correlation directly with the PMT measurements at the same axial locations.

The HF transducers are made by Kulite. The HF transducers water cooled, but cannot be exposed directly to gases at the temperatures present in the combustion chamber. For this reason the HF pressure transducers are recessed in a cavity, where a small orifice bridges the cavity and the domain of measurement. This approach to the measurement is represented schematically below; a similar port design for the optical measurements which may cause a Helmholtz resonance response is also shown.

The problem with this method is that the cavity can produce a Helmholtz resonance response, which will alter the amplitude measurement at or near the Helmholtz resonant frequency or even have an adverse effect on the main flow at the same Helmholtz frequency as described in Section 2.2.1. The port orifice diameters range from 0.0625 in to 0.100 in , while the orifice (neck) length in the chamber ports are 0.155 in ,



(a) Schematic representation of the HF pressure port design.

(b) Schematic representation of the PMT port design.

Figure 3.20.: Port designs affected by Helmholtz resonance effect.

0.105 *in* in the injector recess, 0.205 *in* for each in the oxidizer post and 0.105 *in* in the oxidizer manifold. The cavity length in each case will vary slightly based on the how compressed the sealing gaskets are, but the length will never exceed 0.020 *in*. The cavity diameters are all 0.272 *in*. The difficulty in estimating the resonant frequency of the ports is the sound speed of the gas inside the cavity at any moment in time. The composition of the gases can range from heated oxygen to combustion products and the temperature inside the cavity can be highly transient during the course of a test. For a linear response the transmission loss, calculated using Equation equation (2.7), in the chamber due to Helmholtz resonance at the limiting sound speeds expected to be found in one of the ports is shown in Figure 3.21.

From Figure 2.15 the cavity within each of the pressure transducers will also have a set Helmholtz resonance frequency based on the gas temperature and sound speed. The gas temperature within the cavity could theoretically be determined by correlating the port resonance frequencies with that of the instrument cavity resonance; by determining the sound speed for each case associated with each geometry.

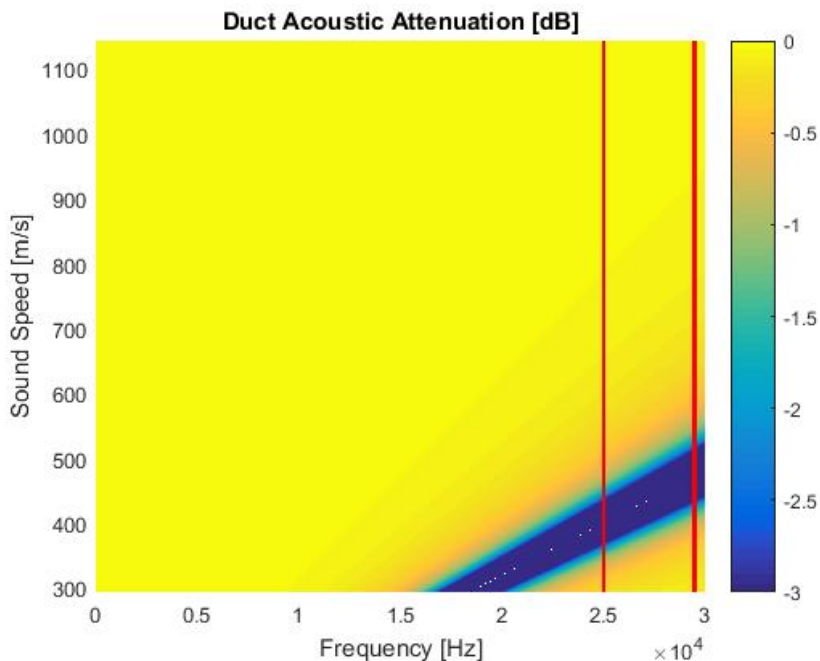


Figure 3.21.: Acoustic attenuation in combustion chamber due to Helmholtz resonance of HF pressure ports. The red lines signify a band where the vortex shedding frequency of the collar is expected to be.

Chemiluminescence

Chemiluminescence from the reacting flow field can give an indication as to where the main reactions are and when they are happening. More importantly, if the domain is more temporally and spatially resolved it is possible to get information about the burning vortices originating from the collar and correlate the information with other measurements such as the HF pressure measurements.

Chemiluminescence measurements are taken using fiber optically coupled photomultiplier tubes (PMTs). The PMT/filter module setup is shown in Figure 3.22. The PMTs used were all identical models (Hamamatsu H11903-210). A total of 9 measurement locations were used, utilizing 27 PMT modules, measuring CH^* , OH^* and a truncated bandwidth of the CO_2^* signals. Calibration on the PMTs to determine the input spectral bandwidth power to output voltage. This would enable a direct

estimation of radiant power collected from the combustion. The signal collected by the CH^* PMT is actually a superposition of the CH^* band and portion of the CO_2^* spectral band. If needed, the extraction of the CH^* from the superimposed CO_2^* signal could be calculated using the CO_2^* PMT signal and a method described by Lauer [65].

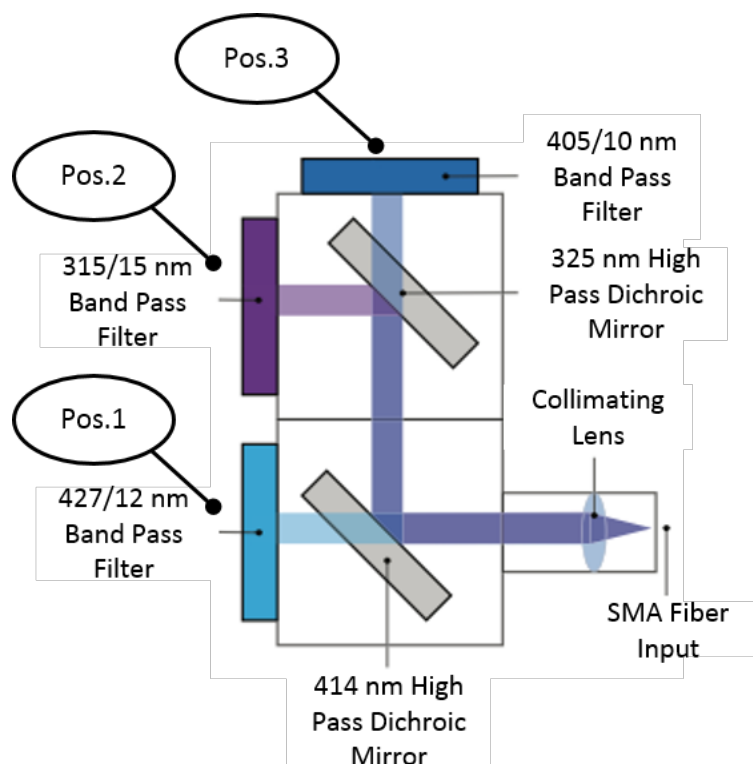


Figure 3.22.: Schematic of the fiber optically coupled optical module, housing the optomechanics and PMTs to measure chemiluminescence [85].

The wavelength response curves for the PMTs, the optical filter transmission curves, and the reflection/transmission curves for the dichroic filters can be found in Appendix D. A more detailed description of the optical collection equipment can be found in Bedard's dissertation [85]. A thorough calibration of the PMTs was done [86], where the response of each PMT module response, the transmission/reflection of the optomechanics was checked over a selected bandwidth pertinent to this study. It

was found that the transmission of the UV signal through the fiber optic cables will deteriorate over time, but are generally consistent over short periods of time. The transmission curve through the optical filters was comparable to what was stipulated in the calibration document provided by SEMROCK. However, the reflection curve of the dichroic filters was grossly overestimate for the UV/Vis bandwidth. This caused some concern with regard to the confidence of the OH^* measurements. In general, the calibration measurements taken over the CH^* band were determined to be on par with the performance reports produce by the various manufacturers. Figure 3.23 shows where the losses in the PMT port and the optical fiber occur. The resultant transmission curves for the PMT system can be found in Appendix D.

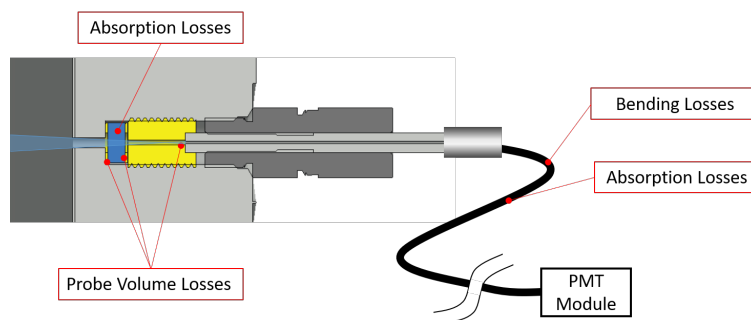


Figure 3.23.: Line losses expected to occur during transmission from chamber to PMT modules. [86].

PMT measurements will be used to determine the frequency of vortex shedding in the injection recess and the hopefully some information about how those structures are convected into the chamber. PMTs connected to the chamber are setup to determine where the trajectory of the shear lies per axial distance from the dump plane. The limits of the shear layer may be determined by measuring at locations that have a parallel offset of a diameter measurement (chordal measurement). This concept is shown below in Figure 3.24; the absence of emissions will help determine where the shear layer is not located so that a shear layer trajectory may be inferred. Further-

more, with a shear layer location approximation inverse methods may be employed to determine the distribution of the emissive sources within the probe volume.

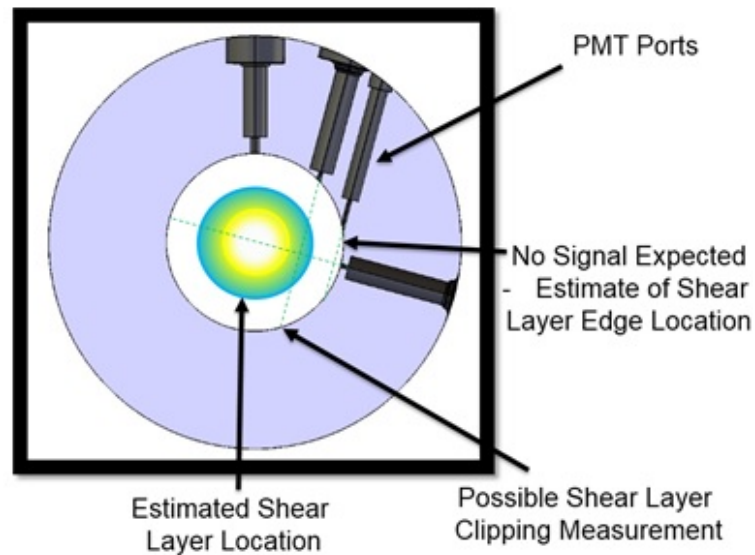


Figure 3.24.: PMT port location and design to measure chemiluminescence in the combustion chamber with high spatial and temporal resolution.

Since the probe volume domain needs to be well resolved spatially the probe volume is very sensitive to port design and geometry. Much care was taken to ensure a precise geometry so that the effect of uncertainty of the manufacturing tolerances on the probe volume is well understood and quantifiable. Limits of the probe volumes were simulated to show the adjustment to the spatial domain, shape and overall volume. Plots showing the probe volume in an ideal fitting and at the limits of the tolerances are shown in Figure 3.25. In the worst case scenario the probe volume is skewed by 0.0347 in and the volume is reduced by 31 %.

This suggests that although the uncertainty of the probe volume may be larger, the probe volume itself becomes more spatially resolved with a worse fitting. Since the probe volume is not dependent on the orifice diameter leading into the chamber, the effects due to thermal expansion of the aperture will not alter the probe volume spatial resolution during a test.

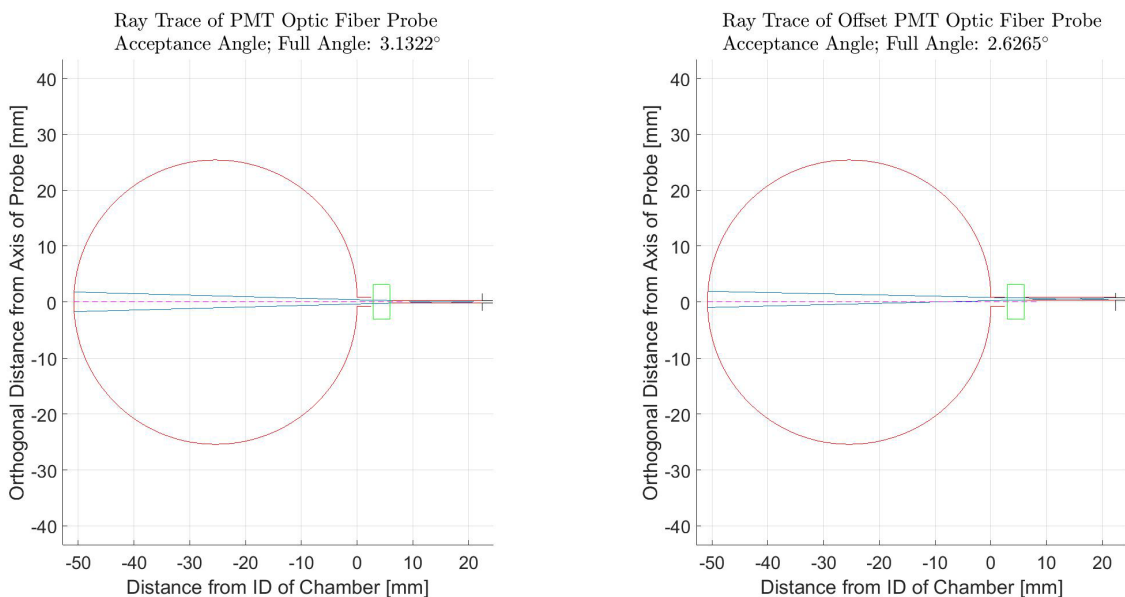


Figure 3.25.: PMT probe volume domains. (Left) Ideal port geometry, (Right) extreme fitting case due to tolerance bounds.

The effect of solid angle bias on the collected emissions within the probe volume was calculated, shown in Figure 3.26. Under the assumption that the each particle is an emitter, emitting radian in 4π steradians, the solid angle bias describes the fraction of light, from each emission point, entering the fiber optic port aperture.

The chemiluminescence emissions from the experiment are directly compared to the chemiluminescence produced by the simulations. A calibration study was conducted to ensure that signals collected by the PMTs were accurate and the relative precision between the instruments remained constant. The signal losses of the hardware were accounted for and quantified, shown in Appendix D. The chemiluminescence data extracted from the simulations was performed using the same method used by Fuller [87], where the self-absorption of the relevant species was analyzed.

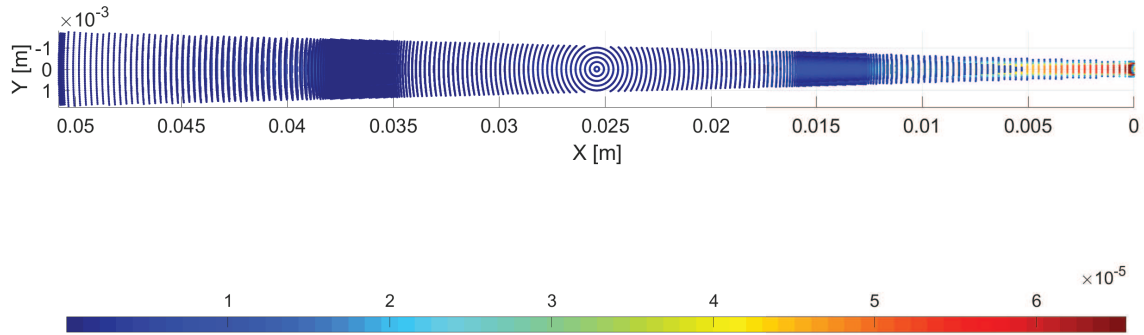


Figure 3.26.: Fraction of light bias within a typical emission probe volume within HAMSTER.

3.2 Observation and Overview of Experimental Results

This section serves to globally analyze the response of the experiment during operation, for various operating conditions. An overview of the tests conducted, hypotheses tested and the intermediate conclusion of the tests conducted will be presented in this section. The experiments conducted will be essentially verified in a global sense to provide a foundation to validate the simulations.

3.2.1 Basic Operation

Figures 3.27 and 3.28 show a typical test cycle. The propellants are initially brought into the chamber at near ambient pressures in order for the oxidizer post to remain unchoked prior to ignition. The oxidizer rich preburner is ignited 1.8 s, while the main chamber is ignited with a laser at 3.25 s. Subsequently, at 3.6 s, the propellants are throttled to steady operating conditions. The system reaches steady propellant conditions at around 5.9 s, and the valves are commanded to close at 6.9 s.

Low frequency measurements are usually good measures of mean properties in the system; the highest frequency response of the pressure transducers is around 2 kHz ,

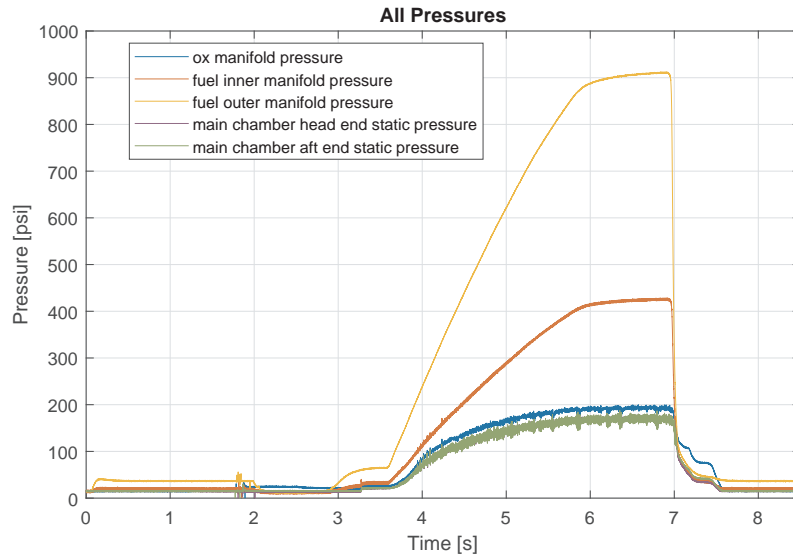


Figure 3.27.: Pressure trace during a typical hotfire cycle.

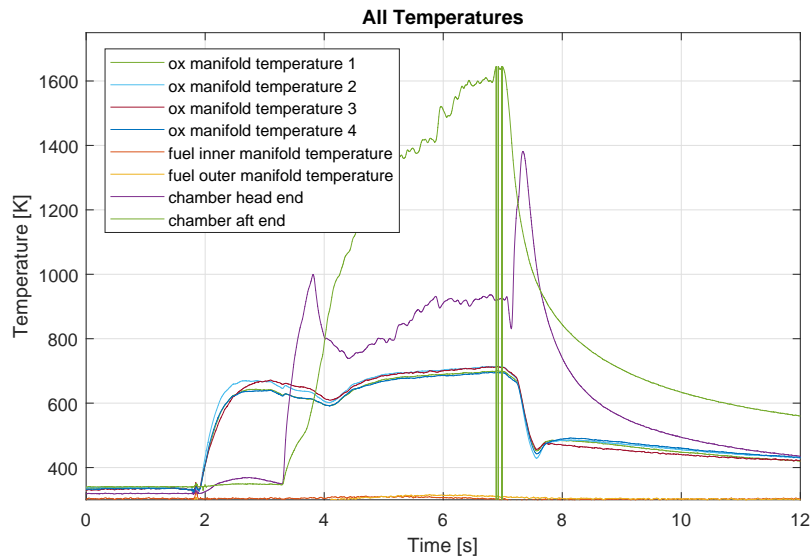


Figure 3.28.: Temperature trace during a typical hotfire cycle.

while the thermocouples are limited to response times no smaller than 0.1 s. The low frequency pressure measurements correspond to static pressure measurements in the manifolds and the chamber.

The temperature values measured are typically close to stagnation temperature. The thermocouples are located in manifolds and chamber, where the thermocouples in the oxidizer manifold are arranged at the same axial location, but at different radial depths in increments of 0.5" starting at a radial distance of 0.5" from the centerline. The thermocouples in the chamber are flush mounted with the inner wall of the chamber. All low frequency measurements spatially complement high frequency pressure and chemiluminescent measurements.

For the fuel rich test cases, because of the limited supply pressure and the pressure regulator used, the settings for the study oxidizer mass flow rate was reduced, while the fuel mass flow rate was increased.

3.2.2 Configuration Listing

Table 3.8.: Geometric configurations, testing parameters and hypotheses tested in HAMSTER.

Testing Configuration	Hypothesis Tested	Result
Nominal $\phi = \{0.8, 1.2, 1.4\}$ $T_{ox} = [440, 800]$	Transitional behavior with ox temp, acoustic tuning	Chug, thermoacoustic transition, fuel rich cases typically chug stronger and at higher frequency
Fuel manifold inclusion $\phi = \{0.8, 1.2\}$ $T_{ox} = \{500, 700\}$	Altered system response	Negligibly lower response in chamber, acoustic frequencies unchanged
No Recess in Injector $\phi = \{0.8, 1.2\}$ $T_{ox} = \{500, 700\}$	Stronger thermoacoustic response	No major change in behavior, small change in thermoacoustic frequency for fuel rich cases
High dP Ox Post Inlet $\phi = 0.8, T_{ox} = \{500, 700\}$	Reduce chugging, alter thermoacoustic response	Thermoacoustic instabilities stronger, chugging slightly reduced

Table 3.9.: Geometric configurations, testing parameters and hypotheses tested in HAMSTER (Continued).

Testing Configuration	Hypothesis Tested	Result
4" Ox Post $\phi = \{0.8, 1.2\}$ $T_{ox} = \{500, 600, 700\}$	Detune system thermoacoustically stabilizing effect	Better acoustically tune at low ox temp, but chugging also stronger at low temps [ox rich]. Fuel rich case higher mode excited in ox post at 700K ox temp, at low ox temp chug dominates
5.1" Ox Post $\phi = \{0.8, 1.2\}$ $T_{ox} = \{500, 600, 700\}$	Acoustically resonate with chamber at ox temp of 500K	Chug amplitude, frequency slightly higher at high ox temp, at 500K chugging still dominates significantly
9.15" Chamber $\phi = 0.8, T_{ox} = \{500, 700\}$	Resonate at higher acoustic frequency, detuned with ox post	Higher order mode excited in ox post at high ox temp, reduced chug slightly and broadened ox post mode Non-repeatable at 700K, at 500K higher frequency chugged, but reduced amplitude
9.15" Chamber, 4" Ox Post $\phi = 0.8, T_{ox} = \{500, 700\}$	Different (better) acoustic tuning of system with short chamber	thermoacoustic mode stronger, but not as strong as longer ox post tests

3.2.3 Performance and Mean Properties

To globally characterize and compare to any model of the system it is necessary to quantify and document the performance and mean properties of how the system operates. Basic properties, such as performance and injector pressure drop, can be symptomatic of how the system behaves dynamically. Other properties, such as injection velocities and propellant states, might give an idea of how the hydrodynamics and mixing might behave. The wall temperature measurements provide a good starting point in determining the heat transfer to the chamber wall, but also might contribute evidence as to the activity and mixing in the recirculation zone, as well as the possible injection jet/shear layer trajectory.

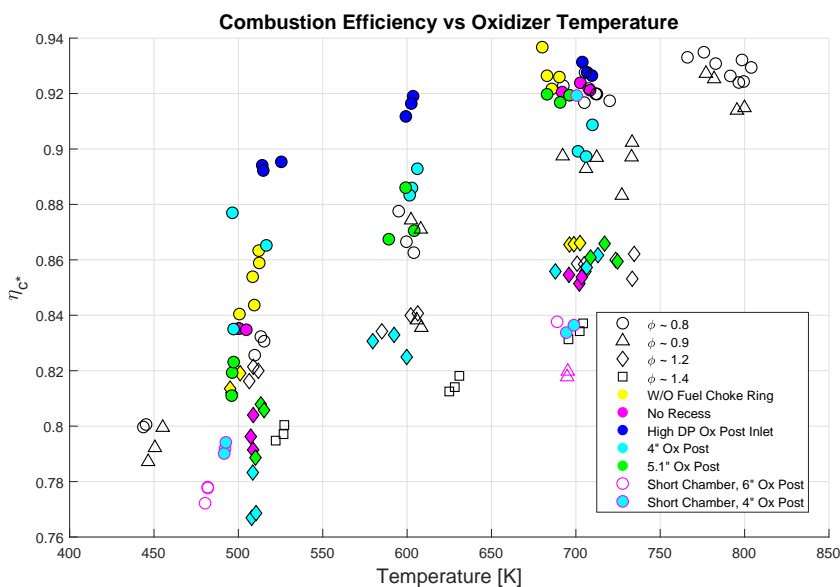


Figure 3.29.: Combustion efficiency of tests conducted in HAMSTER. The trend line is fitted to the nominal geometry, oxidizer rich cases.

Combustion Efficiency

Figure 3.29 shows the combustion efficiency for all tests conducted in HAMSTER. The combustion efficiency is generally proportional to the oxidizer temperature, except for oxidizer temperature exceeding 770 K . The combustion efficiency of the tests

conducted at fuel rich conditions are generally a few percent lower than that at oxidizer rich conditions, but trends at the same approximately linear rate with oxidizer temperature. The high pressure drop oxidizer post inlet geometry produced larger combustion efficiencies at lower oxidizer temperatures than other comparable cases, but trends at a nonlinear rate with oxidizer temperature, normalizing with the other cases at oxidizer temperatures of 700 K.

Injector Pressure Drop

Figure 3.29 shows the injector pressure drop for all tests conducted in HAMSTER. For the oxidizer post lengths of 5.1" and longer, with a recess of 0.4", the pressure drop across the injector remains constant for increasing oxidizer temperature at oxidizer rich conditions. This suggests that the bulk fluid average stagnation temperature in the recess scales linearly with the oxidizer temperature, as per Figure 3.13(a). At oxidizer temperatures exceeding 760 K, the pressure drop increases nearly linearly with oxidizer temperature; this could be attributed to excess burning in the injector recess causing larger Rayleigh losses, or less efficient burning in the chamber, resulting in a lower stagnation pressure in the chamber.

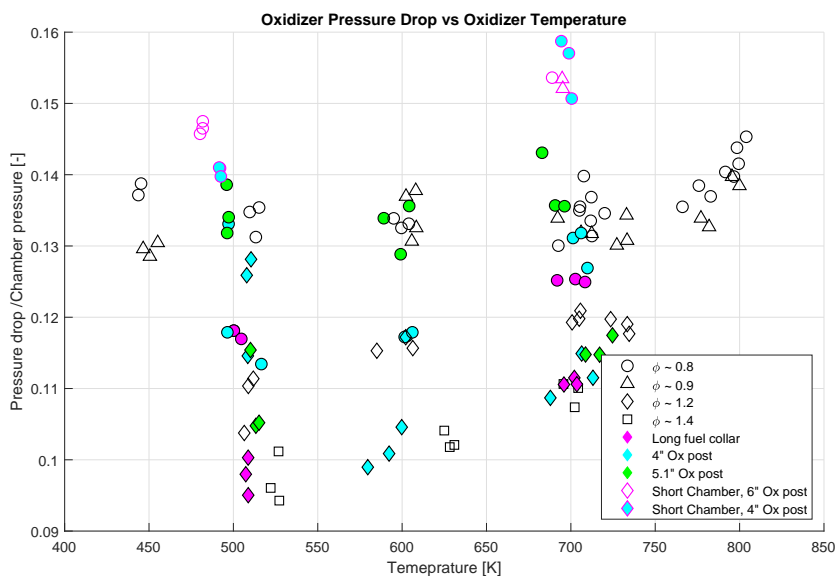


Figure 3.30.: Injector pressure drop of tests conducted in HAMSTER.

The short chamber configurations tend to have a diminished combustion efficiency, which likely results in the higher pressure drop observed. Both the shortest oxidizer post and long fuel collar (no injector recess) configurations have lower pressure drop at lower oxidizer temperatures, but increase nonlinearly with oxidizer temperature. The trend meets up and matches the injector pressure drop trend of the longer oxidizer post configurations at higher oxidizer temperatures. It was observed that the fuel collar was scorched upstream of the tip most tests, especially those with no recess (long fuel collar). This suggests that these configurations are susceptible to Rayleigh losses, which is the likely culprit for increased injector pressure drop for these cases.

At fuel rich conditions, the injector pressure drop is usually lower than that of tests at oxidizer rich conditions because the oxidizer flow rate was reduced to accommodate the equivalence ratio needed, resulting in a lower flow velocity and Mach number in the oxidizer post. The long fuel collar configuration has the lowest pressure drop of all configurations, especially at lower oxidizer temperatures. At low oxidizer temperature with the shortest post configuration, nominal chamber length, the pressure drop is relatively large. In this case, again, the stagnation pressure in the chamber is low causing a larger pressure drop across the injector.

Propellant Density and Velocity Ratios

Figures 3.31 and 3.32 show the propellant injection density and velocity ratios respectively. Each parameter trends linearly with oxidizer temperature. The velocity ratios of the fuel rich cases are lower because of the reduced oxidizer velocity and increased fuel velocity due to the accommodation made to achieve the set equivalence ratios.

Momentum Flux Ratio

Many coaxial injectors are characterized using the momentum flux ratio, for this reason Figure 3.33 represents the momentum flux ratio for all tests conducted with HAMSTER. The momentum flux ratio scales linearly in the same way as velocity ratio scales with oxidizer temperature. Since the density ratio is near unity it does not significantly impact the momentum flux ratio metric.

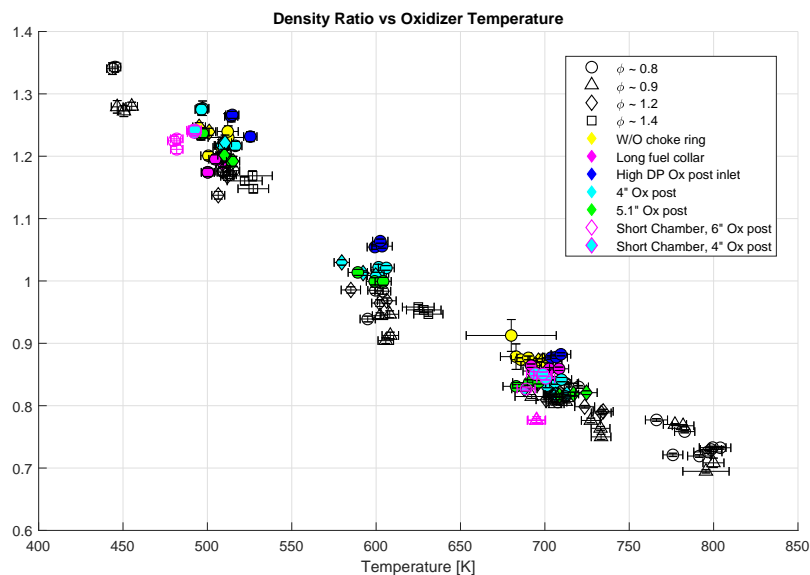


Figure 3.31.: Density ratio of propellants injected during tests conducted in HAM-STER.

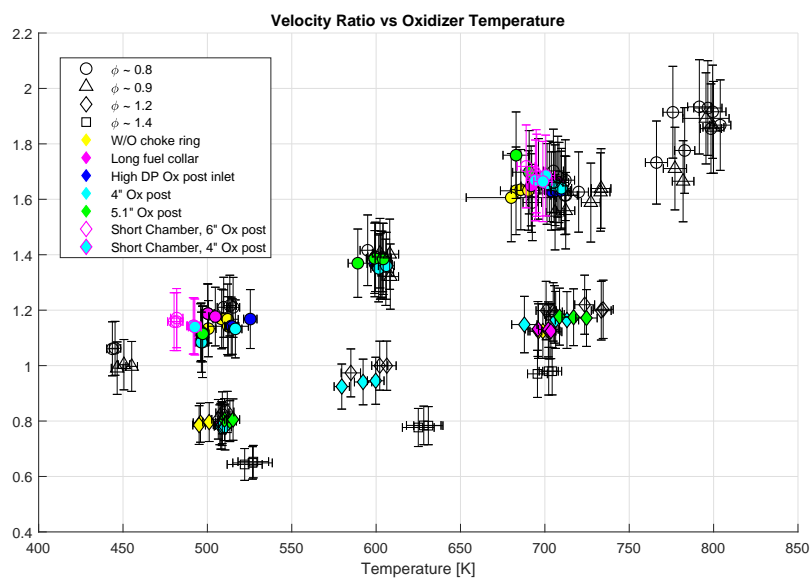


Figure 3.32.: Velocity ratio of propellants injected during tests conducted in HAM-STER.

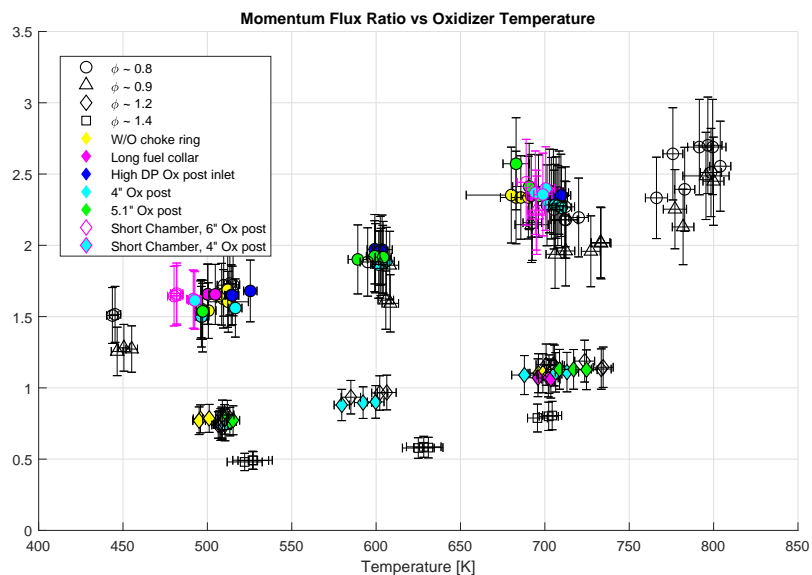


Figure 3.33.: Momentum flux ratio of propellants injected during tests conducted in HAMSTER.

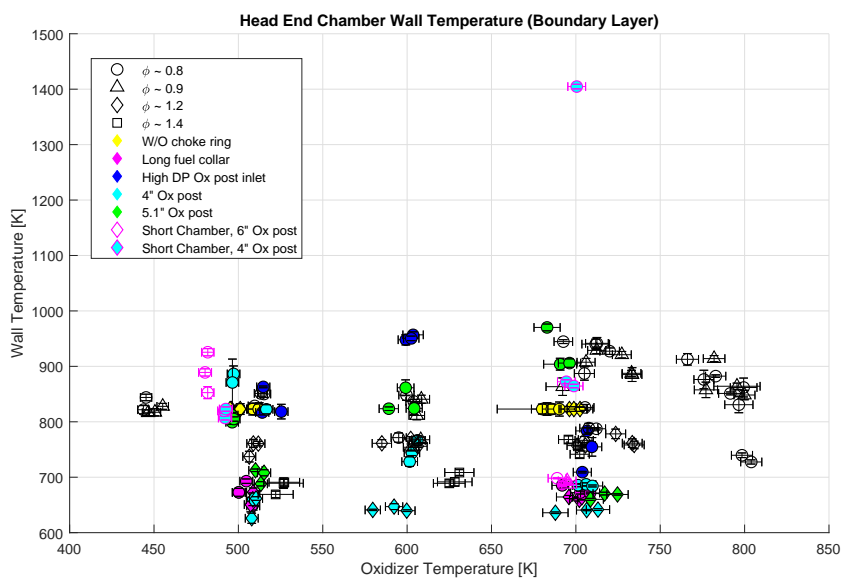


Figure 3.34.: Head end wall temperature during tests conducted in HAMSTER.

Average Wall Temperature

Figure 3.34 represents the temperature of the gas near the wall at the head end of the chamber. At the head end of the chamber is a recirculation zone caused by the backward facing step. The propellants and some amount of combustion products are entrained into the recirculation zone. This measurement is indicative of how the recirculation zone interacts with the reacting shear layer, and the combustion intensity at the local region of the injector face. The temperature measured are significantly lower than one might expect from combustion gases, suggesting that the bulk of the fluid in the recirculation zone is likely made up of fuel. There is one outlier in this dataset: this temperature corresponds to a test that was not repeatable and will be discussed at later stage.

Combustion Trend - Entrainment Ratio

The mass entrainment ratio shown in Figure 3.35 is calculated using Equation 2.17 based on velocity and density ratios for all tests conducted with HAMSTER. The inverse of the mass entrainment ratio (entrainment ratio of fuel to oxidizer in this case) approximately scales at the same rate as combustion efficiency. One might be tempted say postulate that as the entrainment ratio becomes closer to stoichiometric that the combustion might become more complete over the length of the chamber, hence a higher combustion efficiency. However, this metric fails to take into account the enhanced mixing effects - enhanced roll-up of the shear layer, due to local combustion events and acoustic perturbation.

3.2.4 Dynamic Trends

The HAMSTER experiment showed a number of reproducible dynamic trends of behavior. The most significant trends were related to the change in oxidizer temperature. The HAMSTER experiment produced three type of coupled behavior: a chug at very low frequency ranges and thermoacoustic coupling at low to high frequency ranges. The nature of each of these dynamic modes of behavior will be discussed

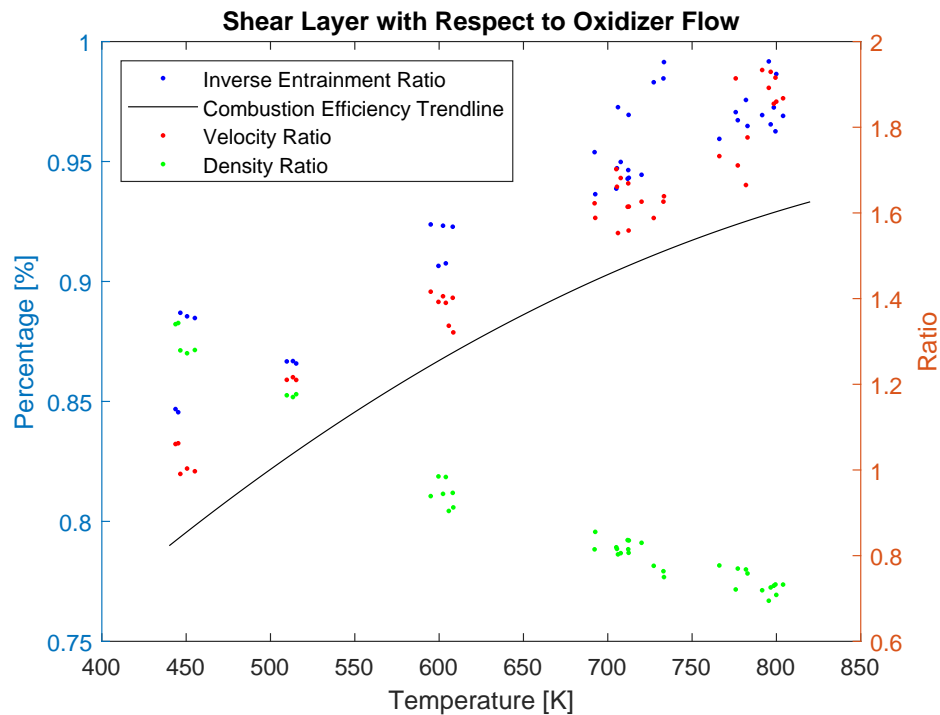


Figure 3.35.: Entrainment of fuel during tests conducted in HAMSTER.

in detail later on, for now, the trends of the thermoacoustic modes with oxidizer temperature will be shown.

The trends shown in this section all relate to a nominal geometric configuration, and only the effect of oxidizer temperature is shown. The trends for all geometric configurations with the associated parametric sweeps are found in Appendix C. Figure 3.36 shows the lower driven (resonant) thermoacoustic mode amplitude as a function of oxidizer temperature. Figure 3.37 shows the corresponding frequency at which this mode occurs for different oxidizer temperature.

The frequency at which this mode usually occurs has some interesting features. The low frequency implies a long wavelength or bulk response in the oxidizer manifold and chamber. Specifically, a bulk response, sometimes referred to as a "lumped response". A lumped response is usually associated with a chugging response of the

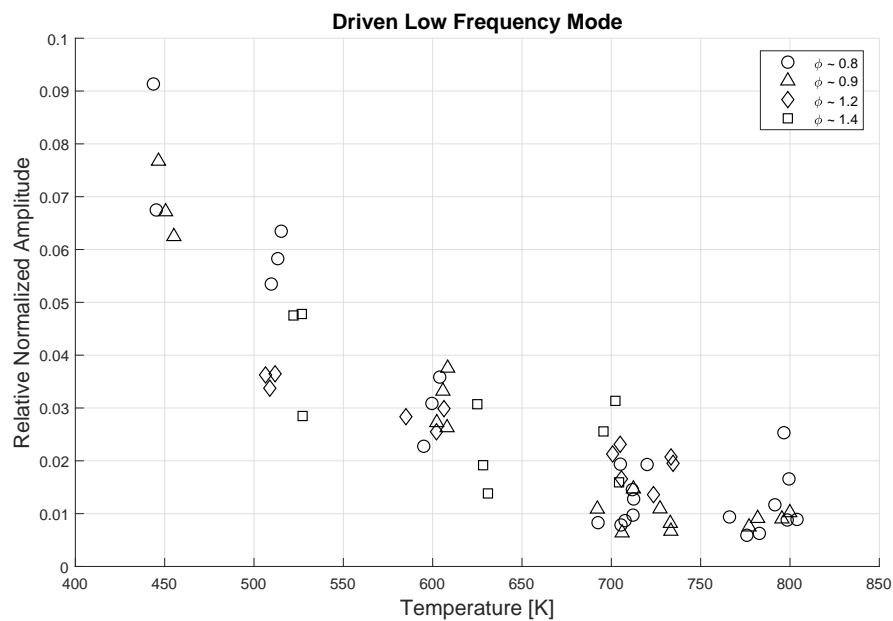


Figure 3.36.: Thermoacoustic chug amplitude as a function of oxidizer temperature.

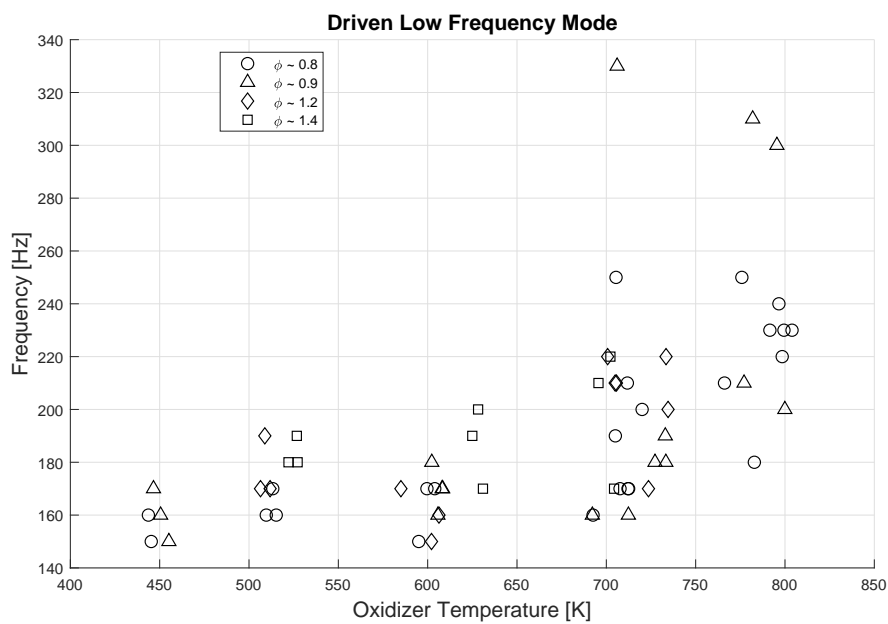


Figure 3.37.: Thermoacoustic chug frequency as a function of oxidizer temperature.

system, but this mode in particular is not a typical feed system chug, hence, this mode is referred to as a thermoacoustic chug.

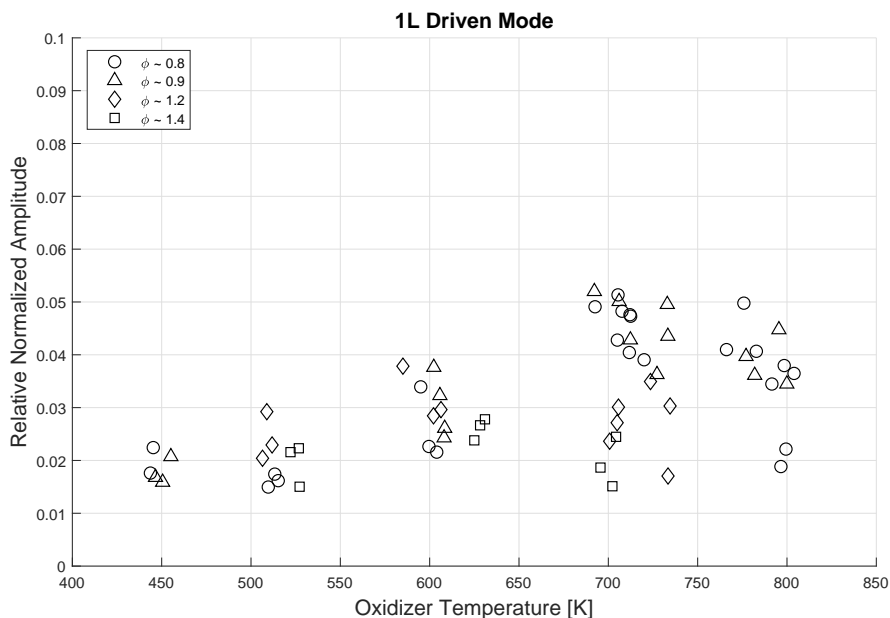


Figure 3.38.: Thermoacoustic fundamental mode amplitude as a function of oxidizer temperature.

A thermoacoustic longitudinal mode, also referred to as an "organ pipe mode" is produced in the system, and the mode amplitude with respect to change in oxidizer temperature is shown in Figure 3.38. Figure 3.39 shows the corresponding frequency at which this mode occurs for different oxidizer temperature.

The normalized amplitude is the single mode amplitude determined from the PSDs of the chamber pressure measurements, normalized by the mean chamber pressure. Comparing Figures 3.36 and 3.38 it is clear that as the oxidizer temperature increases the thermoacoustic chug mode amplitude decreases, while simultaneously the thermoacoustic 1L mode amplitude increases. This suggests that there is a shift in the dominant coupling mechanism of behavior as the oxidizer temperature changes.

Also of note is that the resonant 1L frequency of the system with ox rich conditions, increases nearly linearly with oxidizer temperature. This is unexpected because the

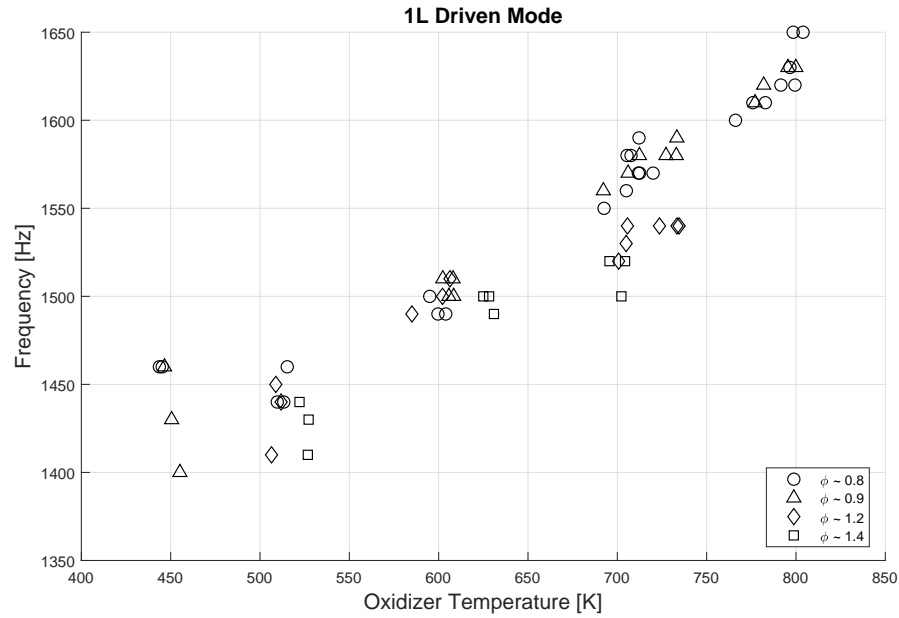


Figure 3.39.: Thermoacoustic fundamental mode frequency as a function of oxidizer temperature.

sound speed scales as a function of the square root of the temperature, and the acoustic frequency is directly proportional to the sound speed, which suggests that $f \propto \sqrt{T_{ox}}$.

For the fuel rich cases it appears that the resonant frequency does scale with oxidizer temperature as one would expect; as the oxidizer temperature increases the ox post begins to acoustically tune better with the chamber. These cases, however, show a significantly lower fundamental acoustic amplitude than for the oxidizer rich cases. Additionally, the thermoacoustic chugging mode in the fuel cases never diminishes to the point where it become nigh negligible.

At this point one might be tempted to make the conclusion that because the velocity ratio scales linearly with oxidizer temperature, and that the resonant 1L mode frequency scales linearly for the oxidizer rich cases, that the thermoacoustic coupling strength might be a function of the velocity ratio. There is an oxidizer temperature

associated with maximum response, this suggests that the acoustic response strength could be related to acoustic tuning of the system.

Another potential cause for the change in oscillation is the impedance at the chamber/ox post interface. Figure 3.40 shows the relative change in the acoustic reflection coefficient at the chamber/ox post interface. At lower oxidizer temperatures less acoustic energy is able to be transmitted into the oxidizer post, but the transmitted energy increases exponentially with increase in oxidizer temperature.

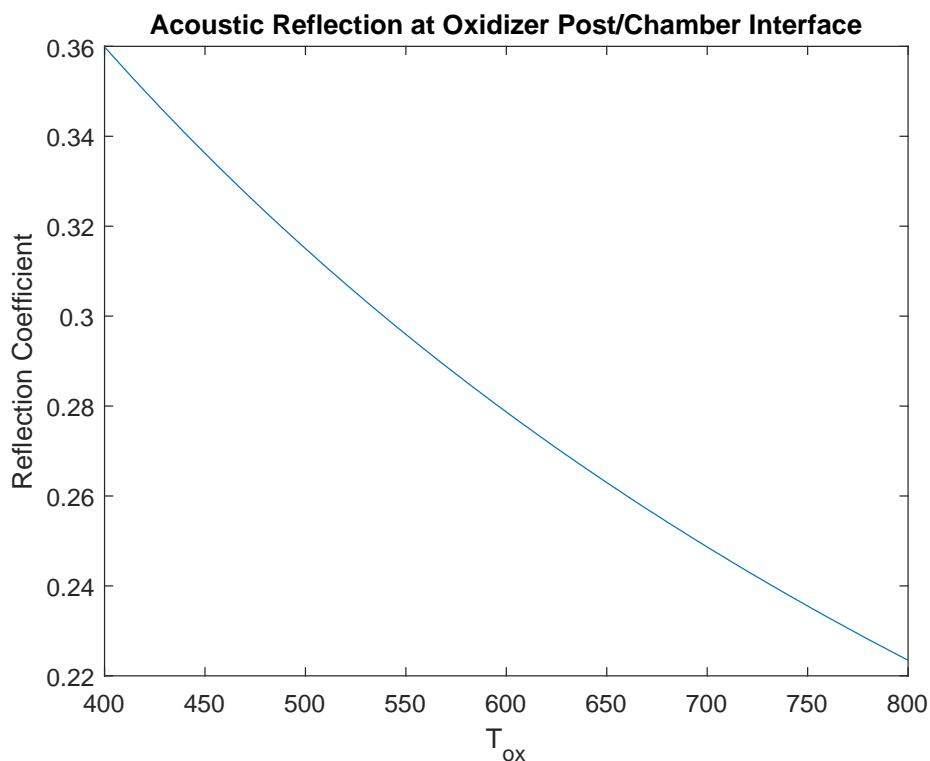


Figure 3.40.: Reflection coefficient at the chamber/ox post interface.

Based on these trends it is still not quite clear which mechanisms/s are directly responsible for when the system is considered to be in a thermoacoustic instability, but at least from Figure 3.41, it can be determined when the system is in a pure thermoacoustic instability (resonance). Figure 3.41 shows a threshold fundamental mode amplitude whereby the first harmonic amplitude begins to scale linearly with the

fundamental mode amplitude. This scaling suggests a non-linearity in the acoustic response in the chamber and therefore implies a strong resonance due to combustion. Looking closely at Figure 3.41 reveals that for the fuel rich cases a strong thermoacoustic resonance never actually takes place; the fundamental mode amplitude does not gain enough strength to induce a nonlinearity and thus higher harmonics.

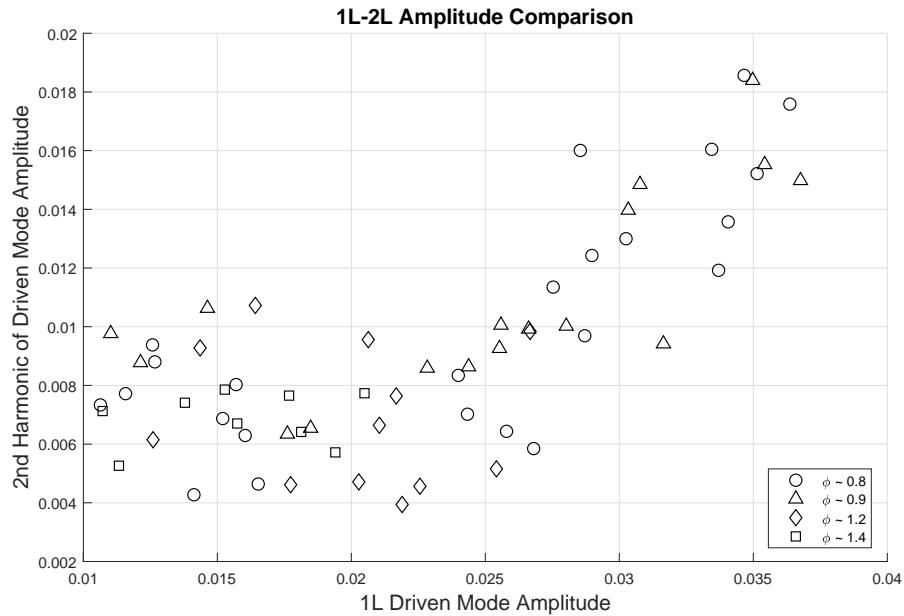


Figure 3.41.: Thermoacoustic mode amplitude comparison, showing the approximate threshold at which a strong thermoacoustic coupling takes place.

From the trends observed there a number of root parameters which appear to possibly drive thermoacoustic instabilities in HAMSTER. The observations and deductions thus far are:

- Oxidizer velocity
 - Velocity ratio - KH instability in chamber (mixing enhancement)
 - Vortex shedding off of injector features (mixing enhancement)
- Oxidizer temperature

- Ignition delay - chemical reaction and mass diffusion rates

- Acoustic tuning of ox post/manifold and chamber

 - Reflection coefficient at chamber/ox post interface

 - Oxidizer sound speed

 - Combustion gas sound speed

The next sections will address the specific mechanisms in more detail; in an attempt to prove which mechanism/s are truly responsible for the behavior observed.

4. METHODS OF DATA ANALYSIS

In this section the tools which will be used to perform detailed analysis on the collected data are briefly described. These tools are necessary to accurately and precisely analyze the data. Once the dominant length and time scales have been identified, they will be measured against the hypothetical instability mechanisms that been proposed.

Initially the type of sets of time series need to be identified. Many of the analysis or signal processing techniques are based on the assumption that a particular process, represented by the time series, has a particular form. Most analyses typically make the assumption that a process is wide sense stationary or autoregressive because these processes are easier to deal with; such processes are statistically linear.

4.1 Statistics and Stationarity

Wide sense stationarity implies that a particular process's statistics do not change, in a non-negligible way, in time. In terms of combustion operation stationarity would also imply that the system has achieved steady operating conditions. Practically, in a highly non-linear dynamics system the statistics of the process may vary in time, depending on the time scales at which the system is analyzed. For exceptionally long time scales, much longer than the mode of the lowest frequency, the process begins to approach a statistically long process, which abides by the assumption of statistical analysis: "law of large numbers". If the process is deemed at least stationary then it may be concluded that the data was collected during steady operation.

One method of computing stationarity of time series is the use of running statistics such as mean and root mean square. However, these methods rely on temporal extent of the conditional expectation applied and tends not to be a robust method. One

robust method is the Augmented Dickey-Fuller (ADF) test [88]. The test is applied by regressing the time series against a simple autoregressive model, a unit root test is then carried out under a null hypothesis. If the null hypothesis is rejected then the time series is considered stationary. For the test to be valid with the available sample sizes, it is required that the time series be detrended by the first order moment. The running statistical quantities are still useful though and can be used to quantify momentary atypical behaviors in a time series, and the development of a nonlinear process.

4.2 Correlation, Transformation and Filtering Methods

Correlation and frequency domain methods are common and well known. The autocorrelation, cross-correlation and the fast Fourier transform (FFT) are all used in an effort to interpret the data. A useful quantity used well in the interpretation of the results is the magnitude squared of the coherence between two time series; this metric gives a normalized quantification of well each of the time series corresponds to one another at particular frequency. This quantity is based off of the power spectral density estimate (PSD), specifically the PSD for each time series and the cross PSD (CPSD). The method used to determine the PSDs and CPSDs is Welch's method, utilizing a Hamming windowing approach [89]. The nonlinear interaction between different modes or frequencies can be determined by calculating the third order cumulant or bicoherence spectrum [90,91].

FFT and PSD methods are limited because they produce an average correlation over the entire time series, but do not account for changes in frequency with time. The Hilbert and Wavelet transforms are useful for determining temporally accurate frequency correlations for a time series. A continuous wavelet transform (CWT) is used to study the data, utilizing an Amor (Gabor) class wavelet [92]. The Hilbert transform is easy to implement, but can only detect frequency changes in time for a monocomponent spectrum, ie: there is only one mode where its frequency varies or

drifts in time [93]. The Hilbert transform can artificially be used by filtering other spectral components out of the time series and studying a small spectral bandwidth, allowing for variation of the frequency in time.

Spectral filtering is a common tool in signal processing. High, low and band pass filtering was used to analyze selected spectral components or remove unwanted components from the data sets. An infinite impulse response filter design (IIR) is always used in the data analyses with a very steep drop-off in response ($> 3dB$). For cases where a monocomponent frequency within the selected bandwidth was to be studied, it was found that the filters may not have been adequate and phase was not always well preserved. This is especially the case where one frequency was modulated by another, as determined by the bicoherence spectrum. It was found that the singular spectrum analysis (SSA) was effective at preserving the main features of the signal as well as the phase [94]. The reason for this is that the SSA is effectively the same as a proper orthogonal decomposition (POD), which projects the time series onto orthogonal basis customized for that signal, as opposed to projecting onto periodic functions described only by $e^{i\theta}$, such as an FFT. This allows some flexibility when extracting the dominant features from a highly nonlinear signal. In the cases where phase was an important parameter SSA was preferred when analyzing the data.

5. ANALYSIS OF EXPERIMENTAL RESULTS

In this section a detailed analysis of the experimental results is done. Three test cases were investigated; the geometrical configuration for each test was identical. The three test cases were differentiated by oxidizer temperature: 440 K , 600 K and 700 K . The test cases of 440 K and 700 K were chosen to most closely complement the simulation work done, while the 600 K case was chosen to show the abridged behavior. The experimental analysis also serves as a precursor to the comparison made against the simulation results. Analysis of the problem is made under a number of assumptions, all of which need to be verified. The assumptions are as follows:

- The data is analyzed during steady operation and has stationary statistical characteristics.
- The thermoacoustic coupling is one dimensional or axisymmetric.
- The nozzle is acoustically short and does not contribute to the resonance significantly.
- The chamber wall is adiabatic.

5.1 Base Level Analysis

A rigorous foundation level analysis of the experimental is presented here. First, the pressure measurements taken are verified. The verification is followed by testing of the assumptions made.

5.1.1 Measurement Verification

Pressure measurements at high and low sampling rates were taken at the same axial position, at numerous locations within the experiment. By comparing the raw data taken by each measurement device per axial location, the measurements can be verified. Figures 5.1 and 5.2 show the raw pressure data collected from the head and aft ends of the chamber respectively. The pressure traces show the high frequency raw data, the corresponding moving mean of the high frequency data and the complementary low frequency pressure data. The high frequency data is sampled at 1 MHz, while the low frequency data is sampled at 5 kHz. The maximum frequency response rate of the high frequency pressure transducers is 250 kHz, and for the low frequency pressure transducers it is 2 kHz.

Comparing the high and low frequency data from the head and aft ends of the chamber it can be seen that there is some discrepancy between the mean values of the low and high frequency data at the aft end, but the head end is in good agreement, within 2%. The mean values of the high frequency data at the aft end are not always as precise as the data collected at the head end because there is usually some thermal drift due to heat loading from the equilibrated combustion gases near the nozzle.

Additionally, the fluctuation amplitude of the low frequency pressure data appears to be much greater at lower oxidizer temperatures. The explanation for this phenomenon is that at higher oxidizer temperatures the dominant dynamics tend to be of higher frequency, which results in an aliasing of the low frequency signal and therefore a reduction in the amplitude of the fluctuations. The low frequency fluctuations of the high frequency data also does not appear to match the phase of the low frequency data at the lower oxidizer temperatures. At low oxidizer temperatures the low and high frequency fluctuation amplitudes (of the lower frequency dynamics) are nearly equivalent. This suggests that the response time of the low frequency versus the high frequency pressure transducers is different. The maximum acoustic length

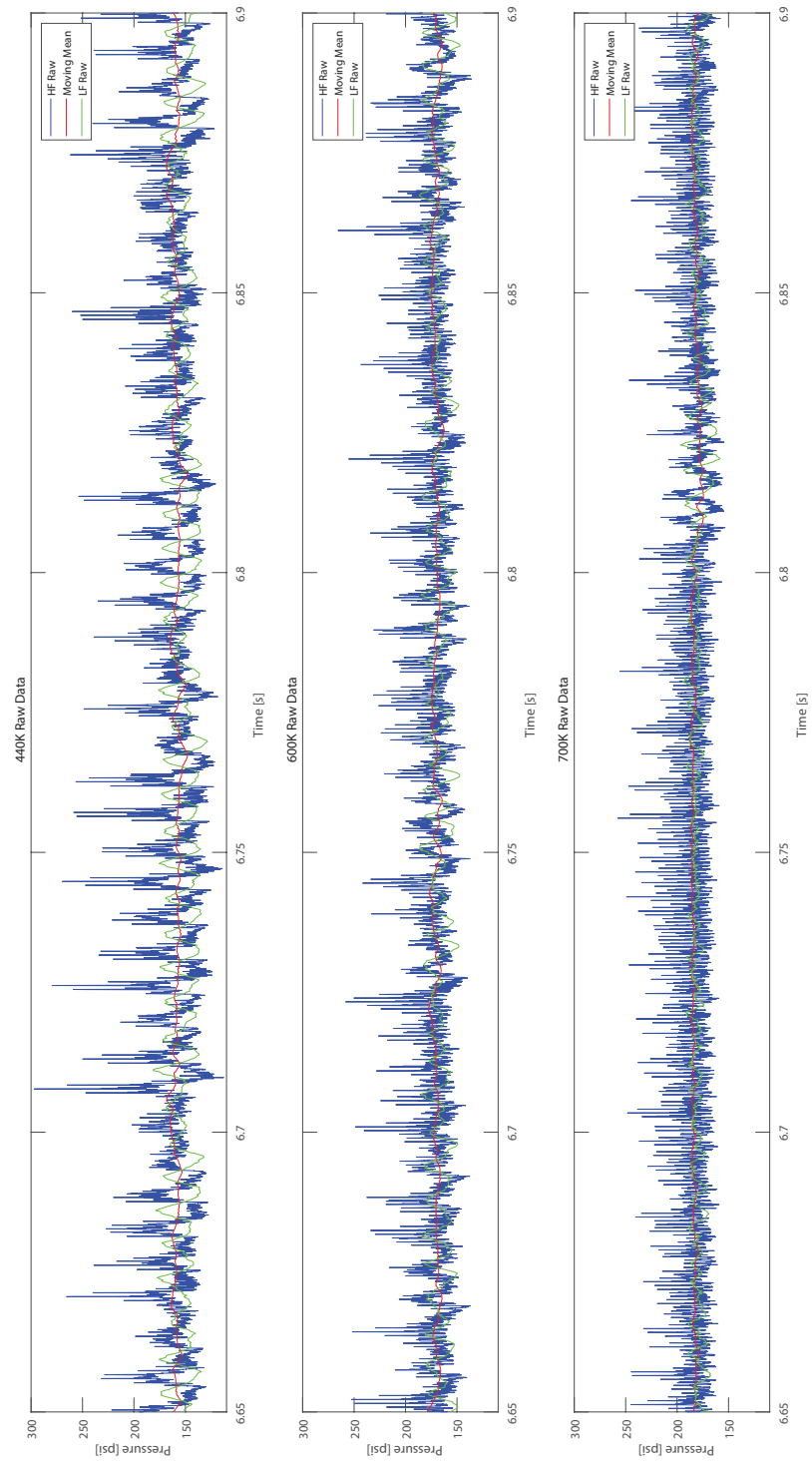


Figure 5.1.: Raw pressure data acquired at the head end of the chamber, 0.300” downstream of the dump plane.

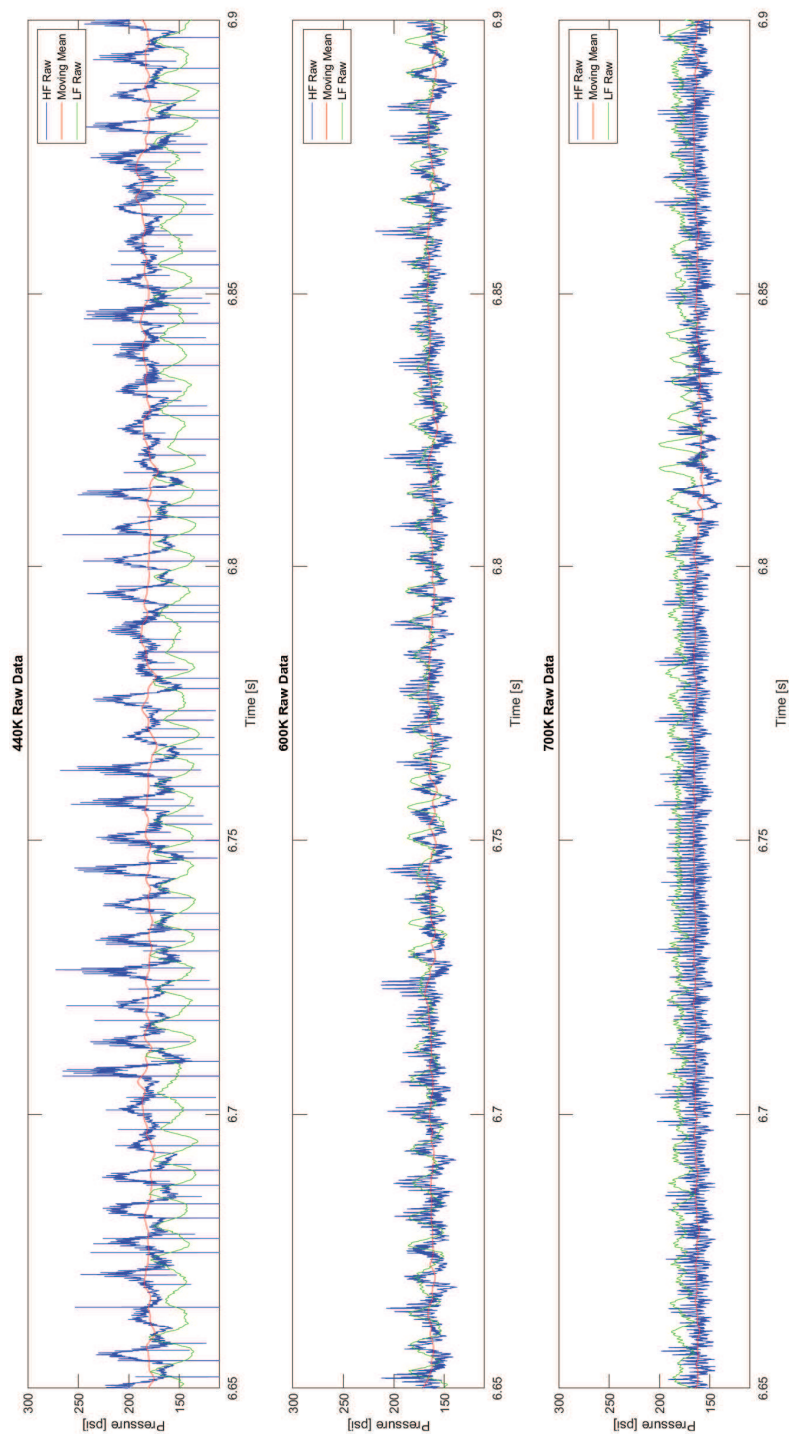
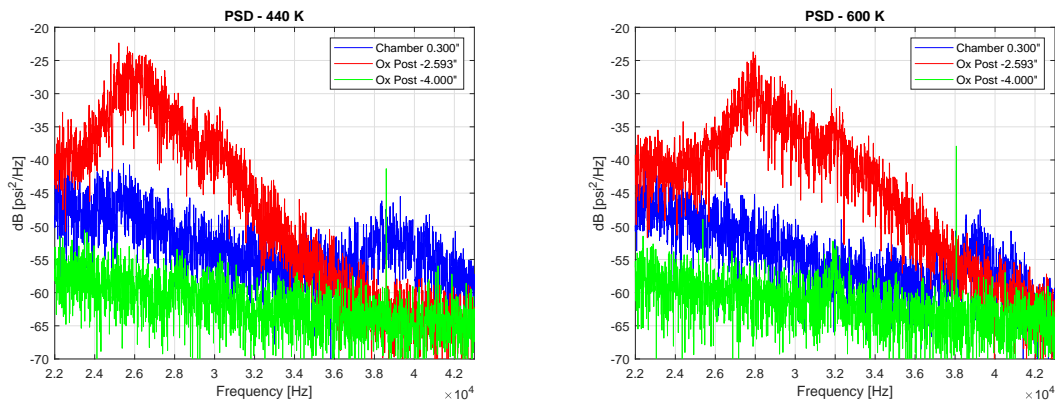
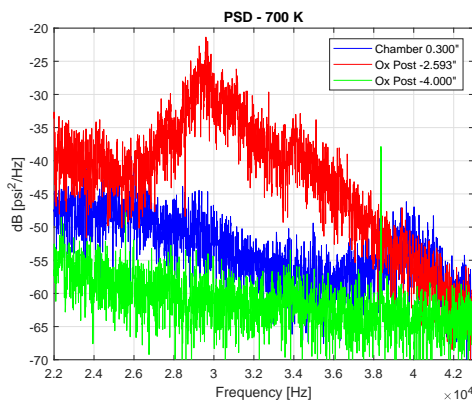


Figure 5.2.: Raw pressure data acquired at the aft end of the chamber, 13.150” downstream of the dump plane.



(a) Helmholtz response of the port cavity at an oxidizer temperature of 440K. (b) Helmholtz response of the port cavity at an oxidizer temperature of 600K.



(c) Helmholtz response of the port cavity at an oxidizer temperature of 700K.

Figure 5.3.: PSDs of the port Helmholtz response of the pressure transducers in the oxidizer post and the chamber for various oxidizer temperatures.

of the port leading up to the high frequency pressure transducers is on the order of 0.21", in contrast to the port of low frequency pressure transducers which is on the order of 2.5". It has been determined that the time lag of the low frequency pressure signal is approximately 0.008 s behind the high frequency pressure signal.

Despite these differences, from Figure 5.1 it is clear that the low frequency data matches well with the moving mean of the high frequency data, even in the event of momentary changes in behavior where the mean pressure droops due to chugging. It

can then be said, with caution, that the pressure related dynamics and the statistical moments should be well represented by the pressure measurements.

Lastly, to ensure that the signal is not contaminated with an unwanted response due to the measurement design, the representative HF pressure transducer port responses are scrutinized, shown in Figure 5.3. Figure 5.3 shows that a Helmholtz resonance occurs at very high frequencies, well beyond the range of interest and does increase with increasing oxidizer temperature.

5.1.2 Assumption Testing

Each assumption about the experiment will be tested in this section, in the order stipulated at the beginning of this chapter. If an assumption does not strictly hold then the discrepancy will be quantified.

Stationarity Assessment and Steady Operation

It is important to determine whether the data to be fully analyzed has predictable characteristics. This process is difficult because the system, which is combustion coupled, is inherently highly nonlinear. However, if the data can be shown to have stationary characteristics then it is implied that the system is operating at steady conditions, despite the possible apparent unpredictability of the dynamics. Stationarity is also important because some of the analysis techniques used depend on the assumption that the data is stationary, such as the PSD.

By assuming an autoregressive (AR) model for the data, meaning that each new time step can at least be predicted based on a linear dependence on the previous data in time, and using with a stochastic influence, a unit root test is performed using the ADF model.

Each dataset tested, corresponding to each oxidizer temperature, was found to be stationary once detrended by their mean values. Hence, each dataset is at least sta-

tionary over the time interval and therefore the assumption of steady state operation of the device is valid.

One dimensionality or Axisymmetry

This study was performed on the basis that the physics are one dimensional. The simulations ran were done under the premise of axisymmetry. At the head end of the chamber two high frequency pressure transducers were placed at the same axial location in the chamber, but azimuthally separated by 135° . This clocking angle was chosen to ensure that tangential acoustic modes can be identified with confidence.

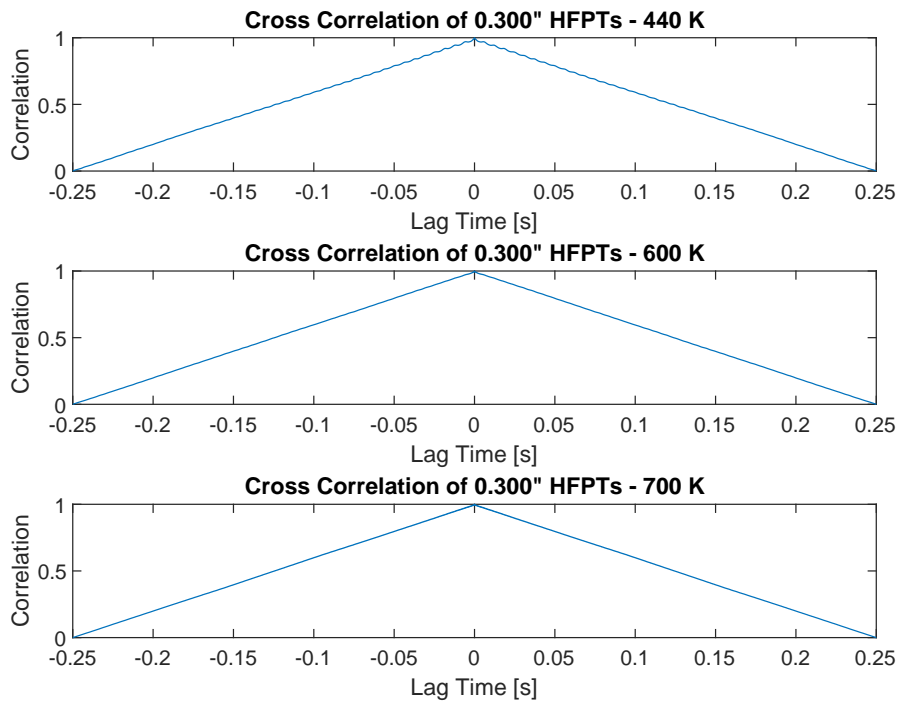


Figure 5.4.: Cross correlation between data collected by transducers at head end of chamber 0.300" downstream for the dump plane.

Figure 5.4 shows the cross-correlation of the data at the head end of the combustion chamber. In each case the signals show near perfect correlation (correlation

factor of 0.999) with a time lag of $0s$. Therefore it can be concluded that the signals are nearly identical and thus the response in the chamber is only longitudinally coupled or one dimensional.

To ensure that out of plane dynamics do not contribute to the physics in the combustion chamber the response of the oxidizer manifold and oxidizer post needs to be evaluated. Figure 5.5 shows the PSDs of the pressure measurements taken in the oxidizer manifold for different oxidizer temperatures. Figure 5.6 shows the expected modes unique to the oxidizer manifold, for the full range of expected oxidizer temperatures.

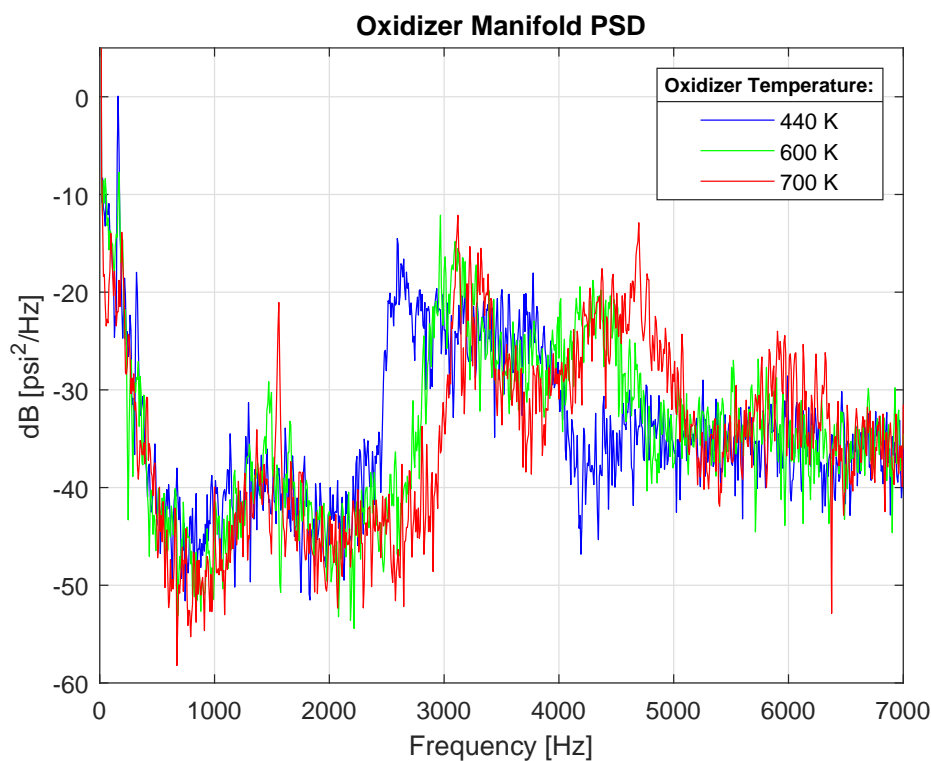


Figure 5.5.: PSD of pressure response in the oxidizer manifolds as a function of oxidizer temperature.

Figure 5.5 shows a diminished response over the frequency range of 800-2200 Hz, where the fundamental frequency of the system is around 1400-1550 Hz (proven

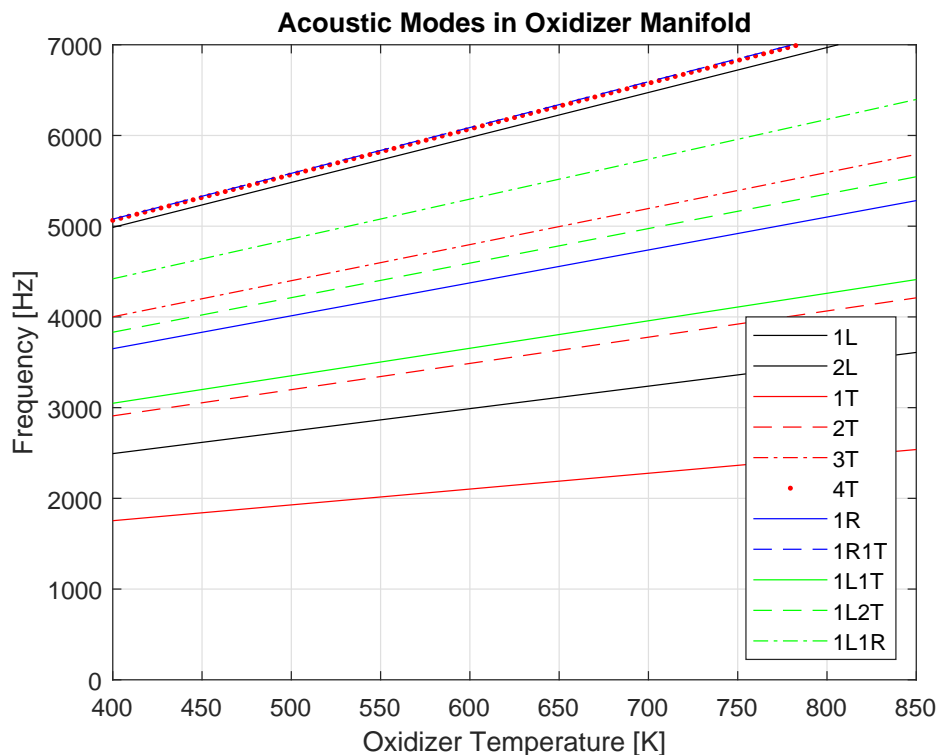


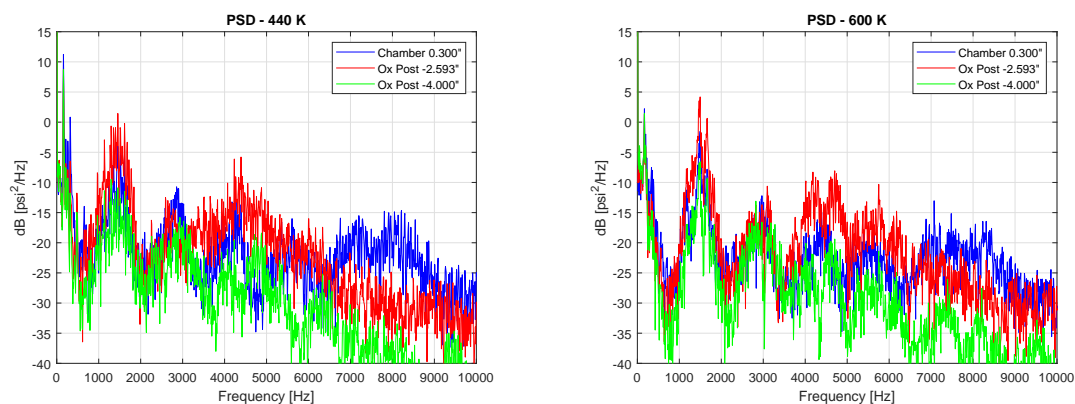
Figure 5.6.: Expected acoustic modes in the oxidizer manifold as a function of oxidizer temperature.

later). At approximately the first harmonic frequency of the system, for each oxidizer temperature, the response in manifold is highly amplified. Comparing Figures 5.5 and 5.6 it is evident that the first harmonic frequency falls in the range of the 1L mode of the oxidizer manifold. Additionally, the 2T and 1L1T modes are comparably close to the first harmonic mode of the system, and show evidence of excitation for all oxidizer temperatures. There is also the possibility that all modes from 3500 to 7000 Hz are excited to some extent in the oxidizer manifold.

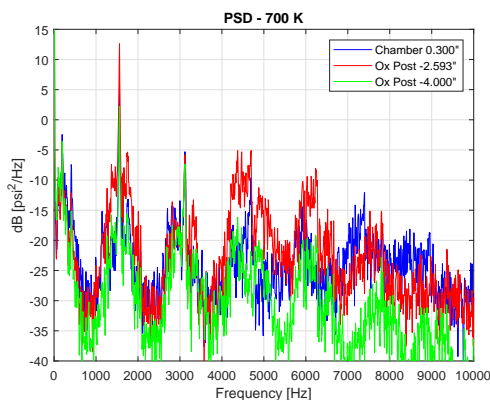
Since it is pretty clear that there are dynamics occurring in more than one dimension in the manifold, it can be concluded that the assumption of pure axisymmetry for the system does not hold. Figure 5.7 shows the pressure response downstream of the oxidizer manifold. In all oxidizer temperature cases the higher frequency dynamics

are mimicked in the response of the immediate downstream pressure transducer, but its effects diminish further downstream where it is not evident in the chamber. This suggests that these modes are evanescent in the oxidizer post, and decay well before reaching the injector recess.

This leads to the conclusion that the higher dimensional physics in the oxidizer manifold do not effect the thermoacoustic coupling in the chamber and therefore the assumption of axisymmetry is still useful and conditionally valid.



(a) Responses at an oxidizer temperature of 440K. (b) Responses at an oxidizer temperature of 600K.



(c) Responses at an oxidizer temperature of 700K.

Figure 5.7.: PSDs of the pressure response in the oxidizer post and the chamber for various oxidizer temperatures.

Fuel Participation in Thermoacoustic Coupling

Other experimental configurations were done to study the effect of the fuel manifold on the thermoacoustic instabilities. These studies, among others, are summarized in the plots in Appendix C. It was found that although the response in the fuel manifold itself differed when unchoked, the effect on the overall system was negligible (no frequency change), with marginal dampening.

Nozzle Effect

In the tests used as representatives the nozzle showed little effect. In other tests, shown in Appendix C some entropic fluctuations are observed, which only propagate halfway upstream in the chamber, but do not have an effect on the combustion at the head end of the chamber.

Adiabatic Wall

Heat transfer through the combustor wall can contribute to a change in the physics of the not only the acoustics, but the combustion as well. To achieve an adiabatic wall condition as best as possible the inner wall of the combustor was lined with TBC. The thermal properties of the TBC are: $2 W/m.K$ (*Max*) - thermal conductivity and $3.5 \times 10^{-6} m^2/s$ - thermal diffusivity.

5.2 Analysis of Main Features

An in depth analysis of the selected data to identify the dominant physics is shown in this section. A number of key physical features are highlighted and quantified, with emphasis on the mechanisms at the head end of the chamber.

5.2.1 Identification of Acoustic Modes

A direct comparison of the data collected from the experiment with the expected response generated by the 1D acoustic model was used to help identify existing modes of behavior in the system. The inherent discrepancies also help to identify shortfalls of the model. Figures 5.8, 5.9 and 5.10 shows these comparisons with the data collected for oxidizer temperatures of 440 K, 600 K and 700 K respectively.

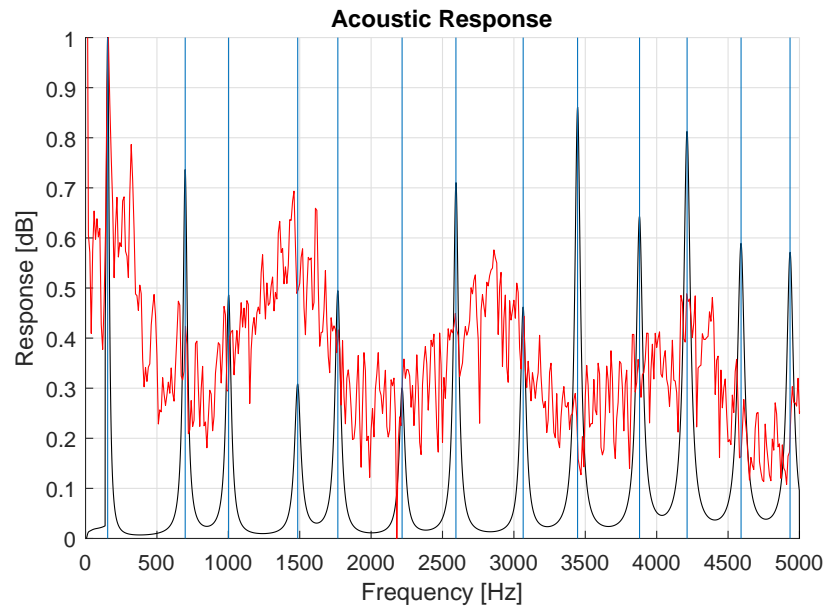


Figure 5.8.: Comparison of the expected acoustic response with the PSD of the experimental data collected for an oxidizer temperature of 440K.

For each case the acoustic model predicts most of the frequencies quite well, especially the low frequency modes. However, as the oxidizer temperature increases the fundamental acoustic mode excited is not predicted well by the acoustic model. Figure 5.8 indicates a better prediction of the acoustic response in the system. The system is less thermoacoustically resonant at the fundamental frequency in this case, and therefore the acoustic response of the system is purely acoustic; there is no dominant mechanism driving the fundamental frequency. It is interesting to note that the frequency at the 150 Hz range is actually an acoustic response, as predicted

by the acoustic model, and has a strong gain without the need for a driving resonant mechanism. A harmonic of the low frequency mode is also present. Another important note is that the harmonics of the fundamental frequency are not integer multiples of the fundamental frequency. This is explained by the frequency dependent impedance at the oxidizer post/chamber interface caused by a sudden change in area. The transfer matrix describing this process is shown in Appendix A.2.

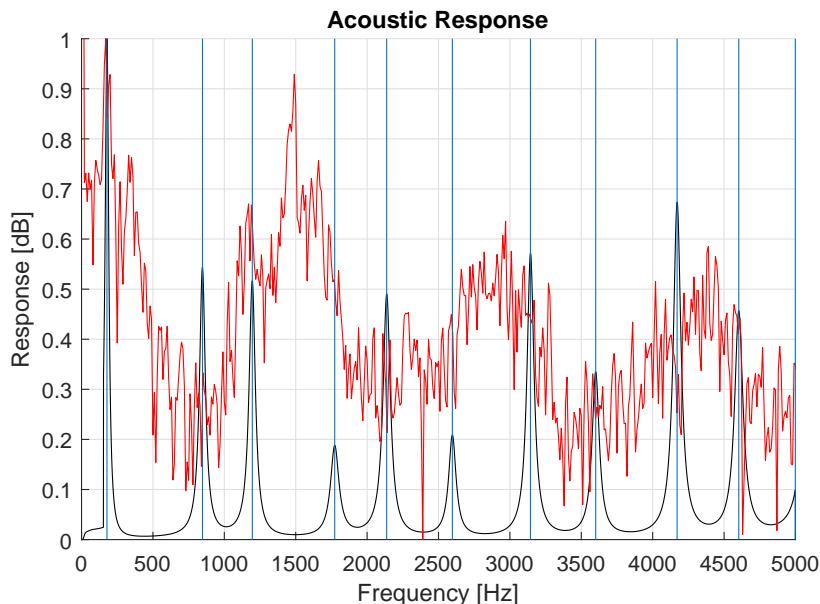


Figure 5.9.: Comparison of the expected acoustic response with the PSD of the experimental data collected for an oxidizer temperature of 600K.

Figure 5.9 is a good representation of transition behavior. The transition from a dominant low frequency mode to a dominant fundamental acoustic mode is shown in Figures 3.36 and 3.38. As the oxidizer temperature increases the low frequency mode diminishes and the higher frequency mode begins to dominate. In this case the driven higher frequency mode does not correspond directly with the model, and the harmonics of the driven mode become integer multiples of the driven fundamental mode. An important feature that begins to show up in the transition phase is the emergence of a mode that has a frequency which is the sum of the low and high

frequency modes. This is the result of modulation of two nonlinear modes and will be discussed in more detail later on.

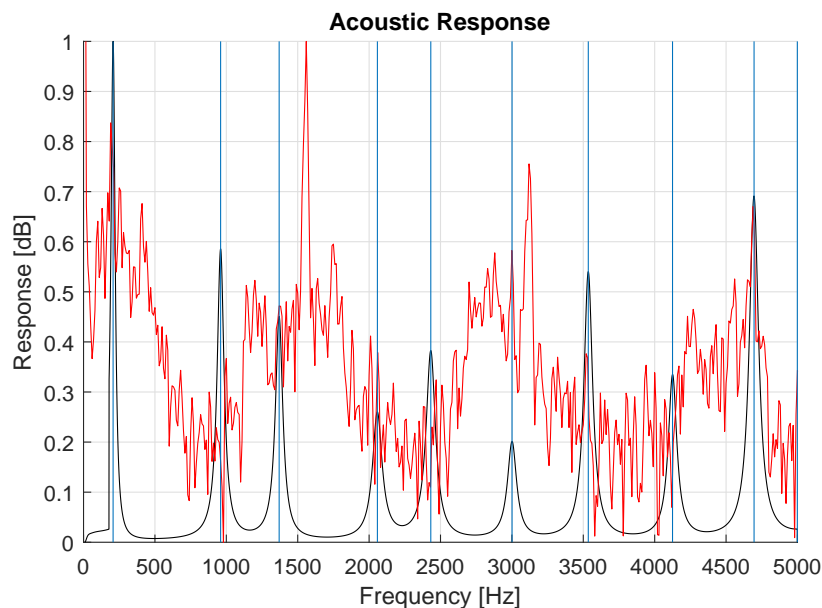


Figure 5.10.: Comparison of the expected acoustic response with the PSD of the experimental data collected for an oxidizer temperature of 700K.

Figure 5.10 shows the relative dominance of the higher frequency mode over the lower one at higher oxidizer temperature. The harmonics of the high frequency modes have a sharp, small band width, and are integer multiples of the driven fundamental mode. The acoustic model does not represent the modes extremely well, but some of the lower amplitude modes correspond to the expected gains. Visualization of the mode shapes can be helpful to understand the nature of each mode better.

Figures 5.11, 5.12 and 3.10 show the mode shapes of the low and high frequency modes as predicted by the acoustic model. Figure 5.11 shows the bulk response of the low frequency mode in the oxidizer manifold and the chamber, while also showing a non-standing wave behavior in the oxidizer post which facilitates a phased communication between the oxidizer manifold and the chamber. The velocity mode shape shows an inherent constant flow acceleration from the beginning of the oxidizer

post to the aft end of the chamber, which only changes as the mode progresses through its cycle.

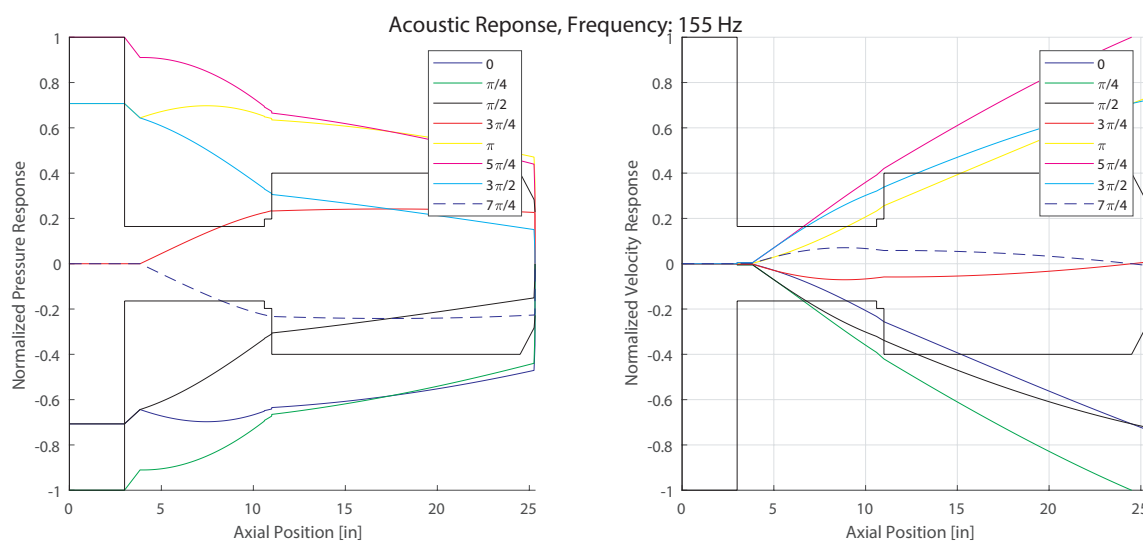


Figure 5.11.: Low frequency acoustic mode shape predicted by 1D model of HAMSTER.

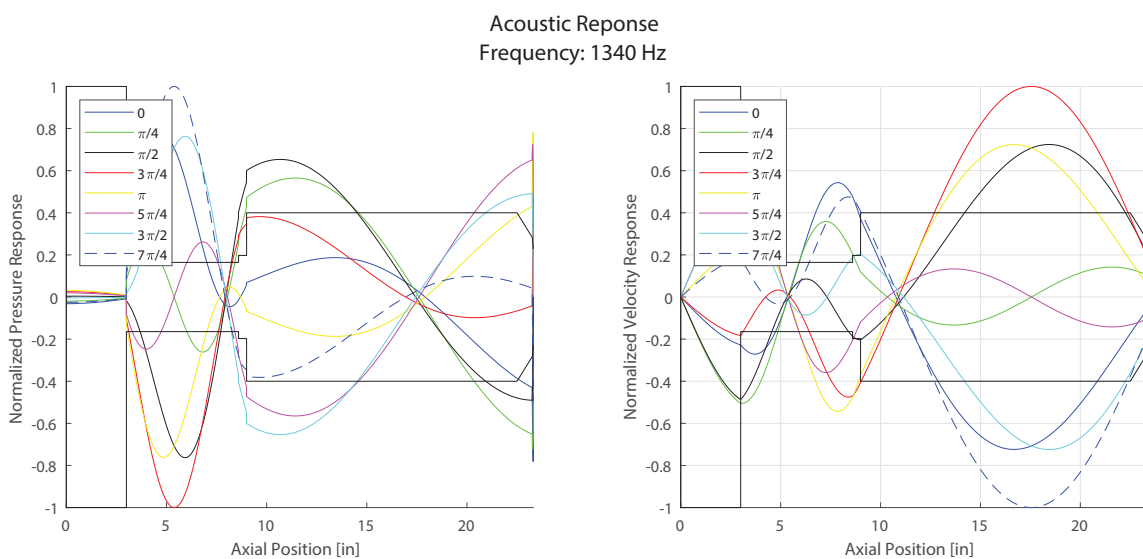


Figure 5.12.: High frequency, one possible fundamental acoustic mode shape predicted by 1D model of HAMSTER.

Figures 5.12 and 3.10 show standing wave behavior in HAMSTER for an oxidizer temperature of 700K, consistent with acoustic theory. The shapes of the modes do not have a typical standing wave shape as one would expect because of the effect of mean flow. The boundary conditions at the aft end of the chamber are set to an infinite impedance (choked condition) at the nozzle throat. This results in a pressure antinode and a velocity node, but the relative response near such locations can have very sharp changes due to the flow acceleration in the contracting portion of the throat. The figures do not show the effect of the contracting portion of the nozzle too well because the modes have a number of nodes and antinodes in this section, resulting from a "horn effect", shown in Figure 5.13.

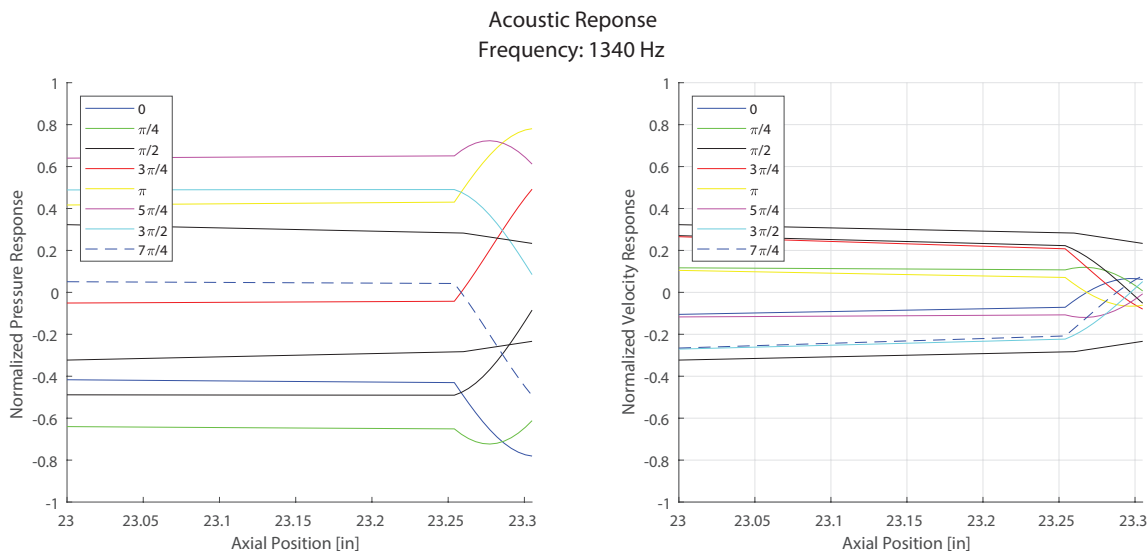


Figure 5.13.: Zoomed in response of the fundamental acoustic mode shape, predicted by 1D model of HAMSTER, in the contracting portion of the nozzle.

Depending on the frequency the effective acoustic length of the chamber can also change. What is important though, is that for all frequencies between these two possible modes there exists a pressure antinode near the head end of the chamber and a corresponding velocity node. Interestingly, the typical expected mode shape in the chamber was a half-wave, but it appears that with not much change in the

response frequency, the chamber can either adopt a half-wave or full-wave mode shape. This is made possible by two things: the frequency dependent impedance at the dump plane and the Mach numbers in the oxidizer post and chamber. The antinodes and nodes for the mode shape only need to shift slightly spatially to accommodate a change between the two mode shapes. This suggests that if the combustion were to couple with the acoustic modes, then depending on the nature and characteristics of the combustion, any favorable acoustic mode shape within range could be driven. Throttling or marginal changes to the geometry would just promote resonance of another, but similar acoustic mode.

From the data collected by the high frequency pressure transducers in the experiment the acoustic mode shapes could be compared to the theory. The mode shape were generated by taking the CPSD of the experimental data, extracting the relative phase, using the dump plane measurement as a datum, and under the assumption of a sinusoidal mode, an artificial phase was used to optimize the fit between the theoretical and experimental responses.

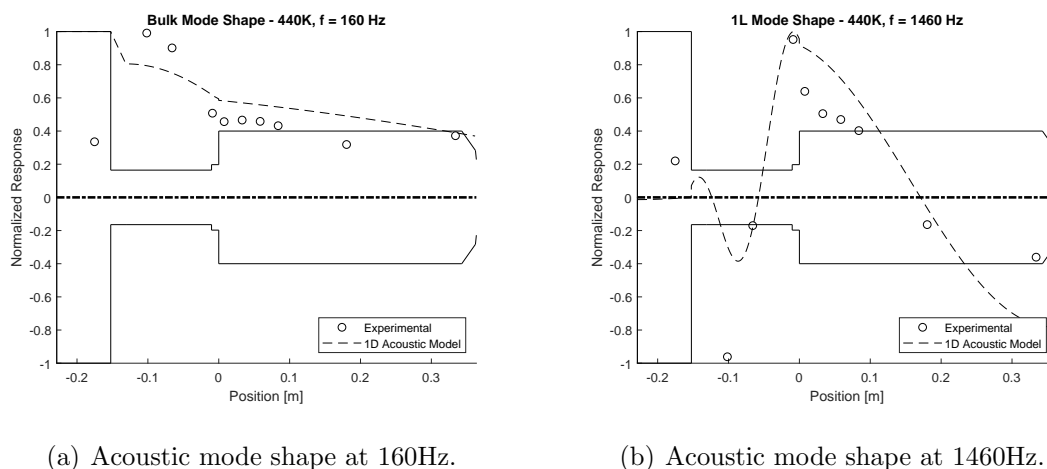
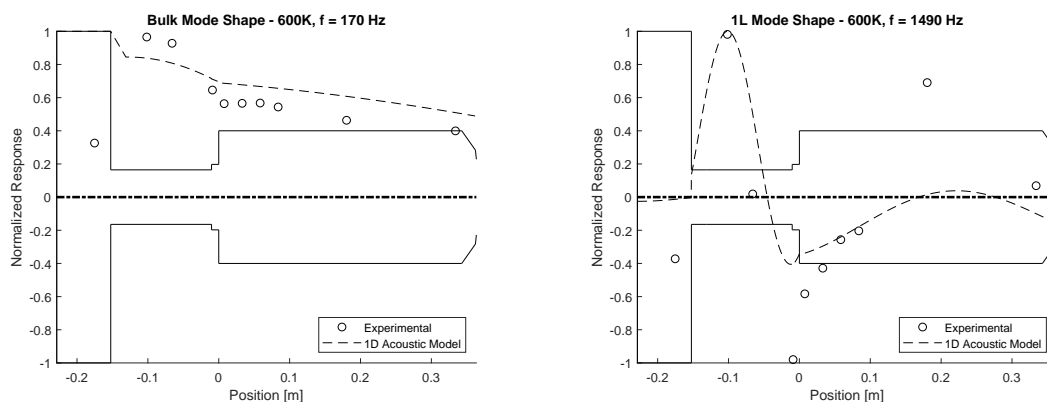


Figure 5.14.: Acoustic mode shape comparison between the experiment and theoretical prediction for an oxidizer temperature of 440K.

Because of the high Mach number in the chamber, the high frequency acoustic modes produced are not typically expected at the higher oxidizer temperatures. For

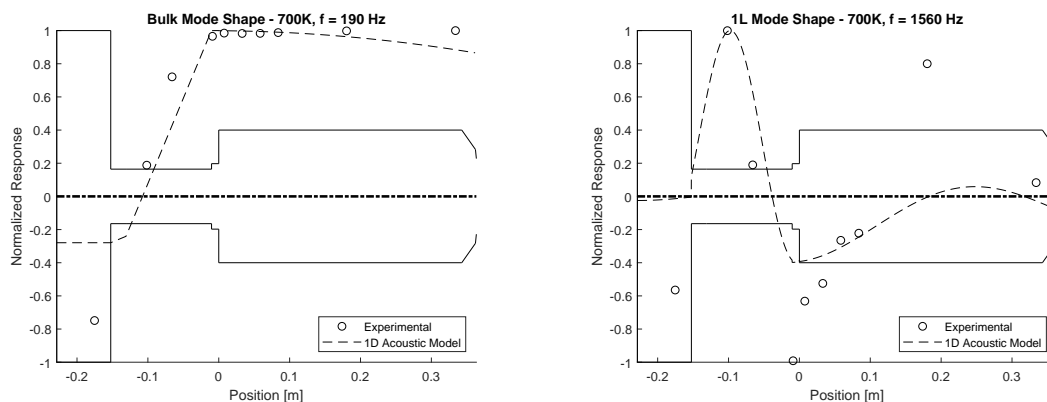
the 600 and 700K cases the high frequency acoustic mode shape appears to be closer to full-wave, but for the 440K case the mode shape appears to be a half wave. It is also interesting to note that the recess location, rather than the chamber head end, generally appears to be the system pressure antinode in all cases.



(a) Acoustic mode shape at 170Hz.

(b) Acoustic mode shape at 1490Hz.

Figure 5.15.: Acoustic mode shape comparison between the experiment and theoretical prediction for an oxidizer temperature of 600K.



(a) Acoustic mode shape at 190Hz.

(b) Acoustic mode shape at 1560Hz.

Figure 5.16.: Acoustic mode shape comparison between the experiment and theoretical prediction for an oxidizer temperature of 700K.

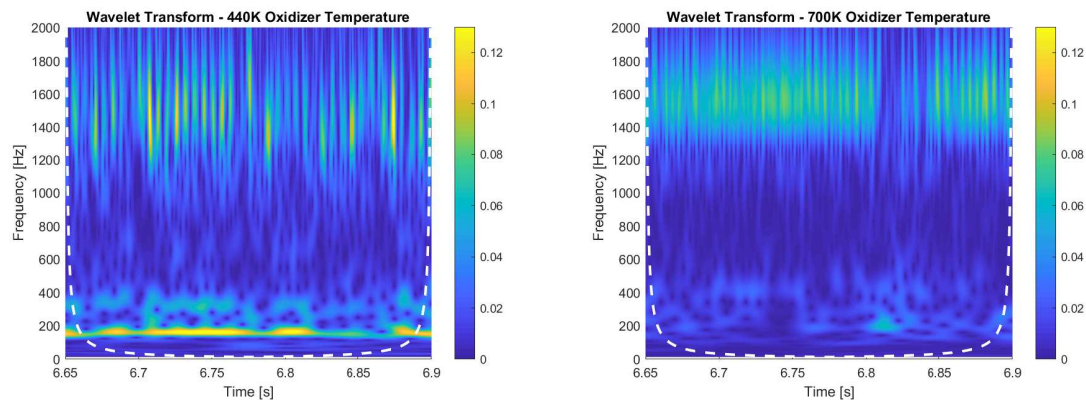
5.2.2 Intermittency and Modulation

With the inability of the 1D acoustic model to predict some of the modes, especially in the cases of high oxidizer temperatures, further analysis is needed. Therefore more emphasis is to be put on the case of high oxidizer temperature (700K) where there appears to be a strong thermoacoustic coupling. Further examination of the raw data of the 700K oxidizer temperature (Figure 5.1) case reveals a number of things:

- A limit cycle occurs with a period consistent with dominant high frequency mode.
- The amplitude and waveform of the limit cycle varies periodically.
- Intermittent or aperiodic deviations from the limit cycle occur and the running statistics change accordingly.

To closely evaluate the contrasting behavior in the raw data, wavelet transforms of the data at the head end of the chamber for the 440K and 700K cases were performed, shown in Figure 5.17. The amplitude scales of each sub-figure are directly comparable. It is clear that the amplitudes in the 440K case are not consistent in time, but when the system is experiencing large amplitudes they are almost always larger than that experienced in the 700K case. Comparing the raw data in Figure 5.1 to the corresponding wavelet transform reveals that the high frequency mode amplitude is modulated in sync with the low frequency mode period; the waveform becomes more regular in shape (akin to a limit cycle) during the high amplitude phase, and incoherent at the low amplitude phase.

On closer inspection of the wavelet transform of the data from the 700K case there appears to be a period, starting at 6.81s, whereby the high frequency limit cycle is broken and the system response adopts a dominant low frequency mode. After a short period the low frequency response becomes less coherent and the high frequency mode starts becoming more coherent, with a growth in amplitude. A zoomed in representation of the raw data from 6.8 to 6.88s is shown in Figure 5.18. Looking at the zoomed



(a) Wavelet transform at an oxidizer temperature of 440K. (b) Wavelet transform at an oxidizer temperature of 700K.

Figure 5.17.: Wavelet transform of data from head end of chamber. The white dotted lines represent the cone of influence; outside of which the edge effects of the wavelet become significant.

in 700K data, especially at the time interval of 6.81-6.825s, shows how the waveform changes from a regular step-fronted wave to a noisy, longer period oscillation, and back again. Not only does the waveform change, but the mean pressure during this transition changes nearly instantaneously with the change in response characteristics. Such a fast change in mean pressure cannot be attributed to thermal drift in the sensor readings. Additionally, the low frequency pressure transducer shows a similar transition in behavior: the mean value and the waveform changes during the transition period. The deviation in mean pressure is approximately 6%, from the mean pressure during the low frequency mode.

To further analyze this deviation in behavior during the 700K oxidizer temperature test a Hilbert transform was performed over the bandwidth (filtered using a band pass filter, frequency range of 1100-2000Hz) associated with the changing high frequency mode. Figure 5.19 shows the instantaneous change in the longitudinal mode frequency in time. In the region denoted by the dashed lines the instantaneous frequency calculation breaks down because the system response is not coherent at

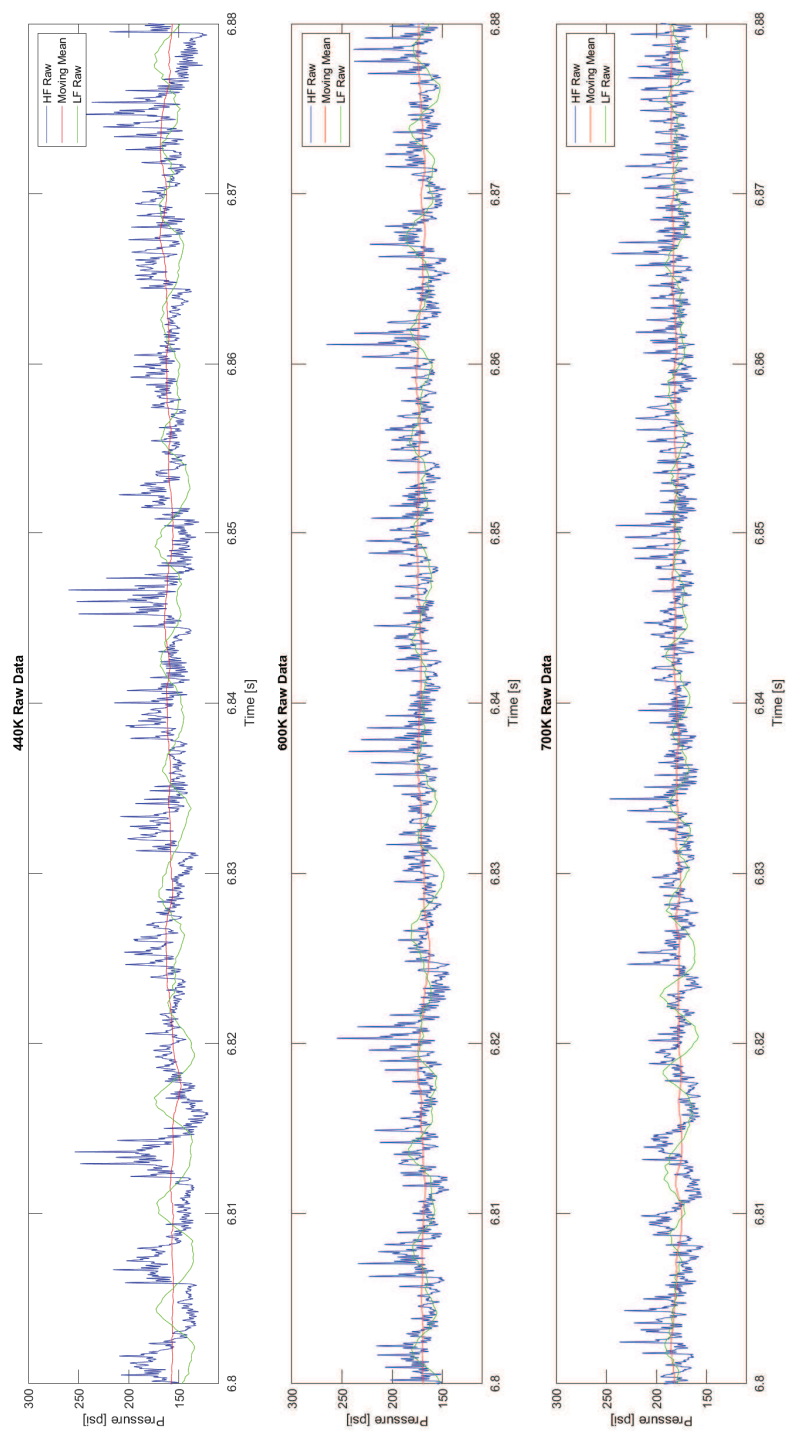


Figure 5.18.: Raw pressure data acquired at the head end of the chamber, 0.300” downstream of the dump plane. Zoomed in plot of Figure 5.1 on an interval of 80 *ms*.

those frequencies during that period. During the extracted time series a periodic fluctuation in the high frequency mode is observed.

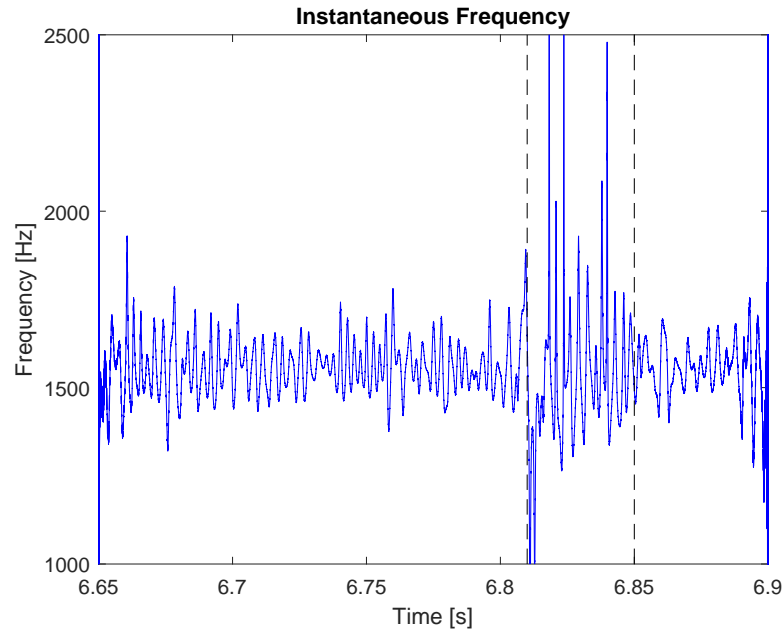


Figure 5.19.: Instantaneous changes in the dominant high frequency mode for the case with an oxidizer temperature of 700K.

From the analysis it appears that high frequency and low frequency modes are interdependent, especially at the higher oxidizer temperatures. To confirm this a bispectrum analysis was performed on the 700K oxidizer temperature case. Figure 5.20 shows the nonlinear interaction and the modes resulting from modulation. The information generated in the plot is symmetric about unit slope; the information in the lower triangle represents all the modal interaction. Any coherence off of the unit slope represents a modulation between the frequencies corresponding to each axis. Figure 5.20 shows modulated frequencies between the dominant high frequency mode at 1560Hz and frequencies at 1140, 1260, 1370 and 1750Hz. The bispectrum analysis also shows the dependence of the fundamental mode and its harmonic at 3120Hz. More interestingly though there is clear relationship between the low frequency mode at 190Hz and the high frequency mode at 1560Hz.

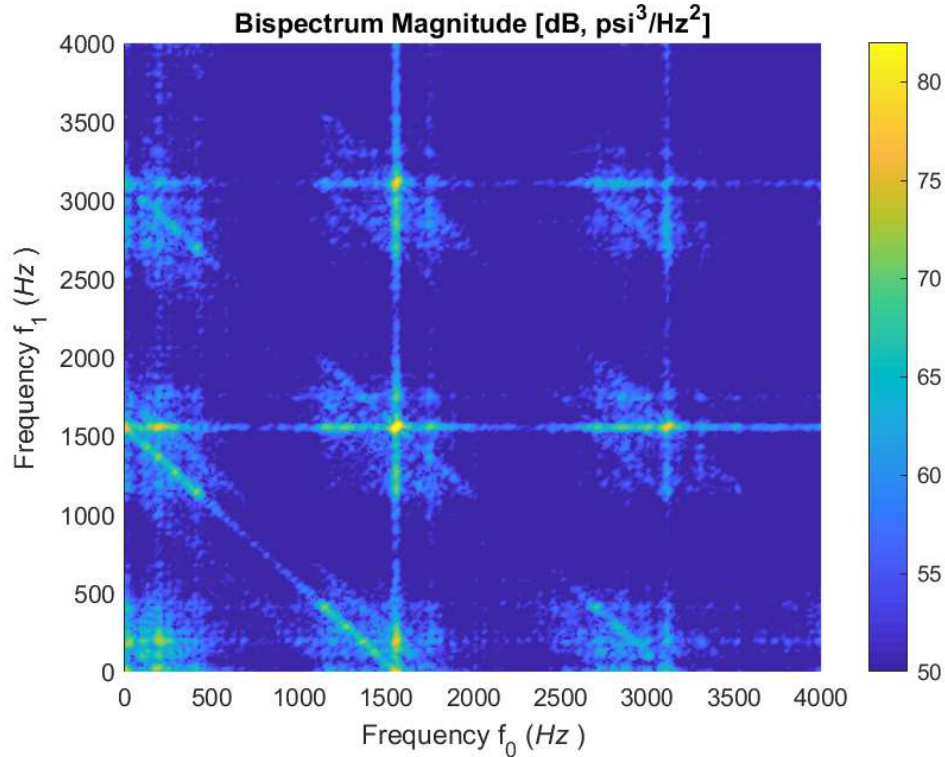


Figure 5.20.: Bispectrum analysis for the case with an oxidizer temperature of 700K.

In short, there are a few key characteristics which can be summarized based on the analysis regarding intermittency and modulation. In each case there are two main modes, and depending on the oxidizer temperature, one mode may dominate. In the event that both modes have a large enough amplitude, there is a nonlinear interaction between them, producing artificial modulation frequencies. The modulated frequencies take on frequency values which are based on the carrier frequency, in this case the high frequency resonant mode, and added or subtracted by the frequency of the modulating mode, in this case the low frequency mode. Typically, linear modulation produces symmetric sets of side lobe frequencies, both in amplitude and frequency, however it has been observed that the side lobes in the pertinent PSDs are usually not symmetric in amplitude, or one of lobes is "missing". This has been characterized as a type of nonlinear combined amplitude-frequency modulation [95].

Although, one mode tends to dominate in each oxidizer temperature case, both modes always feature, and the system momentarily and intermittently may alternate between each mode. There appears to be no case where the system becomes chaotic (stable) with the variation of oxidizer temperature, but there appears to be an optimal case where the amplitudes of both modes are minimized; this case is estimated to be at approximately 625K.

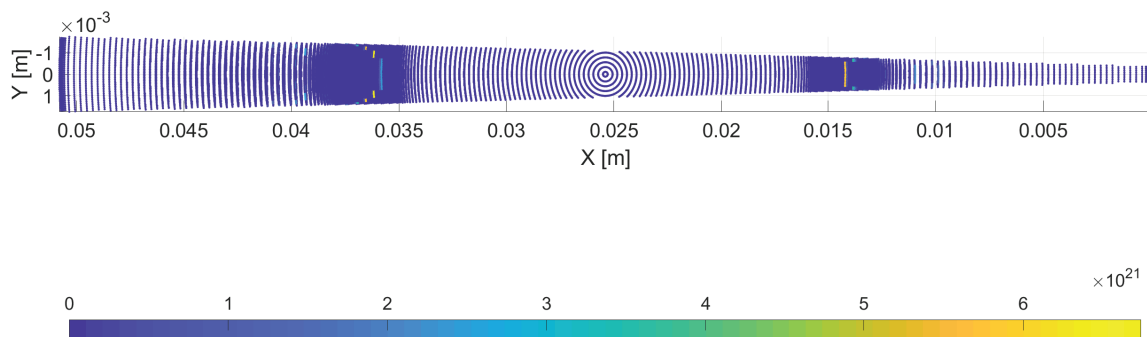
At this point it is still not clear what drives the transition between the low and high frequency modes. It should be pointed out that that both modes are acoustic in nature, despite the bulk fluid response of the low frequency mode. This suggests that both modes are inherently a type of thermoacoustic coupling. The chugging aspect is dealt with a little later on, at this juncture the mechanism which drives the thermoacoustic transition is of importance. The chemiluminescence based measurements are used to study the combustion relate modes; these measurements will help to narrow down which mechanism could be responsible, or at least eliminate contributing candidates.

5.2.3 Thermoacoustic and Hydrodynamic Investigation

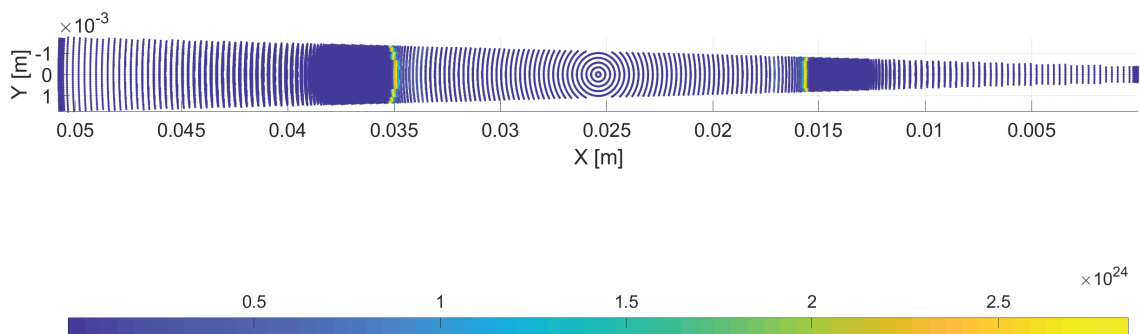
The photomultiplier tube (PMT) measurement technique directly measures chemiluminescent emissions produced by the combustion. Because the response time of the PMTs the chemiluminescence can be measured at incredible rates ($> 100kHz$), which allows temporal resolution of even some of the fastest combustion processes. The limitation of fiber optically coupled PMTs though is that the measurement is line-of-sight integrated and therefore has limited spatial resolution. For this reason, as discussed previously, the probe volume was designed to be restricted spatially as much as possible without sacrificing too much incident light.

There was also an assumption made about the effect of self-absorption on the emitted light; the assumption made was that the combustion gases in the chamber are nearly perfectly transparent, and therefore self-absorption was negligible for all

emitting species. To confirm this assumption, the aid of the simulation results were necessary. Figure 5.21 show the maximum expected number densities of OH and CH radicals within the probe volume. Figure 5.21 also clearly shows the spatial relationship of the number density distribution for each species.



(a) Number density distribution of CH within the probe volume during combustion.



(b) Number density distribution of OH within the probe volume during combustion.

Figure 5.21.: Number density (m^{-3}) distributions of potential absorbing species within HAMSTER during combustion, as predicted by the prior simulations.

From the charts depicting transmissivity as a function of number density and optical path length (Figure 5.22) it is estimated that for the CH^* emission band the chamber is optically transparent, while the average transmissivity for the OH^* emission band is approximately 0.5. This can be determined by estimating a conservative thickness of the reacting shear layer: $1 \times 10^{-4}m$; then with the maximum number density for OH ($2.8 \times 10^{24}m^{-3}$) and for CH ($6.7 \times 10^{21}m^{-3}$), the transmissivity can

be estimated from the charts. From this result the chemiluminescent emissions from CH^* can be considered a valid parameter to analyze confidently, while more work, such as absorption spectroscopy, may be needed to confirm the optical thickness for emissions of OH^* . Therefore, the CH^* emission data will only be used.

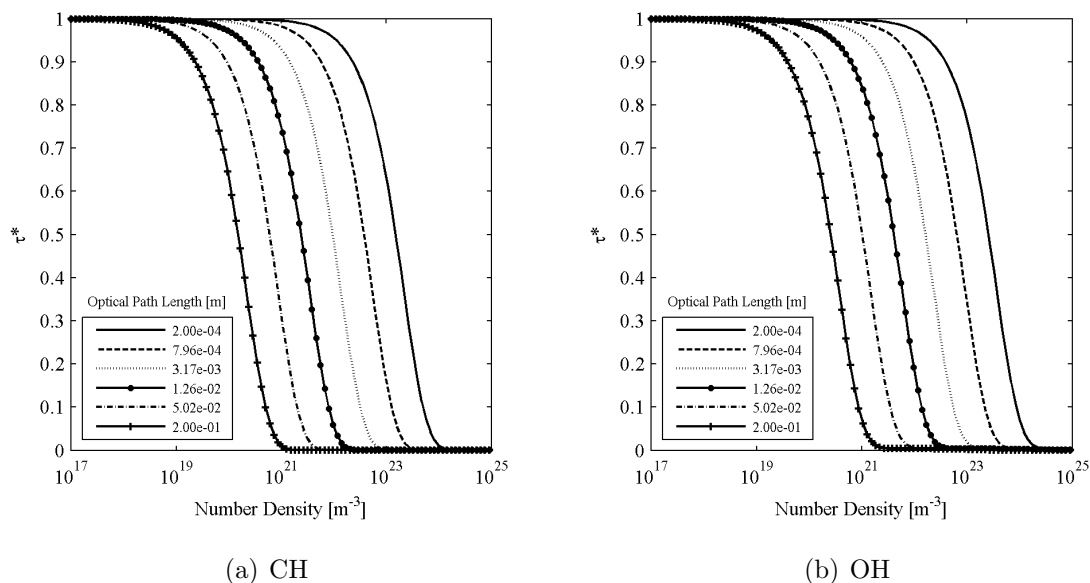
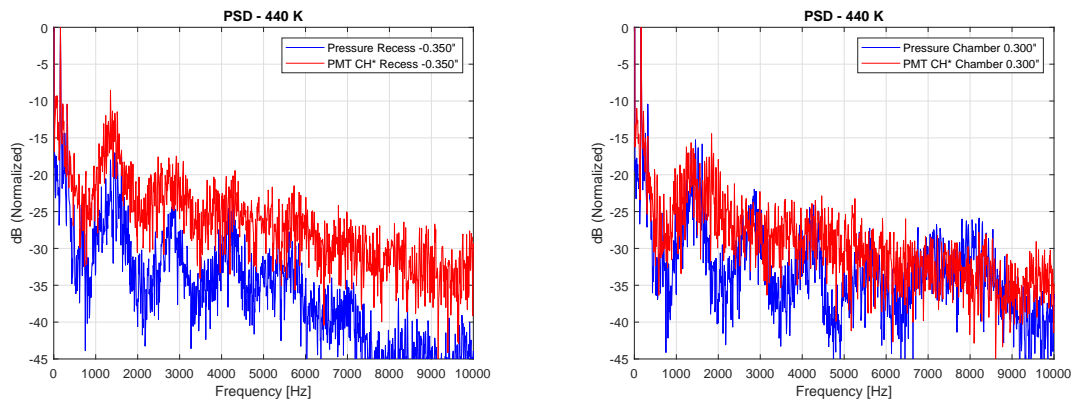


Figure 5.22.: Transmissivity of CH and OH as a function of number density for varying optical path lengths [66].

For each case scrutinized previously, an evaluation of the dominant features produced by the chemiluminescence measurements was done. These results were then compared to the pressure measurements taken at the same exact axial location. Figures 5.23, 5.24 and 5.25 show the PSDs for the 440K, 600K and 700K oxidizer temperature cases, located in the injector recess and at the head end of the chamber, 0.300” downstream of the dump plane. Figures 5.23, 5.24 and 5.25 are all representations of the data from diametric cutting probe volumes.

Figure 5.23 shows that the chemiluminescence signals in both the injector recess and chamber tend to be incoherent at frequencies of +3000Hz. There seems to be a strong correlation between the CH^* and pressure signals for the low frequency



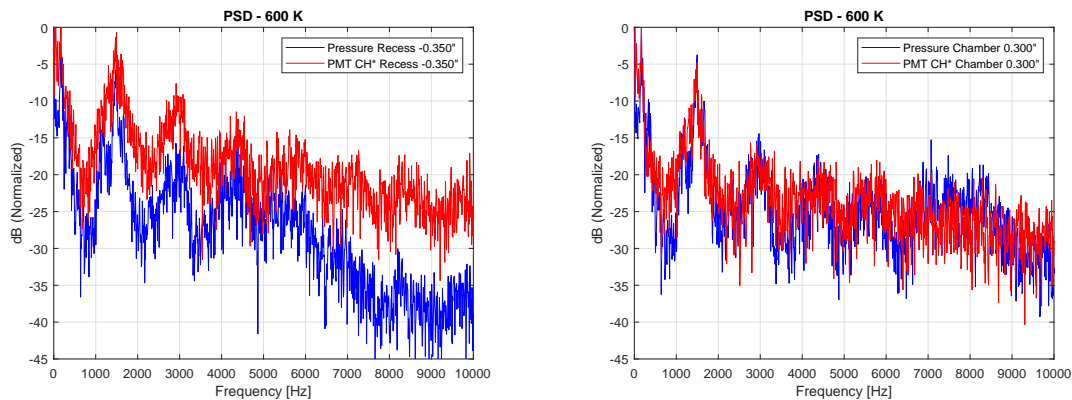
(a) PSD comparison between CH^* chemiluminescence and pressure in the injector recess.

(b) PSD comparison between CH^* chemiluminescence and pressure at the head end of the chamber, 0.300'' downstream of the dump plane.

Figure 5.23.: PSD comparison between CH^* PMT and pressure data for an oxidizer temperature of 440K.

mode, which further supports a combustion-pressure interaction at that frequency. Additionally, the second low frequency mode also appears in the chemiluminescence PSDs, which suggests that the mode itself is real and not an artifact of the signal decomposition. In the injector recess the first longitudinal acoustic mode and the resonant high frequency mode of the chemiluminescence signal seem to have a similar frequency. This evidence would point to a combustion driven acoustic response, however, when comparing similar modes represented in the chamber signals it appears that the chemiluminescence modes do not coincide with the chamber acoustic modes. Furthermore, there appears to be two CH^* high frequency modes in the chamber around the first longitudinal acoustic mode frequency.

As the oxidizer temperature is increased the chemiluminescence oscillations become more coherent with the pressure oscillation, especially in the chamber, as shown in Figure 5.24. Higher order CH^* fluctuation modes become prominent and mimic the pressure up to frequencies of 5kHz. The chemiluminescence tends to not distinctly follow the secondary frequencies (known to be acoustic) at 1150Hz, but predominantly



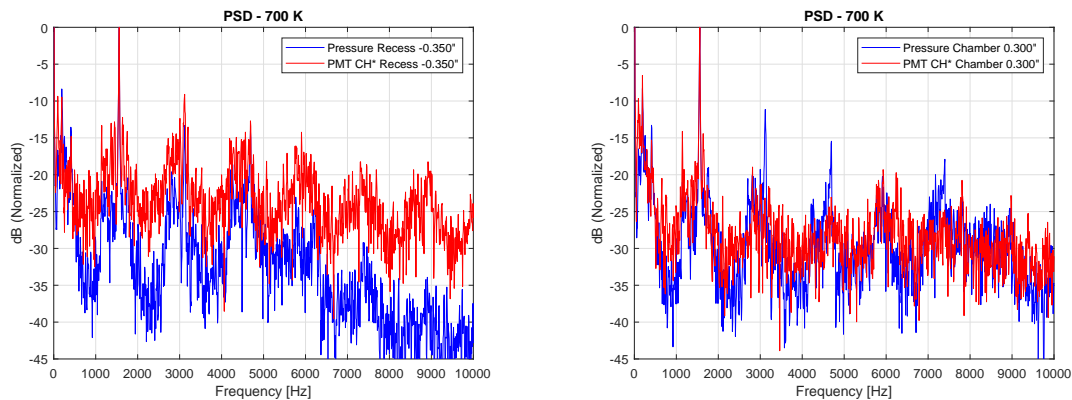
(a) PSD comparison between CH^* chemiluminescence and pressure in the injector recess.

(b) PSD comparison between CH^* chemiluminescence and pressure at the head end of the chamber, 0.300'' downstream of the dump plane.

Figure 5.24.: PSD comparison between CH^* PMT and pressure data for an oxidizer temperature of 600K.

follow only the low frequency chugging and the driven high frequency fundamental modes at 170Hz and 1490Hz respectively. In the injector recess, there appears to be similar coherence for both the pressure and chemiluminescence around 8.1kHz, but it is not definite.

At the peak oxidizer temperature scrutinized, the comparison between the chemiluminescence and the pressure is quite remarkable. As in the case for an oxidizer temperature of 600K, the chemiluminescence signals seems to fluctuate at a number of the same frequencies as the pressure (Figure 5.26). The CH^* correlates well with the low frequency modes and the high frequency acoustic modes in the injector, but the signal does not compare well with the suspected acoustic harmonics in the chamber. This may suggest that the pressure harmonics may be artificial, an artifact of the PSD decomposition. There is good agreement between some of the high frequencies, but the CH^* signal shows a couple frequencies which do not coincide with the pressure response in the chamber. This could be the result of a localized formation near the shear layer which promotes combustion, which the pressure transducer can-



(a) PSD comparison between CH^* chemiluminescence and pressure in the injector recess.

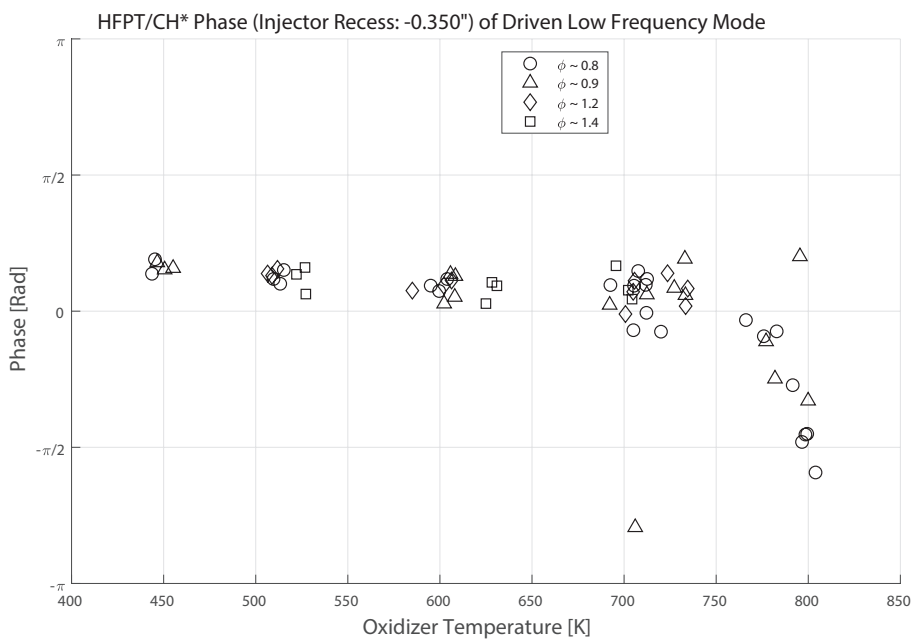
(b) PSD comparison between CH^* chemiluminescence and pressure at the head end of the chamber, 0.300" downstream of the dump plane.

Figure 5.25.: PSD comparison between CH^* PMT and pressure data for an oxidizer temperature of 700K.

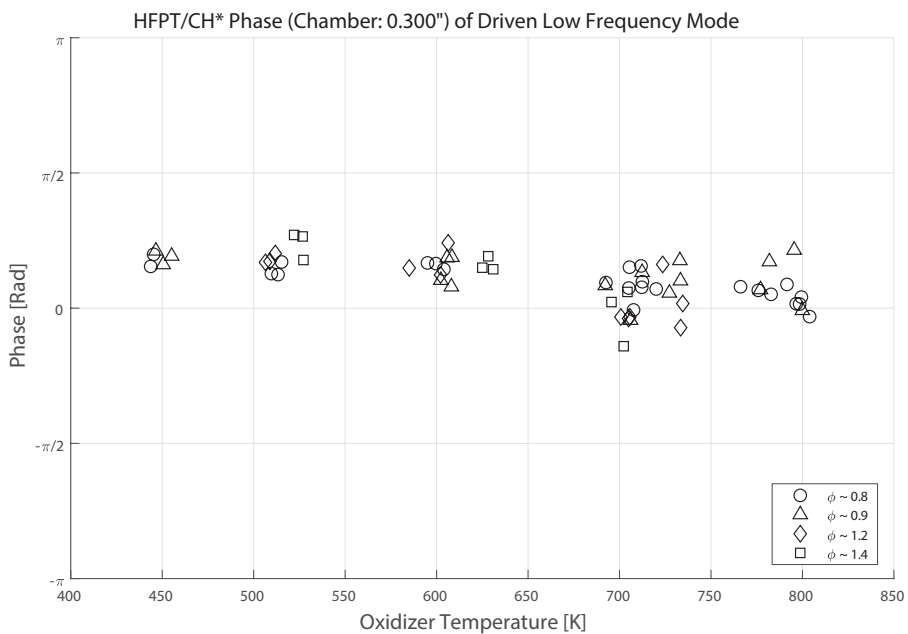
not measure. However, all of these features are circumstantial at best and require a technique that is able to correlate the pressure and chemiluminescence radiation.

Figures 5.26 and 5.27 are representative of the phase difference between the acoustic modes and the CH^* signal in the injector recess and head end of the chamber, 0.300" downstream of the dump plane, for a range of conditions tested with the nominal geometry. For the same representative information, but for all test cases, the plots are found in Appendix C. The plots were generated by applying a CPSD between the signals at the same location and isolating the phase for the respective dominant modes, in this case the low frequency thermoacoustic chug mode and the high frequency thermoacoustic fundamental mode.

In general, for both modes, the phase between the pressure and CH^* signals (correlated in that order) always decreases with increasing oxidizer temperature. For both the injector recess and chamber locations the phase relationship between the pressure and CH^* signals, for the low frequency mode (Figure 5.26), seem to mimic one another; apart from where the chugging becomes decorrelated at high oxidizer

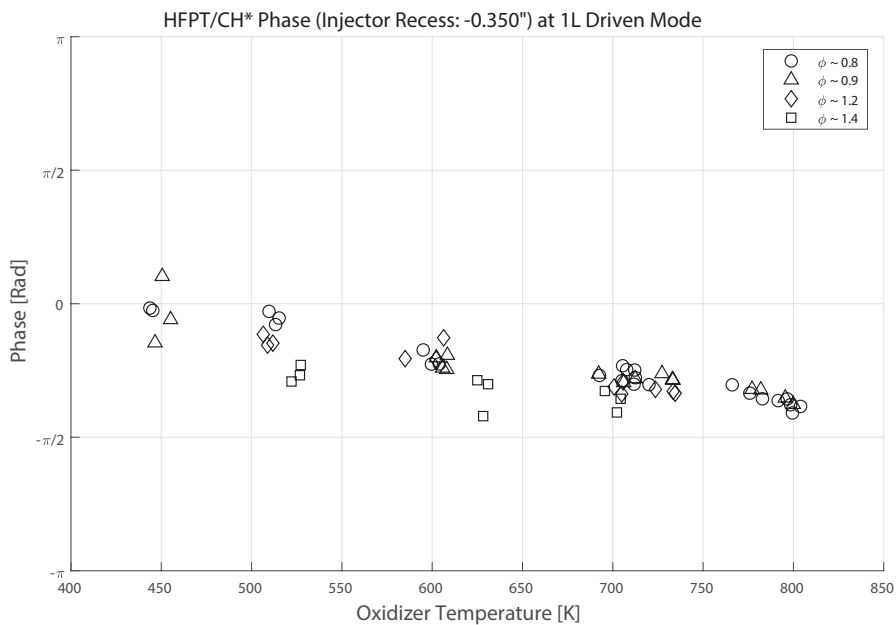


(a) Recess, -0.350"

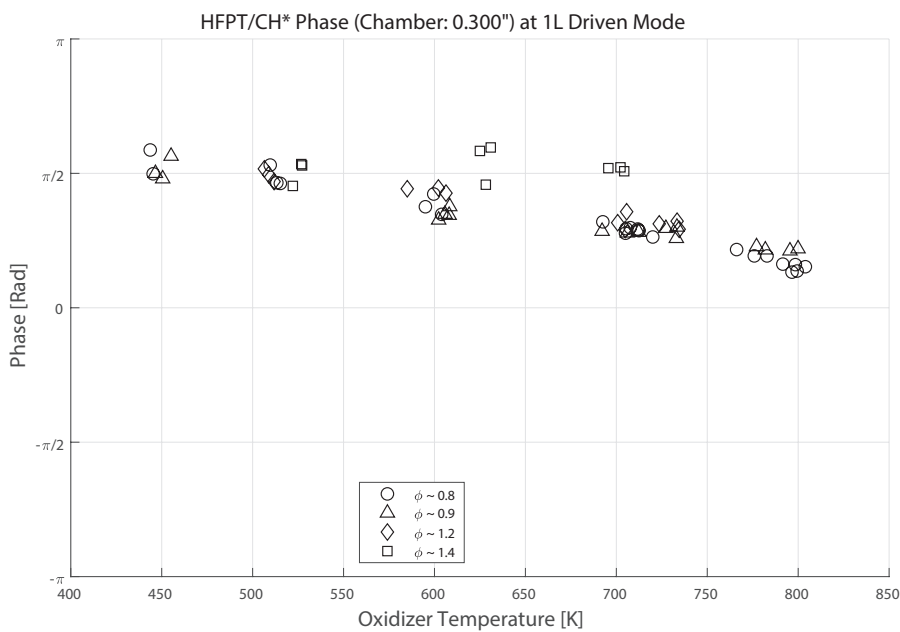


(b) Chamber, 0.300"

Figure 5.26.: Phase relationship between the CH* chemiluminescence and pressure signals for the thermoacoustic chug mode, as a function of oxidizer temperature.



(a) Recess, -0.350"



(b) Chamber, 0.300"

Figure 5.27.: Phase relationship between the CH* chemiluminescence and pressure signals for the thermoacoustic 1L mode, as a function of oxidizer temperature.

temperatures and the phase change with respect to oxidizer temperature has a gradient shift. At oxidizer temperatures above 730K the chugging response of the system is all but completely diminished. It could be hypothesized that at around this critical oxidizer temperature the system can be considered to only have a resonance with the high frequency acoustic modes, or "organ pipe modes". The marked change in the gradient of the phase change with respect to oxidizer temperature in the injector recess could be a clear indication of the decoupling of the thermoacoustic chugging mode; more specifically, a decoupling the low frequency response in the chamber and the injection system as a whole.

With respect to the high frequency mode (Figure 5.27) the general trend remains the same, however, in the recess the CH^* signal leads the pressure signal, while in the chamber it lags the pressure signal. Since this mode is the primary thermoacoustic mode, at higher frequencies, the phase relationship in space would suggest that the pressure is not the primary driver of the combustion modes. On the assumption that there is an optimal phase between the acoustics and combustion based on combustion delay time (resulting from the $n - \tau$ model hypothesis), it can be inferred that as the phase relationship steadily changes with oxidizer temperature the system should thermoacoustically resonate at some oxidizer temperature. Added complication comes from the fact that as the oxidizer temperature changes the acoustic resonance of the injection system, and therefore the whole system in this case, changes as well. To test this hypothesis and the effect of oxidizer temperature on acoustic resonance a series of tests where the oxidizer temperature, equivalence ratio and oxidizer post length were all varied; the conclusions of which will be discussed in the Auxiliary Analysis section.

Additionally, the phase relationship in the highest equivalence ratio cases are seemingly invariant with oxidizer temperature. The cause is not strictly known; the oxidizer velocity is much lower in these cases and may not promote enough vortex formation for the oxidizer temperature to have an effect on chemical kinetic rates, in other words the combustion is extremely diffusion limited. This also provides evidence to directly contradict the $n - \tau$ model.

To analyze the higher frequency mechanics, which may shed light on the shear layer mechanics and modes of combustion, typical CPSDs are not sufficient. The modes at higher frequencies usually do not have high amounts of energy, but can contribute directly to mechanics of combustion. For example: the vortex production in the shear layer enhances mixing and therefore combustion; the fluctuation of combustion results in pressure and radiation oscillations consistent with the frequencies associated with vortex formation. Calculating the magnitude squared coherence highlights which modes are strictly correlated between the pressure and chemiluminescence, while ignoring the inherent amplitudes associated with the energy of the modes. This method allows for the identification of the dominant coupled mechanics in the system.

Figures 5.28 to 5.33 show the coherence plots of pressure and CH^* signals. Typically, the magnitude squared coherence of less than 70% is deemed incoherent, while above 80% is usually a coherent process. The dominant acoustic modes are usually above a 90% coherence; these modes will simply be used for visual comparison, the focus is now on the higher frequency modes.

Figure 5.28 shows that there is a high frequency mode with high coherence at around 10kHz in the injector recess, while there appears to be two modes at approximately 7 and 8.5kHz that could be significant, but unconfirmed. In this location the fundamental acoustic mode is still coherent, but is less coherent than its harmonics. It appears that there is some disconnect happening between the pressure and CH^* signals at this frequency, while the higher order harmonics are free to resonate in the oxidizer post unimpeded. In Figure 5.29 the higher order acoustic harmonics are much less coherent, except for a mode at 6kHz. The high frequency mode at 10kHz does not feature in the chamber signals, however there is a mode at approximately 8kHz which may be significant.

With an increase in oxidizer temperature the fundamental acoustic mode becomes more coherent as expected in Figure 5.30. In the injector recess the high frequency mode around 10kHz is still prominent with some adjacent modes at 8.5 and 11kHz showing coherence. Again, in the chamber Figure 5.31 shows little coherence of the

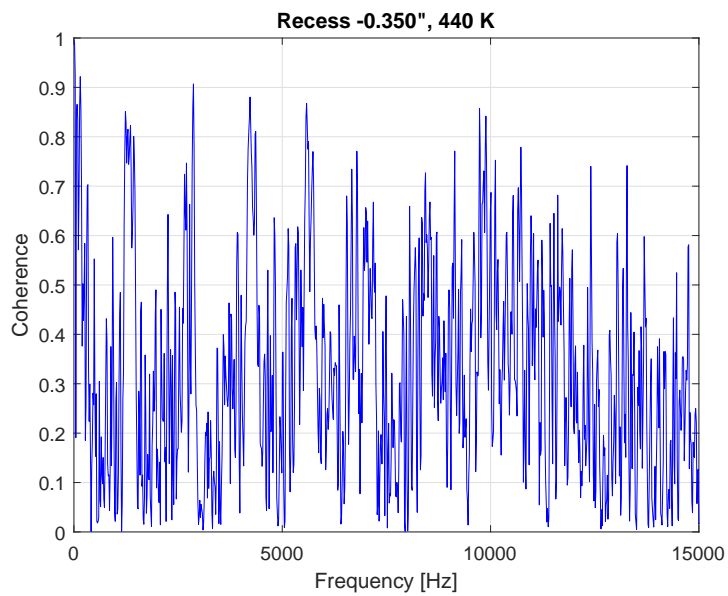


Figure 5.28.: Magnitude squared coherence between the CH^* and pressure measurements in the recess, for an oxidizer temperature of 440K.

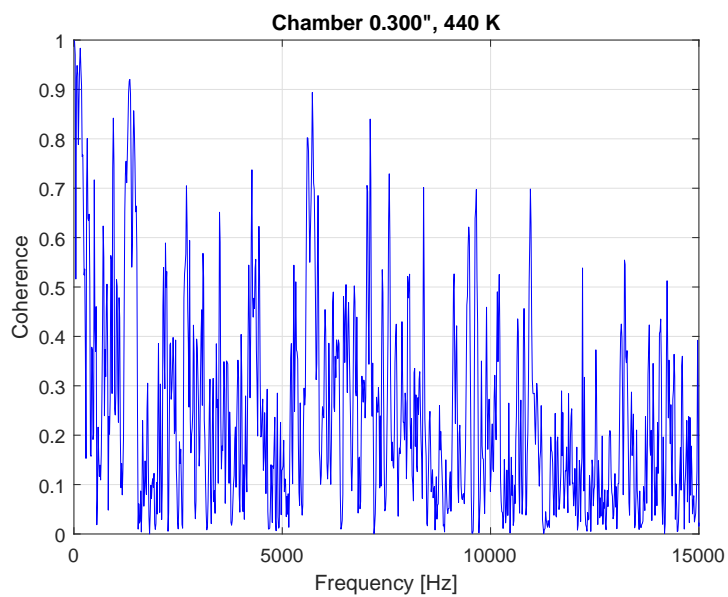


Figure 5.29.: Magnitude squared coherence between the CH^* and pressure measurements at the head end of the chamber, for an oxidizer temperature of 440K.

higher frequency modes, apart from a mode at around 6kHz. It is interesting to note at this point that in both the 440K and 600K cases the acoustic harmonics in the chamber do not correlate well with the CH^* signal.

The acoustic modes in the injector recess correlate well with the CH^* signal in Figure 5.32, apart from the low frequency mode. There are two definitive modes at 8 and 10.5kHz. The coherence plot of the 700K case (Figure 5.33) in the chamber resembles the other oxidizer temperature cases for the same location.

The higher frequency modes found to be significantly coherent are summarized in Figure 5.34. The high frequency modes trend linearly with oxidizer temperature, while the chamber high frequency modes do not seem to vary with oxidizer temperature. A mechanism which has been identified to produce similar frequency modes is the vortex shedding from the fuel collar resulting from the oxidizer flow. Using Equations 2.13 and 3.7 to calculate the Strouhal number and boundary layer thickness respectively, the vortex shedding frequency can be calculated as a function of oxidizer velocity, and therefore temperature.

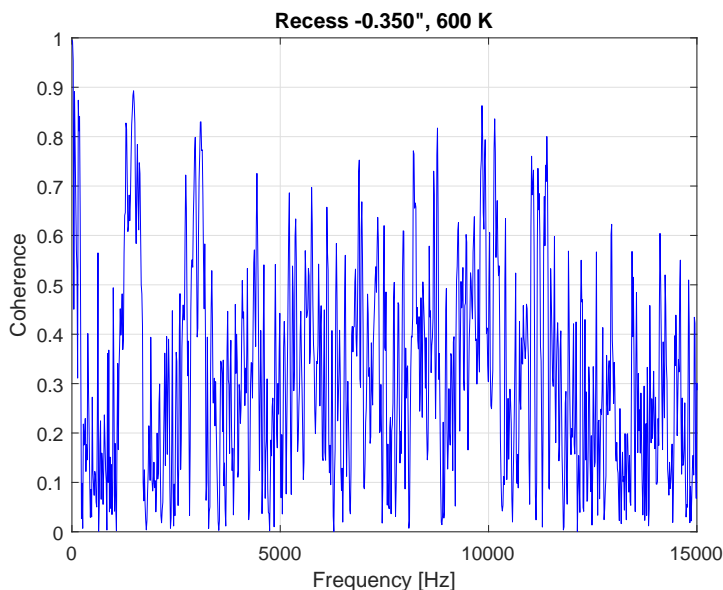


Figure 5.30.: Magnitude squared coherence between the CH^* and pressure measurements in the recess, for an oxidizer temperature of 600K.

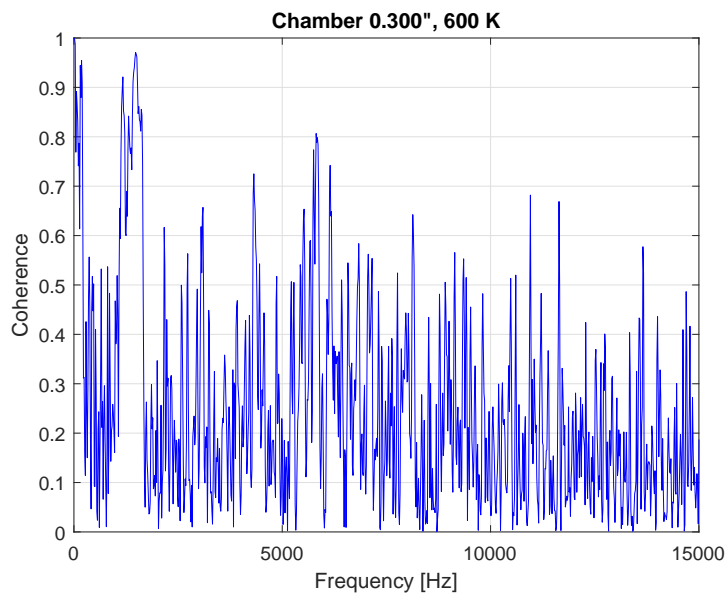


Figure 5.31.: Magnitude squared coherence between the CH* and pressure measurements at the head end of the chamber, for an oxidizer temperature of 600K.

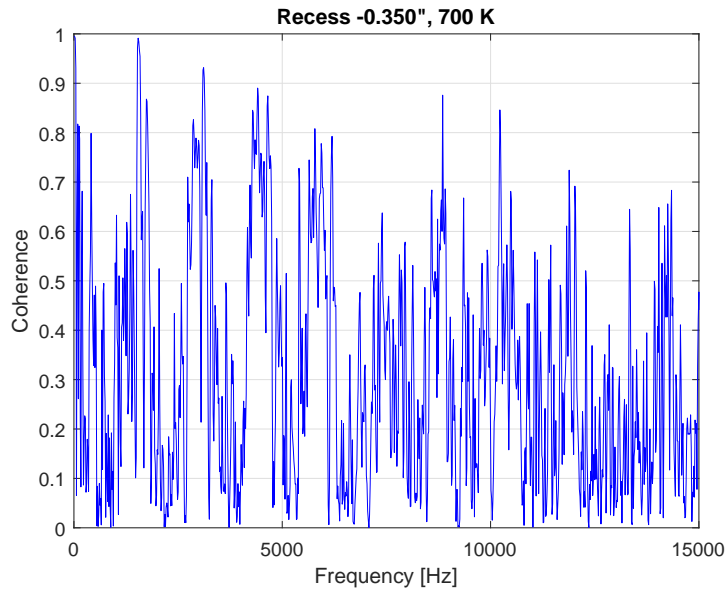


Figure 5.32.: Magnitude squared coherence between the CH* and pressure measurements in the recess, for an oxidizer temperature of 700K.

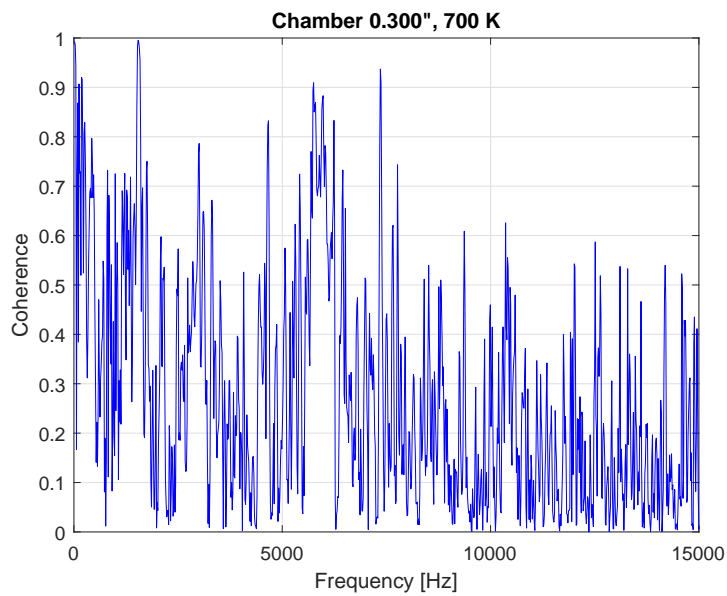


Figure 5.33.: Magnitude squared coherence between the CH* and pressure measurements at the head end of the chamber, for an oxidizer temperature of 700K.

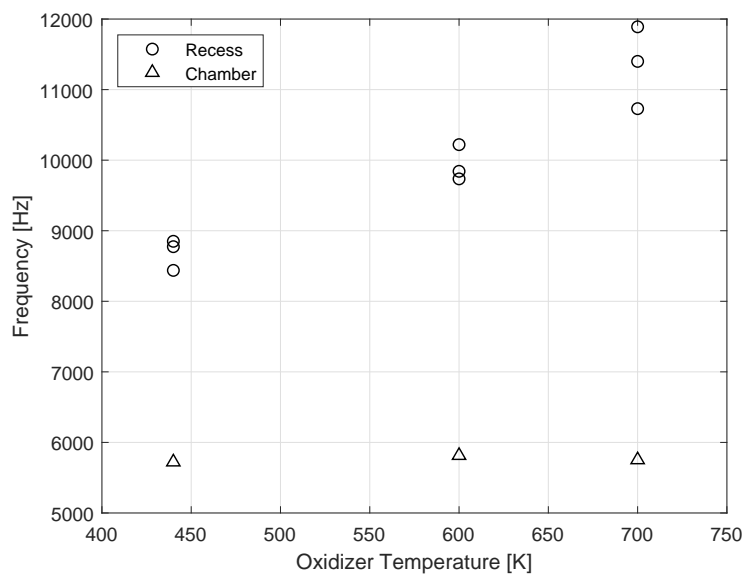


Figure 5.34.: Summary of higher frequency modes calculated by the magnitude squared coherence between the CH* and pressure measurements.

The vortex shedding frequency from the fuel collar was calculated using the conditions from the tests conducted with the nominal geometry. Figure 5.35 shows how the theoretical prediction of the vortex shedding from the fuel collar as a product of the oxidizer velocity compares to the coherence data collected. Although the prediction seems to fair well it is difficult to predict the boundary layer thickness and even the oxidizer velocity in some cases; thus, this analytical prediction tool may not always be accurate enough to determine key physics of interest. Furthermore, these modes predicted and captured in the injector recess do not seem to feature in the chamber at all. This suggests that these modes, which may indirectly contribute to the combustion modes through mixing enhancement, do not appear to be a primary mechanism with regard to the thermoacoustic coupling in the system.

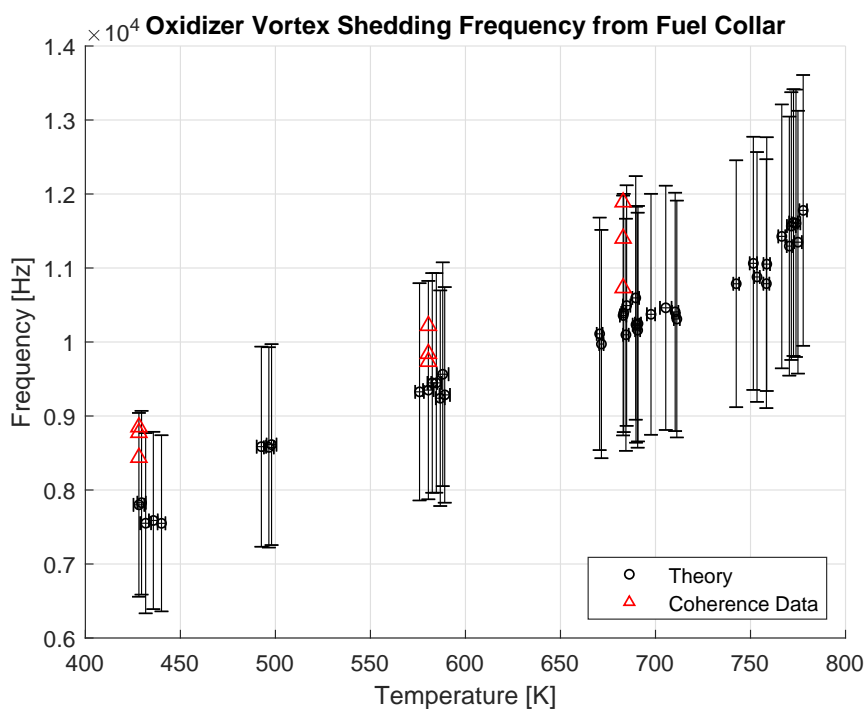


Figure 5.35.: Comparison of estimated vortex shedding frequency off of the fuel collar based on the oxidizer flow, and the high frequency magnitude squared coherence data summarized in Figure 5.34.

5.3 Auxiliary Analysis and Interesting Features

This section is primarily focused on the elimination of possible system properties, features and mechanics that could be responsible for the thermoacoustic coupling in HAMSTER. Some interesting properties and test cases are also presented to supplement the data already examined.

5.3.1 Chug and Buzz

Traditional chugging models have been utilized and proven to be quite accurate. Since HAMSTER presented a low frequency mode which responded somewhat like a chug it was logical to investigate such a feature to determine if the chug could be predicted. Dr. Matthew Casiano was of great assistance in facilitating the processes involved during a chugging phenomenon and provided theoretical models which he had improved upon in his research [4].

The models used to investigate the chugging mechanism are: Wenzel-Szuch; ROCCID-type using the assumptions of closed manifold, injector resistance, injector inertance, and manifold compliance; ROCCID-type with alternate boundary conditions: using the assumptions of opened manifold - injector resistance and injector inertance; SP194-full feed system inclusion; Crocco-based model (thermal): full feed system with incompressible injector, complete chamber integration, contemporary time lag (injection zone physics) and another Crocco-based model with a compressible injector.

All of these models are derived under premise that there exists an unstable point at where in a feed system or combustor, where there exists some sort of flow resistance or impedance due to either a sudden area, abrupt flow path or flow property change, a pressure differential will occur and diverge. To elaborate, for example: oxidizer flowing into the chamber might have slight perturbation, this then results in a slight mass fraction shift in the chamber altering the combustion performance, which, in turn, alters the pressure differential between the oxidizer manifold and chamber, which then further perturbs the oxidizer flow. This process can be exacerbated if the fuel

flow also responds to the changing dynamics in the combustion chamber. This process was nicely described by Summerfield [5]. Ultimately, this chugging mechanism, which can present itself in a combustion or feed system as a chug or pogo instability, is mostly based upon the principles of continuity and momentum.

Figures 5.36 to 5.38 show the predictions made by the various chugging models based on the conditions and geometry of HAMSTER. All cases predict mode gains at frequencies below 100Hz, where the frequency and gain appears to increase with oxidizer temperature. It is to be noted that these models fail to predict the chugging frequencies and response at the dominant chugging modes observed in HAMSTER.

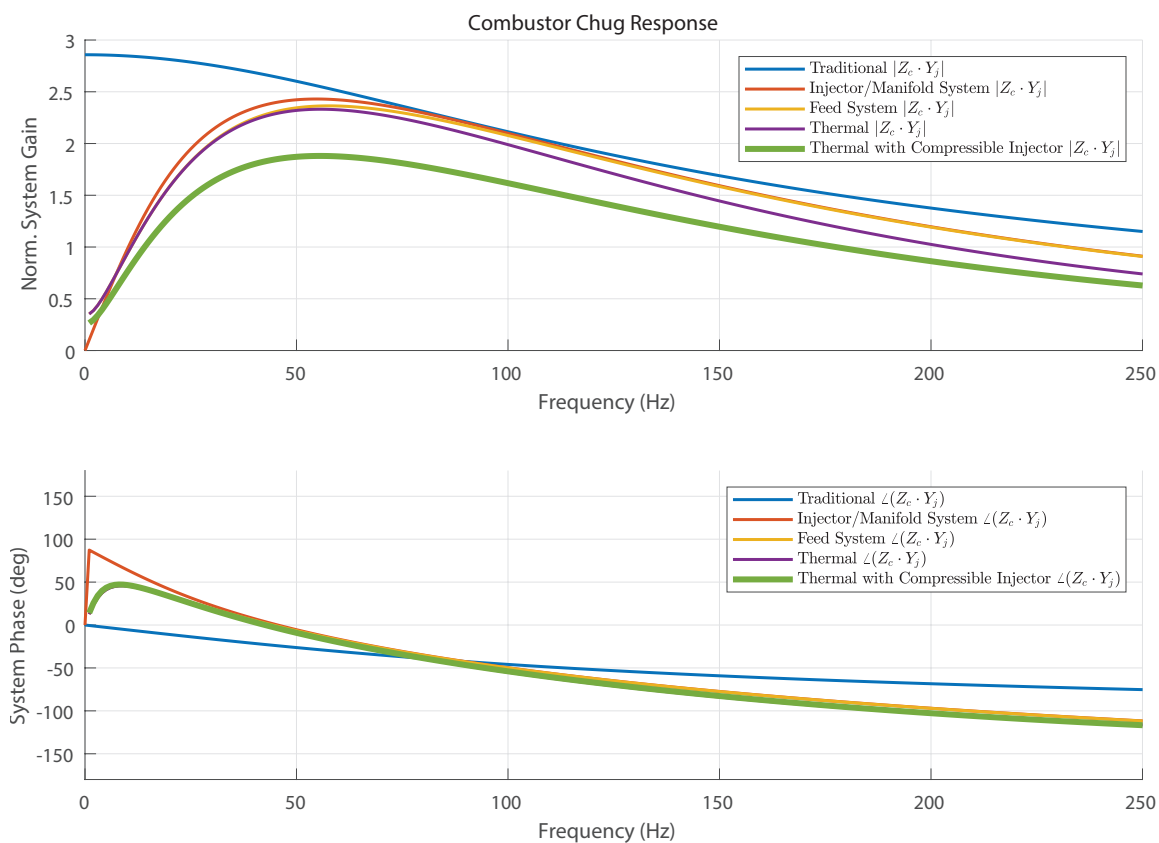


Figure 5.36.: Chug predictions using models stipulated in Casiano's thesis [4]; for the case with an oxidizer temperature of 440K.

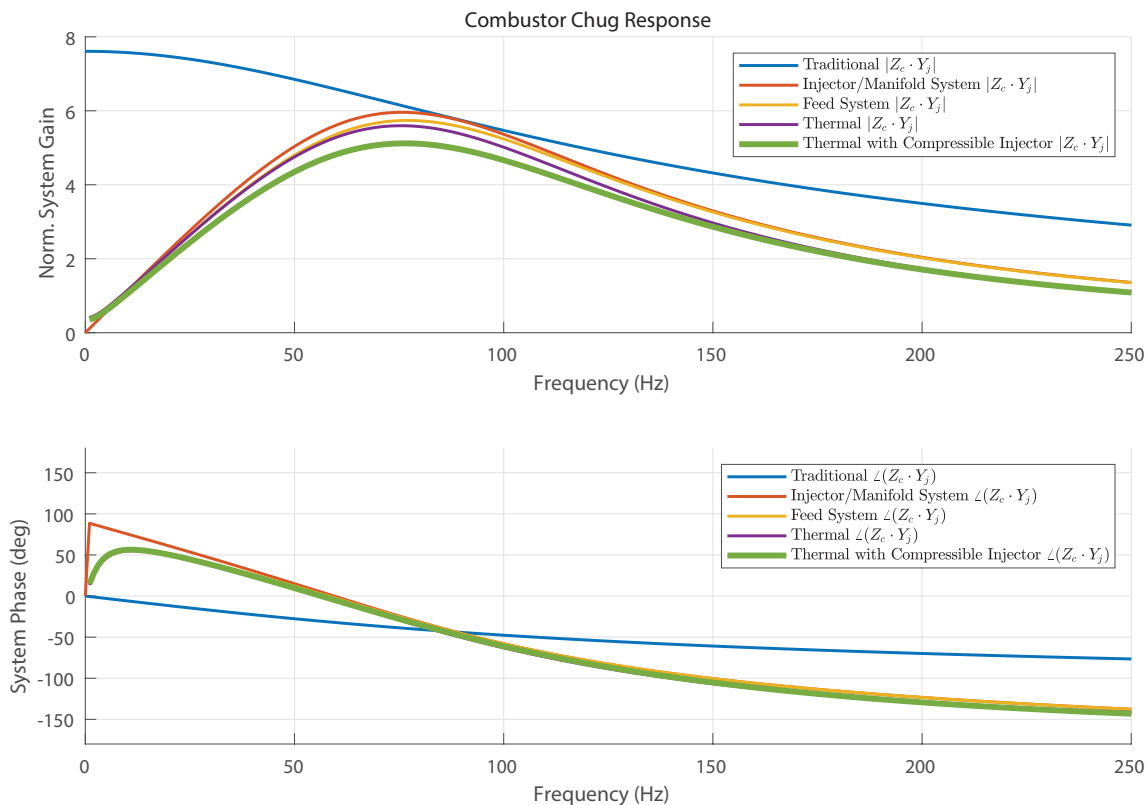


Figure 5.37.: Chug predictions using models stipulated in Casiano's thesis [4]; for the case with an oxidizer temperature of 600K.

To determine why these models failed to predict the chugging behavior a closer look at the experimental data at a low frequency range was taken. To get a coherent frequency map of the lowest frequency modes the time series examined was extended to include 0.4s of data. Figures 5.39 and 5.40 show the response in the oxidizer manifold and combustion chamber for the various cases of interest. Each experimental data location compares well with each other and shows some evidence of very low frequency modes occurring. Typically, at approximately the frequencies the models suggest, there is a frequency which shows some coherence, but relatively low amplitude. The frequency trends with the oxidizer temperature, in agreement with the models and the response increase from the 440K to the 600K case, but diminishes at the 700K case. The response bandwidth also decreases with increasing oxidizer

temperature, also in agreement with the models. Assuming the chugging models are accurately predicting the resonance frequency response then the mode in question are only under-predicted by a maximum of 10%. The trend in the gain with oxidizer temperature is not well predicted at higher oxidizer temperature though, and there also appear to be some extremely low frequency modes present. It is likely that these chugging modes are represented and predicted, but the modes are not dominant, almost negligible, but the evidence is circumstantial.

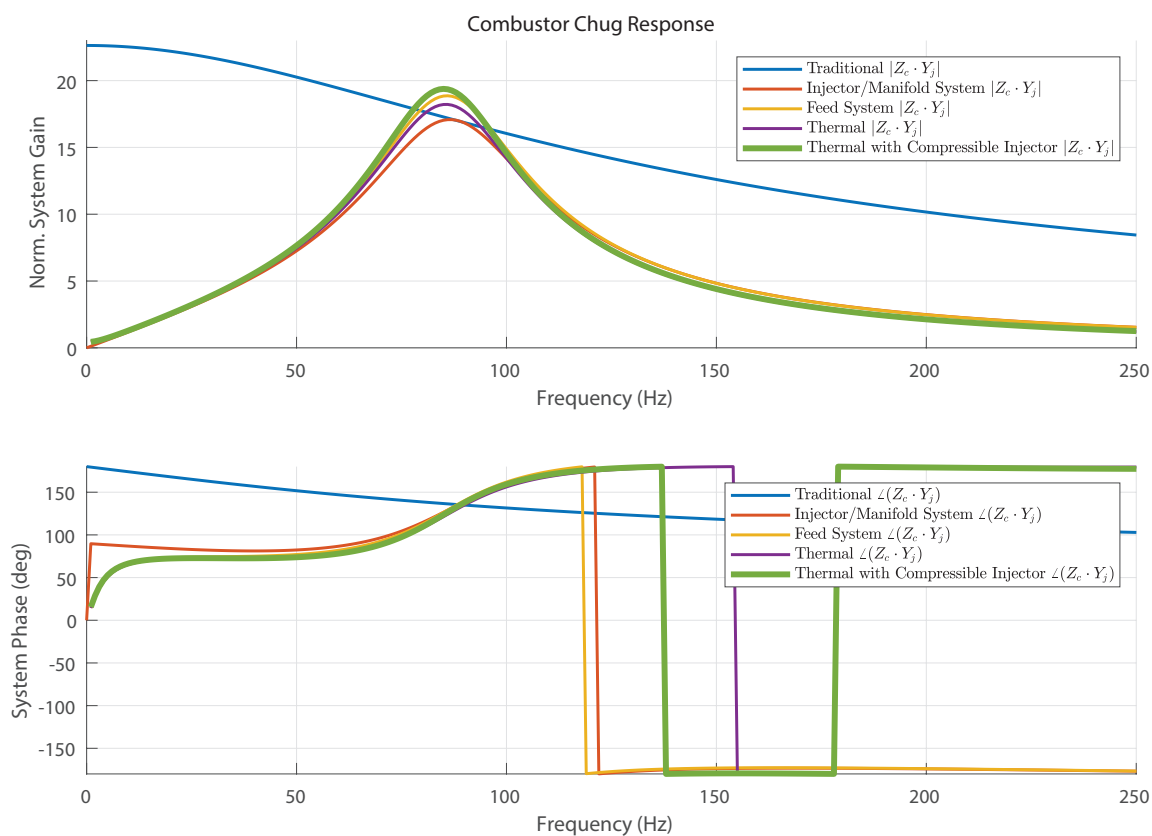


Figure 5.38.: Chug predictions using models stipulated in Casiano's thesis [4]; for the case with an oxidizer temperature of 700K.

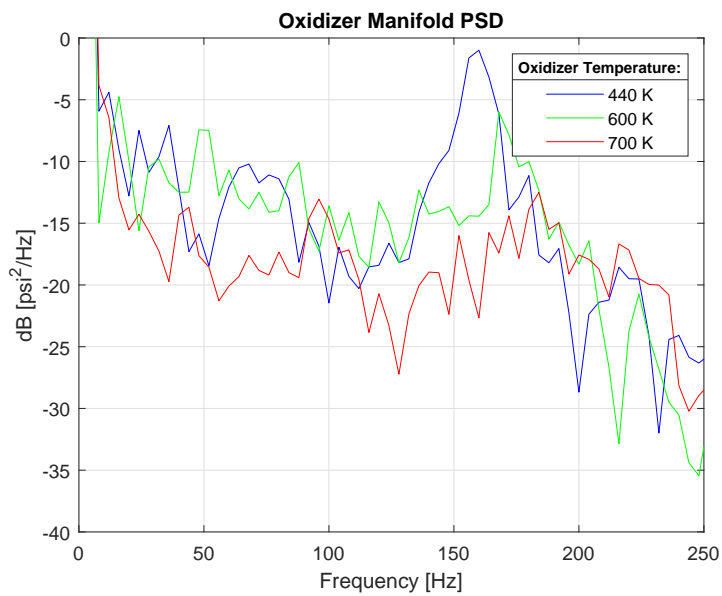


Figure 5.39.: Chug response in the oxidizer manifold for all oxidizer temperature cases. The interval of the time series is over 0.4s

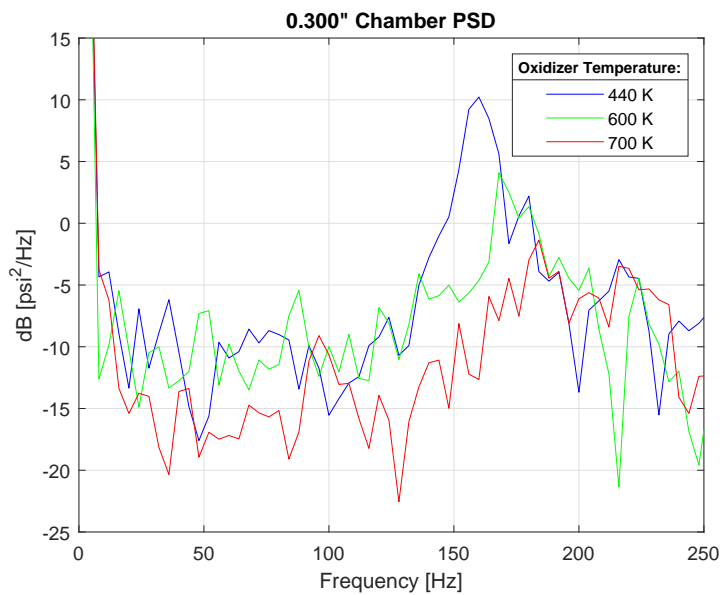


Figure 5.40.: Chug response in the chamber for all oxidizer temperature cases. The interval of the time series is over 0.4s

5.3.2 Growth Rate

With reference to Figure 5.1, the 700K cases showed a momentary transition from a limit cycle to a chugging behavior, and then back to a limit cycle. This is an opportunity to determine the linear growth rate of the fundamental acoustic mode. The signal was reconstructed using a SSA technique and limited to the mode energies associated with the fundamental frequency. The RMS envelope was then calculated to determine the running change in amplitude. Using Figures 5.19 and 5.17(b) as a guide, the growth rate was estimated by using an exponential fit starting from the growth initiation point, after the low frequency mode had diminished. The growth rate of the fundamental mode was estimated to be 22.575 s^{-1} , where it approximately takes 55ms to reach limit cycle gain.

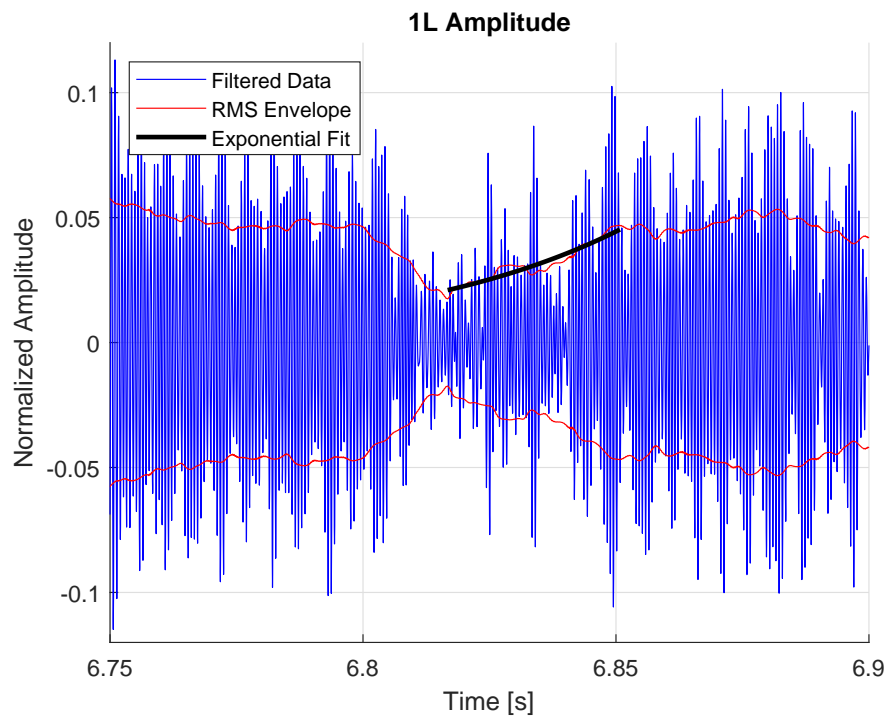


Figure 5.41.: Growth of the longitudinal acoustic mode preceding a transition from limit cycle to chug, for the case with an oxidizer temperature of 700K. The correlation factor of the exponential fit was 0.915.

5.3.3 Exceptional Test Case

When the chamber and oxidizer post were altered to their shortest configuration it was found that the test conditions were not repeatable for the specific case of 700K oxidizer temperature, with an equivalence ratio of 0.8. Figure 5.42 shows how two consecutive tests conducted 10 minutes apart resulted in very different behaviors. The mode/s of Test 2 at 11.5kHz are identified as either the 1T or 1L1T. The dominant mode of Test 2 matches in frequency exactly with one of the less dominant modes in Test 1. The low frequency mode differs significantly between each test, where the Test 2 low frequency mode is not a harmonic or multiple of the low frequency mode in Test 1. The strength of the fundamental mode in Test 2 also seems to drive different harmonic frequencies than Test 1. The stark difference in behavior could be the result of a bifurcation, but it is still not known why this behavior occurs. Test 2 was a unique case.

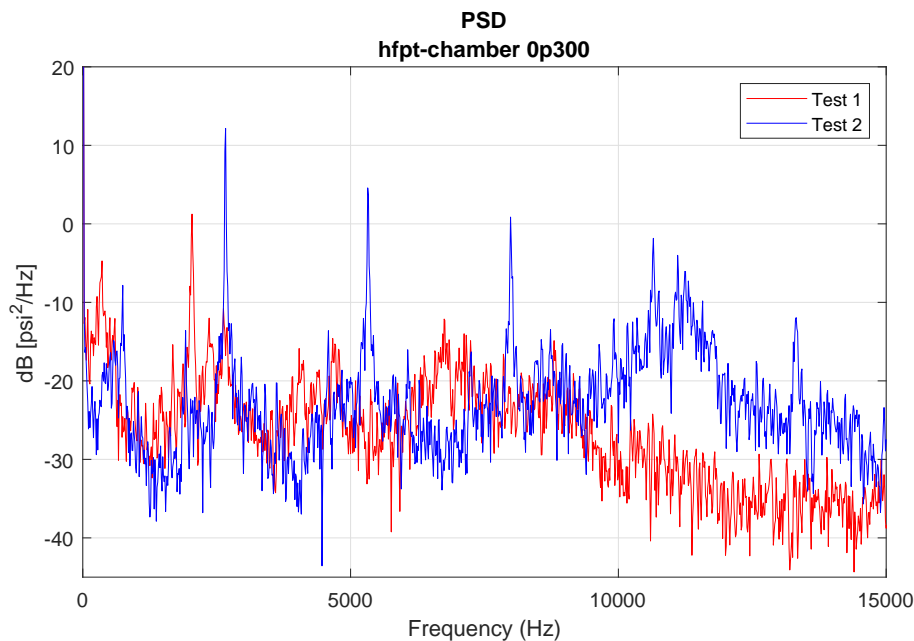


Figure 5.42.: PSDs of two consecutive tests at the same operating conditions.

5.4 Summary of Experimental Results

- Transition from low frequency thermoacoustic chug to a thermoacoustic longitudinal coupling with increase in oxidizer temperature.
- Both thermoacoustic chug and thermoacoustic longitudinal modes always present up until an oxidizer temperature of 750K, where the thermoacoustic chug becomes negligible.
- Tuning of oxidizer post to accommodate lower oxidizer temperature does not result in a significant change in thermoacoustic longitudinal resonance, but rather responds primarily with a thermoacoustic chug.
- Typical chugging may be evident at very low frequencies, but negligible.
- Acoustic response of system is complex and difficult to predict with simple 1D model.
- Higher order acoustic modes occur in oxidizer manifold, but do not contribute to thermoacoustic coupling in chamber.
- Fundamental acoustic mode in chamber driven by combustion mode; system responds accordingly.
- Modulation of the thermoacoustic longitudinal mode by the thermoacoustic chug mode results in side lobes of the thermoacoustic longitudinal mode, but usually only a single side lobe (SSB) is present.
- Modulated thermoacoustic longitudinal mode results in a varying longitudinal frequency in time with a period consistent with the thermoacoustic chug mode.
- Combustion consistently detected by chemiluminescence measurements in the recess near the fuel collar tip for all cases.
- Evidence of mode driving combustion at different frequency than fundamental acoustic mode at low oxidizer temperatures.

- As oxidizer temperature increases chemiluminescence and pressure begin to synchronize.
- At high oxidizer temperature (700K) chemiluminescence tracks well with primary thermoacoustic mode, but does not track with its harmonics; this suggests that higher frequency pressure mode do not drive combustion in this case.
- Phase relationship between pressure and chemiluminescence for the thermoacoustic chug trends with oxidizer temperature in both the chamber and injector recess, but at higher oxidizer temperature trend in phase alters significantly.
- Phase relationship between pressure and chemiluminescence for the thermoacoustic longitudinal mode trends with oxidizer temperature, but does not indicate a pressure driven response due to the dissimilar phase relationship between the recess and chamber.
- Pressure-chemiluminescence coherent higher frequency modes detected in the chamber and injector recess using PMTs.
- High frequency modes in injector recess consistent with vortex shedding off of the fuel collar due to oxidizer velocity.
- Linear growth for fundamental thermoacoustic longitudinal mode for the 700K case determined to be $22.575 s^{-1}$.

6. CFD MODEL COMPARISON

Quantifying properties such as temperature, density and sound speed in a rocket combustion chamber is notoriously difficult, especially in a very dynamic system. To gain real insight of the dynamics in the system it is exceptionally useful to construct a representative model. In the case of HAMSTER, a simulation could give key details about the gas properties, acoustic response, key integral scale fluid mechanics and combustion response. Dr. Swanand Sardeshmukh developed an accurate model of the thermoacoustic response of HAMSTER. This chapter compares results from the simulation with the experiment.

The combustor is simulated as an axisymmetric configuration. This choice allows the use of advanced chemical kinetics models, which was one of the project goals for the AFOSR project. The computational domain of the experiment is shown in Figure 6.1. The simulation boundary conditions are well defined per the experimental configuration; choked inlet into the oxidizer manifold, choked outlet from the fuel manifold, choked nozzle and adiabatic wall. The choked inlets allow the use of a mass flow and total temperature boundary condition. Both quantities required for the specification of the boundary conditions are experimentally measured and utilized for the simulation.

The inner walls of the oxidizer manifold and chamber are lined with a thermal barrier coating (Yttria-stabilized Zirconia). This is consistent with an adiabatic wall condition, which is used at the wall in addition to the no-slip condition. The operation of the combustor at a low reduced pressure and high reduced temperatures implies ideal gas behavior. The structured mesh is composed of 108,291 nodes and 107,200 elements, with a typical resolution of 0.1 mm near the injector. A detailed view of the mesh around the injector recess area is shown in Figure 6.2. Chemical kinetics are modeled with GRI Mech 1.2 [56]. It is well suited for this purpose since the oxidizer

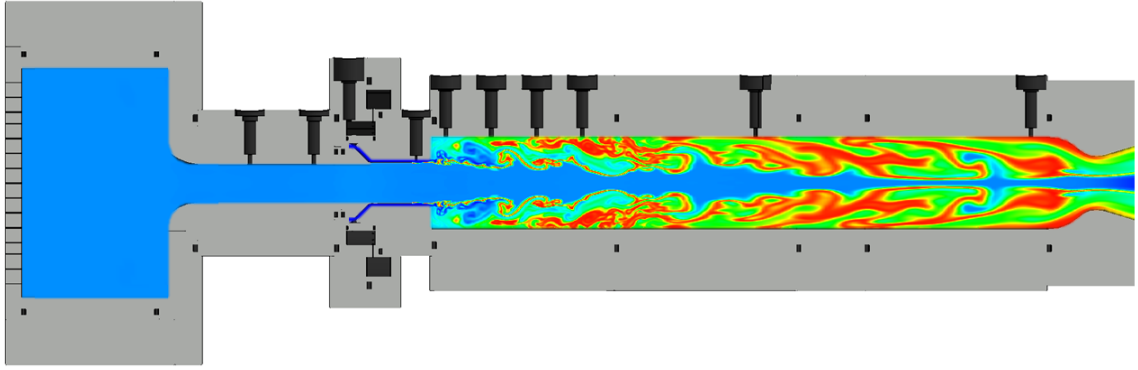


Figure 6.1.: Computational domain for the simulations of HAMSTER [96].

is pure oxygen instead of air. Predictions of ignition delay with this mechanism closely agree with the measurements as well as predictions of other mechanisms from literature [97]. With the detailed kinetics, the chemiluminescent species OH^* and CH^* are modeled. The time scales associated with OH^* require modeling as a transported species. The CH^* can be considered to be in a quasi-steady state due to its short lifespan and its concentration is calculated post-simulation.

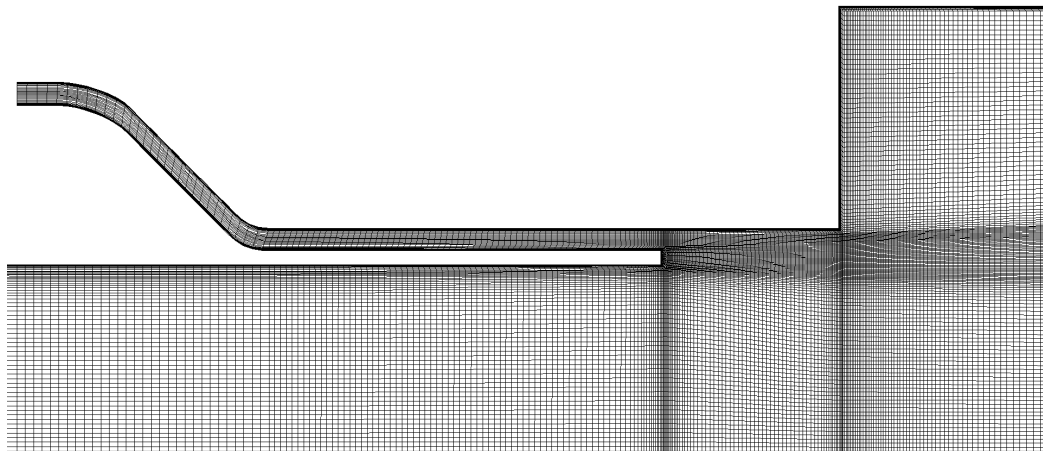


Figure 6.2.: Detailed view of the mesh in the vicinity of the injector recess and dump plane [96].

The simulations are performed with Purdue University's in-house code, GEMS. GEMS is a fully coupled Navier-Stokes solver with second order accuracy in both space and time. The model utilizes the detached eddy simulation (DEM) turbulence modeling technique, where large scale motions are captured up to the grid length scale, while the sub-grid turbulence is modeled with a $k - \omega$ model [98]. The experimental conditions are amenable to the dilute limit and hence the ideal gas equation of state is used. The thermal and transport properties are obtained using NASA polynomial coefficients from McBride et al. [99]. The boundary conditions, fluxes and source terms are treated implicitly for the discretization. The solution of the linearized equations is obtained using line Gauss-Seidel algorithm and the approximate factorization errors are minimized by employing dual time stepping algorithm.

To begin to validate this model, a number of aspects of the problem need to be compared between the experiment and simulation. First, a comparison of the global parameters, such as flow conditions achieved and performance characteristics. Then the dynamics will be compared; initially the basic simulated response of the system is checked, then some of the key acoustic features are analyzed and compared with the experimental observations. Then the general flame characteristics are measured against a qualitative observation from the chemiluminescence measurements. Using the simulated data the heat release mechanics are then used to provide some insight of how the flame might be oscillating, giving a basis to analyze how the hydrodynamic features from the injector might contribute to the thermoacoustic modes. The hydrodynamics generated in the injector recess and shear layer are closely examined and compared to chemiluminescence data collected from the experiments. The coherence of the coupled physics is then estimated and serves to provide a final commentary on the thermoacoustic mechanics found in HAMSTER.

6.1 Global Characteristic Features

To adequately compare the simulations to the experimental observations a top-down approach is logical. By quantitatively comparing the global parameters inherent to each data set, the more detailed features can be better scrutinized within a certain level of context. The flow conditions, the performance and the raw data can be compared directly. Some of the more important parameters, such as oxidizer post velocity statistics, are also listed. The global statistics relevant to each scenario are listed in Table 6.1.

In general, the experiment and computational data are comparable. The simulations were able to accurately predict the effect of oxidizer temperature - at low oxidizer temperature chug instability prevails and at high oxidizer temperature a longitudinal acoustic instability (organ pipe mode) prevails. The mixture ratio and propellant temperatures are within 1.0% of one another, except for the 400K oxidizer case where the lowest oxidizer temperature achieved in the experiment was only 440K. The experiments generally had flowed at higher mass flow rates, but remained within 10%; this could have resulted in slightly higher mean oxidizer post velocities. A higher oxidizer post velocity was estimated for an oxidizer temperature of 700K, but it was higher for the simulation rather than the experiment. It should be noted that the method of determining the oxidizer post velocities in the experiments could have been inaccurate because they were indirectly determined. The same notations can be made about the combustor performance and the oxidizer post Mach number in the experiments. It is also interesting to note that for an oxidizer temperature of 700K the combustor performance exceeds 100% in the simulations.

One especially interesting feature, which coincides with the mechanics in the recirculation zone behind the backward facing step, is the near-wall gas temperature at the head end of the chamber (Figure 6.3). When comparing the simulation data to the experimental data at the exact same location there appears to be very good agreement. From the experimental data groupings it would be expected that the near-

wall gas temperature remains more or less constant until an oxidizer temperature of around 600K or slightly less is used.

Table 6.1.: Comparison summary between the global characteristics of the experimental and simulation data.

	<u>Exp</u>		<u>CFD</u>		<u>Error %</u>	
	440K	700K	400K	700K	400K	700K
O/F	5.05	4.95	5.0	5.0	1.0	1.0
mdot_{Fuel} [kg/s]	0.0846	0.0875	0.0771	0.0771	9.73	13.5
T_{Fuel} [K]	297	297	294	294	0.8	0.8
mdot_{Ox} [kg/s]	0.427	0.433	0.395	0.395	8.10	9.62
T_{Ox} [K]	444	705	400	700	11.0	0.714
V_{OxPost}(mean) [m/s]	136.5	192.1	137	215	0.365	10.7
V_{OxPost}(max) [m/s]	288.5 ¹	277.4 ¹	234	297	23.3	6.60
M(mean)	0.434	0.439	0.360	0.435	20.6	0.920
T_{wall}(mean) [K]	822	887	869	950	5.41	6.63
η_{C^*}	0.806	0.914	0.878	1.04	8.20	12.1

¹ Estimated using a linear acoustic assumption - $u' \frac{P'}{\rho c}$.

From the previous trends shown it could be remarked that as the dominant behavior shifts from a chug to an acoustic response the near-wall gas temperature may vary significantly between tests at the same condition; this may suggest a fundamental shift of the injection mechanics and that it may affect the recirculation zone in a very different way. These mechanics will be discussed in more detail at a later stage.

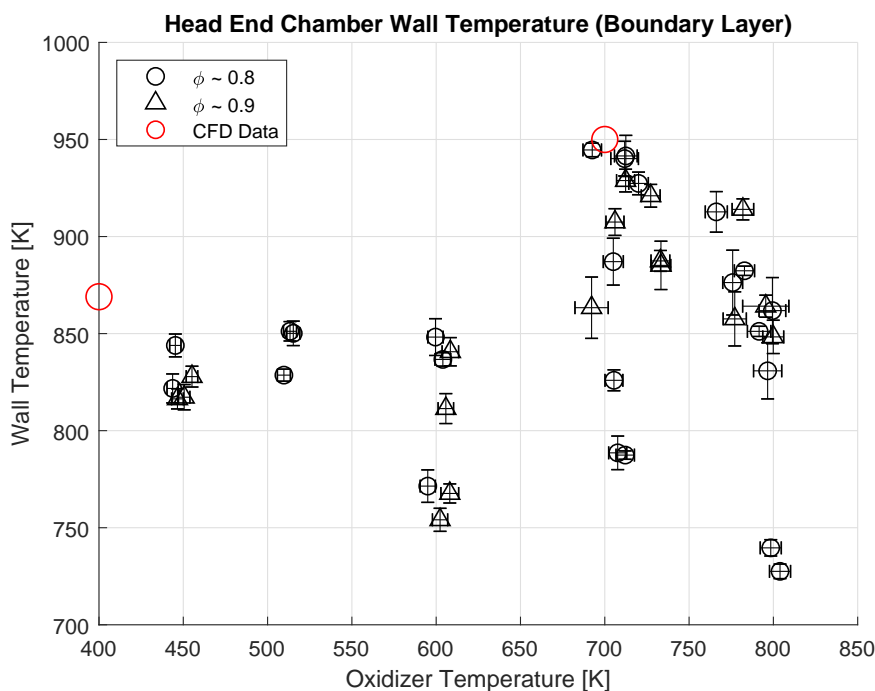


Figure 6.3.: Simulated average near-wall gas temperatures at the head end of the combustor with comparable data from the experiments.

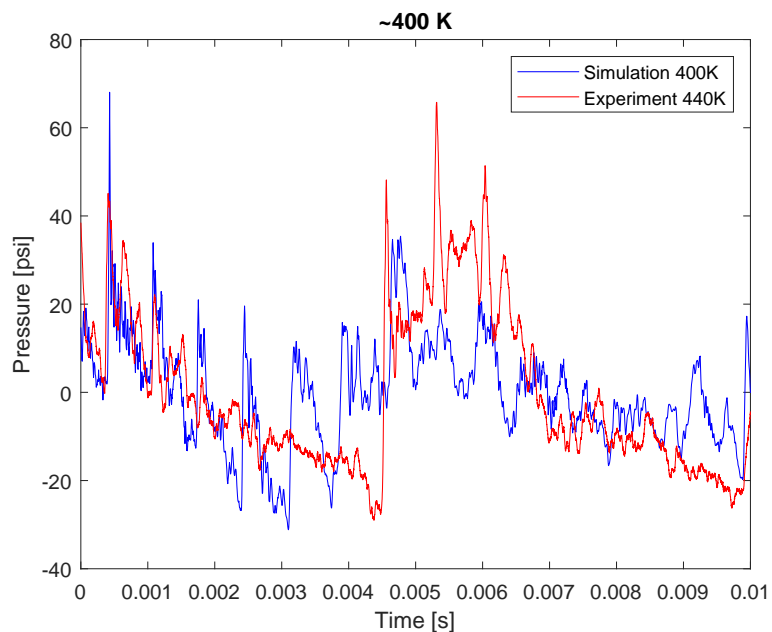
Figures 6.4 and 6.5 show the linearly detrended raw pressure traces in the injector recess and head end of the chamber, for oxidizer temperatures of 400K/440K and 700K respectively. Qualitatively, the pressure traces look quite different from one another. The coherence and regularity of the pressure waves seem to not be captured by the simulation. However, upon closer inspection the simulation does seem to capture some key characteristics which may suggest that the inherent physics modeled is represented, but damped for an unknown reason.

Beginning with the low oxidizer temperature case, it is very clear that at the beginning of each time series where an initial event occurs, the rate at which the pressure rises is extremely well captured. At this point in time the main difference between the two time series is that spatially, the largest amplitude event occurs in the recess for the simulation, while it occurs in the chamber for the experiment. Subsequently, the running mean of each pressure response falls at the same rate. However, the higher frequency components in the experimental data get damped out periodically. The simulation data have what would appear to be a slightly more benign response where the high frequency dynamics do not become damped out very quickly.

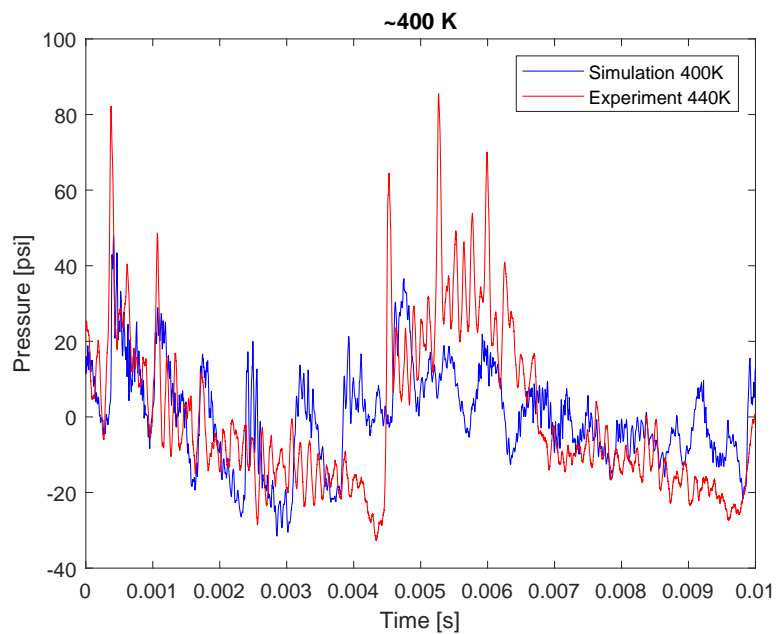
Comparing the high oxidizer temperature cases, it can be seen, especially in the injector recess, that the simulation is able to momentarily capture the amplitude. Additionally, it can be seen that for short periods of time that the oscillations occur at the same frequency between the experiment and the simulation, but shortly afterwards the frequency of the simulations begins to lag slightly. The modulation of the higher frequency modes seem to occur in both locations, for both the experiment and simulation, albeit at different rates.

In general, it appears that the simulations suffer from an inability to stay synchronized at the higher frequencies associated with the longitudinal modes. Qualitatively and speculatively, it appears that some of the dynamics that could be interfering with the thermoacoustic longitudinal modes, and that damping of these modes might be crucial. The axisymmetry of the simulation geometry might not allow for the damping required to assist in the organization of the other system modes represented in the experimental data.

A last remark: the ADF stationarity test was performed on the simulation data and it was found that for an oxidizer temperature of 400K the time series was not stationary, but the 700K case was stationary. This suggests that the 400K case may require additional computation time.

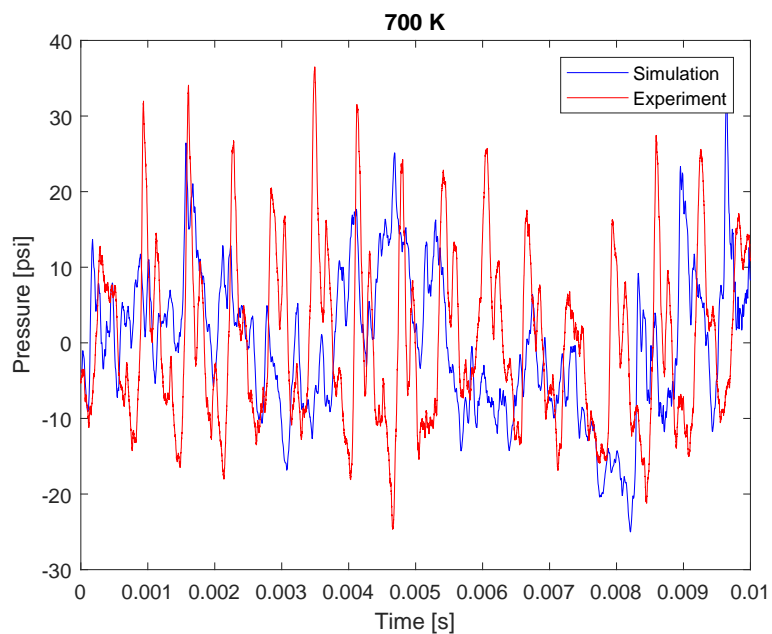


(a) Recess, -0.350"

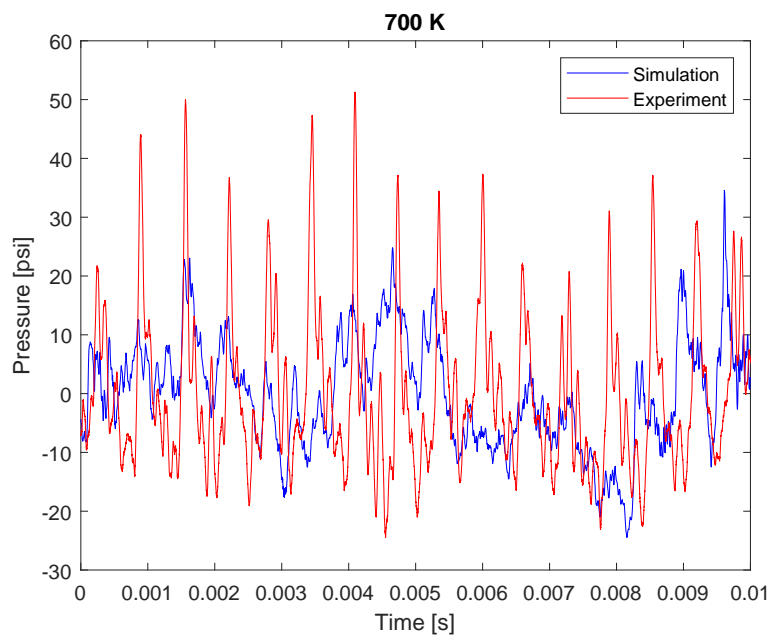


(b) Chamber, 0.300"

Figure 6.4.: Qualitative comparison of the linearly detrended pressure traces between the simulation and experiment at oxidizer temperatures of 400K and 440K respectively.



(a) Recess, -0.350"



(b) Chamber, 0.300"

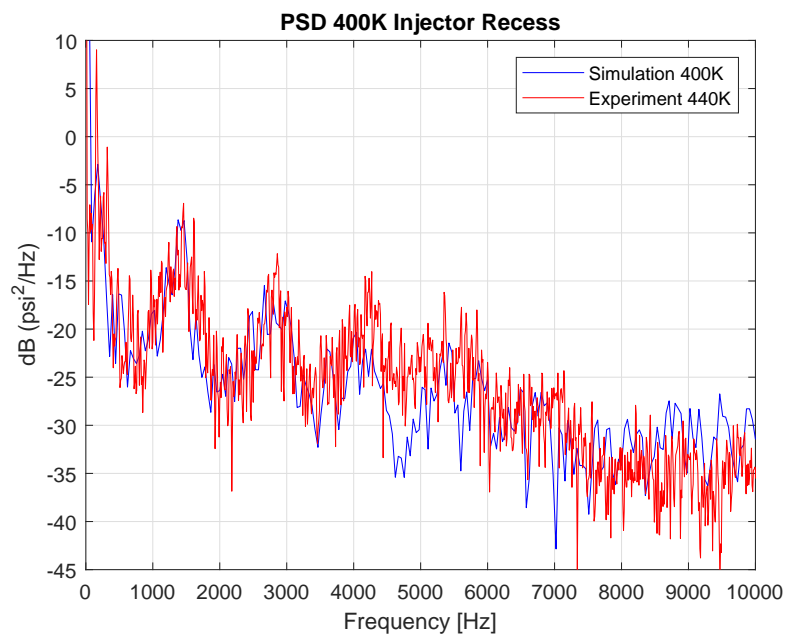
Figure 6.5.: Qualitative comparison of the linearly detrended pressure traces between the simulation and experiment at an oxidizer temperature of 700K.

6.2 Dynamics

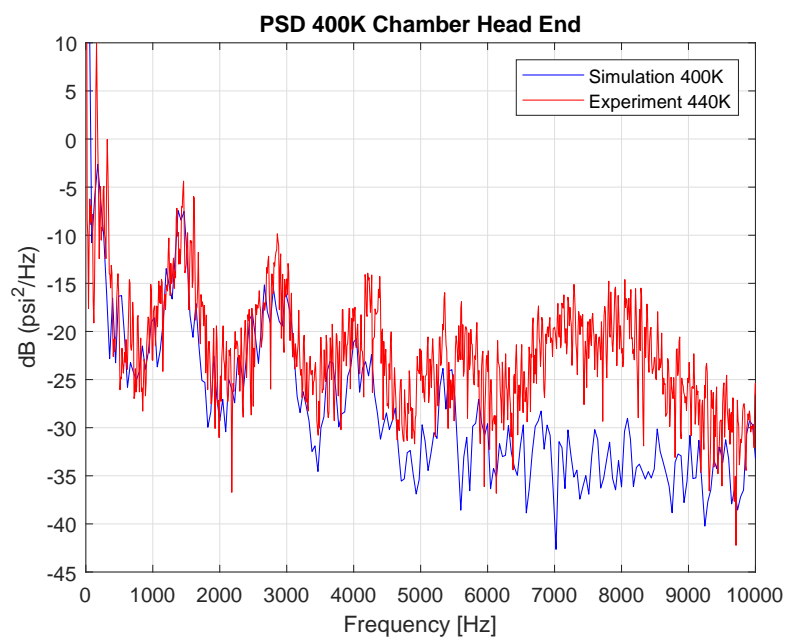
In this section the key dynamics directly related to the thermoacoustic instabilities in HAMSTER will be investigated. First, the acoustics will be analyzed and compared to the experimental data. Once the acoustic response has been dissected and the response is conclusive then the combustion response will be analyzed. First qualitative description of the combustion will be made, before quantitatively comparing the combustion response with the acoustic modes. This type of approach falls in line with the general idea of the Rayleigh criterion, but the complexity of the problem will be elaborated on. The response and the hydrodynamic features produced by the injector will then be investigated and related to the acoustic perturbations. Lastly, an attempt to connect all three sets of mechanics will be made, showing their inherent relationship.

6.2.1 Acoustics

Figure 6.6 shows the pressure PSD comparisons between the experiment and simulations in the injector recess and chamber head-end, for an oxidizer temperature of 440K and 400K respectively. The pressure dynamics compare very well up to 3.5kHz. There appears to be some high frequency dynamics around 6-8.5kHz in the head end of the chamber that are not captured by the simulation. In these PSDs the fundamental mode of the longitudinal acoustic response has non-integer multiples harmonics. This is the result of the total system acoustic response where the frequencies are dependent on the impedance of the oxidizer post/chamber interface. With the sudden area change the end of the oxidizer post acts like an inertance; a lumped mass where its response is frequency dependent. This is shown in Equation A.10.



(a) Recess, -0.350"



(b) Chamber, 0.300"

Figure 6.6.: Comparison of the PSDs between the simulation and experiment at an oxidizer temperature of 400K/440K.

Figure 6.7 shows the acoustic mode shapes generated by a DMD of the simulated data for HAMSTER at an oxidizer temperature of 400K. The selected modes correspond to the (a) chug (bulk) mode, (b) fundamental acoustic mode, and (c) a mode corresponding to acoustic mode resulting from the modulation of the fundamental acoustic mode by the chug mode.

The bulk mode (a) shows phase-less acoustic responses in the oxidizer manifold and the combustion chamber. This corresponds to the mode shapes predicted by the 1D acoustic model and the experimental observations. There is also a phase difference between the response in the oxidizer manifold and the combustion chamber; the oxidizer post does not have a standing wave behavior nor a bulk response, but facilitates the communication between the two large volume ducts. The injector recess appears to have the roughly same response phase as the combustion chamber and fuel annulus.

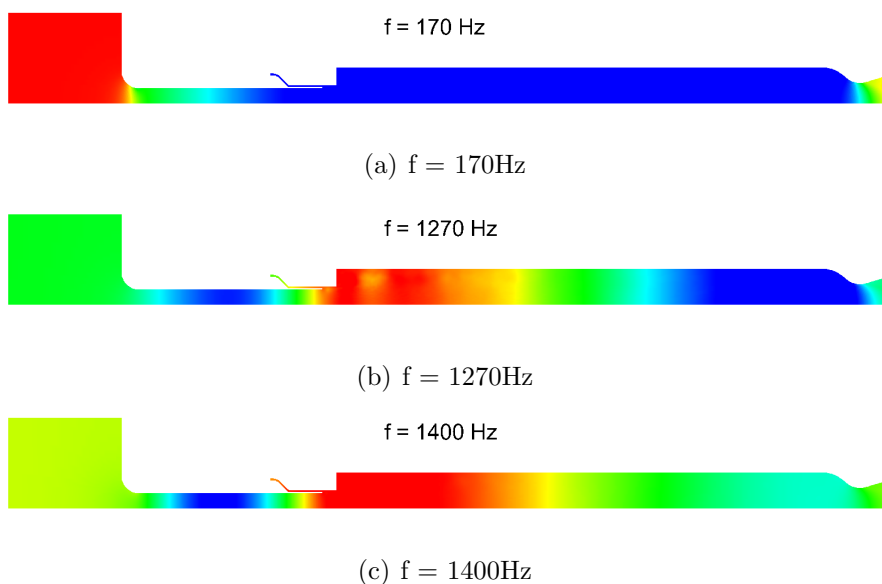
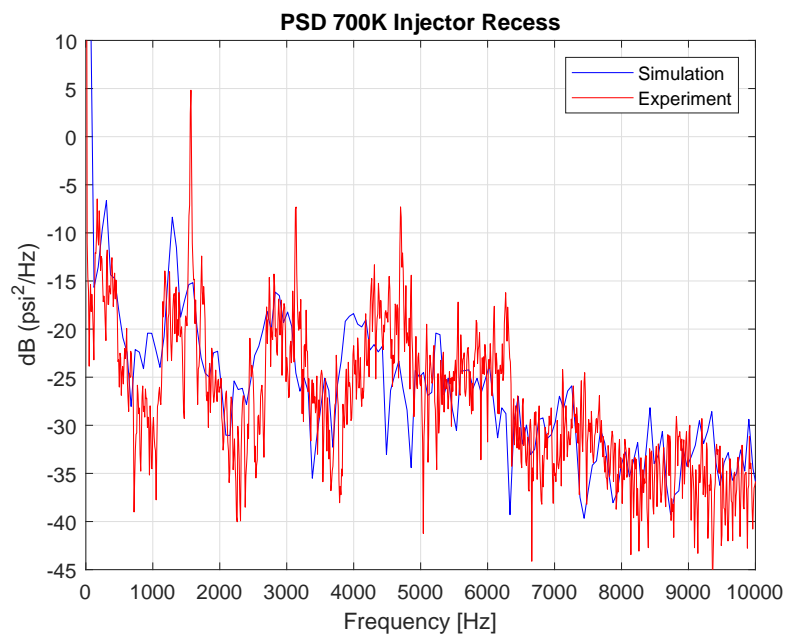


Figure 6.7.: DMD generated acoustic mode shapes for the 400K oxidizer temperature case. The scale ranges from red to blue, where red is the maximum amplitude and blue is the minimum amplitude.

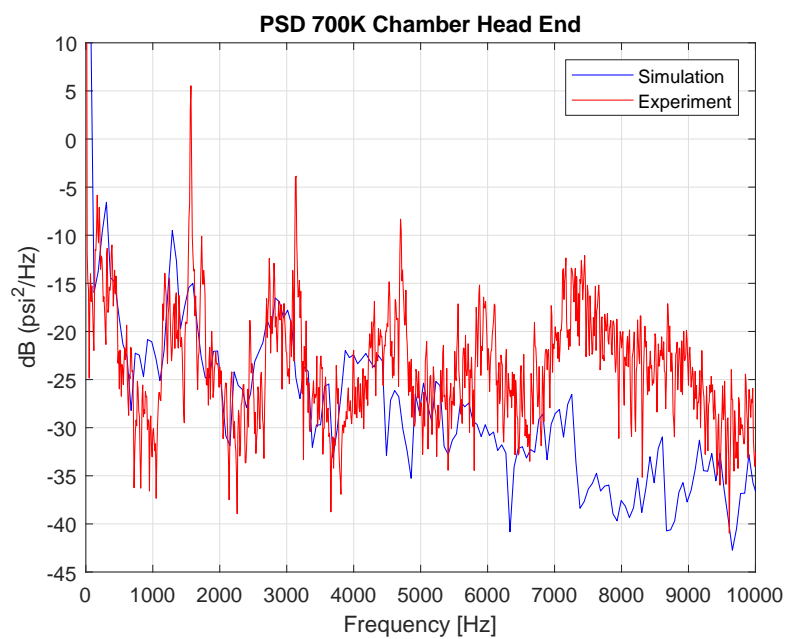
The fundamental mode (b) shows an acoustic half-wave standing mode in the chamber and full-wave between the oxidizer manifold and injector recess. This corresponds to previous observations and predictions. The relative amplitude response of the oxidizer manifold is low, which was intended while designing HAMSTER. The higher frequency mode (c) shows a very similar mode shape to (b), with a slight difference in the chamber.

Figure 6.8 shows the pressure PSD comparisons between the experiment and simulations in the injector recess and chamber head-end, for an oxidizer temperature of 700K. The general system acoustic response (broadband peaks) match well up to 3kHz between the experiment and simulation, as it did with the low oxidizer temperature case. However, the dominant resonance mode and its harmonics are not captured by the experiment.

Despite the discrepancy both sets of PSDs show evidence of modulation, where the dominant longitudinal mode (fundamental mode) is the carrier wave modulated by the chugging mode. Interestingly, the modulated mode from the simulations at 1599Hz corresponds exactly with the dominant longitudinal mode in the experiment. The dominant longitudinal mode is modulated by the chug in the experiment to produce an even higher frequency side lobe. The matching of frequencies in this case might just be coincidental, or it may indicate a mechanism at 1599Hz which is not fully excited in the simulation. In the PSD showing the acoustic response in the chamber, for the case of an oxidizer temperature of 700K, the simulation fails to capture the high frequency response at approximately 7100Hz.



(a) Recess, -0.350"



(b) Chamber, 0.300"

Figure 6.8.: Comparison of the PSDs between the simulation and experiment at an oxidizer temperature of 700K.

Figure 6.9 shows the acoustic mode shapes generated by a DMD of the simulated data for HAMSTER at an oxidizer temperature of 700K. The selected modes correspond to the (a) chug (bulk) mode, (b) fundamental acoustic mode, and (c) a mode corresponding to acoustic mode resulting from the modulation of the fundamental acoustic mode by the chug mode.

Comparing the mode shapes with the 400K oxidizer case, the chug and fundamental modes have the same shape. The modulated mode (c) appears to have a very close resemblance to the fundamental mode. This may indicate, as mentioned previously, that these modes can be interchangeable to optimally suit the combustion spatial distribution.

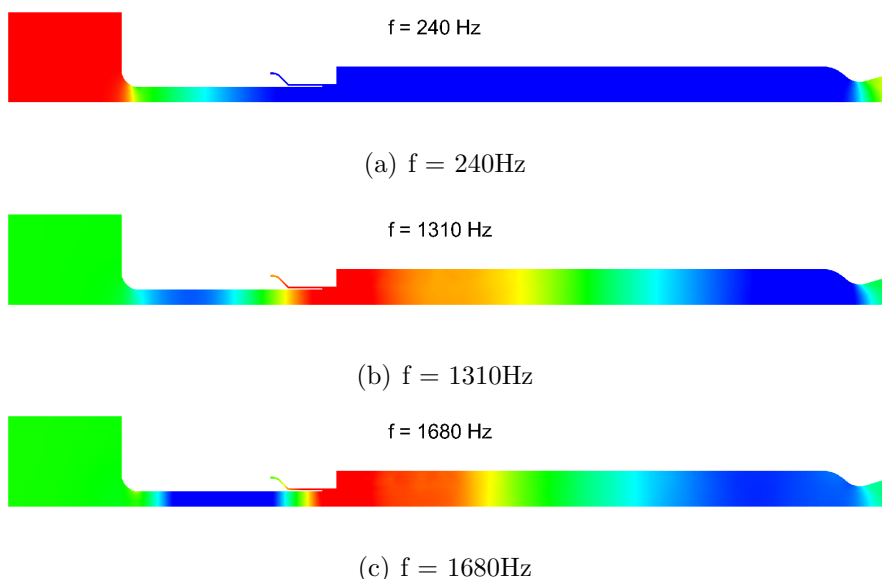


Figure 6.9.: DMD generated acoustic mode shapes for the 700K oxidizer temperature case. The scale ranges from red to blue, where red is the maximum amplitude and blue is the minimum amplitude.

Figure 6.10 shows the simulated raw pressure response in HAMSTER for an oxidizer temperature of 700K. The acoustics in the chamber show a half-wave standing wave mode. In agreement with the experimental observations, the oxidizer manifold shows a combination of the first and second tangential modes (1T, 2T), localized first

longitudinal mode (1L) and the 1L1T combination mode. Additionally, the transverse response in the oxidizer manifold is relatively weak and does not translate into a response in the oxidizer post.

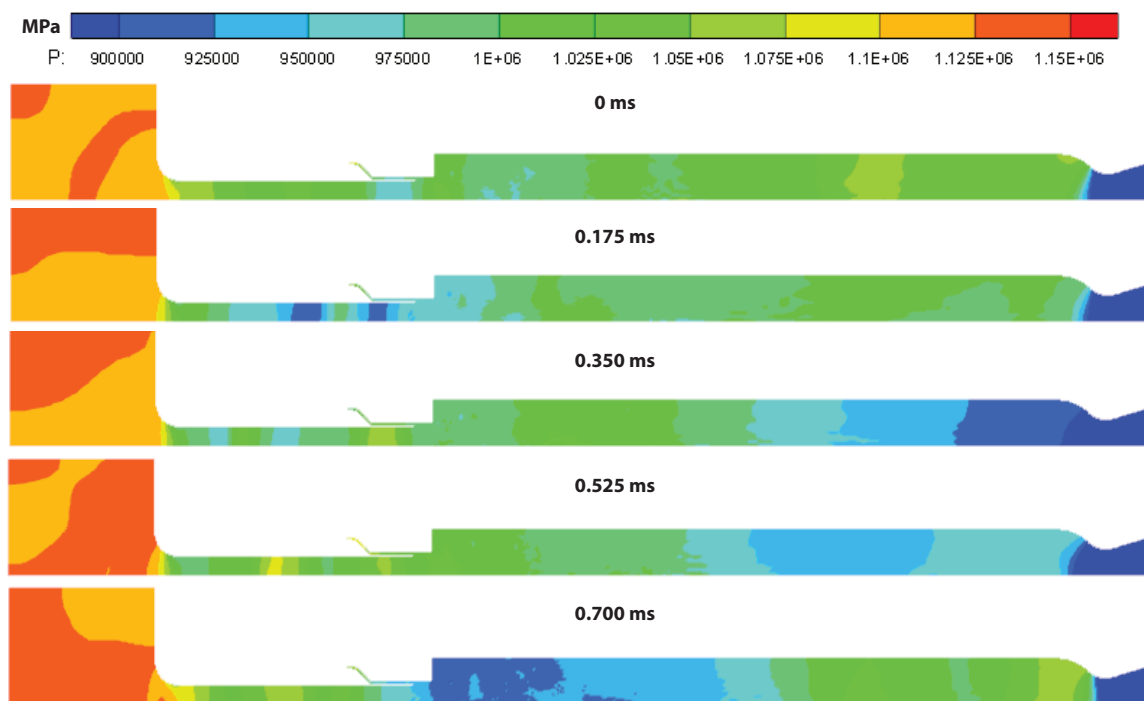
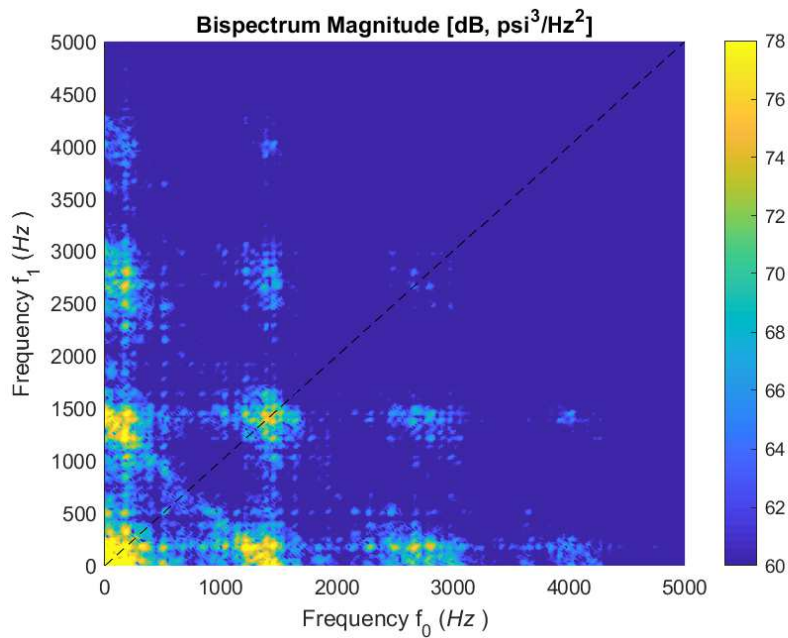


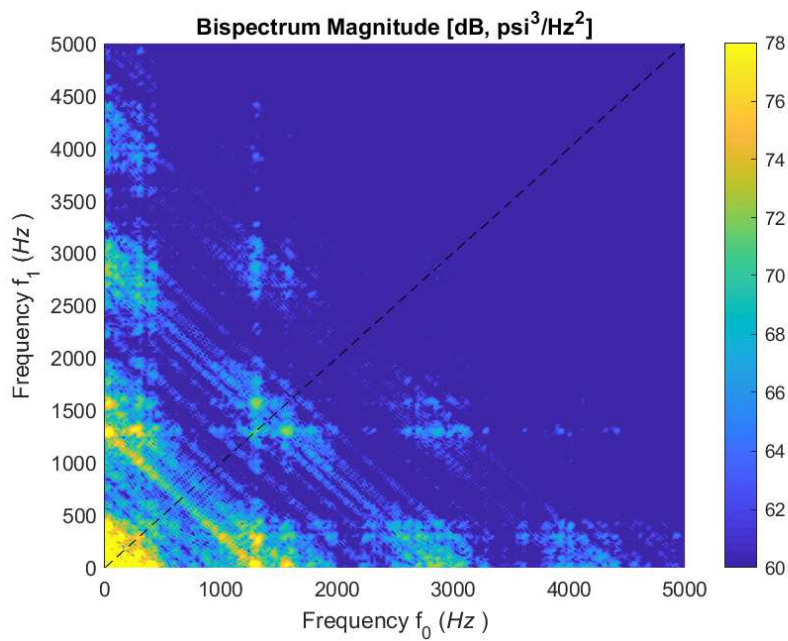
Figure 6.10.: Simulated pressure in HAMSTER for an oxidizer temperature of 700K. This represents approximately one cycle of the fundamental acoustic mode.

Figure 6.11 shows the bispectrum (bicoherence) analysis of the simulated pressure response for the cases of 400K and 700K oxidizer temperatures. Figure 6.11(a) shows that there is only very minor nonlinear interaction between the dynamics modes, adding evidence that the chugging mode dominates with a secondary system acoustic response. This indicates that the modes, at least the longitudinal modes, are purely linear in nature. In contrast, Figure 6.11(b) shows a nonlinear interaction, although not significant, between the chugging and first longitudinal mode. Since the modulation of the first longitudinal mode has been confirmed, where the obser-

variations between the experiment and simulation agree, the simulations can be used to understand the modulation mechanism better.



(a) Oxidizer Temperature: 400K



(b) Oxidizer Temperature: 700K

Figure 6.11.: Bispectral (bicoherence) analysis of the simulated pressure response.

During a chugging cycle, Figure 6.12 shows how the sound speed in the chamber varies. As the sound speed change during the low frequency cycle the acoustic frequency will change as a result. The temperature of the chamber appears to follow the changes in chamber pressure closely. There could be two possible explanations for this: (1) as extra mass flow is injected into the chamber, the equivalence ratio also shifts toward stoichiometric or the combustion becomes more complete, and (2) as the pressure changes the chamber chemical equilibrium shifts resulting in a temperature change. It is important to note that the relative change in chamber temperature corresponds directly to the relative change in chamber pressure.

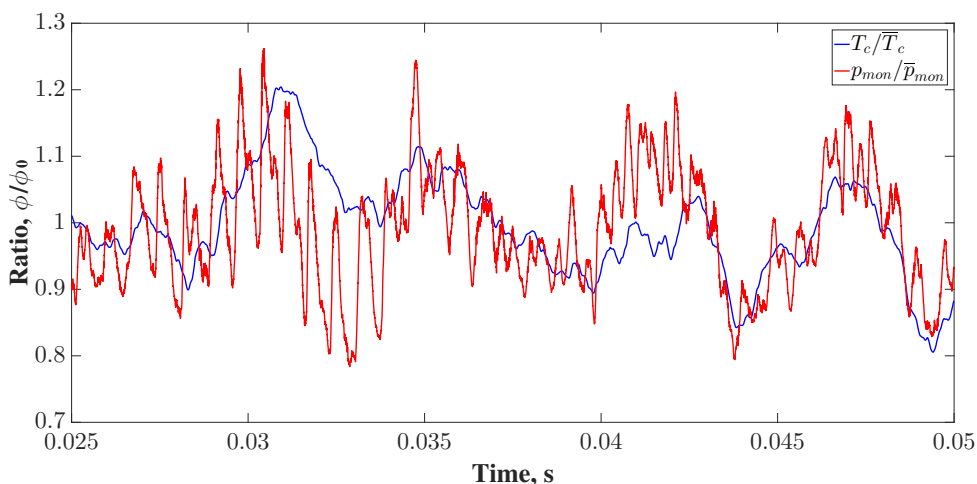


Figure 6.12.: Local temperature fluctuation with pressure during chug cycle.

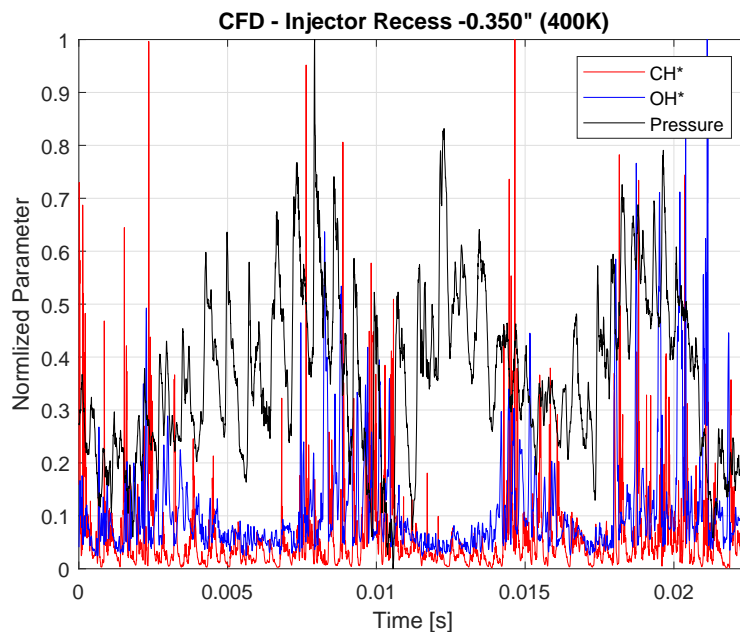
In summary, the simulations are able to capture the linear acoustic response observed in the experiments up to 3kHz. The simulations of the low temperature oxidizer case are nearly identical to the observed response seen in the low temperature oxidizer experiments. The simulated high temperature oxidizer case shows a modulated response similar to what was observed in the higher temperature oxidizer cases in the experiments. Additionally, the first three system acoustic modes were well predicted. However, the dominant response of the high temperature oxidizer experimental case was not accurately captured by the simulation.

6.2.2 Combustion and Heat Release

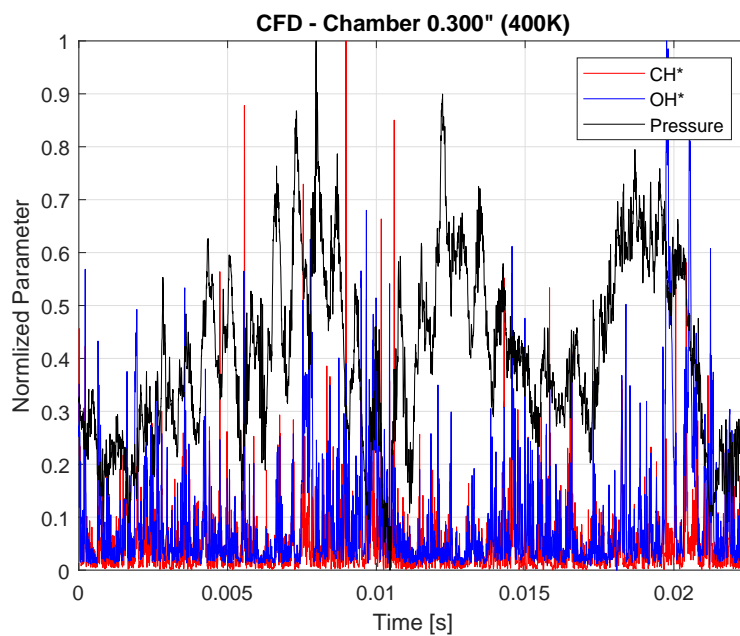
To gather information about short timescale combustion and hydrodynamic events, chemiluminescence measurements were taken in the experiments. The chemiluminescence measurements are line-of-sight integrated and the amount of light entering the PMT is greatly biased toward the port aperture. To spatially resolve the region of interest and from where the light is emitted, the probe volume needed to be minimized. The resulting probe volume was then analyzed and calibrated, and used to extract information from the simulations to be compared to the experimental data. While comparing the chemiluminescence, which is generally generated in the most exothermic combustion regions, the signals could be used for direct comparison between the experiment and simulation while simultaneously providing a link to the information regarding the heat release in the experiment.

Figure 6.13 shows the normalized raw CH^* , OH^* and pressure data extracted from the simulation of the 400K oxidizer temperature case. Generally, the chemiluminescence signals from the simulations do not follow the pressure explicitly. The chemiluminescence signals in the injector recess tend to have short emission bursts following sudden rises in pressure. The chemiluminescence signals in the chamber are more complex and do not seem to have a coherent structure.

Figure 6.13 shows the normalized raw CH^* , OH^* and pressure data extracted from the simulation of the 700K oxidizer temperature case. For both the injector recess and chamber head end locations the chemiluminescence signals are more regular, however it is still not clear whether they follow the pressure signal. To illustrate why the chemiluminescence signal may not be coherent in the chamber Figure 6.15 shows the heat release during a typical cycle.

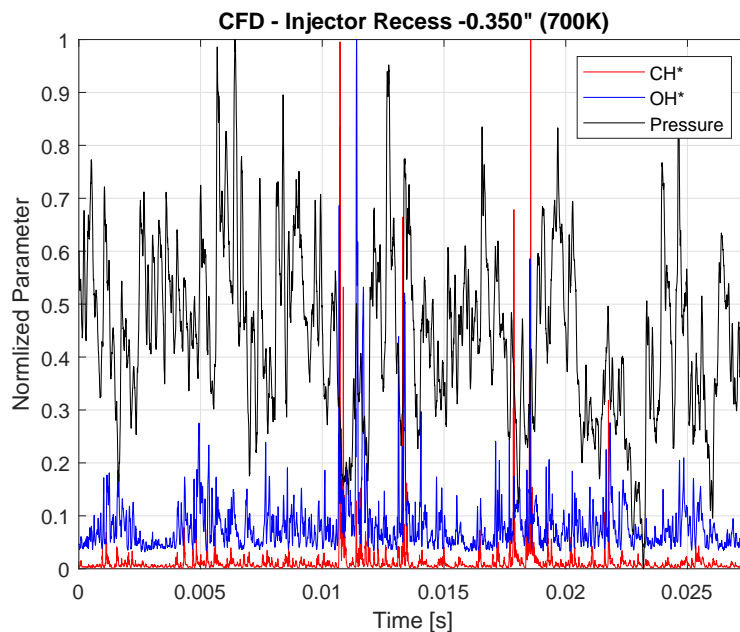


(a) Injector Recess -0.350"

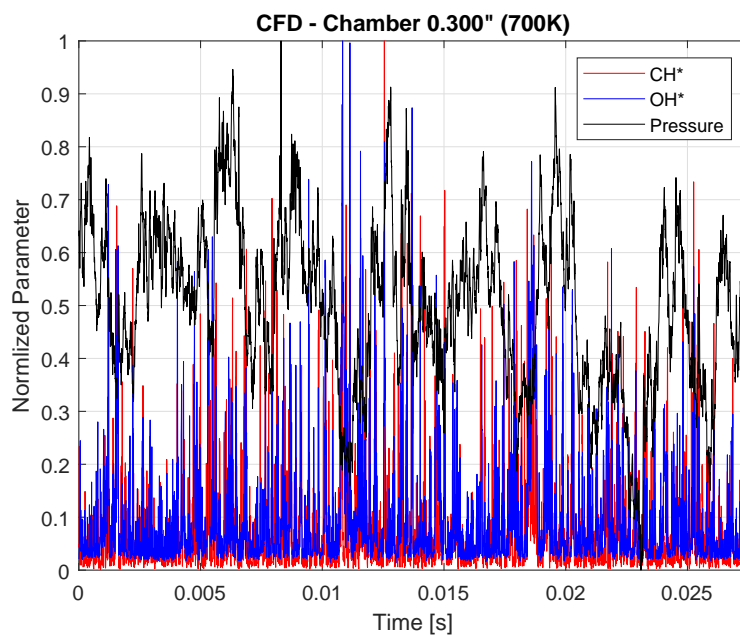


(b) Chamber 0.300"

Figure 6.13.: Comparison of the pressure, CH* and OH* signals in the simulation, complementing the exact locations expected in the experiment, for an oxidizer temperature of 400K.



(a) Injector Recess -0.350"



(b) Chamber 0.300"

Figure 6.14.: Comparison of the pressure, CH* and OH* signals in the simulation, complementing the exact locations expected in the experiment, for an oxidizer temperature of 700K.

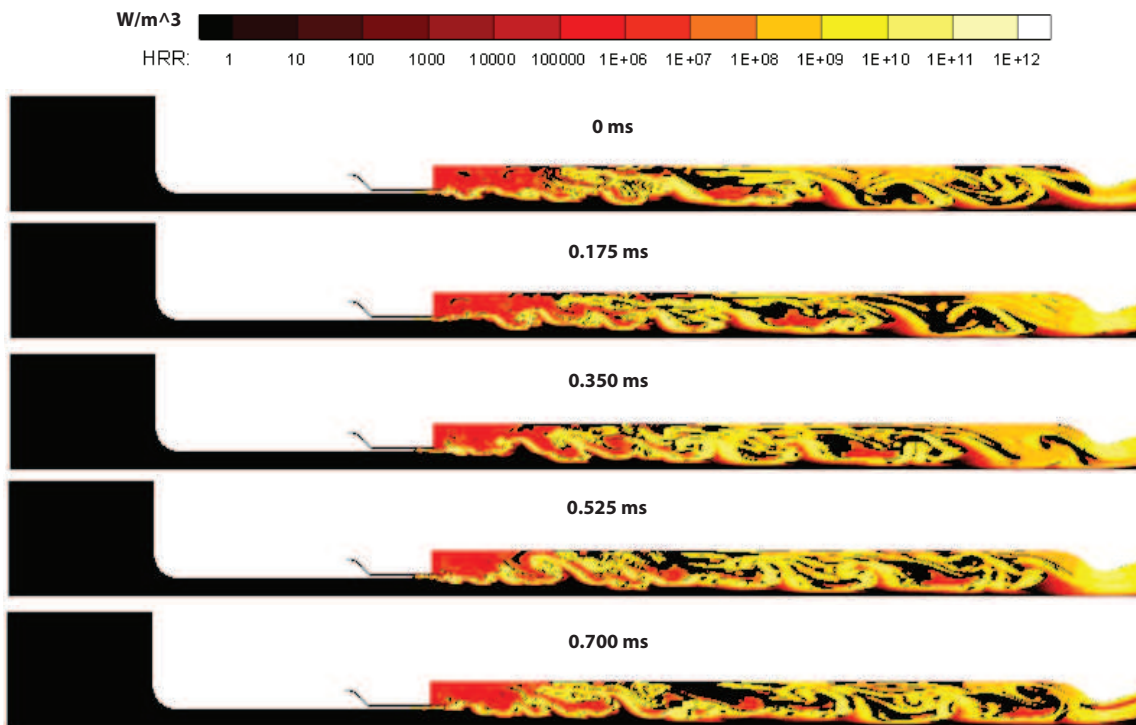


Figure 6.15.: Simulated heat release in HAMSTER for an oxidizer temperature of 700K.

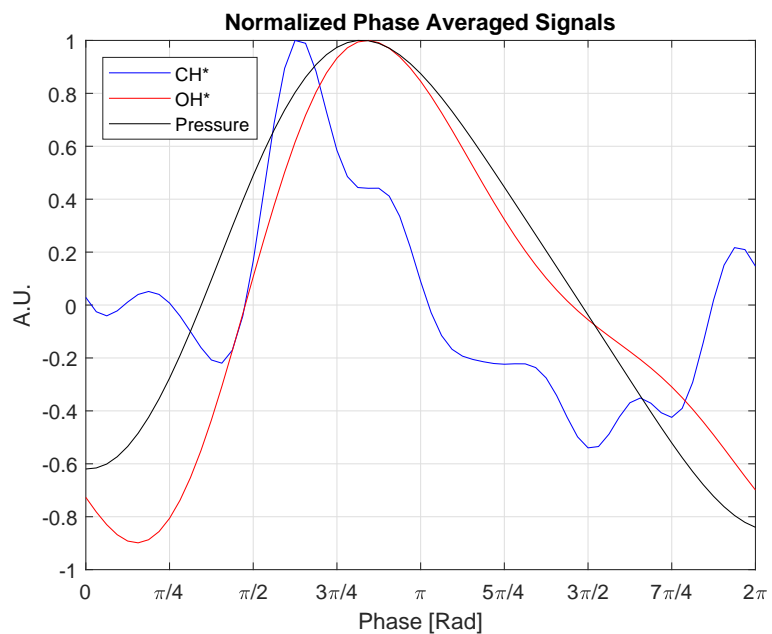
To quantify the relationship between the chemiluminescence and the pressure signals, a phase averaging was used. Before the phase averaging technique was implemented the signal needed to be de-noised. To filter the signals, but not eliminate useful information is difficult, especially on incoherent signals. To provide a ready signal to be phase averaged the SSA technique was used. The reconstructed signals were then phase averaged by applying a window based on an autocorrelation of the signal, where the first longitudinal mode period was selected. All of the signals were normalized prior to phase averaging.

Figures 6.16 to 6.19 compare phase averaged signals between the experiment and simulation at the injector recess and chamber head end for the low and high oxidizer temperatures studied previously. Generally, the OH^* and CH^* signals follow each

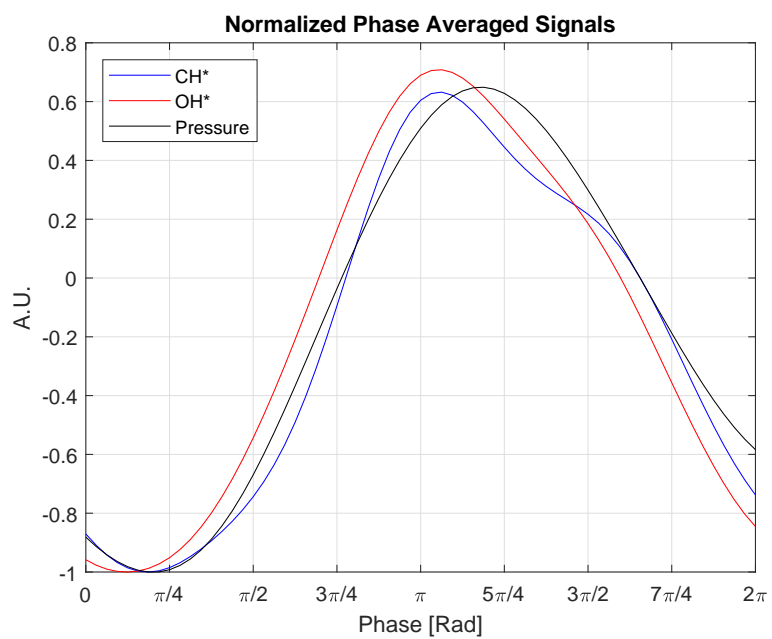
other closely for all the experimental datasets. This may be the result of a poor optical filtering of the selected bandwidths or that the chemiluminescence is strongly dependent on the pressure and hence number density changes, or that both CH^* and OH^* are good indicators of heat release.

Looking at the low oxidizer temperature experiment case it is pretty clear that chemiluminescence is pressure driven in the injector recess, shown in Figure 6.16(b). The windowed time interval corresponds to a frequency of 1270Hz. Figure 6.16(a) shows that OH^* follows the pressure quite well, but the CH^* does not. The simulations fail to take into account of the CO_2^* produced because the CO_2^* emission data is limited at best and cannot be accurately modeled. The CH^* and pressure signals in the simulations at the head end of the chamber do not phase average well over the windowed period. This suggests that they are not very coherent over the period of a longitudinal acoustic mode. The experiment differs in this case as it clearly shows in Figure 6.17(b) that the chemiluminescence signals lag the pressure at the same location by approximately $\pi/2$ radians. The time difference between the pressure and chemiluminescence is a good starting point to determine the time lag necessary to construct 1D models of the thermoacoustic chugging behavior.

From Figure 6.16(a) of the high oxidizer temperature simulated case of the injector recess, the OH^* rises and falls at the same rate as the pressure, but lags constantly by about $\pi/4$ radians. The CH^* signal does not follow the pressure signal. The windowed time corresponds to a frequency of 1460Hz for the simulation. The corresponding experimental data shows that the OH^* and CH^* signals follow each other and also lag the pressure by approximately $\pi/4$ radians. The windowed time corresponds to a frequency of 1599Hz for the experiment. Figure 6.17 shows that the phase averaged signals between the experiment and simulation in the chamber are not in agreement. The chemiluminescence signals lead the pressure in the simulation, but lag the pressure in the experiment.

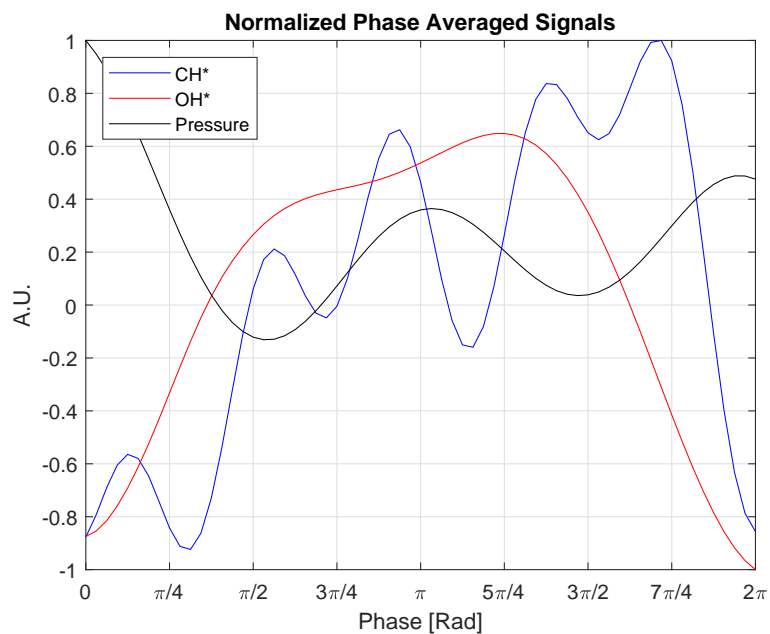


(a) CFD

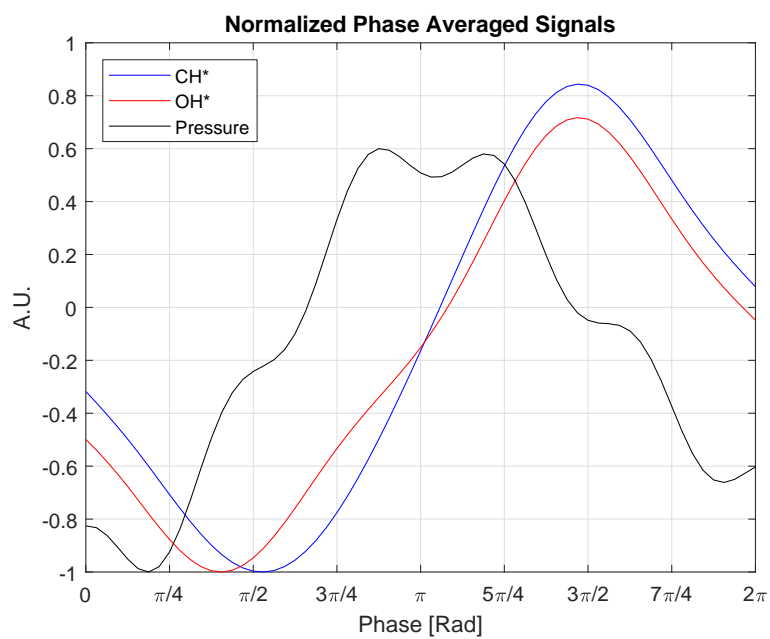


(b) Experiment

Figure 6.16.: Comparison of phase averaged signals of CH*, OH* and pressure at $-0.350''$ (Injector Recess), for an oxidizer temperature of 400K/440K.

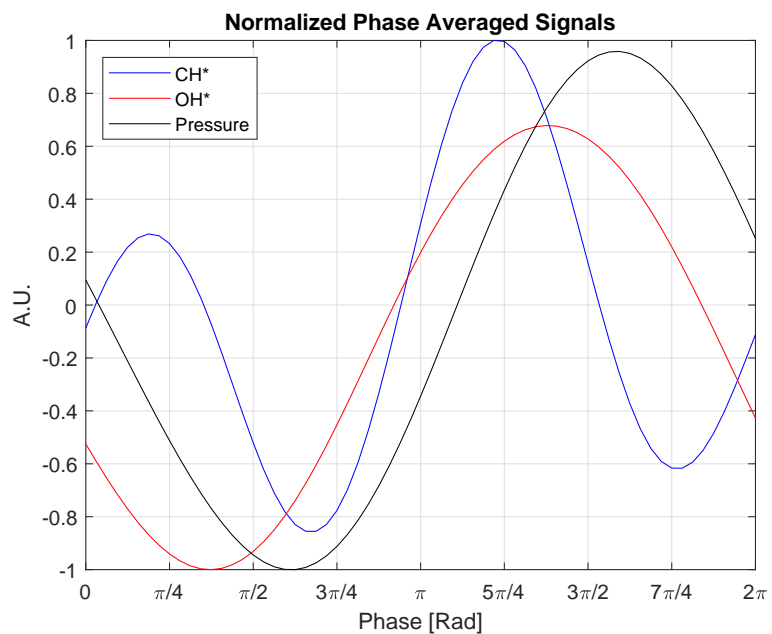


(a) CFD

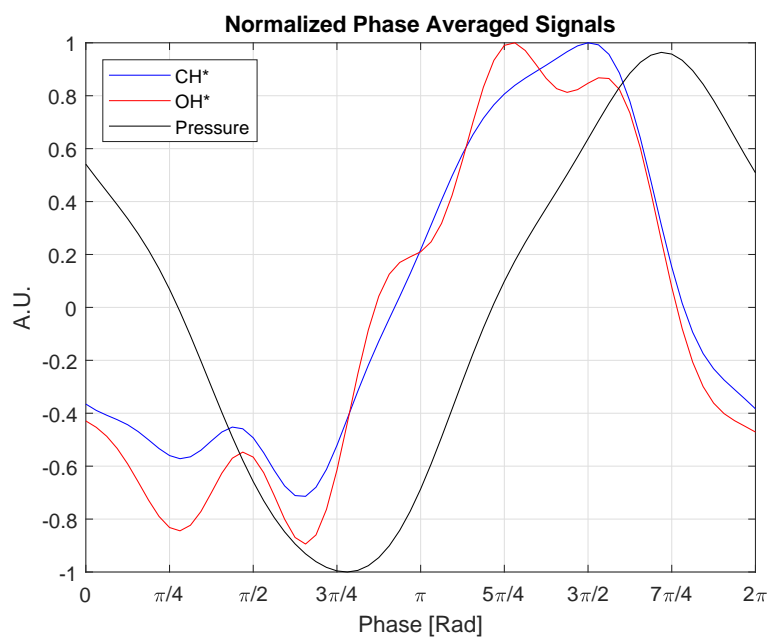


(b) Experiment

Figure 6.17.: Comparison of phase averaged signals of CH*, OH* and pressure at 0.300'' (Chamber Head End), for an oxidizer temperature of 400K/440K.

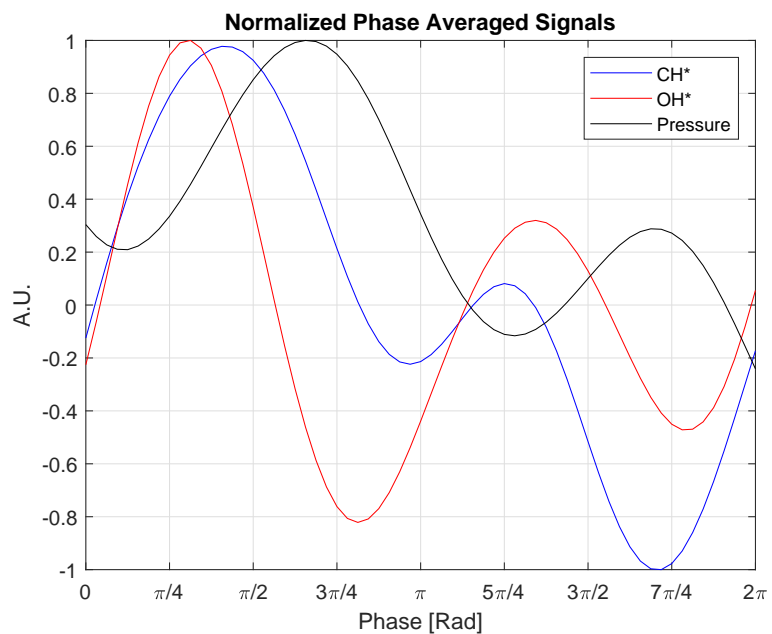


(a) CFD

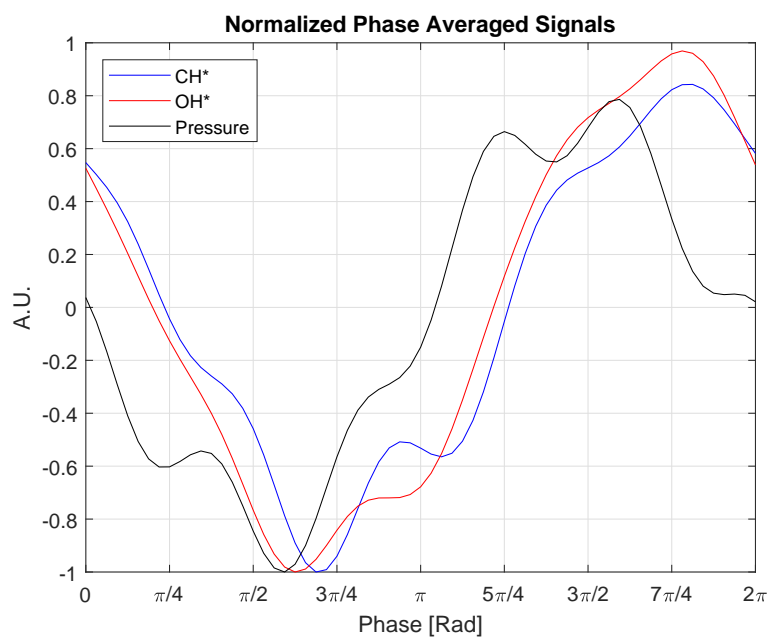


(b) Experiment

Figure 6.18.: Comparison of phase averaged signals of CH*, OH* and pressure at $-0.350''$ (Injector Recess), for an oxidizer temperature of 700K.



(a) CFD



(b) Experiment

Figure 6.19.: Comparison of phase averaged signals of CH*, OH* and pressure at 0.300'' (Chamber Head End), for an oxidizer temperature of 700K.

Figure 6.20 shows the heat release mode shapes generated by DMD of the simulation of HAMSTER for an oxidizer temperature of 400K. In all three modes there appear to be a significant amount of heat release from the shear layer extending into the recirculation zone. Figure 6.20(a) in particular shows a heat release map of the combustion extending far downstream the chamber in line with a bulk response. Figure 6.20(b) shows a striped map of the heat release downstream into the chamber, indicating oscillations spatially. This may be the result of a vortex coupled or modulated heat release.

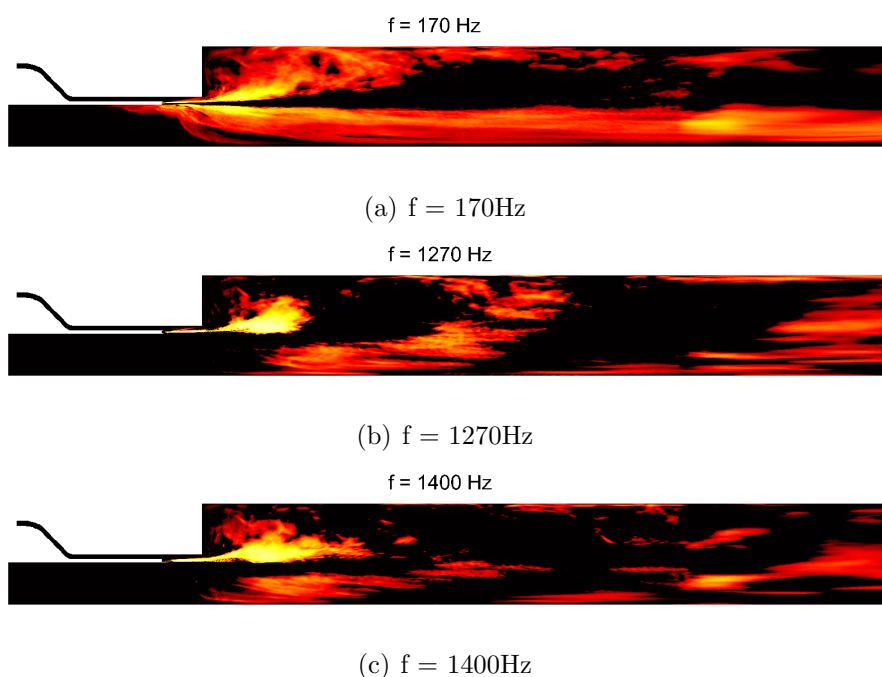


Figure 6.20.: DMD generated heat release spatial maps for the 400K oxidizer temperature case.

Figure 6.21 shows the heat release modes generated by DMD of the simulation of HAMSTER for an oxidizer temperature of 700K. It is clear that the frequency in line with the fundamental acoustic mode (1320Hz) also experiences modulation due to the chugging, which suggests that the heat release is dependent on the mean pressure changes. If the heat release is purely acoustic driven, whereby the acoustics

modulate the injector response and its generated hydrodynamics, it is expected that the combustion modes would follow a similar pattern to the acoustic modes. It is also apparent that the very high frequency modes ($\geq 6\text{kHz}$) of the combustion are do not significantly contribute with regard to driving a thermoacoustic response in this case.

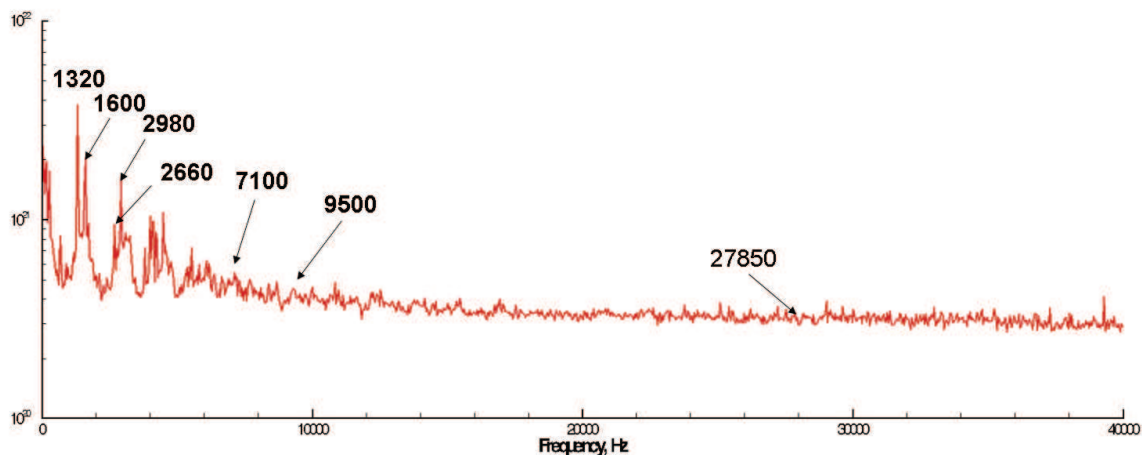


Figure 6.21.: DMD of the heat release in HAMSTER for an oxidizer temperature of 700K.

Figure 6.22 shows the heat release mode shapes generated by DMD of the simulation of HAMSTER for an oxidizer temperature of 700K. In comparison to the 400K case, the low frequency modes shown in Figures 6.20(a) and 6.22(a) appear to have the same shape. The mode in Figure 6.22(b) has the same heat release mode shape in the shear layer and recirculation zone as the mode in Figure 6.20(b), but does not exhibit the same spatial oscillations downstream in the combustion chamber. In fact, the heat release appears to be more abundant further downstream, just downstream of the edge of the recirculation zone. Figure 6.22(c) shows the combustion mode shape to be similar to that of Figure 6.22(b), but less abundant and spatially dispersed. All three modes show evidence of combustion upstream of the fuel collar tip indicating that the oscillations in the recess can transport fuel into the oxidizer flow.

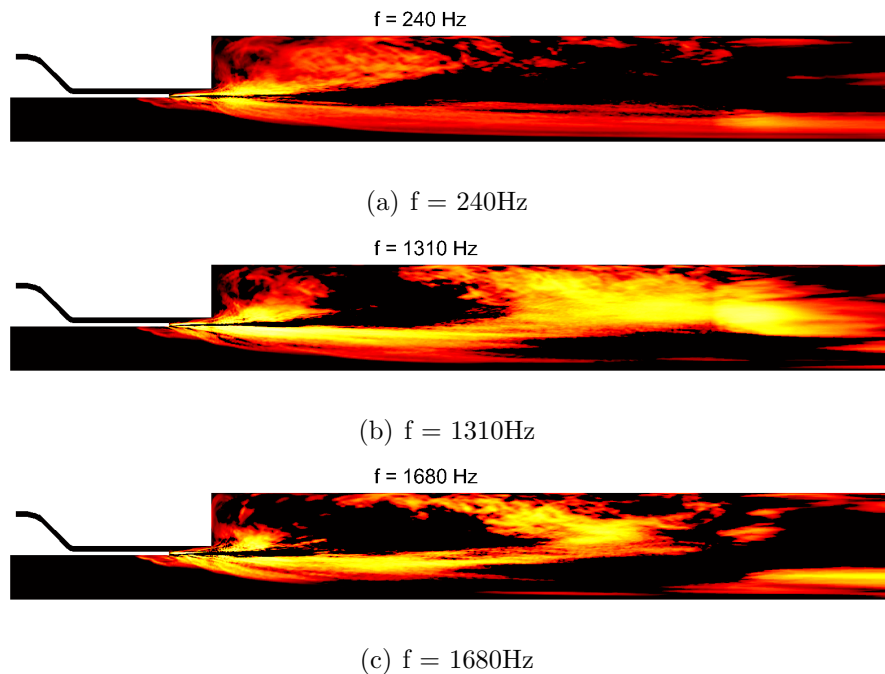


Figure 6.22.: DMD generated heat release spatial maps for the 700K oxidizer temperature case.

In all cases the heat release profile tends to show two distinct regions of heat release: (1) on the fuel side of the shear layer localized to the head end of the chamber, extending into the recirculation zone, and (2) on the oxidizer side of the shear layer extending downstream, where for the more high frequency coupled cases the heat release profile is continuous and "wraps-up" to make contact with the outer wall just beyond the recirculation zone (see Figure 6.15). It follows that the fuel side heat release profile must be influenced by the vortex production from the injector and backward facing step, and the shear layer extending a short way into the combustion chamber. An investigation into the hydrodynamics is required to better understand how the heat release profile might behave during a self-excited instability.

6.2.3 Hydrodynamic Features

Since it is known that vortex shedding from a geometric feature can drive a combustion instability it is at least prudent to investigate the mechanisms producing vortices that may influence the combustion in HAMSTER. For the nominal case the DMD of the vorticity in HAMSTER is shown in Figure 6.23. Besides the typical frequencies one would expect at the excited thermoacoustic resonance modes, some higher frequency modes were identified. The 27.85kHz mode is expected to originate from the fuel flow generating vortices off the fuel collar tip. The 9.5kHz mode, which is not prominent, is expected to originate from the oxidizer flow generating vortices off the fuel collar tip. The frequency at 7.1kHz is in the general vicinity of the frequencies seen in the experiments, but do not seem to participate in the thermoacoustic coupling in the simulations, per the pressure response (see Figure 6.8(b)).

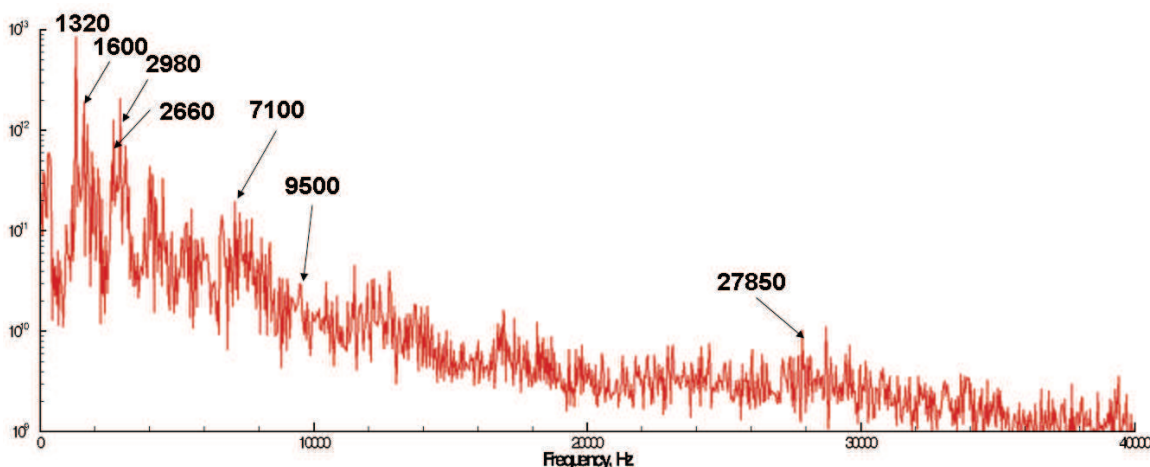


Figure 6.23.: DMD of vorticity in HAMSTER for an oxidizer temperature of 700K.

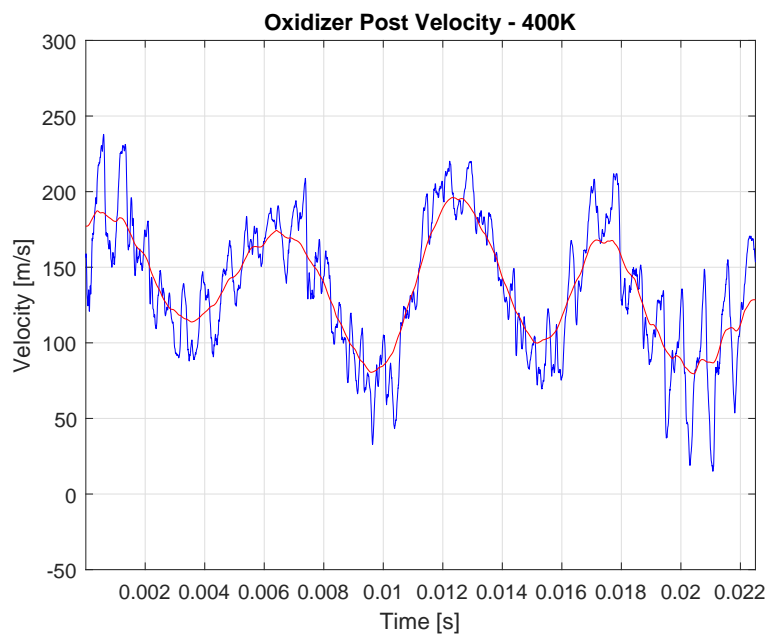
Figure 6.24 shows the oscillation of the free stream oxidizer flow velocity for an oxidizer temperature of 400K, at the tip of the fuel collar axially and at the centerline of the oxidizer post radially. Figure 6.24(b) shows the wavelet transform of the free stream oxidizer post velocity.

It shows that in this case the velocity oscillates mainly with the low frequency chug, but on occasion becomes modulated at a frequency corresponding to the fundamental acoustic mode for the system. Figure 6.24(a) shows that the free stream velocity can oscillate with an amplitude as much as 40% of the mean velocity. This will inevitably alter the boundary layer thickness at the fuel collar tip and result in a modulation of the vortex frequency generated at the fuel collar tip. The boundary layer shows evidence of an adverse pressure gradient (Figure 6.26(a)) because the free stream velocity becomes negative for some cycles. Besides the negative flow velocity, this boundary layer would promote vortex shedding off the fuel collar, and therefore for some moments the vortex production is completely halted.

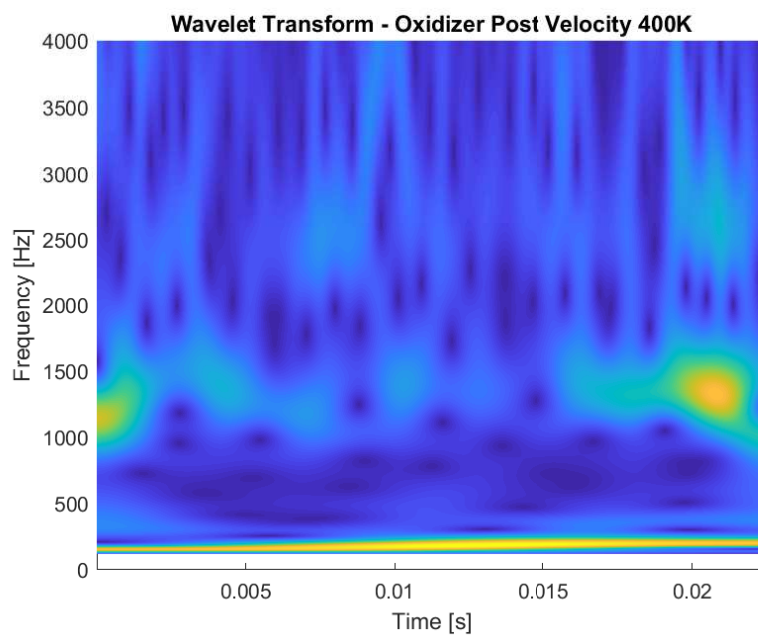
Figure 6.25 shows the oscillation of the free stream oxidizer flow velocity for an oxidizer temperature of 700K, at the tip of the fuel collar axially and at the centerline of the oxidizer post radially. In this case the free stream velocity fluctuations are more rapid, mostly corresponding to the driven first longitudinal acoustic mode frequency. Although the frequency of these oscillations are rapid and produce large changes in free stream velocity the boundary layer thickness does not appear to change much, as seen in Figure 6.26(b).

Because the boundary layer thickness does not change much during the oscillations for the high oxidizer temperature case, the free stream velocity was estimated with a running mean, and this was used concurrently with the boundary layer thickness, to estimate the oxidizer flow based vortex shedding frequency using Equation 2.13. Figure 6.27 illustrates how the vortex shedding oscillates in time due to the oscillation of the free stream velocity and boundary layer thickness.

The boundary layer thickness is estimated using 95% of the free stream velocity. Figure 6.27 shows that vortex shedding frequency due to the oxidizer flow off the fuel collar oscillates greatly, and tends to be larger than 10kHz in both oxidizer temperature cases.

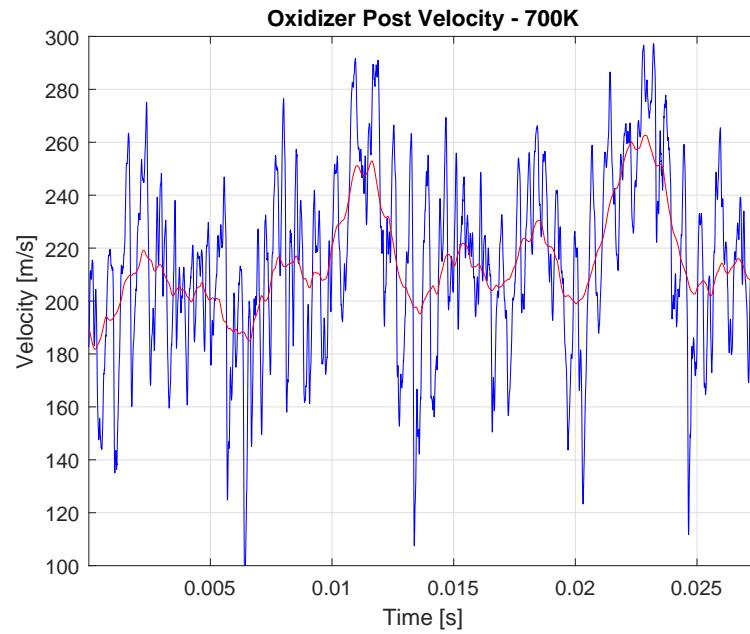


(a) Raw

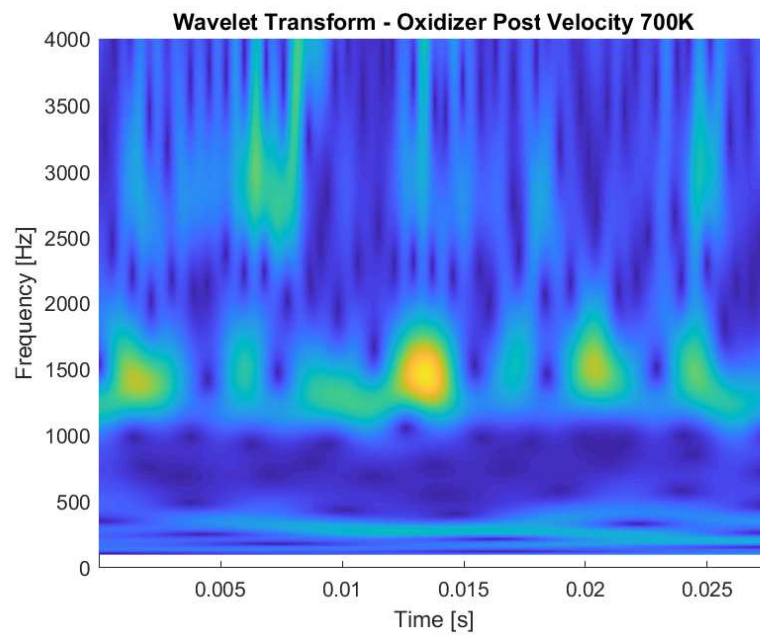


(b) Wavelet Transform

Figure 6.24.: Oscillating oxidizer post centerline velocity near fuel collar tip for the case with an oxidizer temperature of 400K.

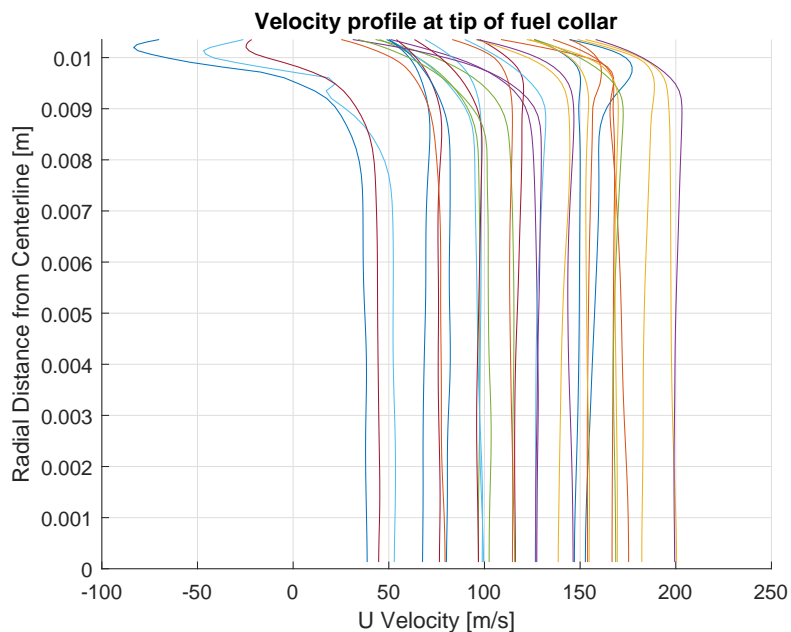


(a) Raw

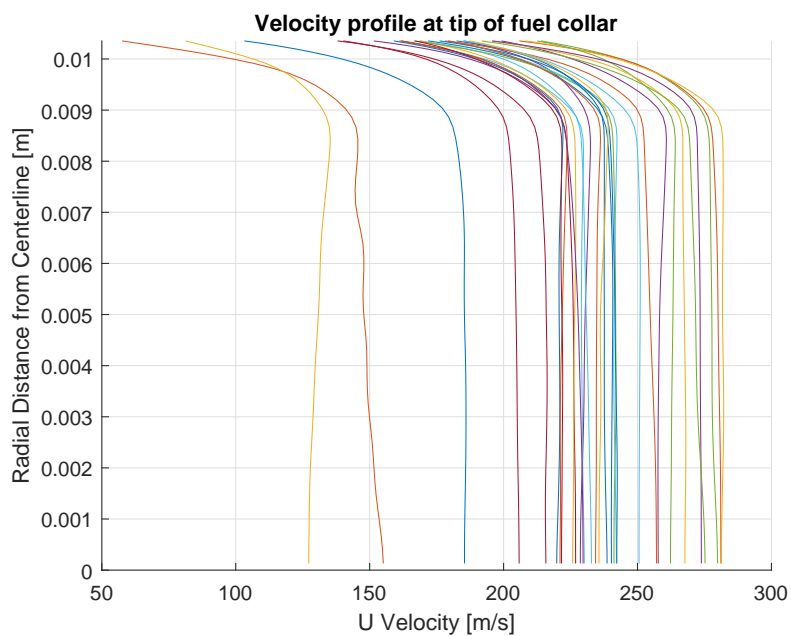


(b) Wavelet Transform

Figure 6.25.: Oscillating oxidizer post centerline velocity near fuel collar tip for the case with an oxidizer temperature of 700K.

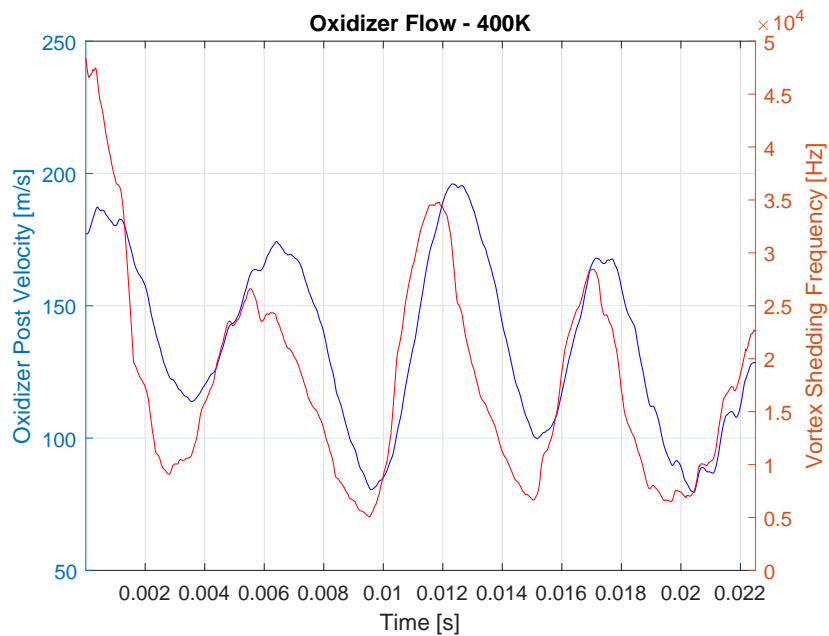


(a) 400K

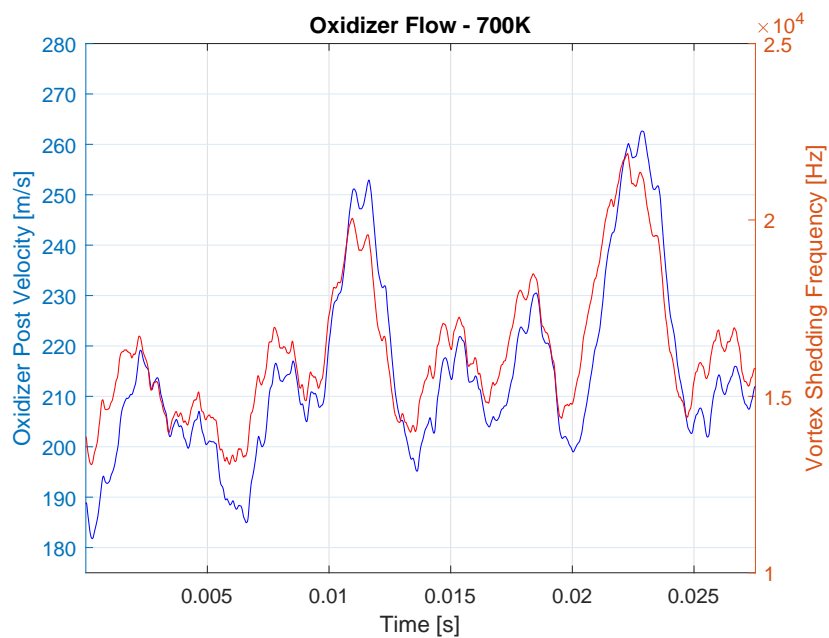


(b) 700K

Figure 6.26.: Simulated velocity profile of the oxidizer at the tip of the fuel collar. The evolution of the velocity profile and boundary layer of the oxidizer flow through 27.5ms, with increments of 0.75ms.



(a) 400K



(b) 700K

Figure 6.27.: Simulated vortex shedding frequency off the fuel collar due to the oxidizer flow calculated using Equation 2.13. The vortex shedding is calculated using a boundary layer thickness approximated by using 95% of the mean velocity profile at each time step.

However, the vortex shedding frequency does have periods, in the high oxidizer temperature case (Figure 6.27(b)), where the frequency is not modulated that greatly. The frequency modulation could result in a mean frequency with side lobes or just a broadband spectrum. From Figure 6.23, there is evidence of vorticity frequencies round 12kHz and 17kHz, which may correlate with the modulation of the vortex shedding from the fuel collar tip.

The low oxidizer temperature case (Figure 6.27(a)) also shows that the vortex shedding frequency modulation appears to lag the free stream velocity oscillations by approximately 0.5-1ms. This is likely due to the boundary layer having a delayed response to the change in free stream velocity. The high oxidizer temperature case (Figure 6.27(b)) shows that the vortex shedding frequency modulation is in unison with the free stream velocity oscillations; which is likely due to the boundary layer thickness not altered during the oscillations. Additionally, the main discrepancy between the experiment and simulated estimations of the vortex shedding frequency off the fuel collar using Equation 2.13 is likely due to the estimated turbulent boundary layer thickness, which is notoriously difficult to estimate a priori.

6.2.4 Coupling Characteristics

The interaction of the shear layer with the recirculating zone behind the backward facing step is of main interest. To interrogate the shear layer and recirculating regions the PMT measurements were arranged in the manner shown in Figure 6.28. The probe volumes of the PMT measurements intersecting with the chords of the cross sectional area were designed to gather chemiluminescence emissions (or lack thereof) produced in the radially convecting shear layer and/or recirculating zones. The probe volumes not intersecting with the diameter of the cross section will now be referred to as "chord inner" and "chord outer" based on the relative position of the probe volume to the diameter of the cross section.

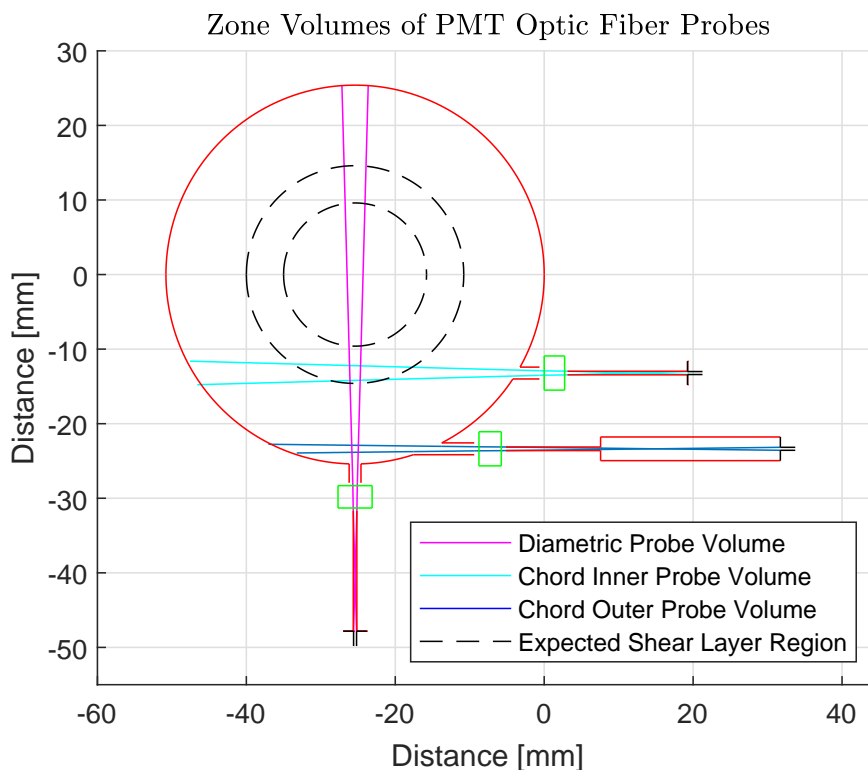


Figure 6.28.: Schematic cross-section of where the PMT probe volumes intersect the domain.

The areas and locations of intersection of the probe volumes were used to extract chemiluminescence data from the simulations in the same manner as mentioned in the previous sections. The data from the experiments and simulations can then be directly compared in the same spatial configurations.

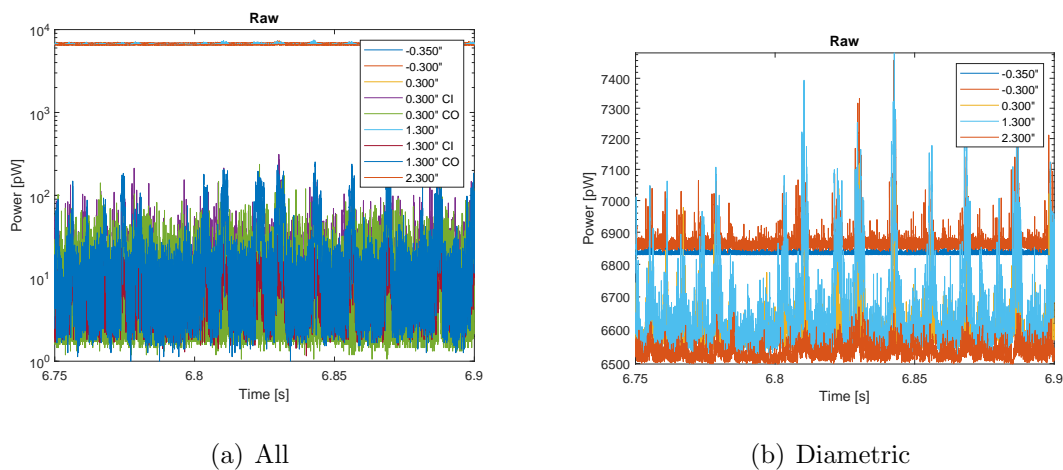


Figure 6.29.: Raw PMT data from experiment at 500K. Only diameter cutting measurements are shown in 6.29(b).

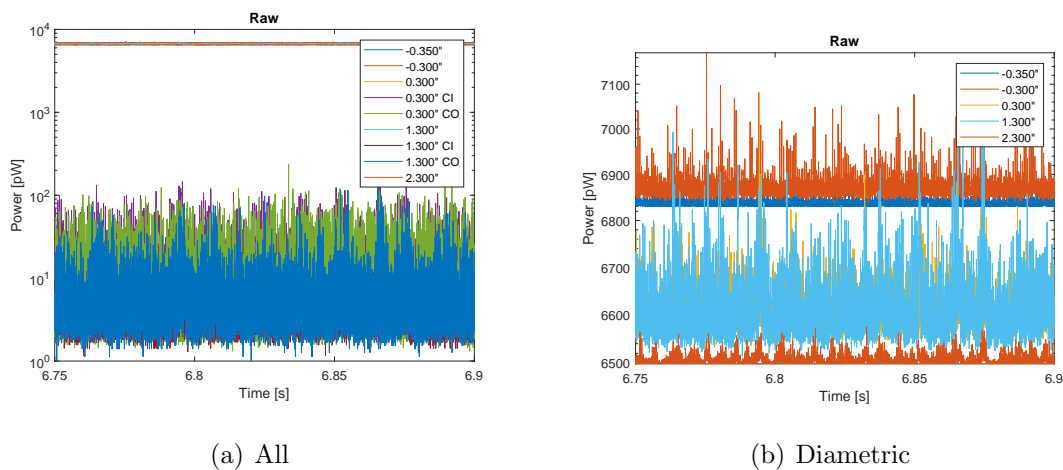


Figure 6.30.: Raw PMT data from experiment at 700K. Only diameter cutting measurements are shown in 6.30(b).

Figures 6.29 and 6.30 are representative of the raw data collected by all PMT positions in the experiments at oxidizer temperatures of 500K and 700K respectively. Similarly, Figures 6.31 and 6.32 are representative of the raw data collected by all PMT positions in the simulations at oxidizer temperatures of 400K and 700K respectively.

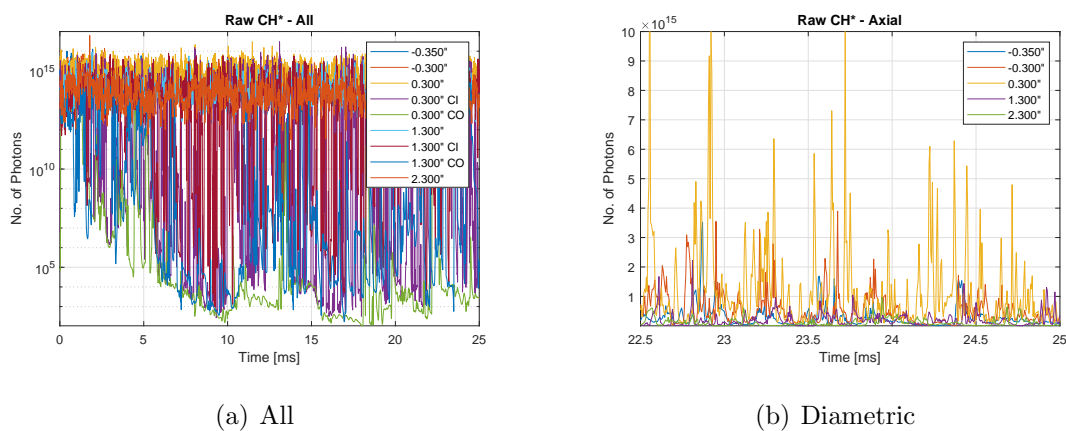


Figure 6.31.: Raw PMT data from the simulation at 400K. Only diameter cutting measurements are shown in 6.31(b).

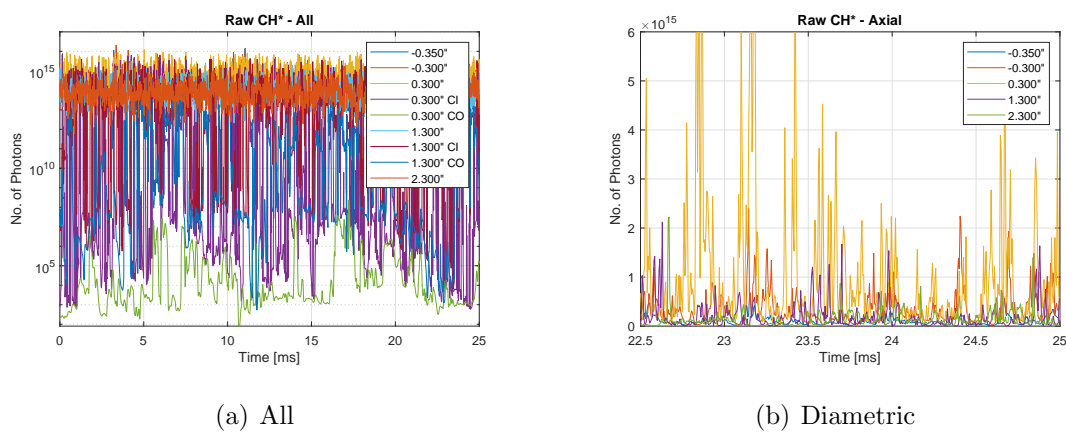


Figure 6.32.: Raw PMT data from simulation at 700K. Only diameter cutting measurements are shown in 6.32(b).

The diametric measurements are isolated to show the irregularity of the signals. This is a consequence of line of sight integrated measurements intersecting a complex arrangement of emitters due to the reacting flow field crossing into the probe volumes at an instance in time. It is therefore required that the signals be analyzed using correlation based methods.

One apparent feature of the raw signals is the relative magnitude of the signal oscillations for the chordal measurements compared to the diametric measurements. The fluctuation in chemiluminescence emissions collected by the chordal measurements tend to fluctuate much more widely than the diametric measurements. This occurs in both the simulation and experimental measurements. For the lower temperature measurements it is evident that in both the simulation and experiment the chord outer locations show a distinctly larger variance in signal fluctuation consistent with a sudden mixing and combustion event in the recirculation zone.

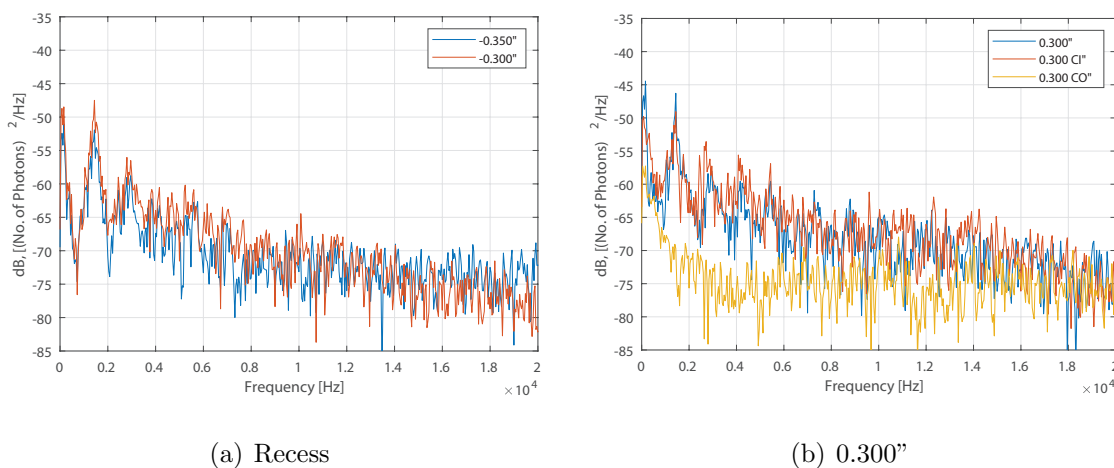


Figure 6.33.: PSDs of PMT data from experiment at 500K, set 1 of 2.

Figures 6.33 and 6.34 show the PSDs corresponding to the raw PMT data from the experiment at an oxidizer temperature of 500K, while 6.35 and 6.36 shows the PSDs for an oxidizer temperature of 700K. The PSDs are grouped by axial locale, apart from the last set which aims to compare the PSDs of the diametric measurements made at different axial locations. In all cases the 1L mode is most apparent except for the

0.300" chord outer location which shows a diminished correlation. The diminished response in the chord outer location nearest to the head end is consistent with a mostly non-reacting recirculation zone.

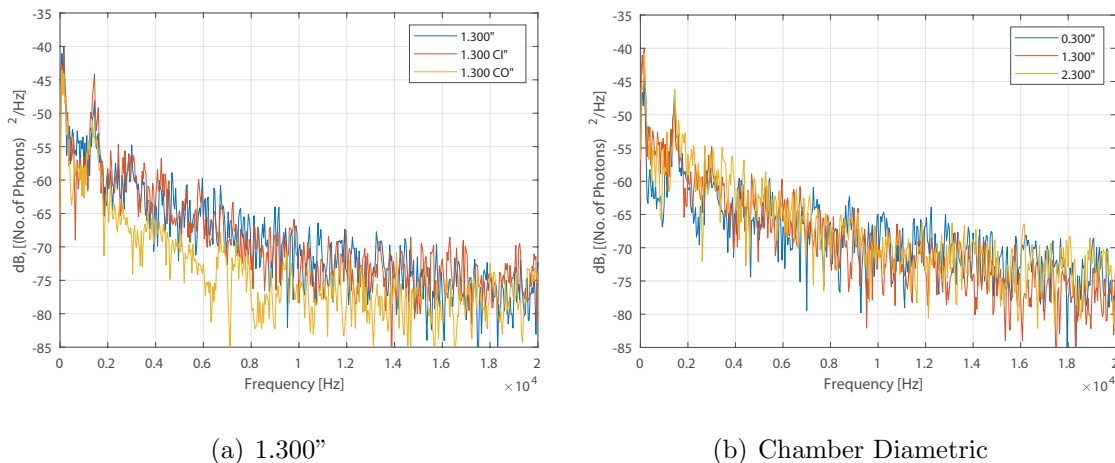


Figure 6.34.: PSDs of PMT data from experiment at 500K, set 2 of 2.

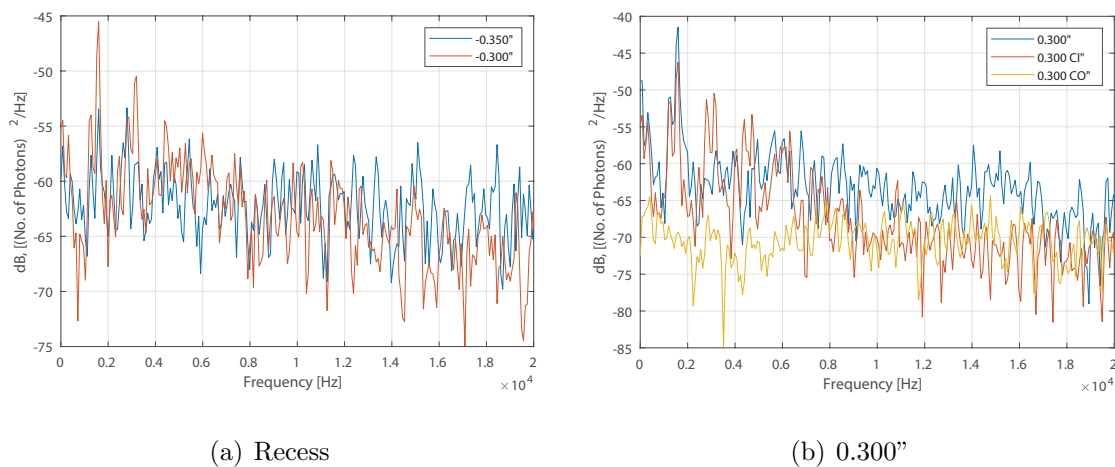


Figure 6.35.: PSDs of PMT data from experiment at 700K, set 1 of 2.

It is also evident that at the 1.300" chord outer locations there appears to be a mode of higher frequency which stands out. It is at approximately 6500Hz for the

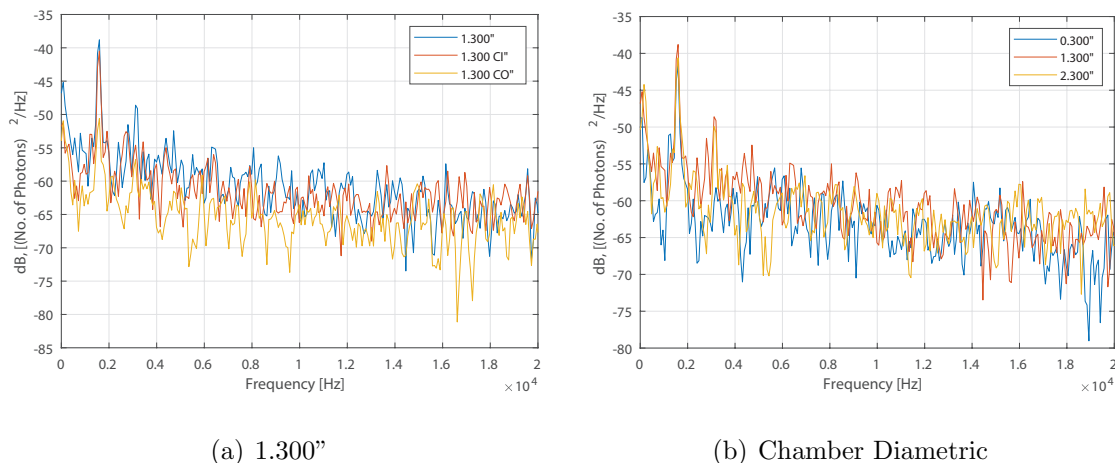


Figure 6.36.: PSDs of PMT data from experiment at 700K, set 2 of 2.

50K case, while for the 700K case there are a few modes at 6-9kHz which may not directly correspond with the longitudinal acoustic modes.

The PMT measurements in the 700K case generally reflect the longitudinal acoustic mode shown in the pressure PSDs. The PMT measurements for the 500K case does not show the higher order modes; the corresponding pressure modes tend to not feature in the 500K case. Especially with regard to investigating any mechanics of higher frequency it seems that drawing conclusions with confidence from the PSDs of the individual channels is not viable. Because of the nature of the measurement the signal ratio of the change in strength between the radial and axial directions may be low. Hence, the correlating the axial signals to other spatial measurements, such as the chordal locations, may be a necessity when taking measurements in the combustion chamber.

Figures 6.37 and 6.38 show the PSDs of the PMT data extracted from the simulation conducted at an oxidizer temperature of 400K. Unlike the experimental data, the PSDs of the extracted simulation data do not show prominent modes directly corresponding with the longitudinal acoustic modes. They do, however, show some prominent modes around the 3-4kHz, especially at the 1.3'' location. In qualitative agreement with the experimental data, the 0.3'' chord outer location shows low level

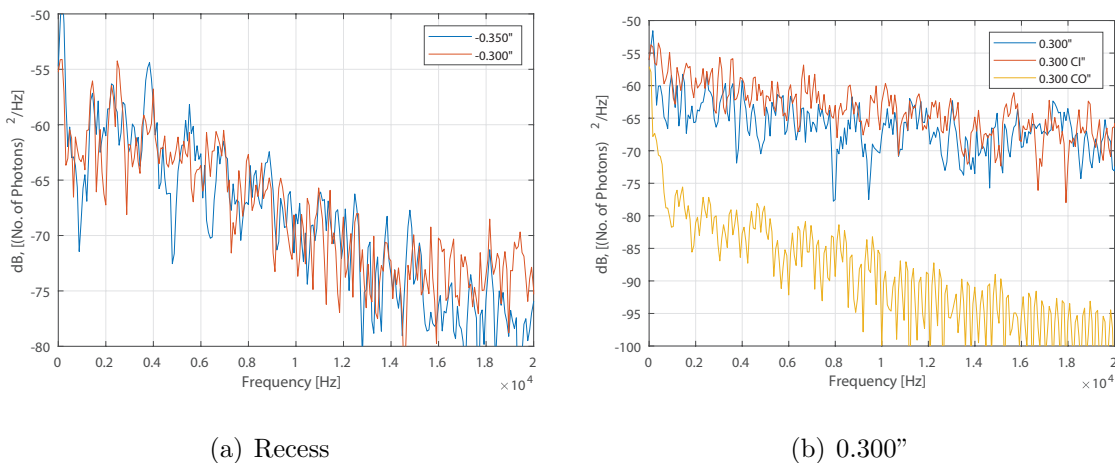


Figure 6.37.: PSDs of PMT data from simulation at 400K, set 1 of 2.

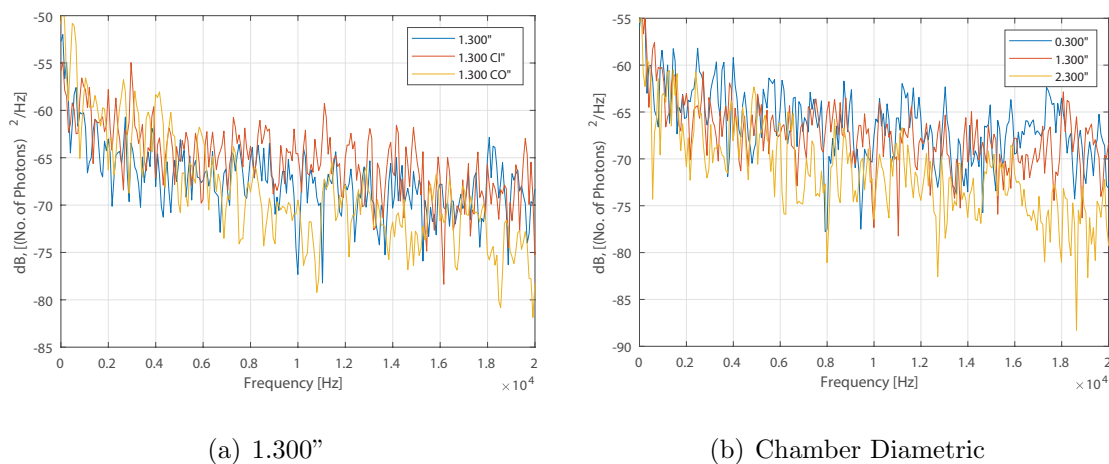


Figure 6.38.: PSDs of PMT data from simulation at 400K, set 2 of 2.

fluctuations corresponding to the emissions from the recirculation zone behind the backward facing step. The 1.3" chord inner location also shows a mode at approximately 11kHz. At 1.3" downstream of the dump plane the 1.3" chord inner location may be intersecting a large portion of the shear layer.

For the simulated 700K oxidizer temperature case, Figures 6.39 and 6.40 show the PSDs of the extracted PMT data. The PSDs of the PMT extracted from the injector recess show modes which correspond to the longitudinal acoustic modes.

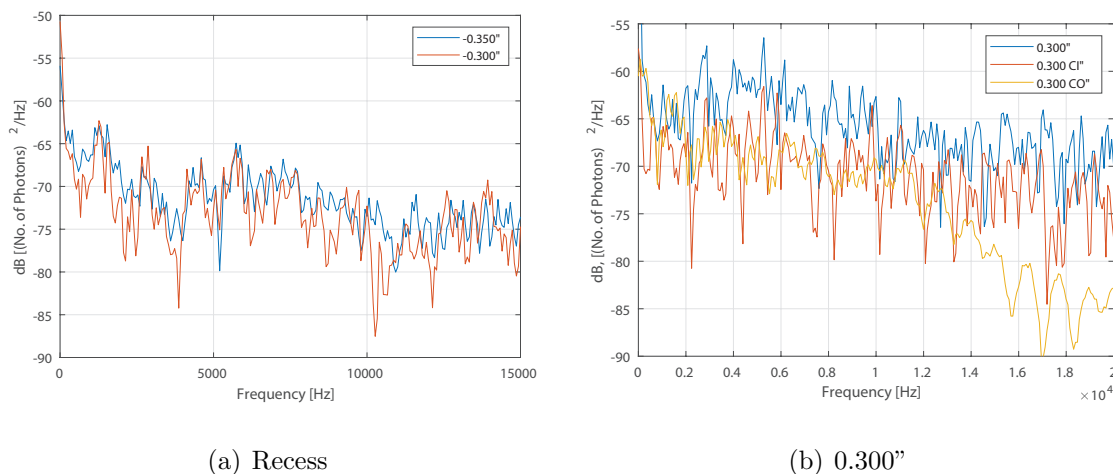


Figure 6.39.: PSDs of PMT data from simulation at 700K, set 1 of 2.

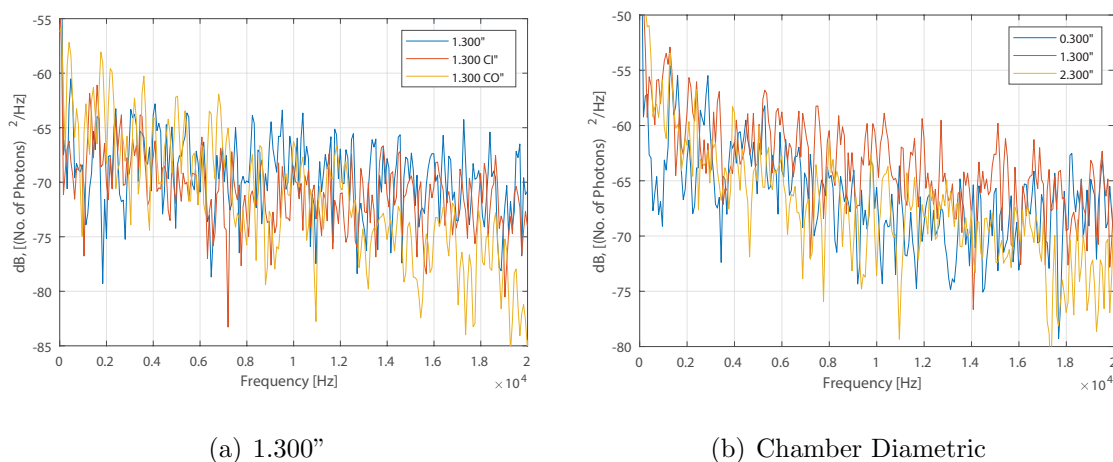


Figure 6.40.: PSDs of PMT data from simulation at 700K, set 2 of 2.

Only the downstream axial positions show some evidence of the longitudinal acoustic modes, it is interesting to note that the 0.3" diametric measurement does not show a significant response to the acoustic modes. But, like the 400K case, high frequency modes around the 5-7kHz range appear to be prominent. Again, the conclusion drawn from these data sets is that emission data from the chamber needs to be analyzed at tomographically for each axial position and correlations need to be made between all positions.

Below are the CPSDs computed on the experimental and simulation PMT data for all chamber locations. As before, the probe volume locations between the experiments and simulations match. In each case a reference location was chosen which was then cross-correlated with another set of locations of interest, usually the chordal locations.

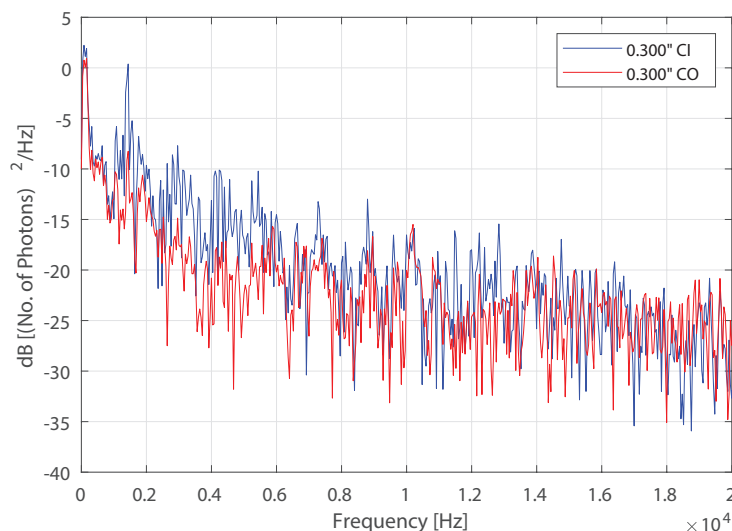


Figure 6.41.: CPSD of the chordal positions relative to the PMT measurement taken at 0.300" downstream of the dump plane, in the experiment for an oxidizer temperature of 500K.

Figures 6.41, 6.42 and 6.43 show CPSDs of the PMT data from the experiment with an oxidizer temperature of 500K. From Figure 6.41 there is a strong correlation between the axial and chord inner signals at the 1L frequency. Interestingly, there is an agreement in correlation at frequencies of about 7.1, 10.3 and 13.8kHz between all the measurements taken at the 0.3" location.

From inspection of Figure 6.42 there does not appear to be any outstanding correlations, or at least that can be said with confidence, other than the frequency associated with the 1L mode. The same conclusions can be drawn for Figure 6.43, aside from the mode at approximately 11.5kHz. The mode only appears to be correlated with the 0.3" and 1.3" locations, but not the 2.3". This mode could be associated

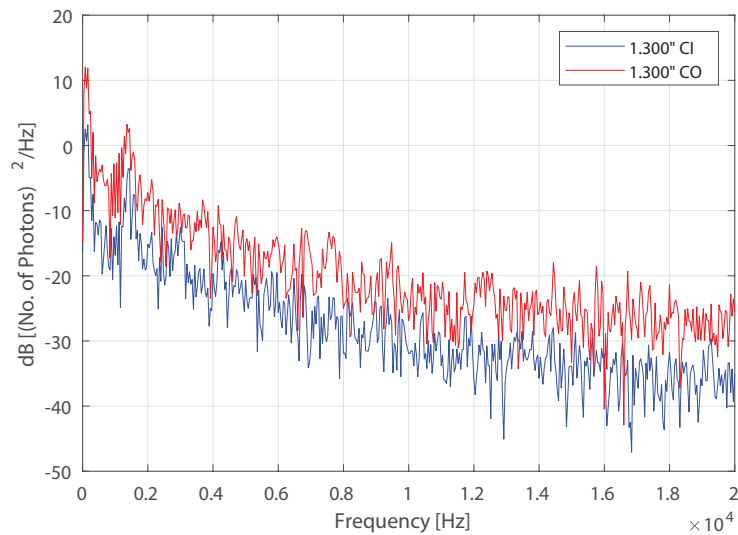


Figure 6.42.: CPSD of the chordal positions relative to the PMT measurement taken at 1.300'' downstream of the dump plane, in the experiment for an oxidizer temperature of 500K.

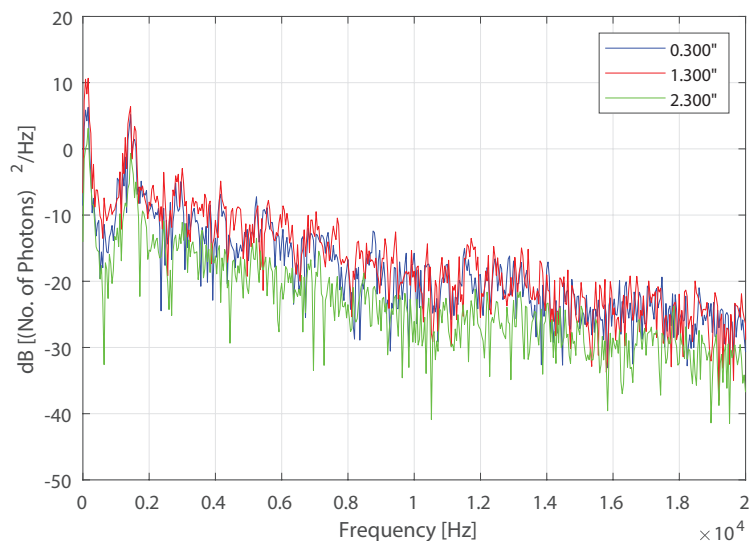


Figure 6.43.: CPSD of the axial chamber positions relative to the PMT measurement taken at 0.300'' upstream of the dump plane (injector recess), in the experiment for an oxidizer temperature of 500K.

with the vortex shedding from the injector collar, where the vortices propagate downstream.

Figures 6.44, 6.45 and 6.46 show CPSDs of the PMT data from the experiment with an oxidizer temperature of 700K. Particularly in Figure 6.44, the main feature of interest is the mode in both CPSDs at approximately 6kHz. Although it appears that this mode might be directly acoustically coupled, its amplitude response does not follow the trend of the acoustic harmonics. This leads to the belief that this mode might originate or be driven by a hydrodynamic mode.

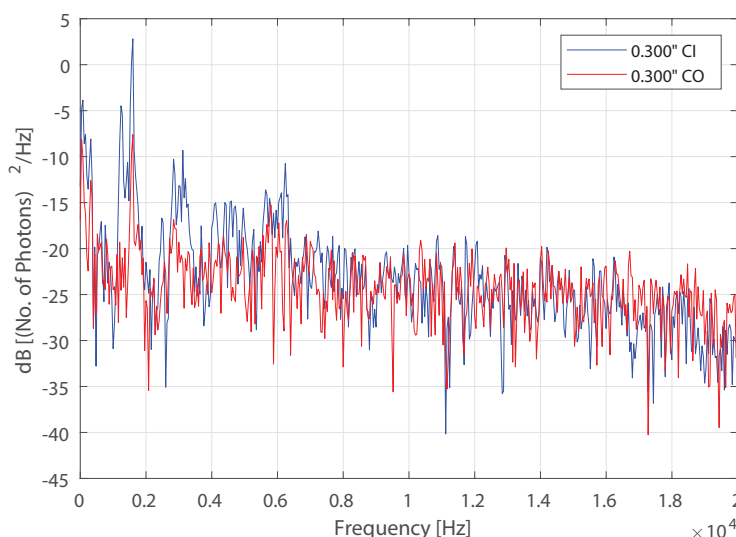


Figure 6.44.: CPSD of the chordal positions relative to the PMT measurement taken at 0.300" downstream of the dump plane, in the experiment for an oxidizer temperature of 700K.

The higher frequencies in Figure 6.44 are not correlated enough to make a confident conclusion. For Figure 6.45 there are no prominent modes above the mode associated with the 1L and its harmonics. The 6kHz mode does not appear to feature at this location. Figure 6.46 generally shows the PMT signals fluctuating at frequencies consistent with the acoustics in the system. Although, the existence of a mode at 6kHz for all diametric channels should be noted.

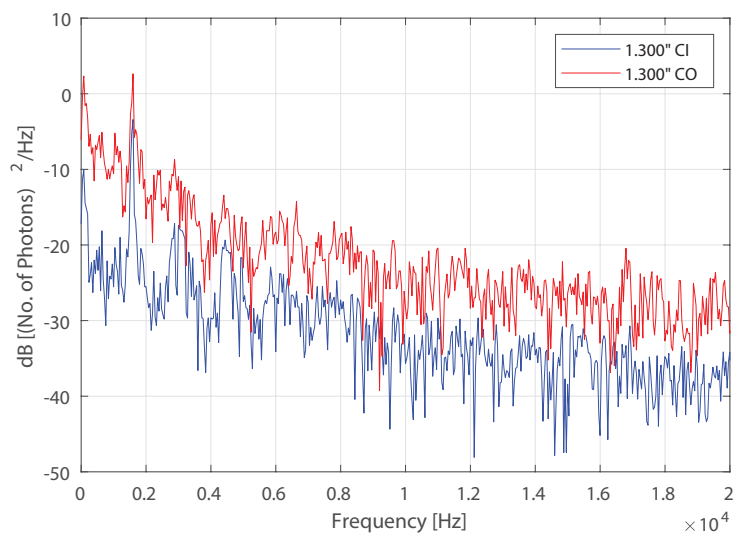


Figure 6.45.: CPSD of the chordal positions relative to the PMT measurement taken at 1.300'' downstream of the dump plane, in the experiment for an oxidizer temperature of 700K.

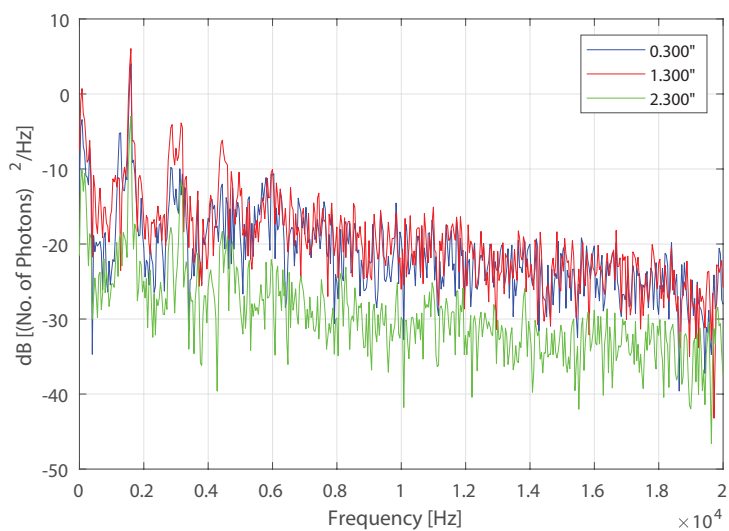


Figure 6.46.: CPSD of the axial chamber positions relative to the PMT measurement taken at 0.300'' upstream of the dump plane (injector recess), in the experiment for an oxidizer temperature of 700K.

Figures 6.47, 6.48 and 6.49 show CPSDs of the PMT data from the simulation with an oxidizer temperature of 400K. In Figure 6.47 some high frequency modes are well correlated; the modes at 13 and 15.4kHz in the chord inner signal appear to correlate well with the diametric signal at 0.3". Generally the chord outer signal does not correlate too well with the diametric signal at this location.

At the location of 1.3" (Figure 6.48) there does not seem to be any modes of prominence worthy of mention, but the change in trend of the signal spectrum noise floor at 6-8kHz may be of interest.

When the comparison is made between all the extracted diametric data in Figure 6.49, a strong correlation is observed between the injector recess and 0.3" locations. There are a number of well formed peaks, most likely associated with the acoustics, from 1.5-7kHz. Although the 1.3" location does not correlate well with injector recess over a good portion of the spectrum, a set of modes around 8kHz is observed. The signal extracted from the 2.3" location does not correlate well with the signal in the injector recess.

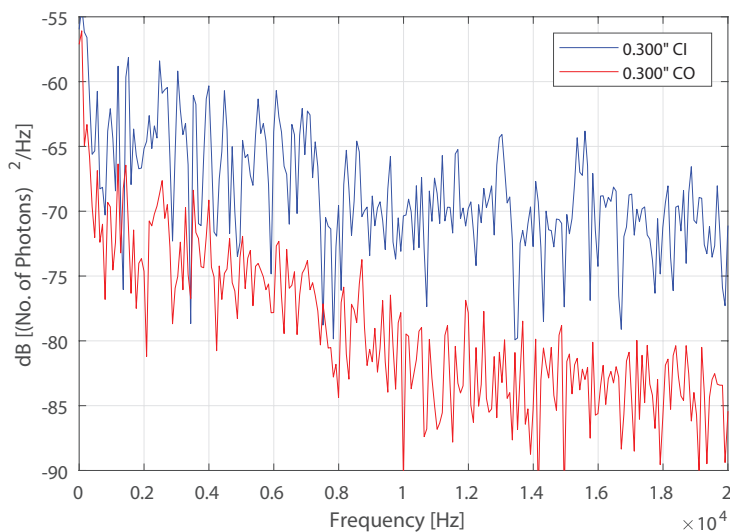


Figure 6.47.: CPSD of the chordal positions relative to the PMT data extracted at 0.300" downstream of the dump plane, in the simulation for an oxidizer temperature of 400K.

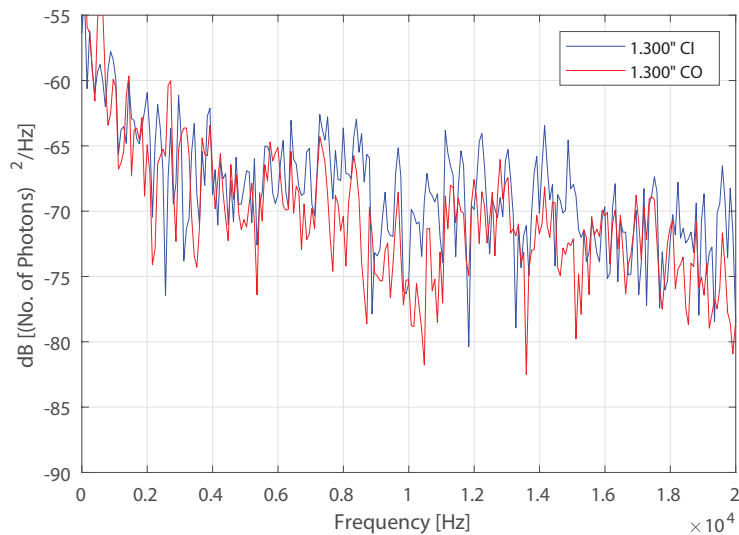


Figure 6.48.: CPSD of the chordal positions relative to the PMT data extracted at 1.300'' downstream of the dump plane, in the simulation for an oxidizer temperature of 400K.

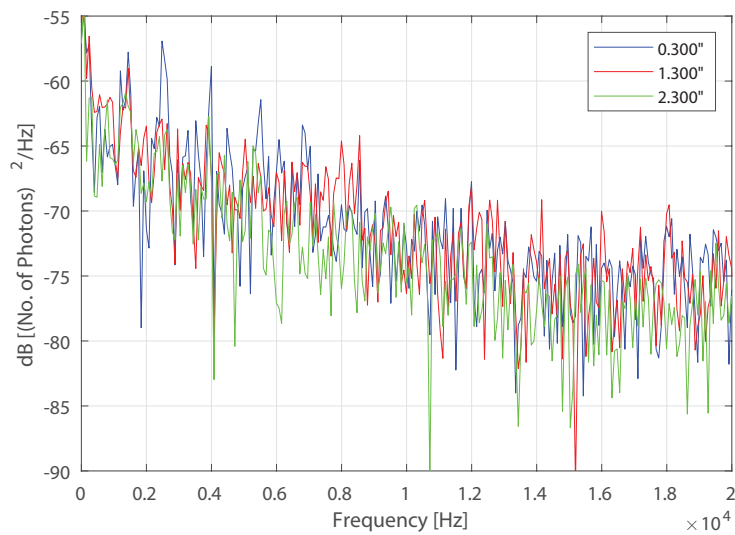


Figure 6.49.: CPSD of the axial chamber positions relative to the PMT data extracted at 0.300'' upstream of the dump plane (injector recess), in the simulation for an oxidizer temperature of 400K.

Figures 6.50, 6.51 and 6.52 show CPSDs of the PMT data from the simulation with an oxidizer temperature of 700K. In Figure 6.50 there is quite good agreement between the chord inner and outer CPSDs with the diametric location. The differences include the prominent mode in the CPSD between the chord inner and diametric location at 2.7, 5.3 and 9.9kHz. The correlation of the diametric location with the chord outer location shows some correlation at the lower modes, but as before in the other cases does not show any correlation at the higher frequency ranges.

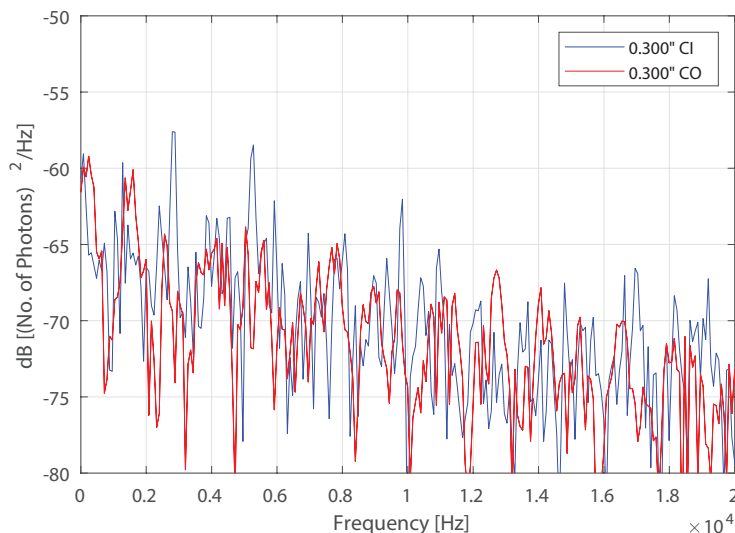


Figure 6.50.: CPSD of the chordal positions relative to the PMT data extracted at 0.300” downstream of the dump plane, in the simulation for an oxidizer temperature of 700K.

In Figure 6.51 there is little correlation with the diametric measurement. With a cautious exception, there may be some correlation at the higher frequencies such as 10 and 16.5kHz. In Figure 6.52 all chamber diametric signals correlate well with the injector recess for the lower frequency ranges, where the 0.3” location correlates the best. All signals seem to correlate well at frequencies around 10 and 16.5kHz; this, again, could be a result of the convection of vortices from the injector collar tip. Additionally, an elevated noise floor band around the 4-6kHz range is also apparent.

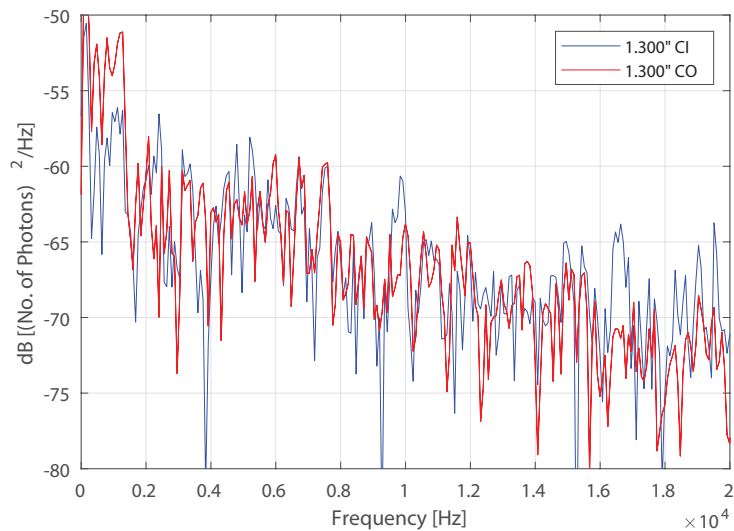


Figure 6.51.: CPSD of the chordal positions relative to the PMT data extracted at 1.300'' downstream of the dump plane, in the simulation for an oxidizer temperature of 700K.

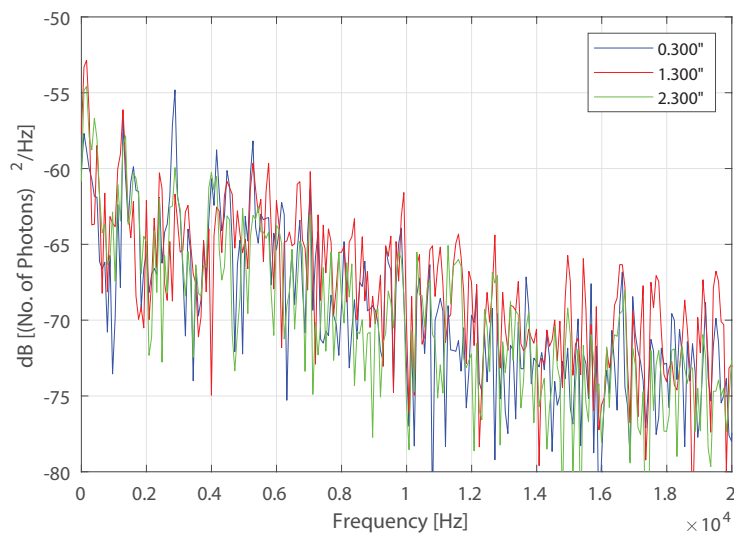


Figure 6.52.: CPSD of the axial chamber positions relative to the PMT data extracted at 0.300'' upstream of the dump plane (injector recess), in the simulation for an oxidizer temperature of 700K.

In general the axial modal decompositions of the simulated data agree with the experiment at a qualitative scale. A number of higher frequency modes are identified that exceed the range of the expected longitudinal acoustic modes. These are likely attributed to vortex formations in the shear layer and produced directly from the injector collar tip.

It is noticeable, however, that the computed data is unable to emulate the spatial trends expected in an experiment and this is reflected in the inability of the cross-correlation of the probe volume data at a specified axial location to yield a comparable result with the experiment. This may be due to the forced axisymmetry of the simulation.

It is advisable that this technique of extracting emission data from the simulation to directly compare to the experiment only be done on a three dimensional computed domain.

6.3 Summary

In general the simulations track the observed experimental behavior well, especially the low oxidizer temperature case. The simulation predicts that at low oxidizer temperature a low frequency bulk (chug) mode dominates, and at high oxidizer temperature a high frequency longitudinal acoustic mode (fundamental mode) dominates, which agrees with the experiments. The main discrepancies lie in the high oxidizer temperature case where the simulation fails to predict the dominant resonance mode accurately, but may be able to model the physical mechanism related to the strong thermoacoustic coupling observed in the experiment. In all cases there are discrepancies with respect to the physics at frequencies beyond 4kHz. The strongly forced axisymmetry might not be able to predict some of the higher frequency vorticity generated from the jet entering the chamber and may alter the growth or decay of some mechanisms dependent on three dimensional physics.

The chemiluminescence data from the injector recess compares well between the experiment and simulations, but the data from the chamber do not. This suggests that the mechanics in the injector recess might be well modeled. Following from that conjecture, the velocity at the injector collar tip was analyzed to determine how the vortex shedding resulting from the flow over the tip would change during an oscillation. It was found that the vortex shedding frequency related to the specific mechanics of vortex shedding over a thick/thin plate varied greatly. It is therefore unlikely to drive a thermoacoustic frequency directly due to its time scale, but may contribute, together with the chemical kinetics, in facilitating a characteristic time scale approaching the fundamental acoustic frequency and thus drive a thermoacoustic instability.

7. CONCLUSIONS

7.1 Summary of Observations

Combustion instabilities were observed in HAMSTER for a wide range of geometries and conditions. There three distinct types of combustion instability mechanism observed in the experiments; with one mechanism tentatively confirmed, but definitely not significant. The three instability mechanisms observed were: (1) combustion coupled feed system chug (combustion driving), (2) vortex driven thermoacoustic chug (combustion driven at low frequency), and (3) longitudinal thermoacoustic instability (high frequency).

The feed system chug is the typical low frequency chugging mode observed in many devices, combustion or purely hydrodynamic. In HAMSTER it was predicted by validated chug models, but did not contribute in any significant way. Additionally, the feed system chug was not predicted in the simulation because the timescales of the mode are far too large to be resolved by the running time of the simulation.

The two thermoacoustic modes were observed in HAMSTER in both the experiment and simulation. The existence of the modes during operation were never mutually exclusive; the low frequency chugging mode usually modulated the higher frequency mode through a nonlinear interaction and resulted in a number of side lobe frequencies. The low frequency mode was shown to alter the sound speed in the chamber during its cycle, thus altering the frequency of the longitudinal acoustic mode in the chamber and the system as a whole. Sweeping through oxidizer temperatures from low ($< 550K$) to high ($> 575K$) a fundamental shift in the dominant mechanism was shown to occur, where the shift in response was from a dominant chugging mode to a dominant longitudinal acoustic mode respectively. The shift in behavior was shown to occur purely based on oxidizer temperature, despite efforts

to alter the oxidizer post length to favor resonance at a lower oxidizer temperature. There is a strong possibility that the chemical kinetics facilitates the transition behavior between a dominant chugging to a dominant longitudinal acoustic response with change in oxidizer temperature. As the oxidizer temperature increases the number of locations with higher temperature increases. The effect of local temperature on the rate of the combustion reactions is exponential, which is why it is sensitive to perturbation and could potentially yield significantly different results with small change in oxidizer temperature.

From the simulations of the low temperature oxidizer case (400K), which quite accurately resembled what was observed in the experiments, the coupled mechanisms which drove the low frequency modes were observed. The experiments and simulations both showed that the low frequency response manifested itself as a bulk fluid response in the system, or a chug. This was quite apparent in the chamber and oxidizer manifold where the constant phase of the acoustic mode in both the chamber and oxidizer manifold were confirmed in both the experiment and simulations. Additionally, the oxidizer post did exhibit a phase relationship between its ends, but it did not correspond to standing wave, but rather a delayed pulsing behavior between the manifold and chamber.

The simulation showed that during this pulsing behavior the oxidizer flow was greatly accelerated, especially when the chamber manifested a rarefaction. The accelerated oxidizer resulted in the formation of a single large vortex shed from the injector and backward facing step. The large vortex was efficient at entraining the excess fuel and heated products from the recirculation zone thereby producing a large localized heat release from the combustion. The accelerated flow into the chamber, together with the sudden combustion then effectively rose the chamber pressure to a point where the flow velocity of oxidizer was suddenly reduced to a near stall. This process is very similar to a typical feed system chug, but the main difference lies in how the instability is initiated. The 1D acoustic model was adept at predicting the low frequency acoustic response in the response even with the coupled effect of the

combustion. This suggests that the oscillations are born from Helmholtz or lumped acoustic response of the system and exacerbated by the vortex-combustion coupling from the injector and backward facing step. It was found that relatively small changes in oxidizer post length or oxidizer temperature did not change the mode frequency. However, a change in combustor length (not shown in this document) resulted in a significant change in the frequency of the thermoacoustic chug mode. This may suggest that the acoustic compliance of the chamber, and possibly the oxidizer manifold is the main cause of this particular type of instability. It should be noted that although the compliant nature of the chamber and oxidizer manifold due to their large volumes may be the root cause, it is very possible and likely that the frequency of the thermoacoustic chug response can take on higher frequencies which may depend on the time scales of the vortices shed from the dump plane. This effect has been shown before in studies of combustion instabilities in ramjet combustors [100]. It has been suggested that a one dimensional approach might be sufficient to predict this kind of instability; in the author's opinion a modified version of the n-tau model to include the synchronization with the vortex shedding, convection and combustion from the injector could be sufficient.

There was less agreement between the simulation and the experiments done at higher oxidizer temperature. Both the experiment and simulation showed the modulating effect of the low frequency chug on the longitudinal acoustic response of the system, but there was a discrepancy between the frequency and amplitude of the dominant longitudinal thermoacoustic mode. The range of experiments conducted did show that there existed an optimal oxidizer temperature to produce the most resonance in the system; this was in line with the predictions made by Dr. Swanand Sardeshmukh based on the computations made of the CVRC.

The experiments showed a highly nonlinear, regular waveform representative of the fundamental acoustic mode response in the system. The harmonics of this mode were integer multiples. The simulations showed a dominant mode at a significantly lower frequency and the waveform was closer to a sinusoid than a steep-fronted wave due

to a lower amplitude. Interestingly, the modulated frequency or side lobe simulated corresponds almost exactly to the high frequency mode excited in the experiment. This may be coincidental or it may be indicative that the simulation was able to produce the physics associated with this mode, but for some unknown reason this mode was not excited.

7.2 Comments on Objectives

- *Experimentally investigate the effect of injector dynamics on thermoacoustic instabilities.*

- *Design, build, and test a model rocket combustor with self-excited thermoacoustic instabilities.*

HAMSTER was constructed and tested. It performed quite well producing a number of interesting self-excited instabilities. The tests were repeatable (except for one case) and the measurements were precise.

- *Investigate the effect of the oxidizer temperature on acoustic and hydrodynamic time scales.*

The variation of oxidizer temperature had a significant and repeatable impact on the response characteristics of HAMSTER. It was found that at lower oxidizer temperatures the system responded predominantly with a chug, regardless of adjusting the oxidizer post length to suit the acoustic time scale in pursuit of longitudinal acoustic resonance. At higher oxidizer temperatures, above expected nominal conditions for the standard geometry, the acoustic resonance was slightly diminished with no signs of chugging. This may have been indicative of acoustic detuning. The resonating fundamental frequency scaled linearly with oxidizer temperature, which was unexpected.

As for the hydrodynamic time scales, the oxidizer post velocity generally increased with oxidizer temperature. It was expected that the time scales of the hydrodynamic features produced as a result would shorten. It is still not clear how the increase in oxidizer velocity contributes to the Kelvin-Helmholtz instability within the shear layer, and how that couples with the combustion and acoustic modes in the chamber.

- *Investigate how much of an effect (if any) the recess length has on system thermoacoustic response.*

The recess length was reduced completely for a series of tests. The effect was negligible on all the instabilities. There were some unique features present, but ultimately non-contributing. This adds to the evidence that the vortex shedding from the fuel collar may not be a major contributor to the coupling mechanics needed to produce a thermoacoustic instability.

- *Investigate the physics of the recirculation zone behind the backward facing step and the reacting shear layer from the injector.*
 - *Determine if the temperature in the recirculation zone correlates with the observed changes in system behavior.*

It was found that the mean wall temperature at the head end of the combustor was generally quite cool for all cases ($< 1000K$), except for one outlying case. This was observed in both the experiments and the simulations. This suggests that some combustion products are entrained into recirculation zone, but the recirculation zone comprises mostly of unburnt fuel, especially in the fuel rich cases. The experiments showed that at higher oxidizer temperatures that the wall temperature did not always correlate well with associated dynamics from the instabilities. The reason is not fully known, but from the simulations at high oxidizer temperature it appeared that the shear layer and jet from the injector, and the dynamics thereof were not significantly affected by the recirculation zone composition and temperature in these cases.

- *Discern oscillations of combustion in the chamber resulting from the vortex generation off of the dump plane backward facing step.*

The low frequency oscillations were identified from the chemiluminescence measurements at the head end of the combustor. The exact coherent frequencies were not identified because of the nature of the measurement (line of sight integrated) and the complexity of the reacting shear dynamics at the head end of the chamber.

- *Attempt to identify vortex shedding frequency off of fuel collar using chemiluminescence measurements in the injector recess.*

It was found that the vortex shedding off of the fuel collar increased in frequency within expectations of the theory of vortex shedding from a thin flat plate. This data was determined from the coherence between the pressure and chemiluminescence measurements at the head end of the chamber. However, the data from the simulations showed that a highly modulated response occurs and that the vortex shedding frequencies are likely much higher than predicted with the estimated values using experimental data.

- *Identify oscillations that may result from free shear layer Kelvin-Helmholtz instabilities.*

The mechanics of the shear layer in the chamber was not discernible by any of the measurements made in the experiments. The simulations helped to visualize the dynamics and showed that the complexity of the reacting shear layer, with vortex roll-up in the free flow, was very high. Only the most coherent frequencies, those associated directly with the resonant modes of the system were able to be identified with high enough confidence. Thus, any information regarding the vortex shedding in the chamber was inconclusive.

- *Produce verifiable high-fidelity measurements to validate computational models.*

- *Design and construct an experiment with well-defined boundary conditions and easily controllable input parameters.*

The designed boundary conditions in HAMSTER were robust and compared well with the simulations. Controlling the overall mass flow rate to within simulated conditions was a little less successful, but was still within a reasonable margin; the equivalence ratios were equal. The propellant conditioning performed well and compared well with the simulated conditions.

- *Use high frequency response pressure measurements to spatially resolve fundamental acoustic mode and determine manifold responses.*

The acoustic mode shapes of the chugging and fundamental longitudinal modes were successfully mapped. Unfortunately, the higher order modes were not able to be spatially resolved.

- *Verify one dimensional acoustics assumption using high frequency response pressure measurements.*

Using azimuthally clocked pressure measurements at the head end of the chamber it was found that for all, but one case, the one dimensional assumption with respect to the instabilities in the chamber held. There was evidence of out of plane motion in the oxidizer manifold, but it was shown that the oscillations were evanescent and decayed quickly within the oxidizer post, never reaching the chamber.

- *Utilize high temporal resolution, spatially refined probes to measure chemiluminescence oscillations related to the combustion.*

Gathering chemiluminescence data in the injector recess was quite successful and useful in determining the dynamics within the initial stages of the reacting shear layer. The measurements were also useful in determining flame position in time. The measurements in the chamber were not very successful because they were plagued by the line of sight integration of complex reacting structures. The chordal measurements provided good information on occasion, but were not always consistent.

7.3 Future Work

- Develop 1D model for the low frequency thermoacoustic chug instability and integrate it into existing chug models.

- Change oxidizer post diameter to effectively change the oxidizer velocity. Performing the same oxidizer temperature sweeps and equivalence ratios might help to robustly determine if the transition from chug to longitudinal instability is strongly related to the vortex shedding from the injector.
- Oxidizer temperature sweep during hot fire might reveal threshold transition point.
- Attempt very localized PIV on the shear layer near the dump plane to gather important velocity information and determine hydrodynamic characteristics.

REFERENCES

- [1] D. T. Harrje. Liquid propellant rocket combustion instability. Technical report, January 1972.
- [2] Mark Dranovsky. *Combustion Instabilities in Liquid Rocket Engines*. AIAA, 2007.
- [3] F. E. Culick and Paul Kuentzmann. Unsteady Motions in Combustion Chambers for Propulsion Systems. Technical Report AC/323(AVT-039)TP/103, NATO RESEARCH AND TECHNOLOGY ORGANIZATION NEUILLY-SUR-SEINE (FRANCE), December 2006.
- [4] Matthew Joseph Casiano. *Extensions to the Time Lag Models for Practical Application to Rocket Engine Stability Design*. PhD thesis, The Pennsylvania State University, August 2010.
- [5] Martin Summerfield. A Theory of Unstable Combustion in Liquid Propellant Rocket Systems. *Journal of the American Rocket Society*, 21(5):108–114, September 1951.
- [6] Rayleigh. The Explanation of Certain Acoustical Phenomena. *Nature*, 18:319–321, July 1878.
- [7] Luigi Crocco. High-Frequency Combustion Instability in Rocket Motor with Concentrated Combustion. *Journal of the American Rocket Society*, 23(5):301–313, 1953.
- [8] R. BYRNE. Longitudinal pressure oscillations in ramjet combustors. In *19th Joint Propulsion Conference*. American Institute of Aeronautics and Astronautics.
- [9] Yen Yu, James C. Sisco, Stanford Rosen, Ajay Madhav, and William E. Anderson. Spontaneous Longitudinal Combustion Instability in a Continuously-Variable Resonance Combustor. *Journal of Propulsion and Power*, 28(5):876–887, 2012.
- [10] Yen Ching Yu. Experimental and analytical investigations of longitudinal combustion instability in a continuously variable resonance combustor (CVRC). *Theses and Dissertations Available from ProQuest*, pages 1–217, January 2009.
- [11] Matthew E. Harvazinski, William E. Anderson, and Charles L. Merkle. Analysis of Self-Excited Combustion Instabilities Using Two- and Three-Dimensional Simulations. *Journal of Propulsion and Power*, 29(2):396–409, 2013.
- [12] R. Smith, G. Xia, W. Anderson, and C. L. Merkle. Computational studies of the effects of oxidiser injector length on combustion instability. *Combustion Theory and Modelling*, 16(2):341–368, April 2012.

- [13] Matthew E. Harvazinski, Cheng Huang, Venkateswaran Sankaran, Thomas W. Feldman, William E. Anderson, Charles L. Merkle, and Douglas G. Talley. Coupling between hydrodynamics, acoustics, and heat release in a self-excited unstable combustor. *Physics of Fluids*, 27(4):045102, April 2015.
- [14] W. E. Anderson, S. V. Sardeshmukh, T. L. Fuller, and A. Pons. AFOSR Annual Report. Technical Update, AFOSR, Purdue University, July 2017.
- [15] Nicolas Guezennec, Matthieu Masquelet, Edward D. Lynch, Brian Lariviere, Ramakanth Munipalli, Douglass G. Talley, and Suresh Menon. Engine-Level Simulation of Liquid Rocket Combustion Instabilities: Transcritical Combustion Simulations in Single Injector Configurations. 2012.
- [16] Romain Garby. *Simulations of flame stabilization and stability in high-pressure propulsion systems; Etude numrique de la stabilisation de flamme et des instabilites de combustions dans les systmes de propulsion*. PhD thesis, 2013.
- [17] Laurent Selle, Rodolphe Blouquin, Marie Thron, Luc-Henry Dorey, Martin Schmid, and William Anderson. Prediction and Analysis of Combustion Instabilities in a Model Rocket Engine. *Journal of Propulsion and Power*, 30(4):978–990, 2014.
- [18] S. Srinivasan, R. Ranjan, and S. Menon. Flame Dynamics During Combustion Instability in a High-Pressure, Shear-Coaxial Injector Combustor. *Flow Turbulence Combust*, 94(1):237–262, January 2015.
- [19] X. Jiayang and K. Duraisamy. Reduced-order reconstruction of model rocket combustor flows. page <xocs:firstpage xmlns:xocs=""/>. American Institute of Aeronautics and Astronautics Inc, AIAA, 2017.
- [20] Tuan Nguyen and William Sirignano. The impacts of three flamelet burning regimes in nonlinear combustion dynamics. *Combustion and Flame*, 195:170, 2018.
- [21] Thierry J. Poinso, Arnaud C. Trouve, Denis P. Veynante, Sebastien M. Candel, and Emile J. Esposito. Vortex-driven acoustically coupled combustion instabilities. *Journal of Fluid Mechanics*, 177:265–292, April 1987.
- [22] K. C. Schadow and E. Gutmark. Combustion instability related to vortex shedding in dump combustors and their passive control. *Progress in Energy and Combustion Science*, 18(2):117–132, January 1992.
- [23] Romain Lacombe, Pierre Moussou, and Yves Aurgan. Whistling of an orifice in a reverberating duct at low Mach number. *J. Acoust. Soc. Am.*, 130(5):2662–2672, November 2011.
- [24] L.E. Kinsler, A. R. Frey, A. B. Coppens, and J. V. Sanders. *Fundamentals of Acoustics*. Wiley, 4 edition, January 2000.
- [25] S. Rodriguez, V. Gibiat, A. Lefebvre, and Stephane Guilain. Input impedance in flow ducts: Theory and measurement. *The Journal of the Acoustical Society of America*, 132(3):1494–1501, September 2012.
- [26] Ana Barjau. On the one-dimensional acoustic propagation in conical ducts with stationary mean flow. *The Journal of the Acoustical Society of America*, 122(6):3242–3251, December 2007.

- [27] T. Y. Lung and A. G. Doige. A timeaveraging transient testing method for acoustic properties of piping systems and mufflers with flow. *The Journal of the Acoustical Society of America*, 73(3):867–876, March 1983.
- [28] Alexander Gentemann, Andreas Fischer, Stephanie Evesque, and Wolfgang Polifke. Acoustic Transfer Matrix Reconstruction and Analysis for Ducts with Sudden Change of Area. In *9th AIAA/CEAS Aeroacoustics Conference and Exhibit*, Hilton Head, South Carolina, May 2003. American Institute of Aeronautics and Astronautics.
- [29] Flavio Bannwart, Guillaume PENELET, Pierrick Lotton, and Jean-Pierre Dalmont. Methods for transfer matrix evaluation applied to thermoacoustics. In Socit Franaise d’Acoustique, editor, *Acoustics 2012*, Nantes, France, April 2012.
- [30] Manohar Lal Munjal. *Acoustics of Ducts and Mufflers*. John Wiley and Sons, 2nd edition, 2014.
- [31] A. S. Hersh and B. E. Walker. Fluid Mechanical Model of the Helmholtz Resonator. NASA Contractor Report NASA CR-2904, NASA/Hersh Acoustical Engineering, 1977.
- [32] Stephen Turns. *An Introduction to Combustion: Concepts and Applications*. TMH, New York, 3 edition edition, 2012.
- [33] G. E. Childs and H. J. M. Hanley. Applicability of dilute gas transport property tables to real gases. *Cryogenics*, 8(2):94–97, April 1968.
- [34] J. O. Hirschfelder, C. F. Curtiss, and R. B. Bird. *The Molecular Theory of Gases and Liquids*. Wiley, New York, 1954.
- [35] R. E. Walker and A. A. Westenberg. Molecular Diffusion Studies in Gases t High Temepature. IV. Results and Interpretation of the CO₂-O₂, CH₄-O₂, H₂-O₂ and H₂o-O₂ Systems. *The Journal of Chemical Physcis*, 32(436), 1960.
- [36] T. H. Chung, L. L. Lee, and K. E. Starling. Correlation of the transport properties of simple fluids at low temperatures and high pressures based on the generalized Eucken relation and the molecular dynamics of hard sphere fluid. *Int J Thermophys*, 1(4):397–416, December 1980.
- [37] Robert Reid, Bruce E. Poling, and John M. Prausnitz. *The Properties of Gases and Liquids*. McGraw-Hill Companies, New York, 4th edition edition, April 1987.
- [38] H. Tennekes and J. L. Lumley. *A First Course in Turbulence*. MIT Press, 1972.
- [39] V. Tesa. Two-equation Turbulence Model Similarity Solution of the Axisymmetric Fluid Jet. *Acta Polytechnica*, 41(2), January 2001.
- [40] V. Tesa. Similarity Solutions of Jet Development Mixing Layers Using Algebraic and 1-Equation Turbulence Models. *Acta Polytechnica*, 46(1), January 2006.
- [41] Alfons Michalke. Survey on jet instability theory. *Progress in Aerospace Sciences*, 21:159–199, January 1984.

- [42] B. F. Armaly, F. Durst, J. C. F. Pereira, and B. Schnung. Experimental and theoretical investigation of backward-facing step flow. *Journal of Fluid Mechanics*, 127:473–496, February 1983.
- [43] Ralph W. Metcalfe, Steven A. Orszag, Marc E. Brachet, Suresh Menon, and James J. Riley. Secondary instability of a temporally growing mixing layer. *Journal of Fluid Mechanics*, 184:207–243, November 1987.
- [44] Ahmed F. Ghoniem and James A. Sethian. Effect of Reynolds number on the structure of recirculating flow. *AIAA Journal*, 25(1):168–171, January 1987.
- [45] Lambros Kaiktsis, George Em Karniadakis, and Steven A. Orszag. Unsteadiness and convective instabilities in two-dimensional flow over a backward-facing step. *Journal of Fluid Mechanics*, 321:157–187, August 1996.
- [46] G. Biswas, M. Breuer, and F. Durst. Backward-Facing Step Flows for Various Expansion Ratios at Low and Moderate Reynolds Numbers. *J. Fluids Eng*, 126(3):362–374, July 2004.
- [47] Daehyun Wee, Tongxun Yi, Anuradha Annaswamy, and Ahmed F. Ghoniem. Self-sustained oscillations and vortex shedding in backward-facing step flows: Simulation and linear instability analysis. *Physics of Fluids*, 16(9):3361–3373, July 2004.
- [48] Pierre-lie Weiss, Sbastien Deck, Jean-Christophe Robinet, and Pierre Sagaut. On the dynamics of axisymmetric turbulent separating/reattaching flows. *Physics of Fluids*, 21(7):075103, July 2009.
- [49] Andrew B. Bauer. Vortex Shedding From Thin Flat Plates Parallel to the Free Stream. *Journal of the Aerospace Sciences*, 28(4):340–341, 1961.
- [50] P. E. Dimotakis. Two-dimensional shear-layer entrainment. *AIAA Journal*, 24(11):1791–1796, 1986.
- [51] Werner J. A. Dahm, Clifford E. Frieler, and Grtar Tryggvason. Vortex structure and dynamics in the near field of a coaxial jet. *Journal of Fluid Mechanics*, 241:371–402, August 1992.
- [52] P. Meunier and E. Villermaux. How vortices mix. *Journal of Fluid Mechanics*, 476:213–222, 2003.
- [53] M. S. Roberts. *Experiments and Simulations on the Incompressible, Rayleigh-Taylor Instability with Small Wavelength Initial Perturbations*. PhD thesis, The University of Arizona, 2002.
- [54] Irvin Glassman, Richard A. Yetter, and Nick G. Glumac. *Combustion, Fifth Edition*. Academic Press, Waltham, MA, 5 edition edition, December 2014.
- [55] Chung K. Law. *Combustion Physics*. Cambridge University Press, Cambridge, 1 edition edition, August 2010.
- [56] G. P. Smith, D. M. Golden, M. Frenklach, N. M. Moriarity, B. Eiteneer, M. Goldenberg, C. T. Bowman, R. K. Hanson, S. Song, W. C. Gardiner Jr., V. V. Lissianski, and Z. Qin. GRI-Mech Home Page.

- [57] S. V. Sardeshmukh, W. E. Anderson, M. E. Harvazinski, and V Sankaran. Prediction of Combustion Instability with Detailed Chemical Kinetics. In *53rd AIAA Aerospace Sciences Meeting*, Kissimmee, Florida, January 2015.
- [58] Gerhard Herzberg. *Molecular Spectra and Molecular Structure: Spectra of Diatomic Molecules*. Krieger Pub Co, Malabar, Fla, 2 edition edition, January 1989.
- [59] V. Nori and J. Seitzman. Evaluation of Chemiluminescence as a Combustion Diagnostic under Varying Operating Conditions. In *46th AIAA Aerospace Sciences Meeting and Exhibit*, Reno, Nevada, USA, January 2008.
- [60] M. Schulze, T. Fiala, and T. Sattelmayer. Radiation Based Validation of Combustion Simulations and Comparison to Heat Release in Rocket Engines. In *54th AIAA Aerospace Sciences Meeting*, San Diego, California, USA, January 2016.
- [61] Habib N Najm, Phillip H Paul, Charles J Mueller, and Peter S Wyckoff. On the Adequacy of Certain Experimental Observables as Measurements of Flame Burning Rate. *Combustion and Flame*, 113(3):312–332, May 1998.
- [62] C. S. Panoutsos, Y. Hardalupas, and A. M. K. P. Taylor. Numerical evaluation of equivalence ratio measurement using OH and CH chemiluminescence in premixed and non-premixed methane-air flames. *Combustion and Flame*, 156(2):273–291, February 2009.
- [63] L. Haber, U. Vandsburger, W. Saunders, and V. Khanna. An Experimental Examination of the Relationship between Chemiluminescent Light Emissions and Heat-Release Rate under Non-Adiabatic Conditions. pages 20–1 – 20–8, 2001.
- [64] Y. Hardalupas and M. Orain. Local measurements of the time-dependent heat release rate and equivalence ratio using chemiluminescent emission from a flame. *Combustion and Flame*, 139(3):188–207, 2004.
- [65] Martin Lauer and Thomas Sattelmayer. On the Adequacy of Chemiluminescence as a Measure for Heat Release in Turbulent Flames With Mixture Gradients. *Journal of Engineering for Gas Turbines and Power*, 132(6):061502, 2010.
- [66] Michael J. Bedard, Tristan L. Fuller, Swanand V. Sardeshmukh, and William E. Anderson. Comparison Between Predicted and Measured Chemiluminescence in an Unstable Rocket Combustor. Krakow, Poland, 2015.
- [67] C. Tropea, A. L. Yarin, and J. F. Foss. *Handbook of Experimental Fluid Mechanics*. Springer, Verlag, Berlin, Heidelberg, 2007.
- [68] R. Shaw. Influence of Hole Dimensions on Static Pressure Measurements. *Journal of Fluid Mechanics*, 7(4):550–564, April 1960.
- [69] M. Frendi Zhang. Testing and Analysis of Sensor Ports. Technical report, May 2016.
- [70] D. R. Englund and W. B. Richards. The Infinite Line Pressure Probe. *NASA Publication*, 1984.

- [71] A. M. Hurst, R. O. Olsen, S. Goodman, J. Van De Weert, and T. Shang. An Experimental Frequency Response Characterization of MEMS Piezoresistive Pressure Transducers. In *Proceedings of ASME Turbo Expo*, Dusseldorf, Germany, June 2014.
- [72] Frank L. Pedrotti, Leno M. Pedrotti, and Leno S. Pedrotti. *Introduction to Optics*. Pearson, Upper Saddle River, N.J, 3 edition edition, April 2006.
- [73] William L. Oberkampf and Timothy G. Trucano. Verification and validation benchmarks. *Nuclear Engineering and Design*, 238(3):716–743, March 2008.
- [74] J. E. Portillo, J. C. Sisco, M. J. Corless, V Sankaran, and W. E. Anderson. Generalized Combustion Instability Model. In *42nd AIAA Joint Propulsion Conference & Exhibit*, Sacramento, California, July 2006.
- [75] B. T. Zinn. Longitudinal mode acoustic losses in short nozzles. *Journal of Sound and Vibration*, 22(1):93–105, May 1972.
- [76] P. J. Linstrom and W. G. Mallard. "Thermophysical Properties of Fluid Systems" by E.W. Lemmon, M.O. McLinden and D.G. Friend. In *NIST Chemistry WebBook*, number 69 in NIST Standard Reference Database. National Institute of Standards and Technology, Gaithersburg MD, 20899.
- [77] *Flow Measurement*. The American Society of Mechanical Engineers, New York, NY, asme ptc 19.5-2004 edition, July 2005.
- [78] Yunus A engel and John M Cimbalá. *Fluid mechanics fundamentals and applications*. McGraw-Hill Higher Education, Boston, Mass. [u.a., 2006. OCLC: 834846067.
- [79] Society of Automotive Engineers, Society of Automotive Engineers, and Subcommittee AC-9B. *SAE aerospace applied thermodynamics manual*. Society of Automotive Engineers, New York, 1989. OCLC: 28158279.
- [80] J. Nikuradse. Laws of Flow in Rough Pipes. Technical Memorandum 1292, National Advisory Committee for Aeronautics, Washington, D.C., U.S.A., November 1950.
- [81] S. Kangovi and R. Page. The turbulent flow through a sudden enlargement at subsonic speeds. page 4, 1977.
- [82] Maurice J. Zucrow and Joe D. Hoffman. *Gas Dynamics, Volume 1*. Wiley, New York, 1 edition edition, August 1976.
- [83] T. Tsuboi and H. Gg. Wagner. Homogeneous thermal oxidation of methane in reflected shock waves. *Symposium (International) on Combustion*, 15(1):883–890, January 1975.
- [84] Yunus A. Cengel and Afshin J. Ghajar. *Heat and Mass Transfer: Fundamentals and Applications*. McGraw-Hill Education, New York, NY, 5 edition edition, April 2014.
- [85] Michael J. Bedard. Detailed Measurement of ORSC Main Chamber Injector Dynamics, 2017.

- [86] Felix Kuehne. Quantitative Optical Investigation of Combustion Instabilities in a Model Rocket Motor vi Chemiluminescence. Interim Masters Report, Technische Universitat Munchen, Purdue University, May 2018.
- [87] Tristan Fuller. Review of Chemiluminescence as an Optical Diagnostic Tool for High Pressure Unstable Rockets. *Open Access Theses*, January 2015.
- [88] Wayne A. Fuller. *Introduction to Statistical Time Series*. Wiley-Interscience, New York, 2 edition edition, December 1995.
- [89] P. Welch. The use of fast Fourier transform for the estimation of power spectra: A method based on time averaging over short, modified periodograms. *IEEE Transactions on Audio and Electroacoustics*, 15(2):70–73, June 1967.
- [90] H. He and D. J. Thomson. The Canonical Bicoherence Part I: Definition, Multitaper Estimation, and Statistics. *IEEE Transactions on Signal Processing*, 57(4):1273–1284, April 2009.
- [91] J. M. Mendel. Tutorial on higher-order statistics (spectra) in signal processing and system theory: theoretical results and some applications. *Proceedings of the IEEE*, 79(3):278–305, March 1991.
- [92] J. M. Lilly and S. C. Olhede. Generalized Morse Wavelets as a Superfamily of Analytic Wavelets. *IEEE Transactions on Signal Processing*, 60(11):6036–6041, November 2012.
- [93] L. Marple. Computing the discrete-time "analytic" signal via FFT. *IEEE Transactions on Signal Processing*, 47(9):2600–2603, 1999.
- [94] Andrew C. Noble, Krishna K. Venkatesan, Galen B. King, Normand M. Laurendeau, and Michael W. Renfro. Singular Spectrum Analysis Applied to Time-Series Measurements in a Self-Excited Tube Combustor. *Journal of Propulsion and Power*, 25(5):1148–1151, September 2009.
- [95] G. Consolo, V. Puliafito, G. Finocchio, L. Lopez-Diaz, R. Zivieri, L. Giovannini, F. Nizzoli, G. Valenti, and B. Azzerboni. Combined Frequency-Amplitude Non-linear Modulation: Theory and Applications. *IEEE Transactions on Magnetics*, 46(9):3629–3634, 2010.
- [96] W. E. Anderson, S. V. Sardeshmukh, T. L. Fuller, and A. Pons. AFOSR Final Report. Project Report, AFOSR, Purdue University, West Lafayette, IN, January 2019.
- [97] Swanand V. Sardeshmukh, Cheng Huang, William E. Anderson, Matthew E. Harvazinski, and Venke Sankaran. Impact of Chemical Kinetics Mechanisms on the Predictions of Bluff Body Stabilized Flames. In *54th AIAA Aerospace Sciences Meeting*, AIAA SciTech Forum. American Institute of Aeronautics and Astronautics, January 2016.
- [98] D. C. Wilcox. Formulation of the k-w Turbulence Model Revisited. *AIAA Journal*, 46(11):2823–2838, 2008.
- [99] Bonnie J. McBride, Martin A. Reno, and Sanford Gordon. Coefficients for calculating thermodynamic and transport properties of individual species - NASA-TM-4513, 1993.

- [100] Ken H. Yu, Arnaud Trounev, and John W. Daily. Low-frequency pressure oscillations in a model ramjet combustor. *Journal of Fluid Mechanics*, 232:47–72, November 1991.
- [101] R. A. Svehla. Estimated Viscosities and Thermal Conductivities of Gases at High Temperatures. Technical Report, NASA, Washington, D.C., U.S.A., 1962.

A. SELECTED IMPORTANT MECHANICS

A.1 Diffusion

The binary diffusion coefficient is determined by:

$$\mathcal{D}_{AB} = \frac{3\sqrt{4\pi k_B T / MW_{AB}}}{16(P/R_u T)\pi\sigma_{AB}^2\Omega_D} f_D \quad (\text{A.1})$$

where k_B is the Boltzmann constant and f_D is a theoretical correction factor that is usually very close to unity. The combined molecular weight is given by $MW_{AB} = 2[MW_A^{-1} + MW_B^{-1}]^{-1}$. The effective hard-sphere collision diameter is $\sigma_{AB} = (\sigma_A + \sigma_B)/2$. The collision integral Ω_D is the result of kinetic theory calculation and is based on the Lennard-Jones potential. The collision integral data has been curve-fit for ideal gases using the following relation [32]:

$$\Omega_D = \frac{A}{(T^*)^B} + \frac{C}{\exp(DT^*)} + \frac{E}{\exp(FT^*)} + \frac{G}{\exp(HT^*)} \quad (\text{A.2})$$

where the dimensionless temperature is defined by $T^* = k_B T / \epsilon_{AB}$. The effective potential well depth for collisions of gas A and gas B is $\epsilon_{AB} = \sqrt{\epsilon_A \epsilon_B}$. The Lennard-Jones constants can be found in Table B.1. The coefficients of Equation equation (A.2) are:

$$\begin{aligned} A &= 1.06036, & B &= 0.15610, & C &= 0.19300, & D &= 0.47635, \\ E &= 1.03587, & F &= 1.52996, & G &= 1.76474, & H &= 3.89411 \end{aligned}$$

The transport properties of the gases are within 1% of the dilute limit if the gas densities do not exceed the reduced density value [33]:

$$\rho^* = \frac{5}{16\sqrt{8}} \frac{1}{\lambda^* \Omega_\mu} \quad (\text{A.3})$$

where Ω_μ is the value of the second collision integral for viscosity. The reduced pressure in terms of gas kinetic theory is expressed as $\rho^* = (\rho\sigma_{AB}^3 N_A) / MW$. The

collision integral values can be found in Table B.2. $\lambda^* = \lambda/\sigma$ is the normalized mean free path, which can also be described as the Knudsen number particle collision scales. Furthermore the mean free path can be calculated using Equation equation (A.4) [33]:

$$\lambda = \frac{3\mu}{\rho} \sqrt{\frac{\pi MW}{8k_B T(1000N_A)}} \quad (\text{A.4})$$

where N_A is Avogadro's number and the factor of 1000 is to compensate for the units of molecular weight (g/mol).

The viscosity of a dilute gas can be well approximated with gas kinetic theory if needed [34]:

$$\mu = \frac{5}{16} \frac{\sqrt{(\pi(MW/(1000N_A))k_B T)}}{\pi\sigma^2\Omega_\mu} \quad (\text{A.5})$$

A.2 Acoustic Theory Pertaining to Circular Ducts

A.2.1 1D Transfer Matrices for Selected Geometries of a Duct

Constant area duct - distributed element

$$\begin{bmatrix} P \\ u \end{bmatrix}_{z=1} = e^{-jMk_c l} \begin{bmatrix} \cos(k_c l) & jY \sin(k_c l) \\ j/Y \sin(k_c l) & \cos(k_c l) \end{bmatrix} \begin{bmatrix} P \\ u \end{bmatrix}_{z=0} \quad (\text{A.6})$$

The specific impedance is denoted by $Y = Y_0 \left\{ 1 - j \frac{\alpha(M)}{k_0} \right\}$, where the change in impedance is determined by the attenuation coefficient $\alpha(M)$. The wave propagation constant is also based on the convective velocity of the flow; $k_c = \frac{k_0 - j\alpha(M)}{1 - M^2}$. The attenuation coefficient is a function of the Fanning friction factor and the diameter of the duct: $\alpha(M) = \alpha + \frac{FrM}{2D}$.

Sudden Area Change

$$\begin{bmatrix} P \\ u \end{bmatrix}_{z=1} = \begin{bmatrix} 1 & j\omega L \\ 0 & 1 \end{bmatrix} \begin{bmatrix} P \\ u \end{bmatrix}_{z=0} \quad (\text{A.7})$$

where L is the Karal correction factor accounting for the inductance effect of the discontinuity: $L = l_{eq}/(\pi r_0^2)$, $l_{eq} = (8r_0 H(\alpha))/(3\pi)$ and $H(\alpha) \cong 1 - \alpha$, where $\alpha = r_0/r$; r_0 being the radius of the smaller tube.

Lumped System

In line (series) element:

$$\begin{bmatrix} P \\ u \end{bmatrix}_{z=1} = \begin{bmatrix} 1 & Z_1 \\ 0 & 1 \end{bmatrix} \begin{bmatrix} P \\ u \end{bmatrix}_{z=0} \quad (\text{A.8})$$

Shunt (parallel) element:

$$\begin{bmatrix} P \\ u \end{bmatrix}_{z=1} = \begin{bmatrix} 1 & 0 \\ 1/Z_1 & 1 \end{bmatrix} \begin{bmatrix} P \\ u \end{bmatrix}_{z=0} \quad (\text{A.9})$$

Z is the impedance of the lumped acoustic element. The impedance takes on the form of any lumped element, such as an inertive, capacitive or a compound element like a Helmholtz resonator. The equivalent length of the neck in the Helmholtz resonator is the same used for Equation 2.5.

$$Z_{inertance} = \frac{j\omega L}{A_{cross-section}} \quad (\text{A.10})$$

$$Z_{capacitance} = \frac{c^2}{j\omega V} = \frac{\gamma P}{j\omega V \rho} \quad (\text{A.11})$$

$$Z_{Helmholtz} = j \left(\omega \frac{L_{eq}}{A_{neck}} - \frac{c^2}{\omega V} \right) + \frac{\omega^2}{\pi c} \quad (\text{A.12})$$

A.2.2 Three Dimensional Waves in Inviscid Moving Medium within a Circular Duct

The arguments corresponding to the zeros of the derivative of the Bessel function of the first kind are:

Table A.1.: Arguments of the functions associated with transverse (m) and radial (n) modes.

n/m	0	1	2	3	4	5
0	0	1.8412	3.0542	4.2012	5.3176	6.4156
1	3.8317	5.3314	6.7061	8.0152	9.2824	10.5199
2	7.0156	8.5363	9.9695	11.3459	12.6819	13.9872
3	10.1730	11.7060	13.1704	14.5859	15.9641	17.3128

B. DATA TABLES

Table B.1.: Lennard-Jones parameters for selected species [101].

<i>Species</i>	σ [Å]	ϵ/k_B [K]	<i>Species</i>	σ [Å]	ϵ/k_B [K]
<i>Air</i>	3.711	78.6	<i>n</i> – C_5H_{12}	5.784	341.1
<i>Al</i>	2.655	2750	C_6H_6	5.349	412.3
<i>Ar</i>	3.542	93.3	C_6H_{12}	6.182	297.1
<i>B</i>	2.265	3331	<i>n</i> – C_6H_{14}	5.949	399.3
<i>BO</i>	2.944	596	<i>H</i>	2.708	37.0
B_2O_3	4.158	2092	H_2	2.827	59.7
<i>C</i>	3.385	30.6	H_2O	2.641	809.1
<i>CH</i>	3.370	68.7	H_2O_2	4.196	398.3
CH_3OH	3.626	481.8	<i>He</i>	2.551	10.22
CH_4	3.758	148.6	<i>N</i>	3.298	71.4
<i>CN</i>	3.856	75	NH_3	2.900	558.3
<i>CO</i>	3.690	91.7	<i>NO</i>	3.492	116.7
CO_2	3.941	195.2	N_2	3.798	71.4
C_2H_2	4.033	231.8	N_2O	3.828	232.4
C_2H_4	4.163	224.7	<i>O</i>	3.050	106.7
C_2H_6	4.443	215.7	<i>OH</i>	3.147	79.8
C_3H_8	5.118	237.1	O_2	3.467	106.7
<i>n</i> – C_3H_7OH	4.549	576.7	<i>S</i>	3.839	847
<i>n</i> – C_4H_{10}	4.687	531.4	<i>SO</i>	3.993	301
<i>iso</i> – C_4H_{10}	5.278	330.1	SO_2	4.112	335.4

Table B.2.: Collision integrals for diffusivity, viscosity and thermal conductivity based on Lennard-Jones potential.

$k_B T/\epsilon$	Ω_D	Ω_μ	$k_B T/\epsilon$	Ω_D	Ω_μ
0.30	2.662	2.785	2.70	0.9770	1.069
0.35	2.476	2.628	2.80	0.9672	1.058
0.40	2.318	2.492	2.90	0.9576	1.048
0.45	2.184	2.368	3.00	0.9490	1.039
0.50	2.066	2.257	3.10	0.9406	1.030
0.55	1.966	2.156	3.20	0.9328	1.022
0.60	1.877	2.065	3.30	0.9256	1.014
0.65	1.798	1.982	3.40	0.9186	1.007
0.70	1.729	1.908	3.50	0.9120	0.9999
0.75	1.667	1.841	3.60	0.9058	0.9932
0.80	1.612	1.780	3.70	0.8998	0.9870
0.85	1.562	1.725	3.80	0.8942	0.9811
0.90	1.517	1.675	3.90	0.8888	0.9755
0.95	1.476	1.629	4.00	0.8836	0.9700
1.00	1.439	1.587	4.10	0.8788	0.9649
1.05	1.406	1.549	4.20	0.8740	0.9600
1.10	1.375	1.514	4.30	0.8694	0.9553
1.15	1.346	1.482	4.40	0.8652	0.9507
1.20	1.320	1.452	4.50	0.8610	0.9464
1.25	1.296	1.424	4.60	0.8568	0.9422
1.30	1.273	1.399	4.70	0.8530	0.9382
1.35	1.253	1.375	4.80	0.8492	0.9343

continued on next page

Table B.2.: *continued*

$k_B T/\epsilon$	Ω_D	Ω_μ	$k_B T/\epsilon$	Ω_D	Ω_μ
1.40	1.233	1.353	4.90	0.8456	0.9305
1.45	1.215	1.333	5.00	0.8422	0.9269
1.50	1.198	1.314	6.00	0.8124	0.8963
1.55	1.182	1.296	7.0	0.7896	0.8727
1.60	1.167	1.279	8.0	0.7712	0.8538
1.65	1.153	1.264	9.0	0.7556	0.8379
1.70	1.140	1.248	10.0	0.7424	0.8242
1.75	1.128	1.234	20.0	0.6640	0.7432
1.80	1.116	1.221	30.0	0.6232	0.7005
1.85	1.105	1.209	40.0	0.5960	0.6718
1.90	1.094	1.197	50.0	0.5756	0.6504
1.95	1.084	1.186	60.0	0.5596	0.6335
2.00	1.075	1.175	70.0	0.5464	0.6194
2.10	1.057	1.156	80.0	0.5352	0.6076
2.20	1.041	1.138	90.0	0.5256	0.5973
2.30	1.026	1.122	100.0	0.5170	0.5882
2.40	1.012	1.107	200.0	0.4644	0.5320
2.50	0.9996	1.093	300.0	0.4360	0.5016
2.60	0.9878	1.081	400.0	0.4172	0.4811

Table B.3.: HAMSTER density ratio for different propellant temperatures [K].

T_{ox} \ T_f	250	260	270	280	290	300	310	320
250	1.95	2.04	2.13	2.21	2.30	2.38	2.47	2.55
300	1.61	1.68	1.76	1.83	1.90	1.97	2.04	2.11
350	1.37	1.44	1.50	1.56	1.62	1.68	1.74	1.80
400	1.20	1.25	1.31	1.36	1.42	1.47	1.52	1.57
450	1.07	1.11	1.16	1.21	1.26	1.30	1.35	1.39
500	0.96	1.00	1.04	1.09	1.13	1.17	1.21	1.25
550	0.87	0.91	0.95	0.99	1.03	1.06	1.10	1.14
600	0.80	0.83	0.87	0.90	0.94	0.97	1.01	1.04
650	0.74	0.77	0.80	0.83	0.87	0.90	0.93	0.96
700	0.68	0.71	0.74	0.77	0.81	0.83	0.86	0.89
750	0.64	0.67	0.70	0.72	0.75	0.78	0.81	0.84
800	0.60	0.63	0.65	0.68	0.71	0.73	0.76	0.78

Table B.4.: HAMSTER velocity ratio for different propellant temperatures [K].

T_{ox} \ T_f	250	260	270	280	290	300	310	320
250	0.70	0.67	0.64	0.61	0.59	0.57	0.55	0.53
300	0.84	0.81	0.77	0.74	0.71	0.69	0.67	0.64
350	0.99	0.94	0.91	0.87	0.84	0.81	0.78	0.75
400	1.13	1.08	1.04	1.00	0.96	0.93	0.89	0.86
450	1.27	1.22	1.17	1.12	1.08	1.04	1.01	0.97
500	1.42	1.36	1.30	1.25	1.20	1.16	1.12	1.08
550	1.56	1.49	1.43	1.38	1.32	1.28	1.23	1.19
600	1.70	1.63	1.56	1.50	1.44	1.39	1.34	1.30
650	1.84	1.77	1.69	1.63	1.56	1.51	1.46	1.41
700	1.99	1.90	1.82	1.75	1.68	1.63	1.57	1.52
750	2.13	2.04	1.95	1.88	1.80	1.74	1.68	1.62
800	2.27	2.17	2.08	2.00	1.92	1.86	1.79	1.73

Table B.5.: HAMSTER momentum flux ratio for different propellant temperatures [K].

T_{ox} \ T_f	250	260	270	280	290	300	310	320
250	0.94	0.90	0.87	0.83	0.80	0.77	0.75	0.72
300	1.14	1.09	1.05	1.01	0.97	0.94	0.90	0.87
350	1.34	1.28	1.23	1.18	1.14	1.10	1.06	1.02
400	1.54	1.47	1.41	1.35	1.30	1.26	1.21	1.17
450	1.73	1.66	1.59	1.53	1.47	1.42	1.37	1.32
500	1.92	1.84	1.77	1.70	1.63	1.58	1.52	1.47
550	2.12	2.03	1.94	1.87	1.79	1.73	1.67	1.62
600	2.31	2.21	2.12	2.04	1.96	1.89	1.83	1.76
650	2.50	2.40	2.30	2.21	2.12	2.05	1.98	1.91
700	2.70	2.58	2.48	2.38	2.29	2.21	2.13	2.06
750	2.89	2.76	2.65	2.55	2.45	2.36	2.28	2.21
800	3.08	2.95	2.83	2.72	2.61	2.52	2.43	2.35

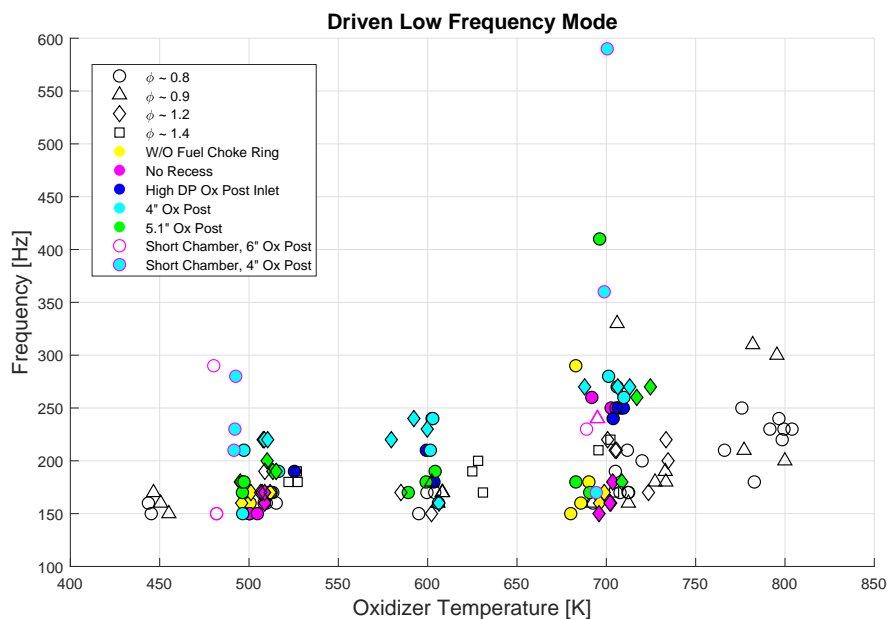


Figure C.2.: Thermoacoustic chug frequency as a function of oxidizer temperature.

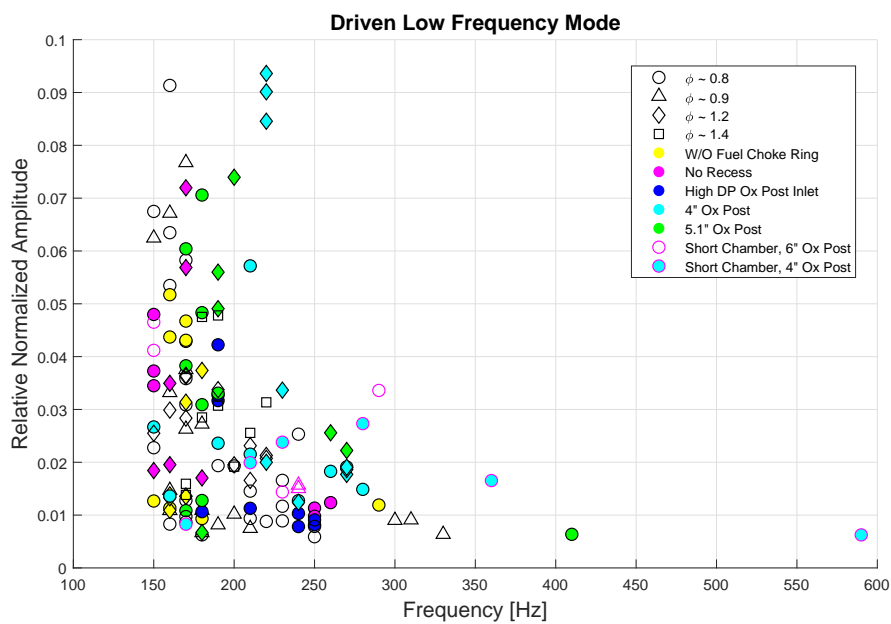


Figure C.3.: Thermoacoustic chug amplitude as a function of frequency.

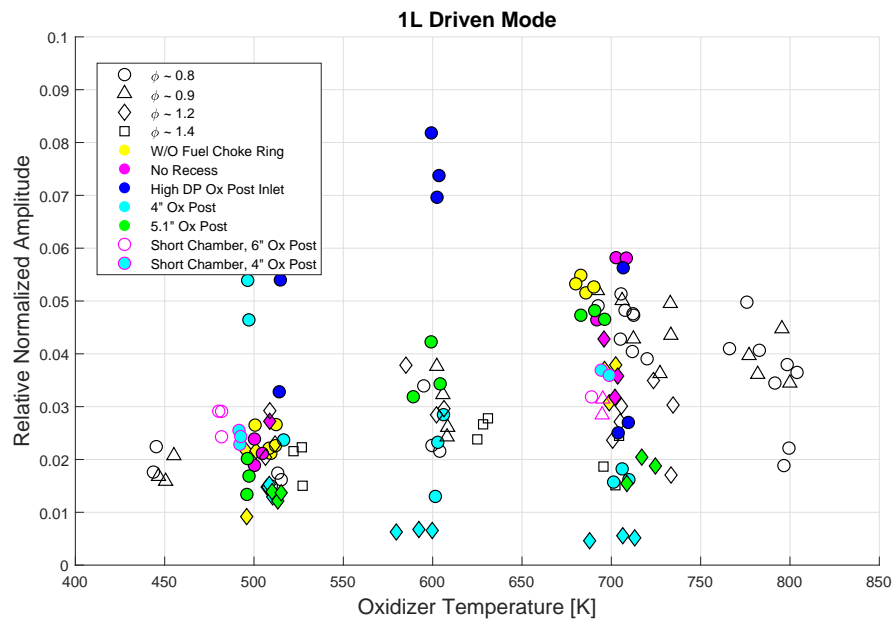


Figure C.4.: Thermoacoustic fundamental mode amplitude as a function of oxidizer temperature.

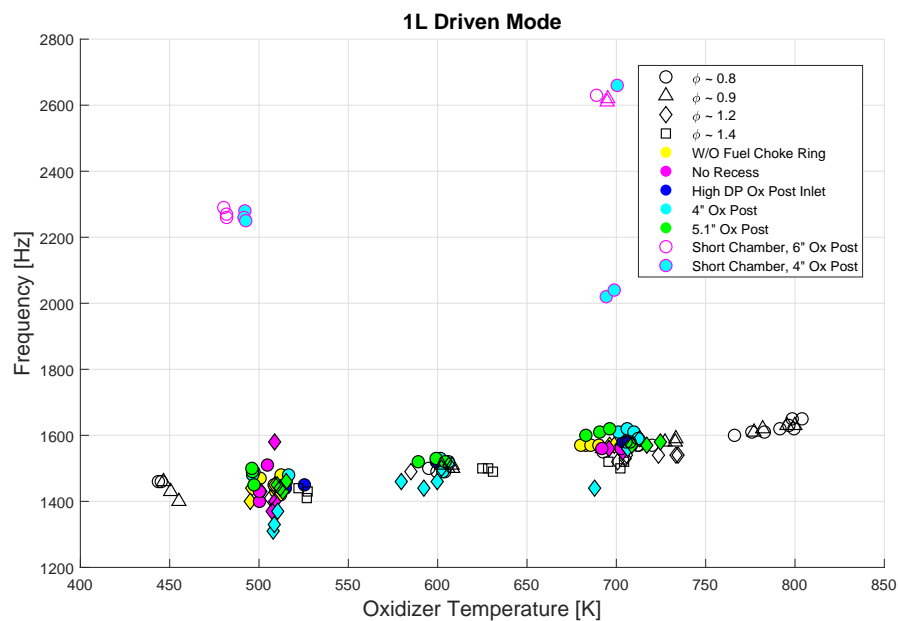


Figure C.5.: Thermoacoustic fundamental mode frequency as a function of oxidizer temperature.

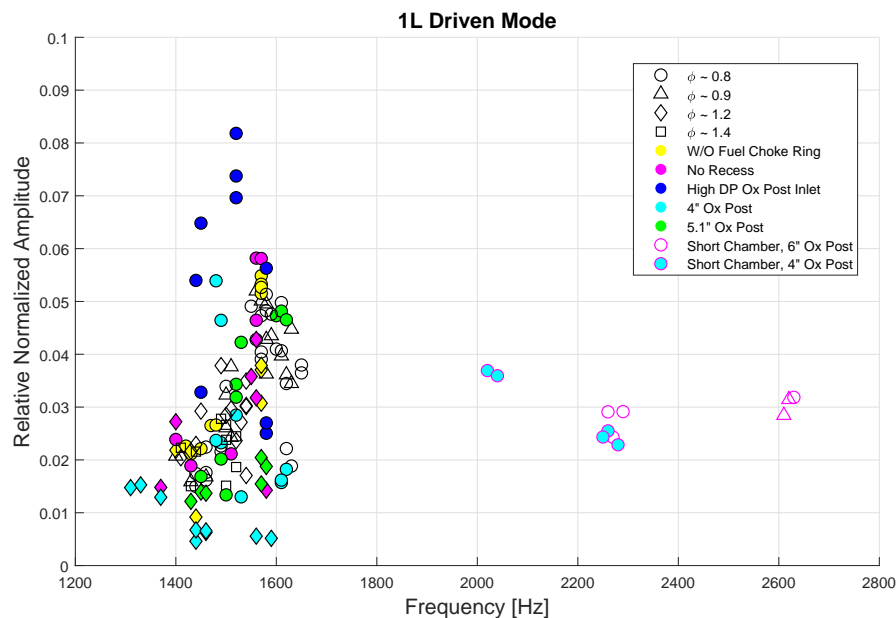


Figure C.6.: Thermoacoustic fundamental mode amplitude as a function of frequency.

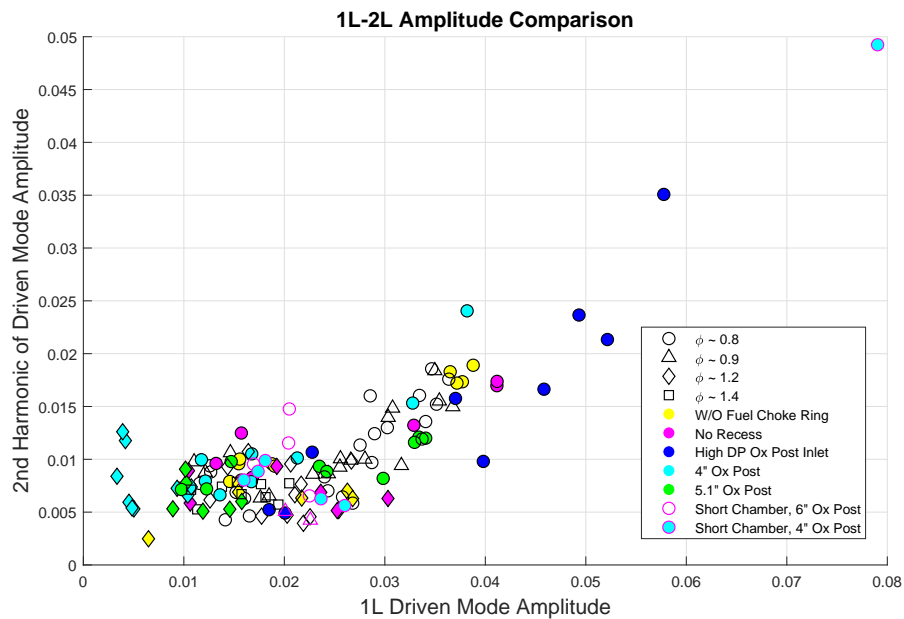


Figure C.7.: Thermoacoustic mode amplitude comparison for all test cases, showing the approximate threshold at which a strong thermoacoustic coupling takes place.

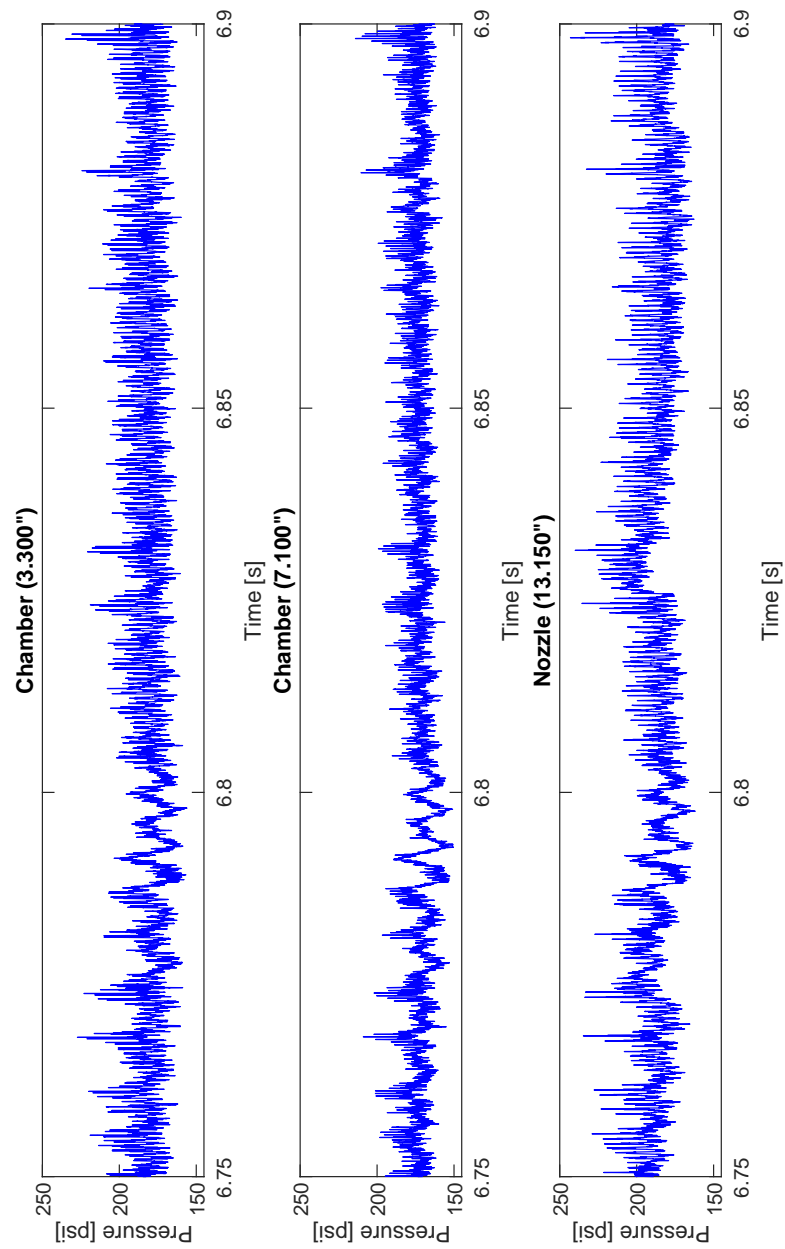


Figure C.8.: Raw pressure data acquired at the aft end of the chamber, showing the entropic fluctuations at the nozzle end, but minimally affecting the upstream mechanics.

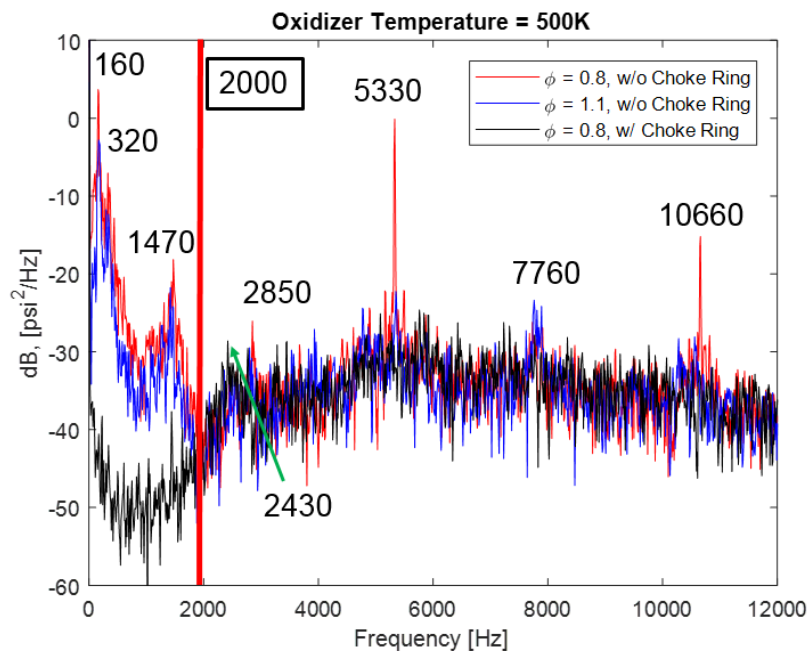


Figure C.9.: PSDs of the fuel manifold response with and without the fuel manifold choke ring at an oxidizer temperature of 500K.

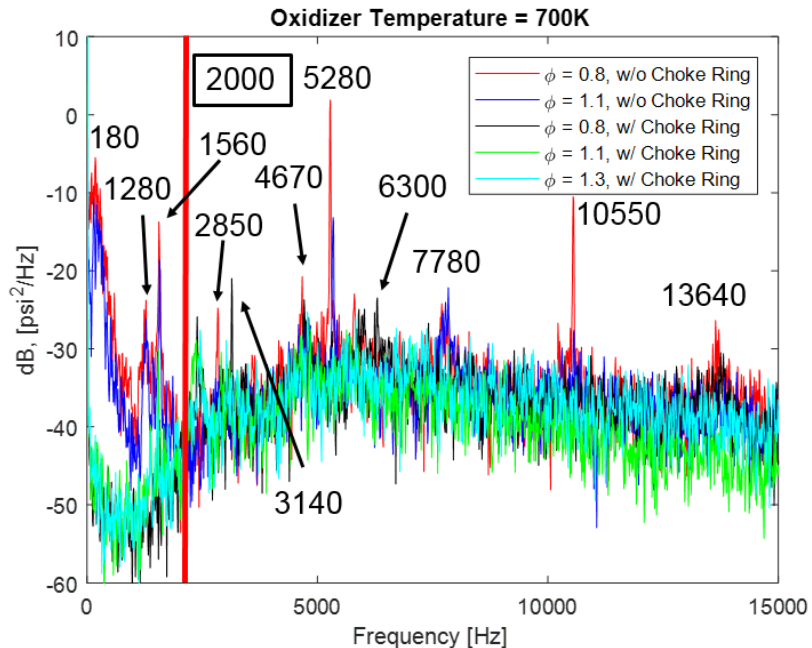


Figure C.10.: PSDs of the fuel manifold response with and without the fuel manifold choke ring at an oxidizer temperature of 700K.

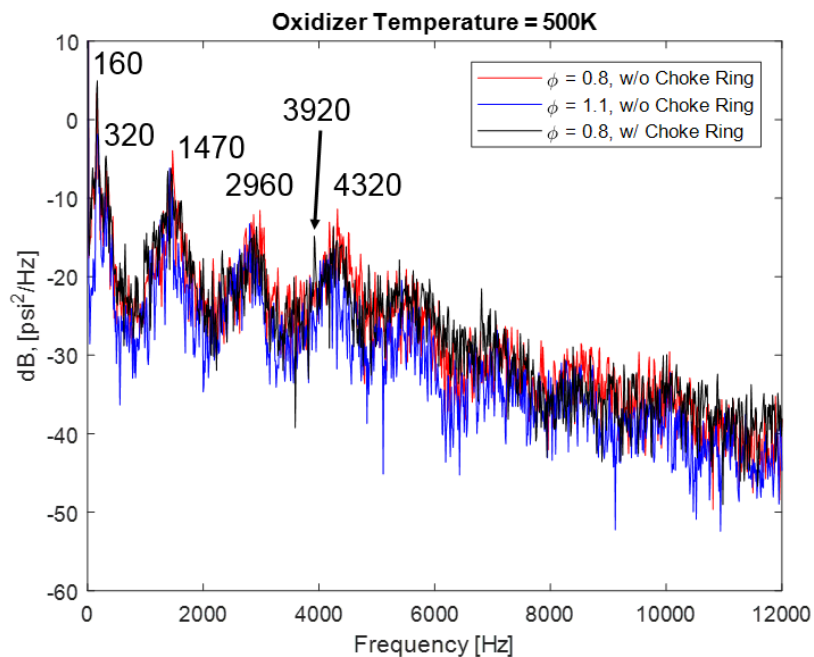


Figure C.11.: PSDs of the injector recess response with and without the fuel manifold choke ring at an oxidizer temperature of 500K.

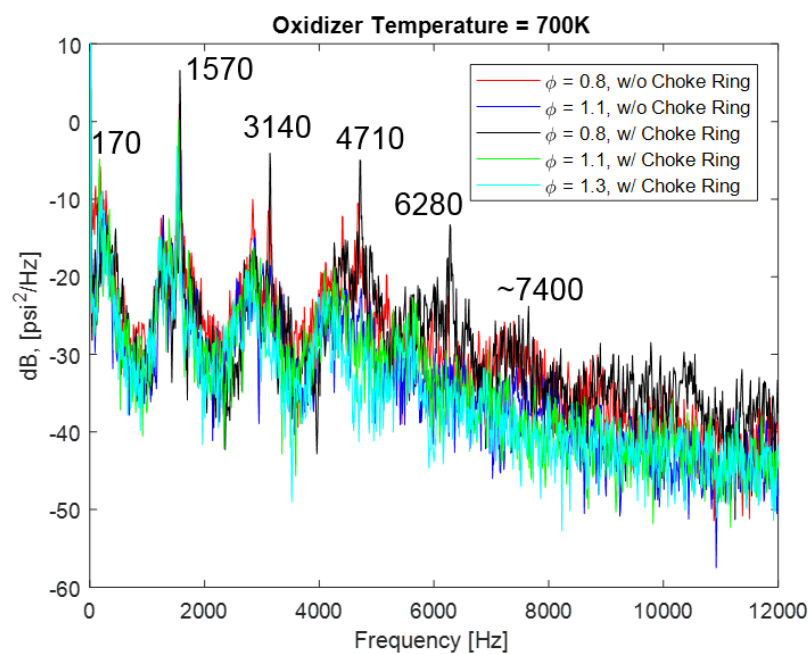


Figure C.12.: PSDs of the injector recess response with and without the fuel manifold choke ring at an oxidizer temperature of 700K.

D. TECHNICAL DATA

D.1 PMT Calibration Curves [86]

Data collected, compiled and researched with assistance of Felix Kuehne.

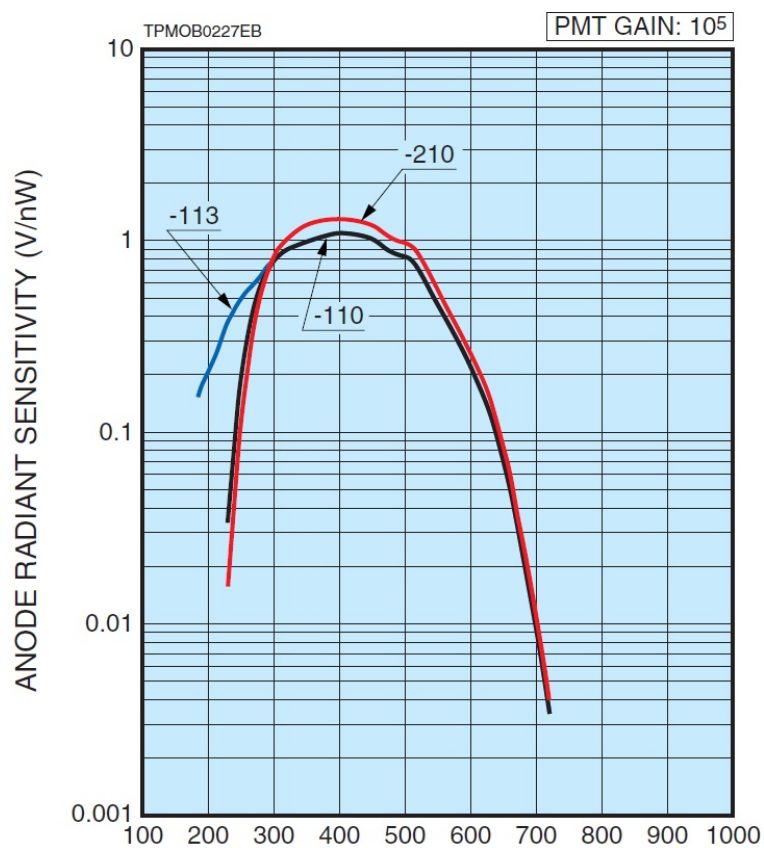


Figure D.1.: Spectral responsivity of the H11903-210 PMTs from Hamamatsu.

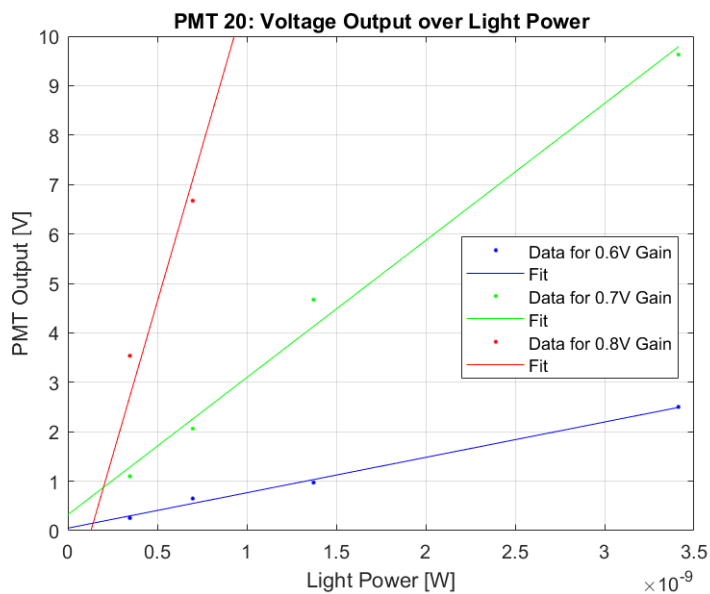


Figure D.2.: Power to voltage calibration check for the PMTs over a series of gains set.

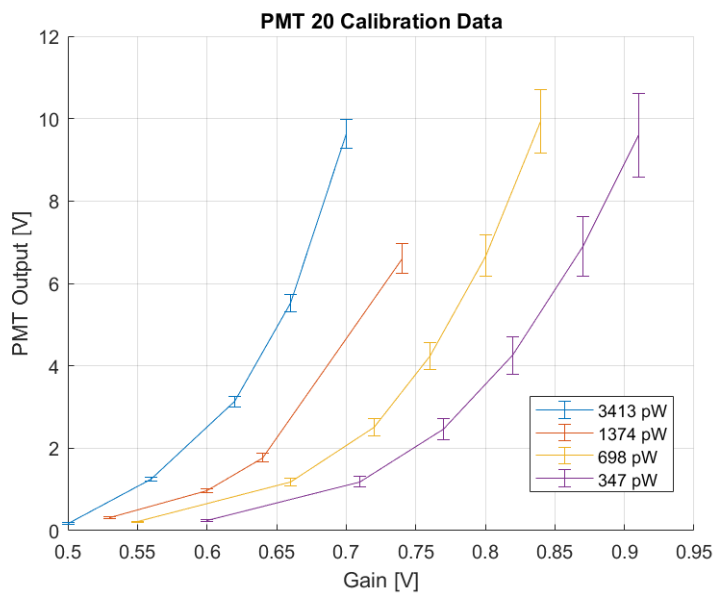


Figure D.3.: Voltage output calibration check versus gain for the PMTs for different levels of inputted light power.

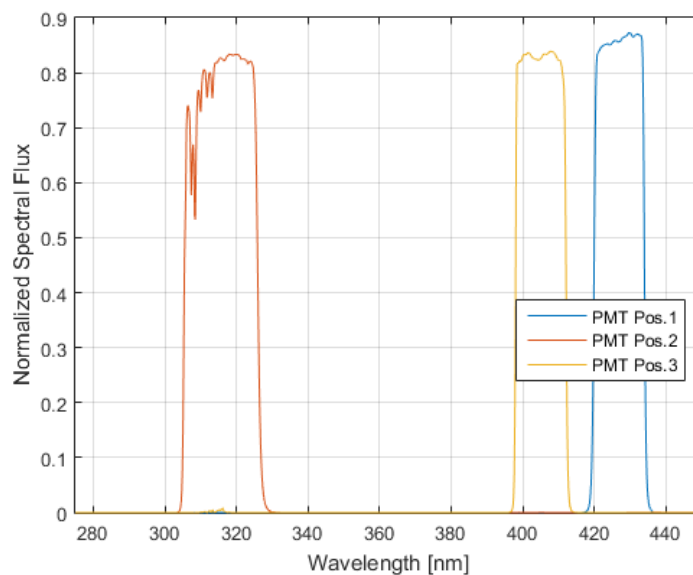


Figure D.4.: Normalized spectral flux transmission into the PMTs over the selected bandwidths corresponding to OH^* , CH^* and truncated band of CO_2^* .

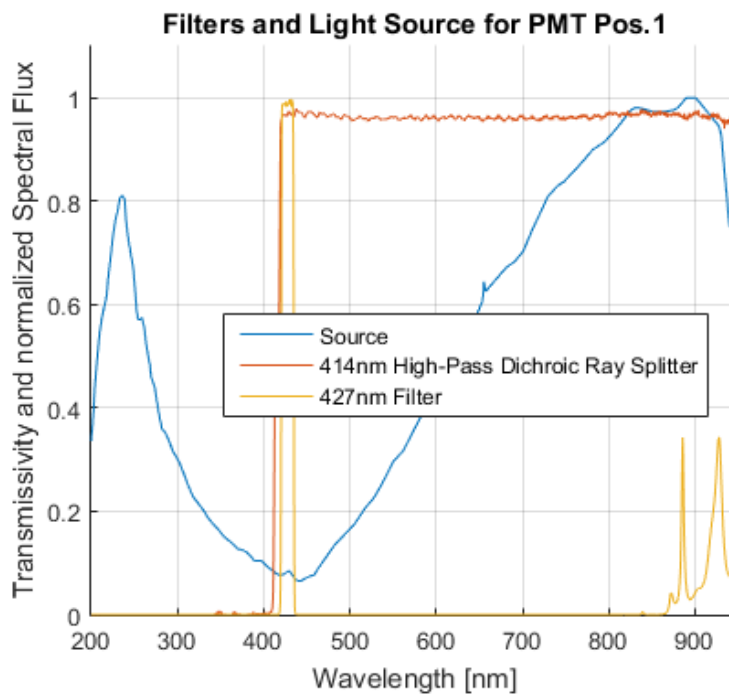


Figure D.5.: Normalized spectral transmission calibration for PMT collecting CH^* chemiluminescence signals.

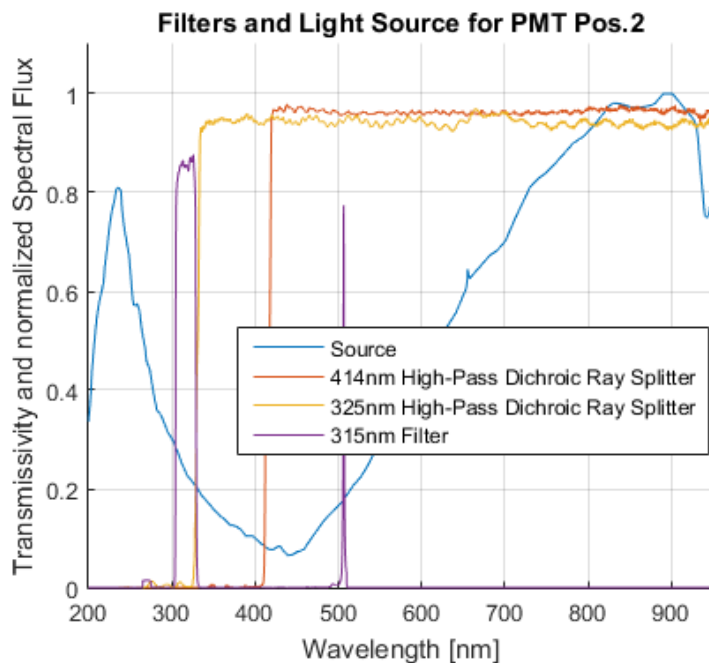


Figure D.6.: Normalized spectral transmission calibration for PMT collecting OH^* chemiluminescence signals.

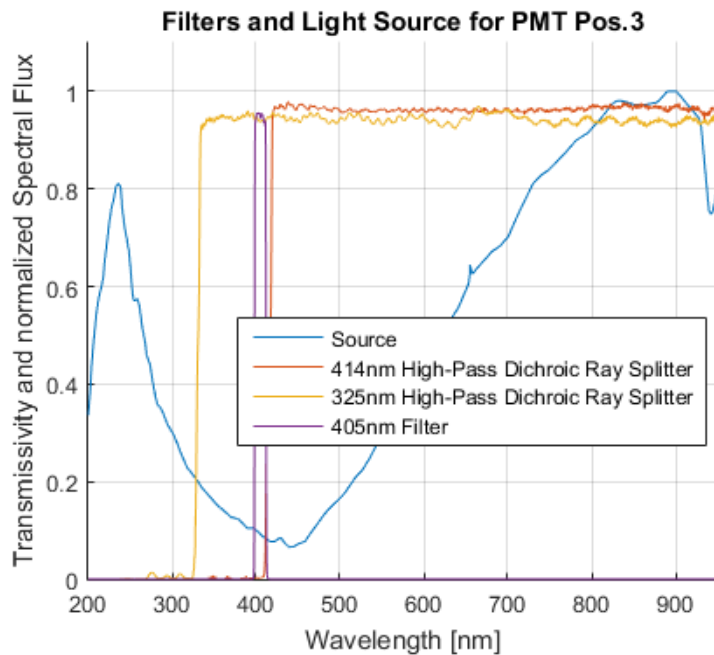
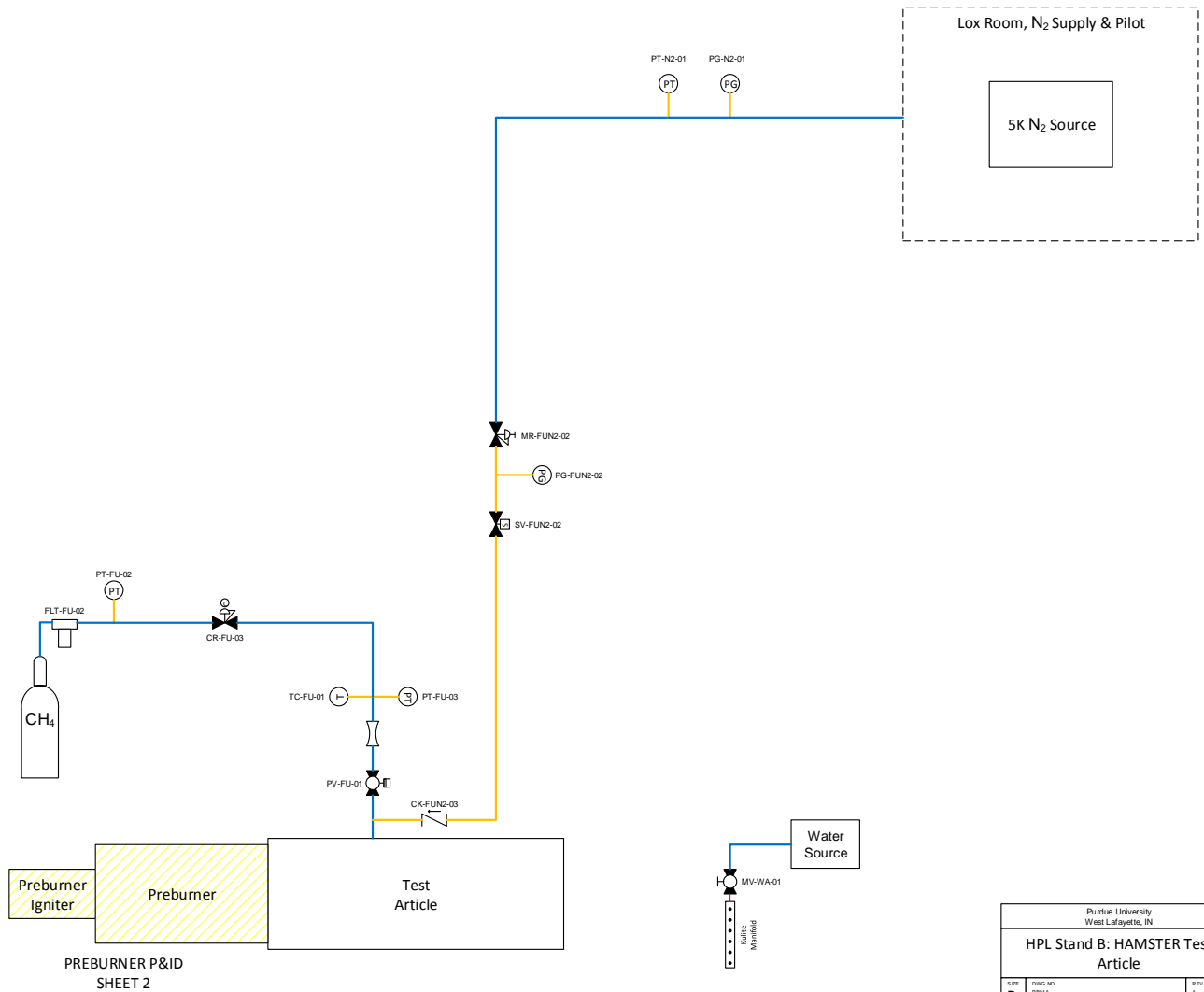


Figure D.7.: Normalized spectral transmission calibration for PMT collecting truncated band of CO_2^* chemiluminescence signals.

E. PLUMBING AND INSTRUMENTATION DIAGRAMS

LEGEND

- VALVE (NORMALLY OPEN)
- VALVE (NORMALLY CLOSED)
- BALL VALVE (NORMALLY OPEN)
- BALL VALVE (NORMALLY CLOSED)
- GLOBE VALVE (NORMALLY CLOSED)
- BUTTERFLY VALVE
- NEEDLE VALVE
- NEEDLE VALVE (DOWN PAPER LOAD)
- THREE WAY VALVE
- CHECK VALVE
- RELIEF VALVE
- MANUAL VALVE OPERATOR
- SOLENOID VALVE OPERATOR
- PNEUMATIC VALVE OPERATOR
- CALCULATING VENTURI
- FLOW MEASUREMENT DEVICE
- PRESSURE REGULATOR
- PRESSURE REGULATOR (HAND LOADED)
- PRESSURE REGULATOR (COMPUTER LOADED)
- QUICK DISCONNECT
- PUMP
- VPS PUMP
- Y STRAINER
- TUBING CONNECTOR
- FILTER
- O-RING PLATE
- THERMOCOUPLE
- PRESSURE TRANSDUCER
- PRESSURE GAUGE
- DIFFERENTIAL PRESSURE TRANSDUCER
- HIGH PRESSURE TRANSDUCER
- O2 PROBE
- SAFETY PIN
- 4" Pipe
- 3" Pipe
- 2" Pipe
- 1" Pipe
- 3/4" Tubing
- 1/2" Tubing
- 3/8" Tubing
- 1/4" Tubing
- Undersized Tubing Size

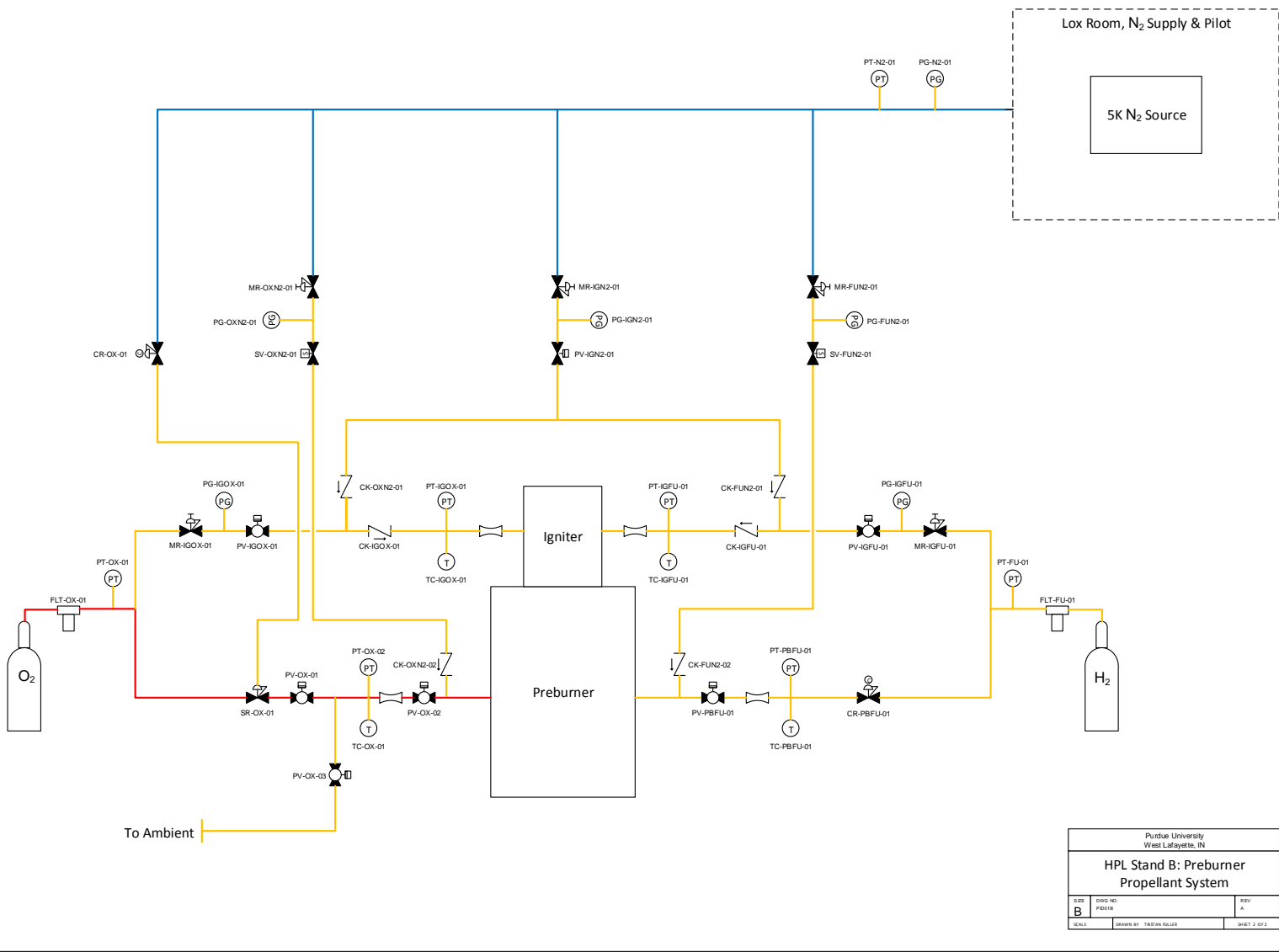


PREBURNER P&ID SHEET 2

Purdue University West Lafayette, IN		
HPL Stand B: HAMSTER Test Article		
SIZE B	DWG. NO. P81A	REV. A
SCALE	DRAWN BY TREDAN ILLER	SHEET 1 OF 2

LEGEND

- VALVE (NORMALLY OPEN)
- VALVE (NORMALLY CLOSED)
- BALL VALVE (NORMALLY OPEN)
- BALL VALVE (NORMALLY CLOSED)
- GLOBE VALVE (NORMALLY CLOSED)
- BUTTERFLY VALVE
- NEEDLE VALVE
- NEEDLE VALVE (LOW FLOW / LOW OR)
- TAPERED SEAT VALVE
- CHECK VALVE
- RELIEF VALVE
- MANUAL VALVE OPERATOR
- SOLENOID VALVE OPERATOR
- PNEUMATIC VALVE OPERATOR
- CAVITATING VENTURI
- FLOW MEASUREMENT DEVICE
- PRESSURE REGULATOR
- PRESSURE REGULATOR (HAND LOCKED)
- PRESSURE REGULATOR (COMPUTER LOCKED)
- QUICK DISCONNECT
- PUMP
- VCS PUMP
- Y STRAINER
- TUBING/FITTING
- FILTER
- O-RING/FLANGE
- THERMOCOUPLE
- PRESSURE TRANSDUCER
- PRESSURE GAUGE
- DIFFERENTIAL PRESSURE TRANSDUCER
- HIGH FREQUENCY PRESSURE TRANSDUCER
- OR PROBE
- SAFETY PIN
- 4" Pipe
- 3" Pipe
- 2" Pipe
- 1" Tubing
- 3/4" Tubing
- 1/2" Tubing
- 3/8" Tubing
- 1/4" Tubing
- Undersized Tubing Size



Purdue University West Lafayette, IN		
HPL Stand B: Preburner Propellant System		
DWS NO. P0010	REV. A	
SCALE	DRAWN BY: TREDAN FULLER	SHEET 2 OF 2